Towards a Complete Census of the Compton-thick AGN Population in the Local Universe

Nur Adlyka Binti Ainul Annuar

A Thesis presented for the degree of
Doctor of Philosophy

Centre for Extragalactic Astronomy
Department of Physics
Durham University
United Kingdom

July 2017

Dedicated to

My beloved husband, Adli;

parents;

brother and sisters.

Towards a Complete Census of the Compton-thick AGN Population in the Local Universe

Nur Adlyka Binti Ainul Annuar

Submitted for the degree of Doctor of Philosophy

July 2017

Abstract

Many studies have shown that the majority of accretion onto supermassive black holes; i.e., active galactic nuclei (AGNs) are hidden from our view by obscuring "torus" of gas and dust with column densities of $N_{\rm H} \geq 10^{22}$ cm^{-2}. Arguably, the most efficient method of identifying AGNs is in the X-ray waveband, where even heavily obscured AGNs have been detected. However, a significant fraction of the AGN population have remained hidden in X-rays due to their extreme torus column densities along our line of sight, $N_{\rm H} \gtrsim 1.5 \times 10^{24}$ cm^{-2}; i.e., Compton-thick (CT). These CTAGNs are predicted to be abundant but their census is far from complete, even in our local universe, due the challenge in identifying them because of their faint fluxes.

In this thesis, I present an updated census of the CTAGN population and the $N_{\rm H}$ distribution of AGN in our local universe, using a volume-limited mid-infrared selected sample of 20 AGNs within $D = 15$ Mpc. The volume-limited selection within a relatively small volume means that the AGN sample is less limited by flux (unlike most AGN samples), and the mid-infrared selection means that it is unbiased against both torus and host galaxy obscuration (unlike X-ray and optically selected AGN samples, respectively). The $N_{\rm H}$ values for each AGN are directly measured, by performing broadband X-ray spectroscopy (up to $\sim$2 orders of magnitude in energy range) using data from multiple focusing X-ray observatories, primarily *NuSTAR* in combination with *Chandra* and *XMM-Newton*. For cases in which this is not possible, I use indirect multiwavelength techniques to identify potential CTAGNs. These techniques involve comparing the observed 2–10 keV fluxes from the AGNs to the [OIII]λ5007Å, 12μm, and [NeV]λ14.32μm fluxes, which act as indicators for the AGN intrinsic emission. The CTAGN fraction that I found; i.e., 30^{+23}_{-14}%, is

significantly higher than that *observed* in the hard X-ray AGN survey by *Swift*-BAT, but agrees very well with that *inferred* from the *Swift*-BAT survey, after taking into account sensitivity effects. I demonstrate that we can identify intrinsically lower luminosity CTAGNs that are missed by the *Swift*-BAT survey (i.e., down to $L_{2-10,\mathrm{int}} \sim 10^{40}$ erg s^{-1}). I provide case studies on two newly identified bona-fide CTAGNs in our local universe (NGC 1448 and NGC 5643), and demonstrate the challenges in characterising the properties of low luminosity AGN, primarily due to significant dilution and contamination by the X-ray emission from the host galaxy. I compare the AGN and host galaxy properties of my sample with that of the *Swift*-BAT AGN sample, and found the following: (1) the star formation rates between the two samples are consistent with each other; however, (2) my sample has a wider range of AGN Eddington ratio, extending down to a lower Eddington ratio than the *Swift*-BAT AGN sample; (3) my sample also shows a more diverse optical nuclear spectral type; and (4) dominates at lower black hole mass and galaxy stellar mass.

Declaration

The work in this thesis is based on research carried out between October 2013 and July 2017 under the supervision of Prof. David M. Alexander, at the Centre for Extragalactic Astronomy, Department of Physics, Durham University, England. No part of this thesis has been submitted elsewhere for any other degree or qualification and it is all the author's own work unless referenced to the contrary in the text.

Portions of this work have appeared in the following papers:

- *Chapter 3*: Annuar, A.; Gandhi, P.; Alexander, D. M.; Lansbury, G. B.; Arvalo, P.; Ballantyne, D. R.; Balokovi, M.; Bauer, F. E.; Boggs, S. E.; Brandt, W. N.; Brightman, M.; Christensen, F. E.; Craig, W. W.; Del Moro, A.; Hailey, C. J.; Harrison, F. A.; Hickox, R. C.; Matt, G.; Puccetti, S.; Ricci, C.; Rigby, J. R.; Stern, D.; Walton, D. J.; Zappacosta, L.; Zhang, W, *The Astrophysical Journal*, 815, 36 (2015).

- *Chapter 4*: Annuar, A.; Alexander, D. M; Gandhi, P.; Lansbury, G. B.; Asmus, D.; Ballantyne, D. R.; Bauer, F. E.; Boggs S. E.; Boorman, P. G.; Brandt, W. N.; Brightman, M.; Christensen, F. E.; Craig, W. W.; Farrah, D.; Goulding, A. D.; Hailey, C. J.; Harrison, F. A.; Koss, M.; LaMassa, S. M.; Murray, S. S.; Ricci, C.; Rosario, D. J.; Stanley, F.; Stern, D.; Zhang, W. W., *The Astrophysical Journal*, 836, 165 (2017).

The work described in Chapters 3-4 was performed in collaboration with the co-authors of the above mentioned paper. The work described in Chapter 5 is being prepared for journal submission, and was performed in collaboration with Alexander, D. M., Gandhi, P., Lansbury, G. B, Asmus, D., Brightman, M., Ricci, C., D. J. Rosario, and the *NuSTAR* team. The author has carried out all of the data

reduction and analysis in this work with the following exceptions: (1) the detection significance of NGC 5643–X1 mentioned in Chapter 3, which was carried out by Lansbury, G. B.; (2) the data reduction of the ESO NTT/EFOSC2 data in Chapter 4, which was carried out by Lansbury, G. B., with the analysis performed by the author; and (3) the data reduction and analysis of the Gemini/T-ReCS in Chapter 4, which was performed by Asmus, D. All of the text has been written by the author.

Acknowledgements

I would like to express my deepest gratitude to my awesome pair of supervisors, Prof. David Alexander and Dr. Poshak Gandhi, for their unlimited support, untiring encouragements and all the great opportunities that they have created for me throughout the course of my PhD study. I have very much enjoyed working with them, and could not have asked for better supervisors. Thank you also to George Lansbury, whom I consider as my unofficial third supervisor for his help throughout my research.

I am very grateful to be surrounded by people who have supported me along the way. Firstly, my beloved husband, Adli – thank you for your unbelievable amount of patience, support and love all these years. You are definitely my number one pillar of strength. Thank you to all my family and friends who have been my cheerleaders throughout these years, especially my parents, for their unrelenting support all my life. I would also like to take this opportunity to acknowledge my grandparents who sadly passed away while I was abroad pursuing my dream. I am sure they would be so proud of me if they are still here today.

Special thanks to Prof. Fiona Harrison and Dr. Daniel Stern at Caltech for the opportunity to work with *NuSTAR*, which I have enjoyed very much. *NuSTAR* has played a significant role in my research and has created many great opportunities for me.

It has also been a pleasure to be surrounded by great people in the Durham astronomy group, including my past and present officemates, fellow PhD students, post-docs and staffs.

Last but not least, I would like to thank Majlis Amanah Rakyat (MARA) Malaysia for the opportunity and financial support to pursue this PhD.

Contents

List of Figures

List of Tables

Chapter 1

Introduction

It is now established that all massive galaxies in the local universe ($M > 10^{10}\ M_{\odot}$) harbour supermassive black holes (SMBHs; $M_{\rm BH} > 10^{6}\ M_{\odot}$) at their centres. This indicates that all massive galaxies must have undergone a phase of rapid accretion in which they hosted active galactic nuclei (AGNs) at some point during their lifetimes (e.g., Kormendy & Richstone, 1995; Magorrian et al., 1998; Gebhardt et al., 2000). The link found between the mass of SMBHs and the host spheroids suggests that AGNs have an impact on the growth of their host galaxies (e.g., Alexander & Hickox, 2012; Fabian, 2012; Kormendy & Ho, 2013). Therefore, a complete census of the AGN population in the local universe is essential for definitive evolutionary studies of SMBHs and their host galaxies. In this introductory chapter, I provide a brief history on the discovery of AGN (Section 1.1), describe the proposed physical structure of AGN (section 1.2), and detail the techniques that have been used to identify AGN across the electromagnetic spectrum (section 1.3). In Section 1.4, I provide a background on Compton-thick AGNs, which is the focus of this thesis, their observational characteristics (Section 1.4.1), and the different techniques used to identify them (Section 1.4.2). Finally in Section 1.5, I provide an overview of the subsequent chapters presented in this thesis.

1.1 A brief history of AGN

The discovery of AGN dates back more than a century to the year 1908 when Edward. A. Fath was performing optical spectroscopy at the Lick Observatory for what was then thought as "spiral nebulae" within the Milky Way, as part of his dissertation work. He noticed that one of the objects, called NGC 1068, has an unusual spectrum, showing strong emission lines, unlike most nebulae observed at that time which showed absorption spectrum associated with stellar activity (Fath, 1909). Vesto. M. Slipher at Lowell Observatory then observed the source at higher quality and better spectral resolution, and noted that these lines are similar to those observed in planetary nebulae. He also found that the emission lines are significantly broader than those of planetary nebulae with widths measuring up to hundreds of kilometres per second (Slipher, 1917).

About 20 years later, Edwin P. Hubble determined that some of these nebulae, including NGC 1068, are located outside of the Milky Way (and now established as galaxies), and therefore marked the beginning of extragalactic astronomy (Hubble, 1926). In 1943, Carl K. Seyfert discovered more galaxies exhibiting similar optical spectral characteristics as NGC 1068 (Seyfert, 1943), and these have since been called "active galaxies" or "Seyfert galaxies" in honour of Seyfert's pioneering discoveries. At the end of 1950s, Lodewijk Woltjer made the first attempt to understand the physics of these sources and established the following: (1) the physical size of the nuclei of these sources must be < 100 pc as they were unresolved; (2) their lifetime must be $> 10^8$ years (given that the age of the universe is 10^{10} years and 1/100 spirals is a Seyfert); and (3) they have extremely high mass ranging between $\approx 10^8$–10^{10} $M_\odot$ (Woltjer, 1959). These are generally consistent with what we know today, except that now we also know that their masses can extend down to $\approx 10^6$ $M_\odot$ (e.g., Greenhill et al., 2003; Trakhtenbrot et al., 2017).

Since then, more and more Seyfert galaxies have been identified, with $\sim$10% of galaxies currently found to host Seyfert nuclei (e.g., Ho et al., 1997; Ho, 2008). Subsequent studies also further reveal their unusual properties which include extremely compact and bright nuclei and high variability across the ultraviolet to optical continuum. It has also appeared that these galaxies can be divided into two main

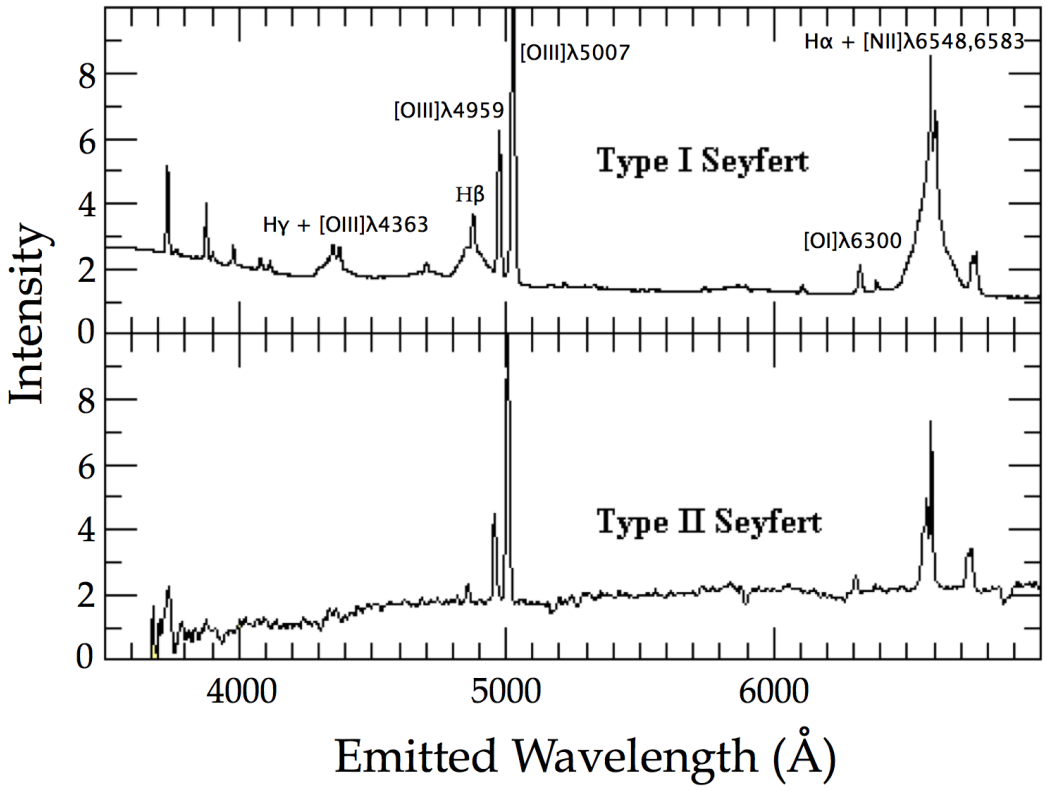

Figure 1.1: Example optical spectra of type 1 and type 2 Seyferts (top and bottom panel, respectively), showing strong emission lines. Type 1 Seyfert shows broader permitted lines (e.g., Hβ) than the forbidden lines (e.g., [OIII]), whilst type 2 Seyfert have comparable permitted and forbidden line widths. Image credit: Bill Keel.

classes on the basis of their distinct optical spectra; i.e., "type 1" and "type 2" (see Figure 1.1). Type 1 Seyferts exhibit significantly broader permitted emission lines (full width at half maximum, FWHM $\sim 10^3$–10^4 km s^{-1}) than the forbidden emission lines (FWHM $\sim 10^2$ km s^{-1}), whilst type 2 Seyferts show permitted lines that have the same widths as the forbidden lines (Weedman, 1970).[1]

Meanwhilst, the development in radio astronomy during the late 1950s allowed for the independent discovery of AGN. By this time, the angular resolution of radio

[1]Permitted lines, also known as recombination lines, are emitted when electrons at high excitation states cascade down the energy levels of an atom, emitting photons at each transition (e.g., Hydrogen Balmer series). Meanwhilst, forbidden lines are produced when electrons undergo transitions that are highly improbable to occur (i.e., very small probability of spontaneously occurring) on the basis of quantum mechanics (e.g., [OIII]$\lambda 5007\mathring{A}$ and [NII]$\lambda 6583\mathring{A}$).

telescopes was good enough to resolve the radio sources and associate them with their respective optical counterparts. The first radio surveys, such as the third Cambridge (3C) catalogue (Edge et al., 1959), provided hundreds of radio source identifications, some of which appear point-like or quasi-stellar in the photographic plates. As a result, these sources were called quasi-stellar radio sources (later abbreviated as "quasars"). In 1963, Maartin Schmidt performed optical spectroscopy on one of these objects, called 3C 273, and determined that it is located at a relatively high redshift; i.e., $z = 0.158$. Assuming that the redshift represents the distance to the source, he suggested that the source could be associated with the nucleus of a galaxy that is 100$\times$ more luminous than other radio galaxies that had been identified at that time (Schmidt, 1963). These findings and follow-up studies on other quasars have led to the belief that these sources must be much luminous than ordinary stars. Today, we understand that these are essentially the more luminous cousins of Seyfert galaxies ($L_{\rm bol} \geq 10^{45}$ erg s^{-1}), located at higher redshifts. These objects, along with their sub-classifications (e.g., type 1, type 2, radio-loud, radio-quiet) are all brought together today under the general term, "active galactic nuclei ".

1.2 The physical structure and multiwavelength emission of AGN

In this section, I will briefly outline the standard physical structure of AGN as proposed by the most widely accepted model – the AGN unification model (Antonucci, 1993; Urry & Padovani, 1995). Although this model does not explain all of the AGN properties we observed (see Netzer et al., 2005 for a recent review), the basic physical picture of AGN that it provides us is sufficient for the purpose of this thesis. A schematic diagram to illustrate this model is shown in Figure 1.2, and the corresponding broadband emission (typically referred to as the spectral energy distribution; SED) across the electromagnetic spectrum is shown in Figure 1.3.

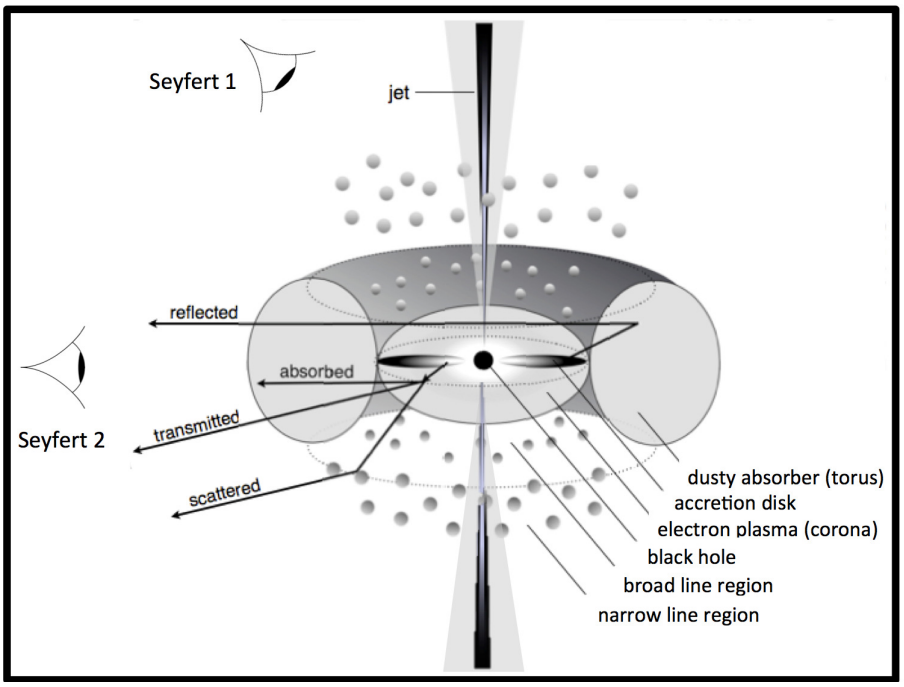

Figure 1.2: A schematic diagram illustrating the standard physical model of AGN and the orientation-based unification scheme proposed by e.g., Antonucci (1993) and Urry & Padovani (1995). The standard model of an AGN proposed that the AGN is powered by a central supermassive black hole, accreting cold material that surrounds it. The cold material forms a geometrically thin and optically thick accretion disk around the supermassive black hole. A hot corona is believed to exist above and below this disk. Surrounding this nuclear region, there is a geometrically thick and optically thick dusty molecular torus that can hinder our direct view towards the central source. There are two distinct emission line regions which consist of gas being ionised by the nuclear emission; i.e., the broad line region which is located within the gravitational influence of the black hole, and the narrow line region which extends over a much larger scale. Some AGNs host radio jets above and below the accretion disk that can extend over kiloparsec scales. The AGN unification scheme dictates that the different properties we observed for the different classes of AGN are due to the orientation of the AGN with respect to our line-of-sight (e.g., type 1 Seyfert poperties are observed when we view the nuclear region of the AGN directly without being hindered by the circumnuclear torus, and type 2 Seyfert properties are observed when our view towards the central source is obscured by the dusty torus). Diagram adapted from Beckmann & Shrader (2012).

1.2.1 The black hole, accretion disk, and corona

It is now well established that an AGN is powered by an accreting supermassive black hole (SMBH; $M_{\rm BH} > 10^6\ M_\odot$). The accretion is fed by cold material from the host galaxy that approaches the vicinity of the SMBH, and becomes bounded by its gravitational influence. This causes the material to orbit the SMBH, and forms an optically thick accretion disk on a physical scale of $\lesssim 0.01$ pc from the central SMBH. Frictional forces cause the material to lose angular momentum and spiral inwards, radiating energy in the form of electromagnetic radiation (blackbody) in the process. The rate at which this energy is radiating; i.e., the bolometric luminosity ($L_{\rm AGN}$), depends on the mass accretion rate ($\dot{M}$) according to the following:

$$L_{\rm AGN} = \eta \dot{M} c^2 \tag{1.2.1}$$

where c is the speed of light, and η is the mass-to-energy conversion efficiency. η is ≈ 0.057 for a non-rotating black hole; however, a spinning black hole can achieve higher efficiency, up to ≈ 0.42 (e.g., Kerr, 1963; Thorne, 1974). Typically, η is assumed to be ≈ 0.1. The SMBH accretes the majority of the material that is not converted into radiative energy, contributing to its mass growth.

The maximum luminosity that can be generated through the accretion process can be calculated by assuming accretion of pure ionised Hydrogen and hydrostatic equilibrium, where the gravitational force of the SMBH is balanced by the radiation pressure from the accretion. The theoretical upper limit to the luminosity is called the "Eddington luminosity", and occurs when the gravitational force and the radiation pressure is in balance. The Eddington luminosity is given by:

$$\begin{aligned} L_{\rm Edd} &= \frac{4\pi G M_{\rm BH} m_{\rm p} c}{\sigma_T} \\ &\approx 1.3 \times 10^{38}\ (M_{\rm BH}/M_\odot)\ {\rm erg\ s^{-1}} \end{aligned} \tag{1.2.2}$$

where G is the gravitational constant, $m_{\rm p}$ is the mass of proton, and $\sigma_{\rm T}$ is the Thomson scattering cross-section for an electron. Astronomers often used the ratio between $L_{\rm AGN}$ and $L_{\rm Edd}$; i.e., the "Eddington ratio" ($\lambda_{\rm Edd}$), to compare the accretion rates between different SMBHs of different masses. AGNs which have $\lambda_{\rm Edd} \gtrsim 0.1$

are often considered as undergoing high accretion. When $\lambda_{\rm Edd}$ is $\lesssim 10^{-3}$–10^{-2}, a different mode of accretion is thought to occur; i.e., radiatively inefficient (e.g., Narayan & Yi, 1994; Yuan & Narayan, 2014).

The spectral shape of the radiation emitted by the accretion disk depends on the temperature distribution of the accretion disk. At high temperature, the spectrum will peak at higher energy/frequency (i.e., shorter wavelength) and vice versa. For a typical AGN, the spectrum peaks in the ultraviolet (UV) part of the electromagnetic radiation ($\lambda \sim$ 100–4000Å), at the most inner, i.e, hottest ($T \sim 10^5$ K), part of the disk. At the outer part of the disk, the temperature is lower and the spectrum peaks at longer wavelength, $\lambda \sim$ 4000–9000Å, emitting light in the optical band. The resultant spectrum that we observed is a composite of blackbody emission at each accretion disk radius (see Figure 1.3). Because the majority of the accretion disk radiation is emitted in the UV, it is very difficult to observe due to absorption by the interstellar medium and the Earth's atmosphere.

An optically thin hot corona ($T \sim 10^9$ K) comprised of relativistic electrons is believed to reside around the accretion disk (e.g., Done et al., 2012), although its exact location, origin and other properties are still poorly known. The high energy electrons in the corona can inverse-Compton scatter the photons emitted by the accretion disk up into the X-ray waveband ($E \sim$ 0.1–300 keV), producing the power-law spectral shape that we observed at X-ray energies (see Figure 1.3). The spectral shape of this emission can be approximated as follows:

$$F_{\rm E} \propto E^{-\Gamma} \tag{1.2.3}$$

where $F_{\rm E}$ and E are the flux and energy of the photon, respectively, and Γ is the power-law index, commonly called the "photon index". The photon index is dependent on the velocity distribution of the electrons in the corona, and is typically measured to be $\approx$ 1.7–2.4 (e.g., Burlon et al., 2011). Throughout this thesis, I will use the term "primary emission" to refer to the AGN emission emitted at these nuclear scales (i.e., the accretion disk and corona).

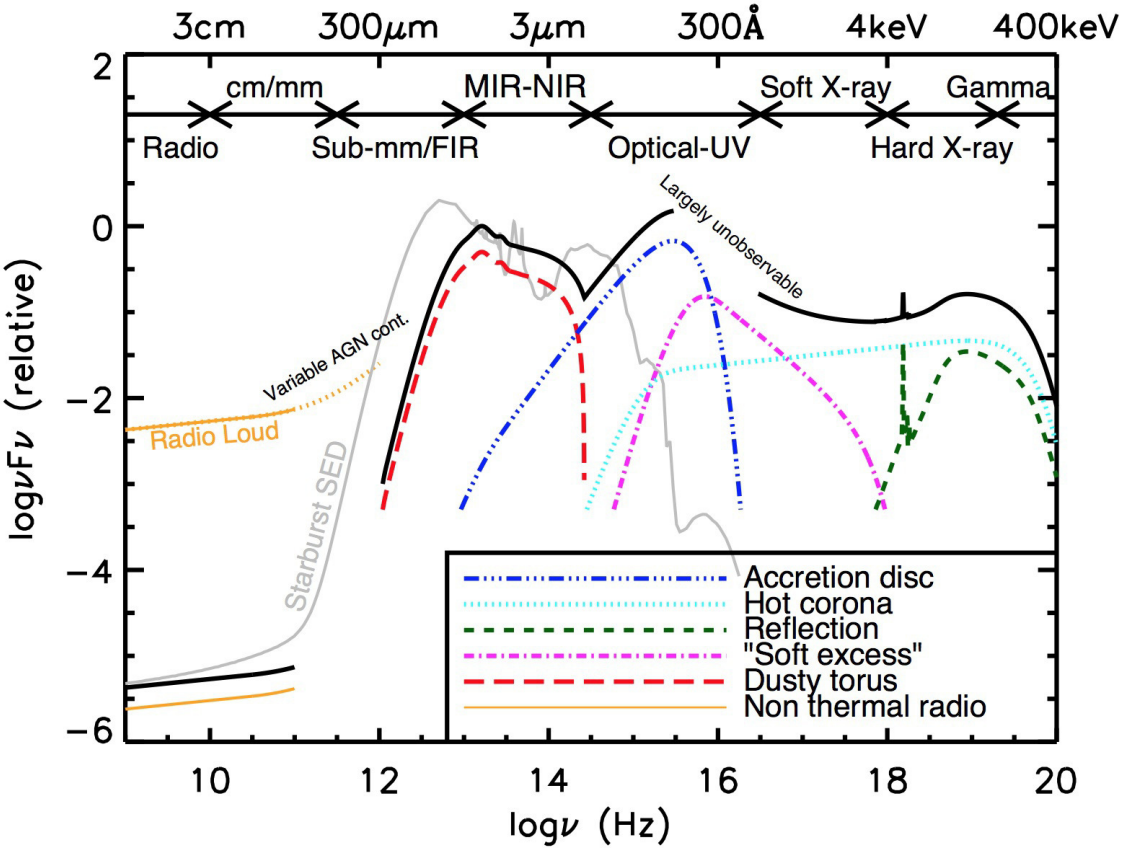

Figure 1.3: A schematic diagram representing the spectral energy distribution (SED) of an unobscured AGN constructed based upon radio-quiet quasars (e.g., Elvis et al., 1994; Richards et al., 2006). The black curve shows the total SED, whilst the coloured curves indicate the individual components of the AGN emission with arbitrary offsets. The primary emission from the accretion disk peaks in the optical–UV wavebands, whilst the corona emission dominates at X-ray energies. The AGN emission at milimetre–far-IR wavelengths is believed to be low and is dominated by the host galaxy emission, with the exception of the most luminous quasars, and radio-loud AGNs. Radio-loud AGNs can emit powerful radio emission, several orders of magnitude higher than radio-quiet AGNs. The curve shown in grey is an example of an SED of a star-forming galaxy (M82; Silva et al., 1998). Image credit: Harrison (2014).

1.2.2 Torus and emission line regions

On larger scales than the accretion disk of the AGN, there is strong evidence for the presence of a geometrically and optically thick distribution of gas and dust in a torus-like shape (e.g., from spectropolarimetry, mid-infrared interferometry and X-ray obscuration). The first direct detection of this "torus" was made in recent years in the nearby galaxy, NGC 1068, using the Atacama Large Millimeter Array (ALMA; García-Burillo et al., 2016; Gallimore et al., 2016). The inner radius of the structure is determined by the dust sublimation temperature ($T \sim 1500$ K; typical radius, $r \sim$ 1–10 pc). Depending on the orientation of the AGN with respect to our line-of-sight (l.o.s), this dusty material can obscure our direct view toward the central region of the AGN (see Figure 1.2). The AGN unification model dictates that the different observational classes of AGN (e.g., Type 1 Seyfert vs. Type 2 Seyfert) are due to this orientation effect; i.e., the amount of obscuration towards the nucleus depends on the viewing angle. The distribution of gas is generally assumed to be smooth and uniform (see Figure 1.2); however, recent studies have found evidence for it to be clumpy (e.g., Hönig et al., 2006; Nenkova et al., 2008; Alonso-Herrero et al., 2011; Mullaney et al., 2011). In both cases however, the gas and dust distributions are anisotropic, which is the key motivation of the AGN unification model. The primary emission from the AGN is absorbed by the torus, and then re-emitted at infrared (IR) wavelength via thermal radiation, peaking in the mid-IR regime ($\lambda \sim 30 \mu m$; see Figure 1.3; e.g., Polletta et al., 2000; Nenkova et al., 2008; Mullaney et al., 2011).

Beyond the accretion disk, there is also strong evidence for two distinct regions of gas being ionised by the primary emission from the AGN. These regions are called the broad line region (BLR) and the narrow line region (NLR). The BLR is located at a nearer distance to the central region of AGN, within the gravitational influence of the SMBH due to the highly variable broad emission line components observed ($r \sim$ 0.01–1 pc). Due to the high velocity of the gas in this region, the widths of the permitted emission lines observed are very broad (FWHM $\sim 10^3$–10^4 km s^{-1}). In addition, because of the high gas cloud density ($n_e \gtrsim 10^8$ cm^{-3}), the probability for the ionised gas to de-excite through collision is significantly higher than through

radiative processes. Therefore, forbidden lines are usually not strongly observed in this region. On the other hand, both the permitted and forbidden lines can be strongly produced in the NLR as a result of the lower gas density ($n_e \lesssim 10^6$ cm^{-3}). The widths of the emission lines in this region are typically in the orders of $\sim 10^2$ km s^{-1} (FWHM). The NLR region is larger than the BLR, and the size has also been directly measured in many objects, extending beyond the scale of the torus ($r \sim$ 10–10^4 pc; e.g., Bennert et al., 2006; Scharwächter et al., 2011; Villforth & Hamann, 2015). Based on the AGN unification model, the different characteristics we observed in the optical spectra of Seyfert 1 and 2 are due to the fact that the torus obscures our view towards the BLR for Seyfert 2, and therefore we do not see broad emission lines in these sources. One of the key pieces of observational evidence supporting this theory comes from spectropolarimetry in which Seyfert 2 sources show broad permitted lines in their polarised spectra (scattered flux spectra), consistent with that seen in Seyfert 1's total spectra, indicating that the nuclear regions of Seyfert 2s are obscured from our direct view, but can be seen if the emission is scattered into our l.o.s (e.g., Antonucci & Miller, 1985; Capetti et al., 1995; Kishimoto, 1999; Antonucci, 2002).

1.2.3 Jets and other emission

Some AGNs can produce a highly collimated pair of relativistic jets close to the accretion disk which can extend across the whole galaxy (i.e., kiloparsec scale), and are typically seen at radio wavelengths. A large fraction of the radio emission is powered by synchrotron emission, and is therefore associated with enormous amounts of mechanical energy (due to acceleration of relativistic electrons by a magnetic field). However, the mechanism of the jet production at the smallest scale (i.e., at the core) is still not well understood at present. The wide diversity in the AGN SED in the radio waveband provides further evidence for the AGN unification model, in which the spectral properties of, for example, Blazars (another class of AGN), are thought to be caused by our direct view toward the pole of the jets.

An additional component of the AGN emission is produced at low X-ray energies, beyond that expected from a simple accretion disk model (see Figure 1.3). This X-

ray emission is termed as the "soft excess", and its origin is still not clearly known (see e.g., Done et al., 2012 for studies on this emission). On the other hand, AGNs are observed to be relatively quiet at sub-milimetre and far-IR wavelengths, as compared to the emission from the host galaxy (e.g., due to thermal emission from cool dust heated by star formation activity; e.g., Alexander et al., 2005; Mullaney et al., 2011). However some AGNs, such as extremely luminous quasars and radio-loud AGNs, can significantly emit at these wavelengths (e.g., Willott et al., 2002; Tadhunter et al., 2007; Hill & Shanks, 2011). There are relatively few AGNs that are detected in the high energy gamma-ray waveband (MeV–TeV energy range; beyond the energy range shown in Figure 1.3). AGN emission in this waveband is thought to originate from the relativistic jet (e.g., due to synchrotron radiation, inverse Compton-scattering and electron-positron annihilation) as it is most commonly seen in Blazars and rarely detected in radio quiet AGNs (e.g., Ackermann et al., 2012).

1.3 Multiwavelength identifications of AGN

In the previous section, I have described the physical structures of an AGN which give rise to the multiwavelength emission of AGN that we observed. This broadband emission across the entire electromagnetic spectrum allows us to identify AGN using various approaches. In this section, I provide a brief overview on the different AGN selection techniques across the four main wavebands; i.e., X-rays, optical, IR and radio.

1.3.1 X-rays

The X-ray selection of AGN can provide a clean sample of AGN as they suffer relatively little contamination by the host galaxy (see Brandt & Alexander, 2015 for a review). The high penetrative power of X-ray energies at $E \gtrsim 2$ keV also means that they suffers little absorption by the host galaxy, which has a typical gas and dust column density of $N_{\rm H} < 10^{22}$ cm^{-2} (see section 1.4.1).[2]

[2]Column density is the number of particles/atoms/molecules observed along a line of sight per unit area. The column density is commonly measured in terms of neutral hydrogen (H) given that

Typically, astronomers select AGN in X-rays using a hard band ($E \geq 2$ keV) luminosity cut-off of $L_{\rm X} \geq 10^{42}$ erg s^{-1}. This luminosity threshold is chosen to avoid contaminations from host galaxy emission, such as X-ray binaries and ultraluminous X-ray sources (ULXs) which can have X-ray luminosities of up to about 10^{41} erg s^{-1} (individually).[3] The most sensitive X-ray surveys at $E \lesssim 10$ keV are provided by the *Chandra* and *XMM-Newton* X-ray observatories (see Chapter 2 for further details). These observatories have performed a number of deep field surveys, providing large samples of AGN across a wide range of redshifts, finding AGN densities of up to $\sim$23,900 deg^{-2} (e.g., Brandt et al., 2001; Alexander et al., 2003; Luo et al., 2008; Xue et al., 2011; Luo et al., 2017). This is over a magnitude higher than that found in the deepest optical surveys (e.g., Treister & Urry, 2012). However, X-ray surveys at $E \leq 10$ keV are often biased against finding heavily obscured AGNs, in which the nuclear X-ray emission are significantly absorbed by the torus along our l.o.s (see Section 1.4). The recent advancements in X-ray astronomy, however, have launched X-ray telescopes that are sensitive to photons above 10 keV, such as the *Swift* Burst Alert Telescope (BAT; Barthelmy et al., 2005) and the *NuSTAR* telescope (Harrison et al., 2013; see Chapter 2). These have provided us with cleaner and more complete selections of AGN than at $E < 10$ keV as these telescopes are able to detect the high X-ray energy emission from obscured AGNs that is able to penetrate through the obscuring torus (e.g., Baumgartner et al., 2013). However even at this hard X-ray energy, it will still be difficult to find the most heavily obscured AGNs (i.e., Compton-thick AGNs; $N_{\rm H} > 10^{24}$ cm^{-2}; see Section 1.4).

Despite the advantages of AGN selection at X-ray energies, there is often ambiguity on the origin of the X-ray emission; i.e., it can suffer significant contamination by X-ray sources other than the AGN at $L_{\rm X} < 10^{42}$ erg s^{-1} (e.g., ULXs). This is demonstrated throughout this thesis in which the X-ray emission of the majority

it is the most abundant astrophysical element. However, the material will include other elements as well, which can dominate the absorption due to their larger interaction cross-sections.

[3]Individually, X-ray binaries and ULXs can have X-ray luminosities of up to 10^{38} erg s^{-1} and 10^{41} erg s^{-1}, respectively. However we note that an entire galaxy can have X-ray luminosity of $\gtrsim 10^{42}$ erg s^{-1}.

of low luminosity AGNs in my sample often suffer significant contamination by the host galaxy even at $E \gg 2$ keV. In this thesis, I present approaches to measuring AGN emission when there is significant contamination by the host galaxy.

1.3.2 Optical

Historically, AGNs have mostly been identified at optical wavelengths. As detailed in Section 1.2.1, the primary emission from an AGN is produced at optical–UV wavelengths. Therefore, these wavebands should provide us with the most accurate tracer for the AGN accretion power. The optical–UV colours for AGNs are usually different from stellar emission, and hence many studies have used this distinction to identify AGNs and quasars (e.g., Boyle et al., 1990; Richards et al., 2001). Large surveys conducted in this waveband, such as the Sloan Digital Sky Survey (SDSS; Abazajian et al., 2009) and the 2 Micron All-Sky Survey (2MASS; Skrutskie et al., 2006), have boosted the numbers of AGN identified to $\gg$ 100 000 out to high redshifts ($z \sim 6$) using this colour selection technique. However, this approach can be highly inefficient for selecting AGN in which the accretion disk is obscured along our l.o.s by the torus (e.g., Seyfert 2) and the host galaxy, as well as faint AGN in which the emission can be significantly diluted by the host galaxy starlight.

Another technique that has been developed to identify AGN in the optical wavelength is by comparing the relative strength between the forbidden and the narrow permitted emission lines of the AGN optical spectrum (e.g. Baldwin et al., 1981; Veilleux & Osterbrock, 1987; Ho et al., 1997 Kewley et al., 2001). Because the emission lines are produced in the NLR, which can extend to a much larger scale than the torus, they do not suffer from obscuration by the circumnuclear material. The "Baldwin, Phillips & Terlevich" diagrams are often used to distinguish AGNs from LINERs (low ionisation nuclear emission line regions) and HII regions (star forming regions) based upon the strength of a pair of relatively high ionisation emission lines as compared to the Hydrogen Balmer lines; e.g., [OIII]λ5007Å/Hβ and [NII]λ6583Å/Hα (e.g., Baldwin et al., 1981; Kewley et al., 2001; Kauffmann et al., 2003). These forbidden lines are used due to their high excitation states and high ionisation energies (e.g., 35.1 eV and 21.6 eV for [OIII] and [NII], respectively).

Although they can be produced by both star forming regions and AGNs, AGNs will often occupy the region of higher emission line ratios than star forming galaxies due to the higher degrees of ionisation (e.g., [OIII]/H$\beta \gtrsim 3$ and [NII]/H$\alpha \gtrsim 0.5$). These emission lines are not affected by extinction through the obscuring torus; however, they can be significantly absorbed by dust in the host galaxy, and even completely extinguished in extreme cases (Goulding & Alexander, 2009). Therefore, this technique can miss AGNs that are severely obscured by dust in the host galaxies (e.g., NGC 4945).

1.3.3 Infrared

As detailed earlier, the primary continuum emission of an AGN can be absorbed by the circumnuclear torus, and then re-emitted in the IR via thermal radiation. The advantage of selecting AGN using the IR waveband is that the optical depth is relatively low, and therefore the IR emission suffers very little obscuration from the host galaxy. The shape of an AGN SED in the IR differs from that of star forming emission, with the AGN emission peaking in the mid-IR and the star forming activity peaking at the far-IR (see Figure 1.3). Based on this, various studies have developed several AGN selection criteria on the basis of IR colours (e.g., Mateos et al., 2012; Stern et al., 2012; Assef et al., 2013), using photometry from IR observatories such as the Infrared Astronomical Satellite (*IRAS*; Neugebauer et al., 1984), *Spitzer* (Werner et al., 2004) and the Wide-Field Infrared Survey Explorer (*WISE*; Wright et al., 2010). Whilst this technique is useful in identifying AGNs in systems where they are the dominant contributors to the IR emission, it can miss AGNs that are severely diluted by star formation emission in the galaxy (e.g., Assef et al., 2013; Kirkpatrick et al., 2013). Besides colour selection, AGN can also be identified in the IR waveband using the detection of luminous high ionisation emission lines such as [OIV]$\lambda 25.9 \mu m$ (ionisation energy = 54.9 eV) and [NeIII]$\lambda 15.56 \mu m$ (ionisation energy = 41.0 eV). However, selecting AGN based on these emission lines can also cause ambiguity given that other host galaxy processes, such as energetic starbursts, can also produce significant [OIV] and [NeIII] emission.

1.3.4 Radio

In addition to optical waveband techniques, AGNs have also been historically identified using radio selection (e.g., Edge et al., 1959; Becker et al., 1995; Condon et al., 1998). Sources with radio luminosity of $L_{1.4\mathrm{GHz}} \gtrsim 10^{25}$ W Hz^{-1} are usually associated with AGN emission, and therefore, they are often selected on the basis of this luminosity threshold (below this luminosity, rapidly star forming region can significantly contaminate the emission). Radio selection of AGN can be powerful as this sometimes selects an extreme population of AGN, in which most are not identified in the optical (e.g., Ivezić et al., 2002). In addition, radio surveys can achieve incredibly high angular resolution using interferometry with very long baselines, giving us accurate positions of the AGNs and useful spatial information. However, radio surveys are highly incomplete since they are biased toward finding radio-loud AGNs ($L_{1.4\mathrm{GHz}} \gtrsim 10^{25}$ W Hz^{-1}), which account for only $\lesssim$10% of the entire AGN population (White et al., 2000). In addition, whilst most radio-quiet AGNs produce radio emission, the fraction of the total AGN emission radiated in this wavelength is very small, making it challenging to identify them.

1.4 Compton-thick AGN

In recent years, many studies aimed to find the most heavily obscured AGNs, particularly Compton-thick (CT) AGNs, in the local universe. In short, CTAGNs are AGNs that are obscured along our l.o.s by gas with column density of $N_{\mathrm{H}} \geq 1/\sigma_T = 1.5 \times 10^{24}$ cm^{-2} (where σ_T is the Thomson scattering cross-section). The obscuring gas is predominantly attributed to the AGN circumnuclear torus posited by the AGN unification model, but can also be contributed by larger-scale molecular clouds and dust lanes (e.g., Elvis, 2012; Prieto et al., 2014). The high column density of gas results in severe attenuation of the primary X-ray emission from CTAGN at energies below 10 keV. This is why observations at higher energies are needed to probe this primary component and provide unambiguous identification of CTAGN. However even at $E > 10$ keV, the remaining flux that we observe in the most extreme CTAGN ($N_{\mathrm{H}} > 10^{25}$ cm^{-2}) will be from photons scattered or reflected from

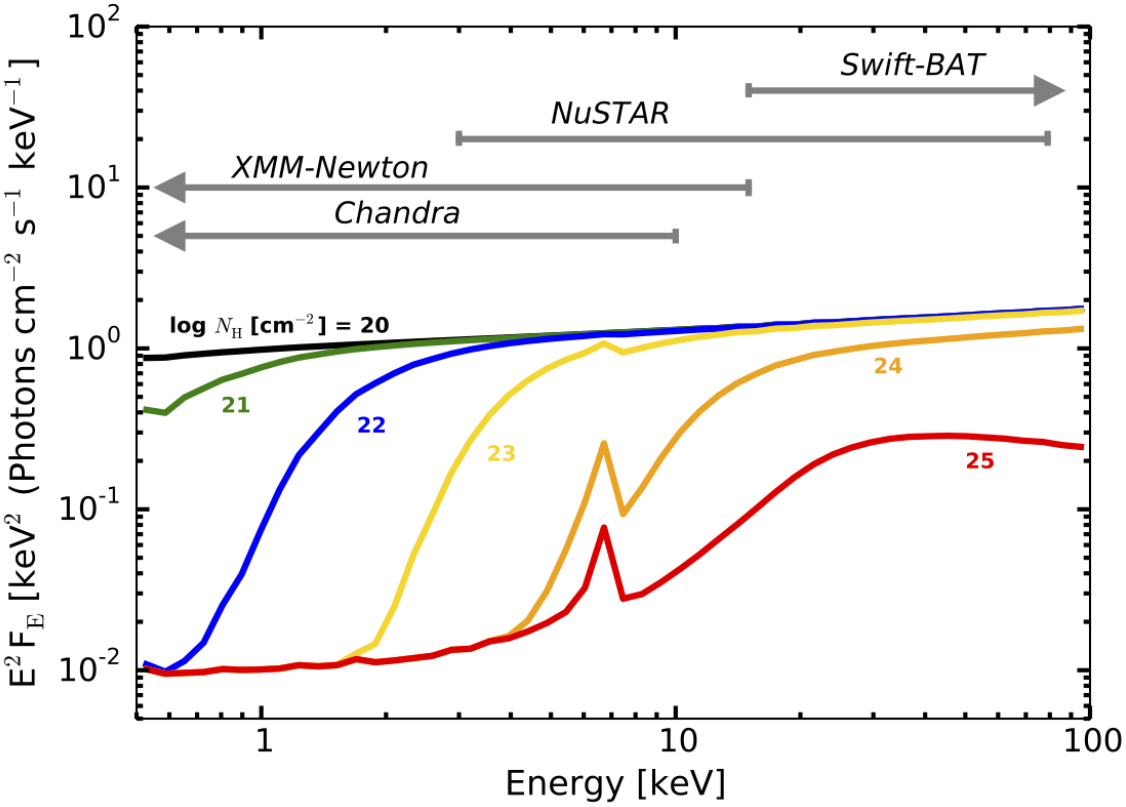

Figure 1.4: X-ray spectra of AGN for different absorbing column densities (labelled on the plot), modelled using the physically-motivated torus model simulated by Brightman & Nandra (2011) (see Chapters 3–4). A primary power-law emission with photon index of $\Gamma = 1.9$ and scattering fraction of 1% were assumed in the model. The X-ray energy coverage provided by the most sensitive X-ray observatories available today; i.e., *Chandra*, *XMM-Newton*, *NuSTAR* and *Swift*-BAT, are also indicated in the plot.

the back-side of the torus, which comprise of just a few percent of the intrinsic AGN power (e.g., Iwasawa et al., 1997; Matt et al., 2000; Baloković et al., 2014; see also Figure 1.4). This makes the identification and characterisation of CTAGN a challenging task, even in our local universe.

Nevertheless, CTAGNs are expected to constitute a significant fraction of the overall AGN population in the local universe. Based on the synthesis of the cosmic X-ray background (CXB) spectrum, CTAGNs are predicted to provide a substantial contribution to the CXB radiation, responsible for 10–25% of the flux at the peak energy, $\sim$ 30 keV (e.g., Gilli et al., 2007; Treister et al., 2009 Draper & Ballantyne, 2010; Akylas et al., 2012; Ueda et al., 2014; see Figure 1.5). Multiwavelength studies of nearby AGN also predict that CTAGN should be numerous, accounting for $\sim$30% of the AGN population (e.g., Risaliti et al., 1999; Goulding et al., 2011). In fact, of the three AGNs identified within $D = 4$ Mpc (Cen A, Circinus, NGC 4945), two are found to be CT (Circinus and NGC 4945), corresponding to a CTAGN fraction of $\sim$67%! Yet at larger volumes, their census seems to be far from complete. To date, only $\sim$8% of AGN at $z \simeq 0.055$ have been *directly* identified as CT on the basis of hard X-ray study using the *Swift*-BAT survey (Ricci et al., 2015).[4] This suggests that we are still missing a significant number of CTAGN, even in the local universe. Having a complete census of the $N_{\rm H}$ distribution of AGN, especially at the CT regime is important in our understanding of the CXB radiation.

In addition, the tight link found between the mass of SMBHs and their host galaxy bulges indicates that black hole accretion and star formation must have co-evolved across cosmic time. Based on this, we would expect that most accretions at higher redshifts are heavily obscured (due to the higher gas fraction at higher redshifts; e.g. Geach et al., 2011), with a large fraction occuring in the CT phases (e.g. Fabian, 1999; Alexander & Hickox, 2012). This seems to be supported by observational studies in which $\approx$35–40% of the AGN population is *inferred* (see

[4]CTAGN can only be *directly* identified using X-ray spectral analysis. In X-ray surveys, due to limited sensitivity of the X-ray instruments, a large fraction of CTAGN can be missed. The actual fraction of the CTAGN population is therefore often *inferred* by taking into account for this instrument sensitivity.

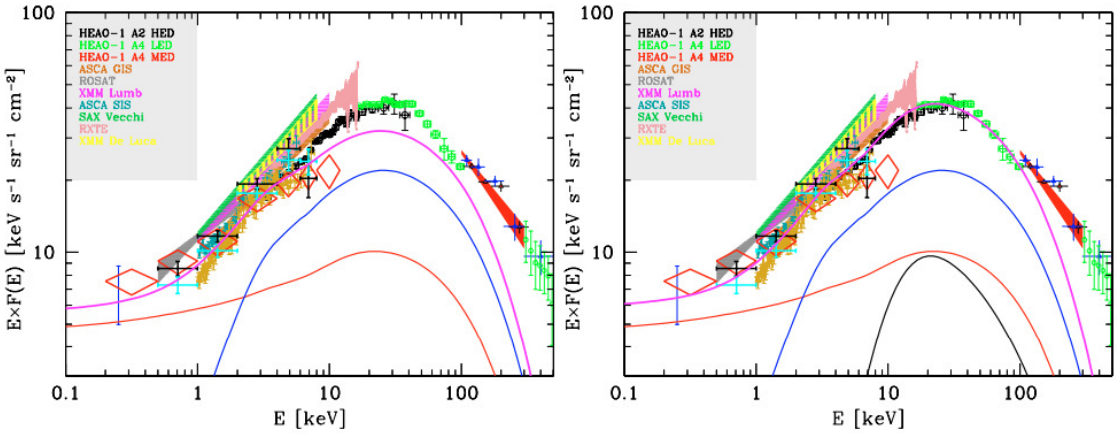

Figure 1.5: The observed CXB spectrum (data points) and predicted contributions from unobscured AGN ($N_{\rm H} < 10^{22}$ cm^{-2}; red lines), obscured Compton-thin AGN ($N_{\rm H} = 10^{22}$–10^{23} cm^{-2}; blue lines) and Compton-thick AGN ($N_{\rm H} \gtrsim 10^{24}$ cm^{-2}; black lines). The different CXB measurements were obtained from different X-ray observatories, instruments, and surveys, and are explained on the top left of the plots. The solid magenta lines refer to the total model of the CXB spectrum. The left and right plots show the CXB spectrum without and with contributions from CTAGN, respectively. Based in these plots, it can be seen that CTAGN population is required to explain the CXB emission we observed, particularly at $E > 5$ keV. Image credit: Gilli et al. (2007).

footnote 4) to be CT at $z \approx 0.1$–1 by the deepest *Chandra* and *XMM-Newton* surveys (e.g., Georgantopoulos et al., 2013; Vignali et al., 2014; Lanzuisi et al., 2015), and a lower fraction of $\sim$30% has been *inferred* by the *Swift*-BAT survey at lower redshift of $z \lesssim 0.05$ (Ricci et al., 2015). Some studies have also suggested that obscuration is related to AGN evolution; e.g., as a result of a galaxy merger (e.g., Hopkins et al., 2008; Kocevski et al., 2015). In this scenario, the SMBH undergoes rapid growth due to the large amount of gas being driven to the centre of the galaxy (e.g., Draper & Ballantyne, 2010; Treister et al., 2010). This phase is mostly hidden from us due to the enshrouding gas and dust. Once the radiation pressure (or winds) from the AGN is able to expel this material, the central source is revealed. Having a complete census of the AGN population over a broad range of obscuration, luminosities and redshifts is therefore also important to help us understand the growth of SMBHs, as well as the accretion history of AGN across cosmic time to allow us to test the co-evolution model between AGNs and their host galaxies.

The focus of this thesis is to provide the most complete census of the CTAGN population in our local universe (out to just 15 Mpc) which can be used as a benchmark for more distant AGN studies. In the next subsections, I will describe the observational characteristic signatures of CTAGNs (Section 1.4.1), and the direct and indirect techniques that can be used to identify them (see Section 1.4.2).

1.4.1 Characteristic signatures

Figure 1.4 shows the X-ray spectra of AGN for different obscuring column densities. Based on this plot, we can see that for CTAGN; i.e., $N_{\rm H} \gtrsim 10^{24}$ cm^{-2}, the X-ray spectrum exhibits a flat spectral shape at $E \lesssim 10$ keV, a prominent emission line at ~ 6.4 keV, and a broad bump peaking at $E \sim 30$ keV. In this section, I will describe the physical processes that give rise to these characteristic features of CTAGNs.

At larger scales than the AGN nucleus, the primary X-ray emission from the corona can be scattered down to lower X-ray energies by ionised gas (hereafter "scattered" X-ray emission). The primary X-ray emission can also be absorbed and reflected by optically thick material, such as the accretion disk and the dusty torus (see Section 1.2.2), producing the "reflection" component of the AGN X-

ray spectrum (see Figure 1.3). The amount of reflection depends on the relative importance between electron scattering and photoelectric absorption. For neutral material, the probability for photoelectric absorption to occur at lower energies is higher than electron scattering, and therefore the reflection fraction is smaller at this energy regime. For instance, for neutral Hydrogen (H), the minimum energy required to eject its electron out from the inner most shell of the atom (i.e., $n = 1$, also termed the K shell) is 13.6 eV. The photoelectric absorption cross-section ($\sigma_{\rm abs}$), i.e., the probability for absorption, peaks at this threshold energy ($E_{\rm Edge}$) at a value of 6×10^{-18} cm^2. It then declines as follows:

$$\sigma_{\rm abs} = \left(\frac{\tau}{N}\right) \propto \left(\frac{E}{E_{\rm Edge}}\right)^{-3} \tag{1.4.4}$$

where τ is the optical depth, N is the column density of the material and E is the threshold energy at which photons below this energy will be absorbed by the material. This means that at $E = 13.6$ eV, the optical depth for the material is unity, i.e., $\tau = 1$, when $N_{\rm H} = 1.7 \times 10^{17}$ cm^{-2}. Based on the equation above, as the column density of the material increases, it progressively absorbs photons of higher energy (e.g., when $N_{\rm H} = 10^{20}$ cm^{-2}, the optical depth is unity at $E \sim 0.1$ keV, allowing us to observe the emission above this energy, but not below). As a result of this photoelectric absorption, the observed X-ray spectrum below the threshold energy will take a form of power-law with a flat photon index ($\Gamma_{\rm obs} \lesssim 1$ for $N_{\rm H} \gtrsim 10^{24}$ cm^{-2}; i.e., CTAGN).

In reality, the column of material that is absorbing the X-ray emission from the corona will not be made up of pure H, but will include other heavier elements such as Carbon, Nitrogen and Oxygen. Since the atomic numbers of these elements are higher than H, the electrons in the K shell are more tightly bound and require higher energy to be ejected out (therefore absorb higher energy photons). However, these elements are less abundant than H, and therefore they contribute small increases to the total absorption cross-section (see Figure 1.16 in Done, 2010).[5] Iron (Fe) is the

[5]We note that although H is the most abundant element, it is largely ionised; therefore other

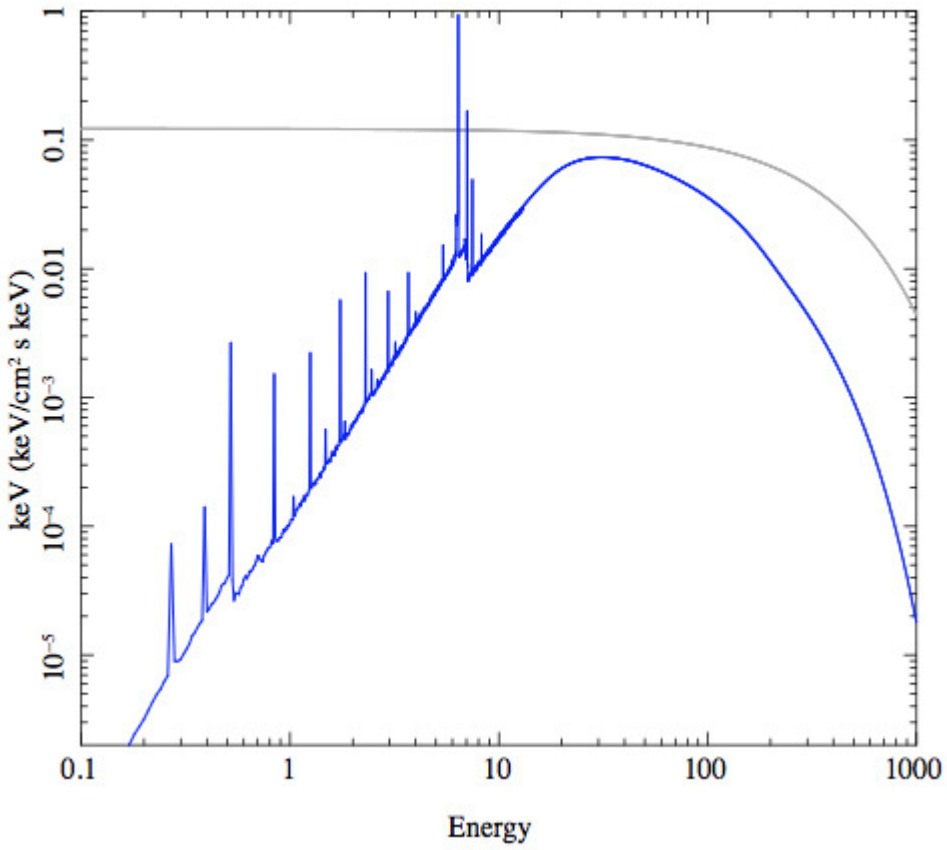

Figure 1.6: A simulated X-ray reflection spectrum for reflection of continuum emission by neutral material with a column density of $N_{\rm H} = 1.5 \times 10^{24}$ cm^{-2}; i.e., CT, assuming solar abundances (blue). The illuminating primary continuum is shown in grey. The much larger absorption cross-section at lower energies means that most incident photons are absorbed rather than reflected. The reflection fraction increases as the photoelectric absorption cross-section decreases with the incident photon energy. However, higher energy photons do not reflect elastically due to Compton down-scattering. The combination of these two effects produces the characteristic peak between ∼20–50 keV that we observe for CTAGN. The atomic features produced as a result of these processes are also illustrated in the plot. Atoms with lower atomic numbers will emit ionisation lines at lower energies, meaning that they are more susceptible to dilution by the illuminating continuum. As a result, the Fe emission lines, particularly the Fe Kα line at $E \approx 6.4$ keV, becomes the most prominent line in the spectrum. Image credit: Done (2010).

last astrophysically abundant element, and there is no more significant absorption at $E > 7.1$ keV, since the K shell edge energy for Fe is at 7.1 keV.

When photoelectric absorption takes place, an electron from the inner most shell of the atom is liberated. The vacancy in the shell will be filled when an electron at a higher energy level decays, emitting energy in the process. The energy can be released as a photon in the form of a fluorescence line (e.g., Kα for electron transition from $n = 2$ to $n = 1$); however, the energy can also be transmitted to another electron in the atom, causing it to be ejected (Auger effect). Elements with higher atomic number have a lower probability to de-excite via Auger, which means that Fe fluorescence lines will be the dominant lines observed in a reflection spectrum. The high atomic number of Fe also means that the lines will be emitted at higher energies, where the reflection spectrum is less diluted by the incident (primary) emission (see Figure 1.6). As a result, the Fe Kα line at $\sim$6.4 keV becomes the most prominent line in the neutral reflection spectrum of an AGN. Reflection off the torus will result in a stronger and narrower Fe Kα line, with equivalent width of $\mathrm{EW_{FeK\alpha}} \gtrsim 1$ keV when $N_\mathrm{H} \gtrsim 10^{24}$ cm^{-2} (i.e., CT). A strong narrow Fe Kα line is therefore one of the characteristic features for CTAGN (e.g., Maiolino et al., 1998; Comastri, 2004). Reflection from the accretion disk will result in weaker ($\mathrm{EW_{FeK\alpha}} \lesssim$ 300 eV) and broader line features than reflection off the torus as the material has a higher velocity.

As the photoelectric absorption cross-section decreases with the incident photon energy, electron scattering starts to dominate, and therefore the reflection fraction increases. The absorption cross-section becomes equal to the Thomson scattering cross-section at about 10 keV. Above this energy, the reflected X-ray flux increases, reaching a peak at about 20–50 keV. Above this energy, Compton down-scattering starts to dominate. Because the scattering is no longer elastic, the incident photons lose some of their energies to the electrons, and are reflected back at lower energies. The combination of these processes (photoelectric absorption at low energies, and predominantly Compton down-scattering at higher energies) gives rise to the

heavier elements often dominate the absorption.

characteristic peak in the reflection spectrum of an AGN at ∼20–50 keV (George & Fabian, 1991; Matt et al., 1991). This peak is often called the "Compton hump". The presence of this peak, together with a narrow Fe Kα fluorescence line, and a flat photon index at $E < 10$ keV (i.e., $\Gamma_{\rm obs} \lesssim 1$) in the X-ray spectra of AGN, are key characteristic signatures for CT absorption.

1.4.2 Identifying Compton-thick AGNs

As described in the previous section, CTAGNs exhibit characteristic signatures in their X-ray spectra. Therefore, broadband X-ray spectral characterisation is essential to identify CTAGN. Low X-ray energy data ($E \lesssim 10$ keV) of a particular source can be provided by the two most sensitive X-ray telescopes available today, *Chandra* and *XMM-Newton*, whilst hard energy X-ray data ($E \gtrsim 10$ keV) can be acquired through the *Swift*-BAT survey, or the more sensitive pointed observations by *NuSTAR* (see Figure 1.4 and Chapter 2). For sufficiently bright AGNs in which the photon statistics are high ($> 10^2$ photon counts), we can perform X-ray spectral modelling using physically-motivated torus models that self-consistently predict the absorption/reflection features in AGN spectra (e.g., Murphy & Yaqoob, 2009; Brightman & Nandra, 2011; see Chapter 3–5). This modelling allows for direct measurements of the column density of the obscuring material that is absorbing the primary X-ray emission across our l.o.s, and therefore allows for the unambiguous identifications of CTAGN. In the absence of broadband X-ray spectra or insufficient quality X-ray data, we can infer the existence of absorption through the presence of individual or multiple CT signatures described earlier (e.g., flat $\Gamma_{\rm obs}$, strong Fe Kα line). However, this technique is not always accurate (e.g., some CTAGNs have $\rm EW_{FeK\alpha} < 1$ keV; Della Ceca et al., 2008; Gandhi et al., 2016) and does not provide the direct measurement of the obscuring column density.

The strongest and most direct identifications of CTAGN come from X-ray spectral modelling. However in most cases, CTAGNs are only weakly detected, or even undetected, in X-rays. Therefore, a direct constraint of CT absorption at X-ray energies is not always possible. Because of this, a number of multiwavelength approaches have been developed to indirectly estimate the amount of absorption suf-

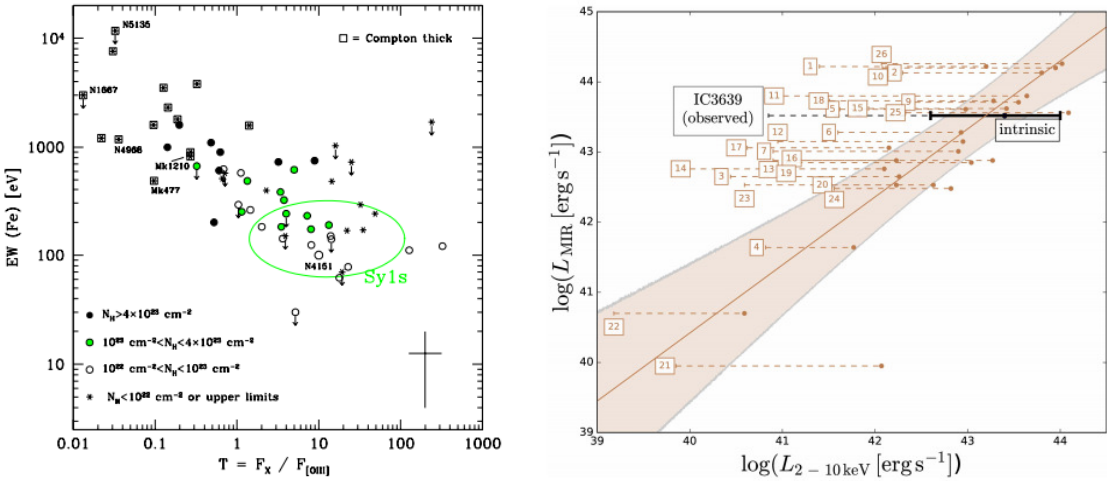

Figure 1.7: Multiwavelength identifications of CTAGN. *Left*: The Bassani et al. (1999) diagnostic diagram. The plot shows the distribution of the equivalent width of Fe Kα line as a function of the ratio between the observed 2–10 keV flux and the [OIII] emission line flux (corrected for the Balmer decrement; i.e., Hα/Hβ), for a sample of Seyfert 2 galaxies with reliable $N_{\rm H}$ measurements from X-ray spectroscopy. The plot indicates that CTAGNs (squares) typically have $f_{2-10,obs}/f_{\rm [OIII]} \lesssim 1$, and $\rm EW_{FeK\alpha} \gtrsim 1$ keV. *Right*: The $L_{\rm MIR}$ vs. L_{2-10} distributions of the local bona-fide CTAGNs (Boorman et al., 2016). The intrinsic relationship derived by Asmus et al. (2015) (brown solid line) is plotted with a 1-σ scatter (brown shaded region). Observed 2–10 keV luminosities of the CTAGNs are plotted in squares, whilst the absorption-corrected 2–10 keV luminosities as measured from X-ray spectral analyses are plotted in filled circles. This plot shows that the observed 2–10 keV luminosities of CTAGNs typically deviate significantly from the intrinsic relationship by Asmus et al. (2015) ($\sim$2 orders of magnitude fainter in the 2–10 keV band); however after correction for absorption, the intrinsic luminosities measured agree with the relationship. Image credit: Bassani et al. (1999), Boorman et al. (2016).

fered by AGNs (see Figure 1.7; e.g., Maiolino et al., 1998; Bassani et al., 1999; Cappi et al., 2006; Panessa et al., 2006; Gandhi et al., 2009; Asmus et al., 2015). These approaches work by comparing the observed X-ray emission of the AGN with the intensity of the high ionisation emission lines emitted by the NLR (e.g., [OIII], [OIV], [NeV]) or the mid-IR continuum emission produced by the torus, which act as proxies for the intrinsic power of the AGN (see Chapter 3–5). If the luminosity of the observed X-ray emission is found to be significantly lower than that predicted from these indirect indicators, this suggests that the primary emission from AGN is heavily obscured along our l.o.s. Although the uncertainties from these indirect estimates are relatively large, and these techniques do not provide direct measurements for the absorbing column density, they are useful in highlighting potential CT sources, which can then be followed up by higher quality X-ray observations to confirm whether or not they are CT.

1.5 Thesis overview

The main aim of this thesis is to provide a constraint on the CTAGN population and the column density distribution of AGN in the local universe ($D \leq 15$ Mpc), which can be used as a benchmark for more distant AGN studies. I used multiwavelength techniques to achieve this, focusing on broadband X-ray spectroscopy using data from various X-ray observatories, mainly *NuSTAR*, in combination with *Chandra* and *XMM-Newton*. Below, I provide a brief outline of each chapter presented in this thesis.

1.5.1 Chapter 2 – Data: the AGN sample and the X-ray observations overview

In this chapter, I first describe the AGN sample that was used for this research, which consists of mid-IR selected AGNs, complete out to $D = 15$ Mpc. I then detail the different X-ray observatories that were extensively used in this research to measure the X-ray emission and absorption properties of the AGNs; i.e., *NuSTAR*, *Chandra* and *XMM-Newton*. As part of this research, I have carried out multiple

X-ray observations using these observatories for the less well-studied AGNs in my sample. I provide a summary of the X-ray data available for each individual AGN, and describe the data processing procedures that I have adopted throughout this thesis.

1.5.2 Chapter 3 – *NuSTAR* observations of the Compton-thick active galactic nucleus and ultraluminous X-ray source candidate in NGC 5643

In this chapter, I present the first high energy *NuSTAR* observations carried out as part of this research; the first of two newly identified bona-fide CTAGNs in the local universe (see also Chapter 4). The observations were conducted for the AGN in NGC 5643, which was the strongest CTAGN candidate in our sample, as suggested by multiwavelength techniques. Our data not only provide the first detection of the AGN in the galaxy at high X-ray energies ($E \gtrsim 10$ keV), but also the first detection of the ULX candidate located near the AGN that was not resolved in previous high X-ray energy observations. We performed the first broadband X-ray spectroscopy on the AGN over an energy range of ∼0.5–100 keV, and unambiguously confirmed that the AGN is CT. Meanwhile, analysis of the *NuSTAR* spectrum of the ULX provides evidence for a spectral cut-off at $E \sim 10$ keV, consistent with that seen in other ULXs observed by *NuSTAR*. In addition, we also analyse the archival X-ray data for the ULX and found that it has significantly varied between different observations carried out over a period of ∼11 years. These results further support the ULX classification of the source. This work is published in Annuar et al. (2015).

1.5.3 Chapter 4 – A new CTAGN in our cosmic backyard: Unveiling the buried nucleus in NGC 1448 with *NuSTAR*

In this chapter, I present the multiwavelength observations of NGC 1448 across X-rays, optical and mid-IR continuum, using the *Chandra* and *NuSTAR* observatories,

the Gemini-South/T-ReCS telescope and the European Southern Observatory New Technology Telescope, respectively. Our data provide the first identifications of the AGN in this nearby galaxy ($D = 11.5$ Mpc) at these wavelengths. Not only that, our data also reveal that the AGN is heavily obscured in X-rays by a CT column of obscuring gas along our l.o.s. The intrinsic 2–10 keV luminosity determined for the AGN ($L_{2-10,\mathrm{int}} \sim 10^{40}$ erg s^{-1}) makes it one of the lowest luminosity CTAGN known to date. This discovery demonstrates *NuSTAR* capabilities of finding faint CTAGN that were missed by previous high energy X-ray observatories (e.g., *Swift*-BAT). In addition, our analysis of the optical spectra of NGC 1448 also demonstrates the challenges in identifying AGNs at optical wavelengths, especially when they are located in highly inclined galaxies that can significantly dilute the optical emission from the AGNs. Our findings may explain why the AGN in NGC 1448 was misclassified in a previous optical study as an HII galaxy. This work is published in Annuar et al. (2017).

1.5.4 Chapter 5 – Towards a complete census of the CTAGN population and the N_{H} distribution of AGN in the local universe

In this chapter, I present a multiwavelength analysis of all of the AGNs in my sample to identify CTAGNs and CTAGN candidates in the sample. Our approach includes direct CTAGN identifications through X-ray spectral analysis, as well as indirect identifications of potential CTAGNs using multiwavelength intrinsic luminosity indicators such as the [OIII], [NeV] and $12\mu m$ luminosities. We show that using our sample, we are able to directly resolve the CTAGN population in our local universe, as predicted from previous studies, into individual sources. Our sample has also allowed us to identify intrinsically lower luminosity CTAGNs that have been missed by previous hard X-ray observatories such as *Swift*-BAT; i.e., down to $L_{2-10,\mathrm{int}} \sim 10^{40}$ erg s^{-1}, about an order of magnitude lower than that identified in the *Swift*-BAT survey. We also discuss the reliability of the different multiwavelength techniques used to identify CTAGN candidates in the sample, and compare the AGN and host

galaxy properties in our sample with that of the *Swift*-BAT AGN sample. This work is being prepared for journal submission.

1.5.5 Chapter 6 – Summary and future work

In this final chapter, I provide a summary of the work presented in this thesis as well as ongoing and future work to address outstanding questions and potentially extend the research carried out in this thesis into further projects.

Chapter 2

Data: the AGN sample and the X-ray observations overview

In order to form a complete census of the Compton-thick (CT) active galactic nucleus (AGN) population in our local universe, we first need a complete AGN sample that is least limited by flux and unbiased against obscuration. A volume-limited selection within a relatively small volume is probably the best approach to construct an AGN sample that is least limited by flux. This means that the sample will include more low luminosity sources as compared to a flux limited sample. In addition, a volume-limited sample can also be used to form representative volume-averaged statistics. In Chapter 1, I have briefly discussed the pros and cons of the different AGN identification methods. Constructing an AGN sample on the basis of X-ray selection (e.g., an X-ray luminosity threshold) would produce a sample that is biased against finding CTAGN, due to the weak flux observed. On the other hand, AGN selection using radio wavelengths can miss a significant fraction of AGN since most AGNs are radio-quiet. Whilst an optical selection technique on the basis of emission line diagnostics (e.g., Baldwin et al., 1981; Ho et al., 1997; Kewley et al., 2001) is not affected by obscuration by the AGN torus, it can miss AGNs that are significantly obscured by the host galaxies (e.g., Goulding & Alexander, 2009). Conversely, an infrared (IR) AGN selection technique will be relatively unbiased against obscuration due to the lower extinction suffered at this waveband (e.g., the extinction at $12\mu m$ is $\sim$27$\times$ lower than that in the optical V-band for a standard dust extinction law; Li

& Draine, 2001). Therefore, it should be the best approach for constructing an AGN sample that is least affected by both host galaxy and torus obscuration. Clearly, a multiwavelength selection approach would yield an even more complete sample that is independent of AGN diagnostics at any one wavelength. However, the advantage of forming a sample using a single waveband selection is that the selection effect is simpler and better understood.

In this chapter, I will describe the volume-limited AGN sample that I have used throughout this work in an attempt to form the most complete census of the CTAGN population in our local universe (Section 2.1). As described in Chapter 1, detailed broadband X-ray spectroscopy is essential in identifying CTAGN. Therefore, I have used this approach as the main technique to unambiguously identify CTAGN in my sample. In Section 2.2, I provide an overview of the most sensitive focusing X-ray observatories available today that I have extensively used throughout this thesis. I also summarise the X-ray observations that have been carried out for my AGN sample using these observatories, and briefly describe the data reduction process that I have adopted in this thesis.

2.1 The $D \leq 15$ Mpc AGN sample

The parent AGN sample that I have used for this work was constructed by Goulding & Alexander (2009) (hereafter GA09). Here, I briefly describe their AGN selection, and refer the reader to the GA09 paper and its subsequent paper, Goulding et al. (2010), for further details on the sample. Their sample consists of 17 IR-selected AGNs within a small volume of $D = 15$ Mpc. It was derived using the *Infrared Astronomical Satellite* (*IRAS*) Revised Bright Galaxy Sample (RBGS; Sanders et al., 2003) which provides the most complete census of all IR-bright galaxies in the local universe ($f_{60\mu m} > 5.24$ Jy) above a Galactic latitude of $|b| = 5°$. The constraint of 15 Mpc on the distance was placed to avoid the Virgo cluster at ≈16 Mpc (see Figure 2.1) so that the AGN sample is representative of the field-galaxy population, as demonstrated in Goulding et al. (2010). The distances were calculated using the Mould et al. (2000) cosmic attractor model which adjusts heliocentric redshifts to

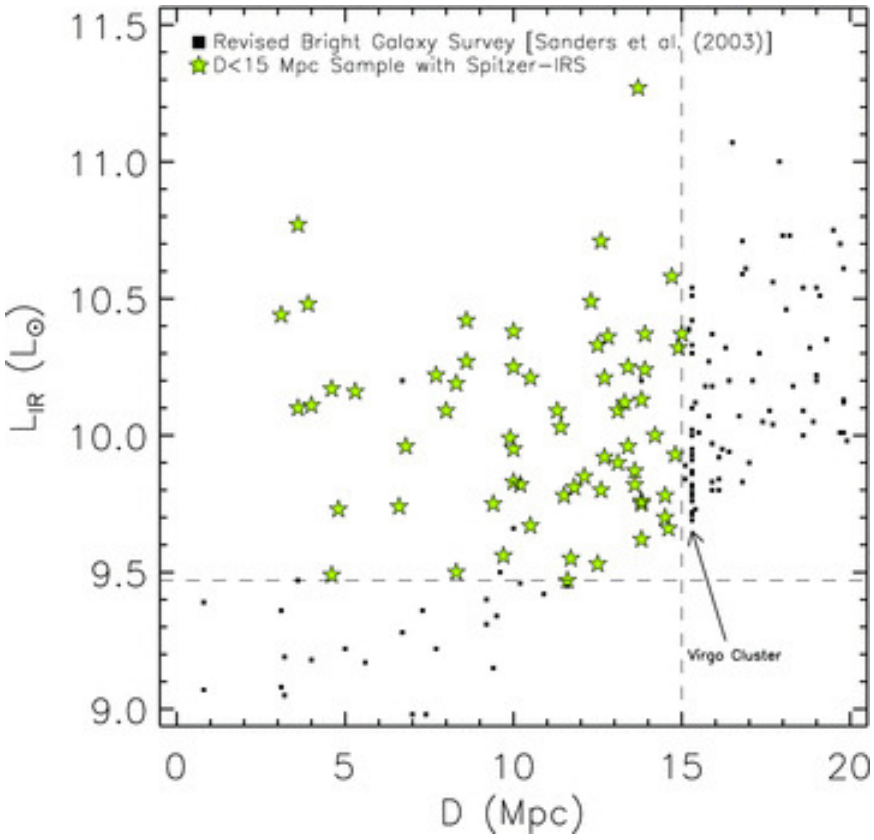

Figure 2.1: The total IR (8–1000μm) luminosity versus distance for the galaxies in the RBGS sample (squares; Sanders et al., 2003). The 64 galaxies which match the GA09 selection criteria; i.e., $L_{\rm IR} > 3 \times 10^9$ $L_\odot$ and $D \leq 15$ Mpc (dashed lines), and have high resolution *Spitzer*-IRS data, are indicated with green stars. Image credit: GA09.

the centroid of the Local Group, taking into account the gravitational attraction towards the Virgo Cluster, the Great Attractor and the Shapley supercluster. In addition, GA09 also apply a total IR (8–1000μm) luminosity cut-off of $L_{\rm IR} > 3 \times 10^9\ L_{\odot}$ to their sample to match the flux sensitivity limit of RBGS (see Figure 2.1), and exclude low luminosity dwarf galaxies as well as relatively inactive galaxies. GA09 found that there are 68 galaxies detected by IRAS with $L_{\rm IR} > 3 \times 10^9\ L_{\odot}$ within $D \leq 15$ Mpc.

GA09 then used the detection of the high ionisation [NeV]λ14.3μm emission line from the *Spitzer* Space Telescope (Werner et al., 2004) high resolution IR Spectrographs (IRS) Short-High (SH) module (λ = 9.9–19.6μm; spectral resolution, $R \sim 600$; aperture size = 4.7 × 11.3 arcsec^2; Houck et al., 2004) to identify the presence of AGNs in these galaxies. Out of the 68 galaxies, 64 have *Spitzer*-IRS SH data (∼94% complete). The [NeV] line is produced in the narrow line region (NLR) of AGN through ionisation by the primary emission of the nuclear source (see Chapter 1). Because the line is produced in the NLR, it is not strongly affected by obscuration by the AGN torus, unlike the primary emission. In addition, given that it is emitted at mid-IR wavelength (i.e., λ = 14.32μm), it does not suffer significant absorption by the host galaxy, unlike the NLR emission lines that are produced at optical wavelengths (the extinction at 14.32μm is ∼50× lower than that in the optical V-band; Li & Draine, 2001). The energy required to ionise this line is also relatively large; i.e. 97.1 eV, meaning that it can only be produced by extremely energetic phenomena such as AGN activity. This is why the detection of this line provides an almost unambiguous identifier of AGN. Although the line is predicted to be produced by a dense population of Wolf-Rayet stars (Schaerer & Stasińska, 1999) and extremely high velocity shocks caused by starburst, these have not yet been observed, and do not appear to be the case for the AGNs in the GA09 sample (see GA09 for further details).

Based on this technique, 17/64 galaxies (∼27%) have significant [NeV] line detections, and thus are identified as AGNs. Out of these 17 AGNs, 9 (∼53%) are not identified as AGNs using the optical emission line diagnostic diagram (see Table 2.1) due to significant dilution by the host galaxies (e.g., highly inclined, presence of dust

Table 2.1: Complete list of AGN at D $\leq$ 15 Mpc and their basic properties.

Name	D	Hubble	Spectral	*Swift-BAT*	log $M_{\rm BH}$	log $L_{\rm [OIV]}$	log $L_{\rm [NeV]}$	log $L_{12\mu m}$	log $L_{\rm [OIII],corr}$	log $L_{\rm IR}$
	[Mpc]	Type	Class	AGN?	[$M_\odot$]	[erg s^{-1}]	[erg s^{-1}]	[erg s^{-1}]	[erg s^{-1}]	[$L_\odot$]
(1)	(2)	(3)	(4)	(5)	(6)	(7)	(8)	(9)	(10)	(11)
Circinus	4.0	Sb	S2[1]	Yes	6.23[3]	40.11[5]	39.62[6]	42.60	40.52[10]	10.15[12,13]
ESO121-G6	14.5	Sc	H II	No	6.10	39.04	38.21	< 41.00[8]	-	9.70
NGC 0613	15.0	Sbc	H II	No	7.34	39.38	38.25	41.27	39.67	10.37
NGC 0660	12.3	Sa	L	No	7.35	39.71	38.85	41.89[9]	40.03	10.49
NGC 1068	13.7	Sb	S2	Yes	7.20	41.66	41.30	43.76	42.61	11.27
NGC 1448	11.5	Scd	S2[a,2]	No	5.99	39.40	38.76	40.60[2]	38.84[2]	9.78
NGC 1792	12.5	Sbc	H II	No	6.83	38.26	37.88	< 40.47[8]	-	10.33
NGC 3486	9.2	Sc	S2	No	6.50[4]	38.53	37.71[7]	< 40.10	38.19[11]	9.31
NGC 3621	6.6	Sd	S2	No	6.50	38.18	37.18	40.47[9]	37.19	9.74
NGC 3627	10.0	Sb	L	No	7.30	38.38	37.55	40.59	39.01	10.38
NGC 3628	10.0	Sb	L	No	6.53	38.81	38.05	< 40.47	36.97	10.25
NGC 4051	13.1	Sbc	S2	Yes	6.15	39.88	39.36	42.38	40.25	9.90
NGC 4565	10.0	Sb	S2	No	7.56[4]	38.40	37.58[6]	40.81[9]	38.84[11]	9.66
NGC 4945	3.9	Scd	H II	Yes	6.04	38.72	38.11	40.00	35.04	10.48
NGC 5033	13.8	Sc	S2	Yes	7.62	39.08	37.98	40.96	39.78	10.13
NGC 5128	4.0	S0	H II	Yes	8.38	39.38	38.62	41.86	38.09	10.11
NGC 5194	8.6	Sbc	S2	No	6.88	38.85	37.81	40.80	40.18	10.42
NGC 5195	8.3	Irr	L	No	7.31	37.89	37.22	40.51[9]	37.12	9.50
NGC 5643	13.9	Sc	S2	Yes	6.44	40.43	39.75	42.17	41.32	10.24
NGC 6300	13.1	Sb	S2	Yes	6.80	39.78	39.41	42.45	40.02	10.09

Notes. Column (1) Galaxy name; (2) Distance in Mpc; (3) Hubble classification of the host galaxy; (4) Optical spectral class on the basis of emission line diagnostic diagrams (Kewley et al., 2001; Kauffmann et al., 2003); (5) Whether the AGN is detected in the 70-month *Swift*-BAT survey (Baumgartner et al., 2013); (6) Black hole mass relative to the mass of the sun, $M_\odot$; (7)-(10) [OIV], [NeV], 12 μm continuum, and [OIII] (corrected for the Balmer decrement; i.e., Hα/Hβ) luminosities in erg s^{-1}, respectively; (11) total IR luminosity in solar luminosity, $L_\odot$. References are given for data that were not obtained from GA09 or Goulding et al. (2010).

[a] NGC 1448 was previously classified as an HII galaxy in optical (Veron-Cetty & Veron, 1986), however our new data indicates that it is a Seyfert galaxy (see Chapter 4; Annuar et al., 2017).

References. [1] Moorwood & Glass (1984); [2] Annuar et al. (2017) (see Chapter 4); [3] Greenhill et al. (2003); [4] McKernan et al. (2010); [5] Diamond-Stanic et al. (2009); [6] Pereira-Santaella et al. (2010); [7]; Predicted from the [OIV]:[NeV] luminosity relationship in GA09; [8] Private communication with D. Asmus; [9] Predicted from the [NeV]:12 μm luminosity relationship (see Appendix A.2); [10] Bianchi et al. (2002); [11] Ho et al. (1997); [12] Helou & Walker (1988); [13] Sanders & Mirabel (1996).

lanes, strong star formation activity; GA09). Furthermore, 10/17 (∼59%) are found to be unidentified as AGNs in X-rays on the basis of high X-ray energy detection by the *Swift* Burst Alert Telescope (BAT) 70-month all sky survey (Baumgartner et al., 2013).[1] This demonstrates the relative inefficiency of identifying AGN using optical and X-ray wavelengths as compared to IR (i.e., <60% in this case).

To further extend the GA09 sample, we included three other known AGNs within 15 Mpc that were not selected by GA09 – Circinus, NGC 3486 and NGC 4565. Circinus is selected as AGN in optical and X-ray (e.g., Moorwood & Glass, 1984; Baumgartner et al., 2013), but was not selected in the original RBGS sample (therefore GA09) due to its low galactic latitude; i.e., $\sim 4^{o}$ below the Galactic plane. NGC 3486 and NGC 4565 were among the four galaxies in GA09 that lacked high-resolution *Spitzer*-IRS spectroscopic data at the time of that study. NGC 3486 did have high-resolution *Spitzer*-IRS data at the time, however no useful spectral information can be extracted from the data as they are noisy. Pereira-Santaella et al. (2010) provide *Spitzer*-IRS data for both Circinus and NGC 4565, and detected [NeV] emission lines in both of these galaxies. Both NGC 3486 and NGC 4565 are identified as Seyferts on the basis of optical emission line diagnostic diagram (Ho et al., 1997) and [OIV]λ25.89μm line detections (Diamond-Stanic et al., 2009).[2] Our final AGN sample thus consists of 20 AGNs in total, complete to $D = 15$ Mpc. The complete list of the AGNs and their basic properties are tabulated in Table 2.1 (see also Chapter 5 for the overall properties of the AGN sample as compared to the *Swift*-BAT AGN sample; e.g., star formation rate and stellar mass distributions).

Figure 2.2 shows a plot of the ratio between $L_{\rm [NeV]}$ and $L_{\rm IR}$ as a function of $L_{\rm IR}$ (adapted from GA09). Using the relationship between AGN bolometric luminosity

[1] The *Swift*-BAT telescope provides a hard X-ray all sky survey in the 14–195 keV band. The 70-month survey is sensitive down to an X-ray flux of $f_{14-195,\rm obs} \sim 10^{-11}$ erg s^{-1} cm^{-2} (Baumgartner et al., 2013). This means that at $D = 15$ Mpc, it will be able to detect an AGN down to an observed X-ray luminosity of $L_{14-195,\rm obs} \sim 3 \times 10^{41}$ erg s^{-1}, or $L_{2-10,\rm obs} \sim 10^{41}$ erg s^{-1} on the basis of the scaling relation derived by Rigby et al. (2009).

[2] [OIV]λ25.89μm emission line is also often used for AGN identification due to its high ionisation energy (59.4 eV), however it is a less unambiguous AGN indicator than the [NeV] line given that energetic starbursts can also produce this line.

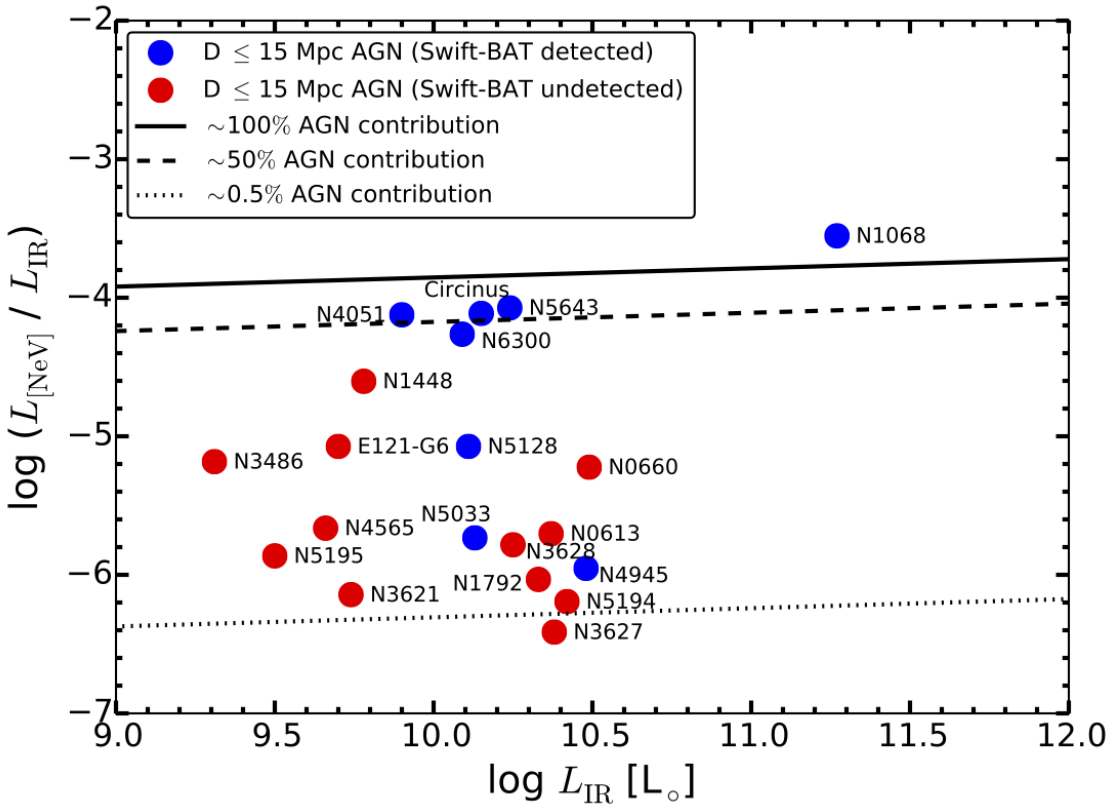

Figure 2.2: $L_{[\mathrm{NeV}]}$ to L_{IR} ratio vs. L_{IR} for the D $\leq$ 15 Mpc AGN sample (adapted from GA09). AGNs that are detected by the 70-month *Swift*-BAT survey are plotted in blue, and those that are not detected are plotted in red. The solid, dashed and dotted lines indicate the $L_{[\mathrm{NeV}]}$ to L_{IR} ratio estimated for 100%, 50% and 0.5% AGN contributions to the total IR luminosity, respectively, based on the L_{bol}:$L_{[\mathrm{NeV}]}$ luminosity relationship derived by Satyapal et al. (2007). This plot shows that our AGN sample consists of both AGN dominated and host galaxy dominated systems.

($L_{\rm bol}$) and the [NeV] luminosity derived by Satyapal et al. (2007), we calculated the $L_{\rm [NeV]}$ to $L_{\rm IR}$ ratios estimated for 100%, 50% and 0.5% AGN contributions to the total IR luminosity, on the basis that the [NeV] line is an unambiguous tracer for AGN activity. Based on Figure 2.2, we can see that our sample consists of both AGN dominated systems as well as host galaxy dominated systems. The plot indicates that the [NeV] emission line is sensitive to finding AGNs that contribute as little as $\sim$0.5% to the total IR emission observed.

2.2 X-ray observations

In this section, I will firstly describe the principle behind the operation of X-ray telescopes (Section 2.2.1). I will then provide an overview on the high (*NuSTAR*; Section 2.2.2) and low energy (*Chandra* and *XMM-Newton*; Section 2.2.3 and 2.2.4, respectively) focusing X-ray observatories that I have predominantly used throughout this thesis. High X-ray energy data ($E > 10$ keV) are essential to trace the primary emission from CTAGN that is able to pierce through the thick layers of obscuring gas and dust. On the other hand, low X-ray energy observations ($E < 10$ keV) are crucial to probe the fluorescence iron (Fe) Kα line emission emitted at $\sim$6.4 keV and the photoelectric cut-off at $E < 10$ keV. Combining both of these low and high X-ray energy data together will provide us with a broadband X-ray spectrum of the AGN, and allow us to accurately measure the column density of the obscuring material.

2.2.1 Basic principles of focusing X-ray telescope

Because the cosmic X-ray emission is absorbed by the Earth's atmosphere, X-ray observatories must be sent into space to carry out their operations. Whilst the history of astronomical visible light focusing goes way back to $\sim$400 years ago when Galileo Galilei first observed the sky using his homemade telescope, scientists only discovered how to focus X-ray photons 65 years ago when Hans Wolter invented a reflective optic specifically for this purpose. Due to the high penetrating power of X-ray emission, the photons are very difficult to focus as they can easily pass

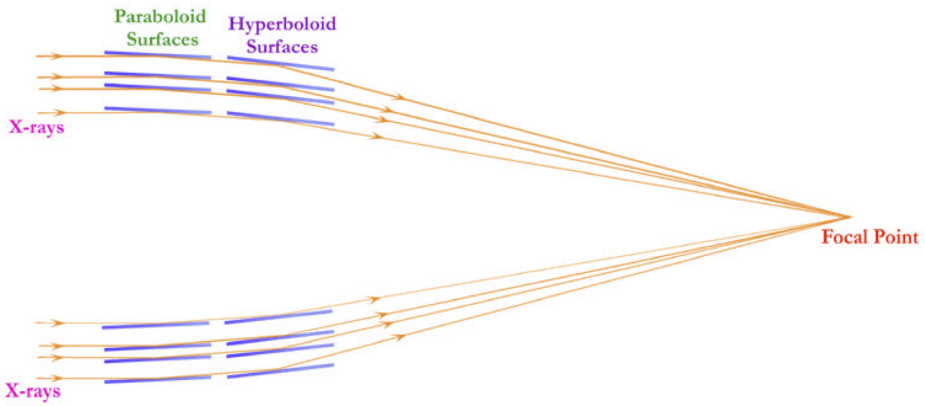

Figure 2.3: A schematic diagram illustrating grazing incidence mirrors which consists of paraboloid (primary mirror) and hyperboloid (secondary mirror) surfaces used in the current generation of X-ray telescopes. Multiple mirrors are usually nested together to increase the effective area of the telescope. In order to increase the efficiency of the X-ray photons being reflected off the mirrors (instead of being absorbed), the incoming X-ray photons must hit the mirror at very small grazing angles (i.e., almost parallel to the mirrors). Image credit: NASA/CXC/S. Lee.

through the telescope mirrors, instead of being reflected, unlike photons emitted in the ultraviolet (UV), optical and IR wavebands. Therefore, the mirrors used in X-ray telescopes have to be built differently from those used in UV/optical/IR telescopes. These mirrors are called "grazing incidence" mirrors (see Figure 2.3). They are aligned almost parallel to the incident X-ray emission (i.e., small "grazing angles") to increase the probability of the X-ray photons being reflected rather than absorbed by the mirror. This probability increases with smaller grazing angles, lower X-ray energy photons and higher mirror density. These mirrors induce the direction of the incident photons toward the detectors at the focal point by progressively modifying the direction of the photons by small amounts for each reflection. The shallow incident angles however, result in a very small photon collecting area. In order to increase this effective area, multiple shells of mirrors are commonly nested together (see Figure 2.3).

There are typically two types of reflecting surfaces included in the mirrors; i.e., a paraboloid (primary mirror) and a hyperboloid (secondary mirror). A paraboloid

surface alone can effectively focus the incident X-ray photons to a point, however images of off-axis objects will be severely distorted (i.e., producing a coma effect). This problem can be overcome by adding a secondary mirror in the form of hyperboloid surface (Wolter, 1952). The Wolter Type I mirror design which consists of this paraboloid and hyperboloid optics, and the advantage of a relatively short focal length, is often employed in X-ray telescopes. This mirror design was used for the *Einstein* observatory (also known as the High Energy Astrophysics Observatory 2; i.e., HEAO-2), which was the first orbiting X-ray telescope with the capabilities of focusing X-ray photons (launched in 1978).[3] This classic design has also been adopted in the most sensitive X-ray observatories operating today; i.e., *NuSTAR*, *Chandra* and *XMM-Newton* (see Section 2.2.2, 2.2.3 and 2.2.4, respectively).

The detectors installed at the focal point of the telescope record the information of the incident photons such as their energies, spatial positions and arrival times. In the modern generation of X-ray telescopes, the detecting instruments used are solid state detectors or charge-coupled devices (CCDs), which allow for simultaneous recording of the source image and spectroscopic information. The incident X-ray photons are absorbed by the detector which causes the atoms in the detector pixels to be ionised. This will result in the production of electrons, and the resulting charges created (which are proportional to the incident photon energies) are then digitally recorded. In optical telescopes, an image is created by accumulating charges from many individual photons during the exposure time. However in X-rays, when a single photon hits the detector, it produces enough charge for the detector to measure its energy. This provides a unique advantage to X-ray observations as they allow individual photons to be counted (therefore the properties of each individual photons; e.g., the energy, position and arrival time, can be recorded). In practice, the instruments will not only detect X-ray photons, but also other events such as non-X-ray emission and particle flares associated with soft protons. These events are usually variable and can be excluded using various methods such as extracting the data during the "good time intervals"; i.e., when the flare level is not significant.

[3]The Wolter Type I mirror design was first employed in X-ray telescope in a rocket-borne experiment performed in 1965 to obtain X-ray images of the Sun (Giacconi et al., 1965).

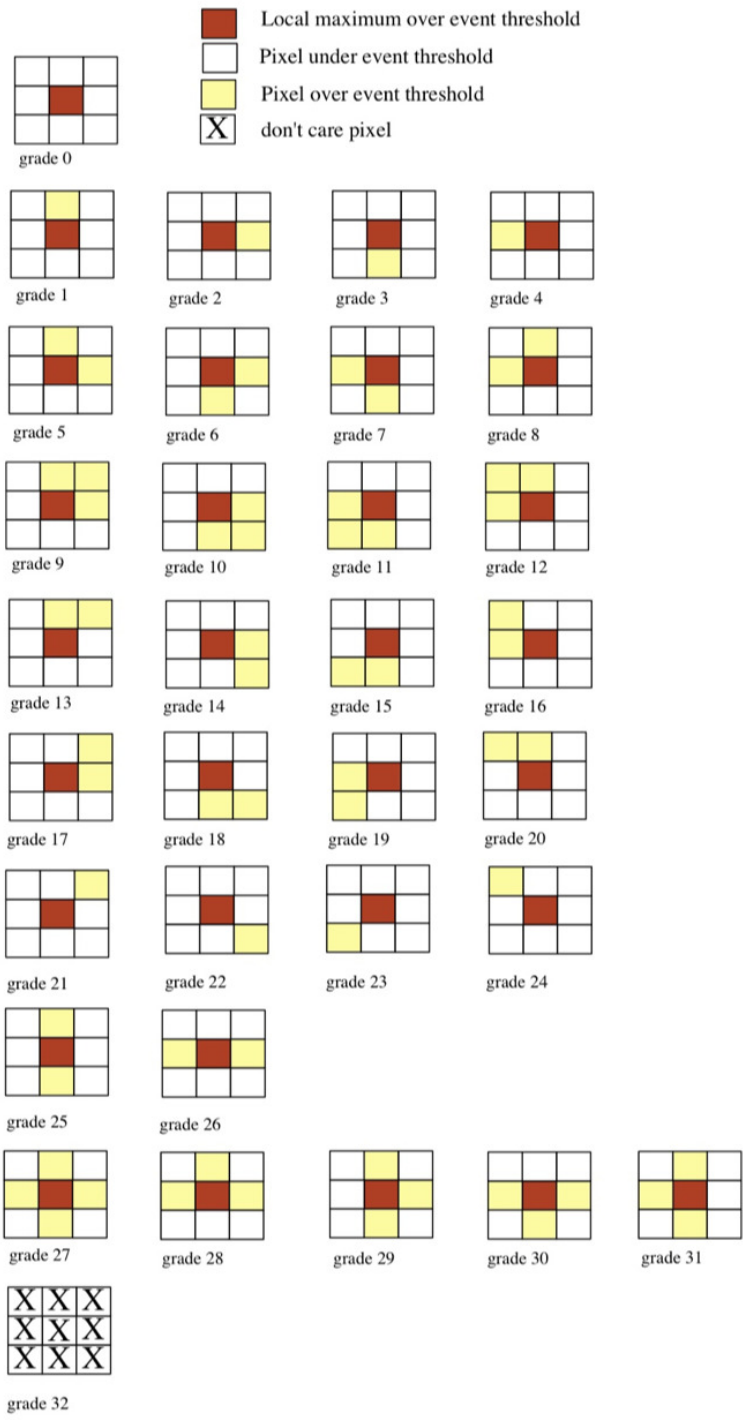

Figure 2.4: Definition of the *NuSTAR* event grades. Grades 27–32 are rejected in the standard processing of the *NuSTAR* data as they are less likely caused by real X-ray events (see Rana et al., 2009 and Kitaguchi et al., 2011 for further details). Image credit: the *NuSTAR* data analysis guide (see footnote 5).

Table 2.2: Basic properties of the focusing X-ray observatories predominantly used in this thesis.

Observatory	Energy range	Spatial resolution	Energy resolution	Effective area	Field of view
	[keV]	[″]	[eV]	[cm^2]	[′]
(1)	(2)	(3)	(4)	(5)	(6)
NuSTAR	3–79	18	400	900	12.5 × 12.5
Chandra (ACIS-S)	0.1–10	0.5	100	555	8.3 × 50.6
XMM-Newton (PN)	0.1–12	6	50	3500	27.5 × 27.5

Notes. Column (1) X-ray observatory; (2) energy range in keV; (3) spatial resolution at full width half maximum, FWHM in arcsecond; (4) energy resolution at 1 keV (10 keV for *NuSTAR*) in eV; (5) effective area at 1 keV (10 keV for *NuSTAR*) in cm^2. The effective area reported here correponds to the mirror collecting area and does not include the efficiency of the detector (this is shown in Figure 2.5); (6) field of view in arcminute.

These events can also be filtered out during the data processing step by excluding the bad event "grades". This is done by examining the signal patterns of the incident events; e.g., in a 3 × 3 pixel for *Chandra* and *NuSTAR* (centred on the pixel with the largest charge; see Figure 2.4 for *NuSTAR* event grades). Each 3 × 3 pixel will be assigned a grade, and the grades that are believed not to be caused by real X-ray events can be excluded during the data screening stage.

In the subsequent sections, I provide an overview of the most sensitive focusing X-ray observatories operating today that I have extensively used throughout this thesis. I summarised their properties in Table 2.2 and show a comparison between their effective area as a function of energy in Figure 2.5. In Table 2.3, I briefly summarised the X-ray observations that have been carried out for the AGN in my sample, including those that have been taken specifically for this research.

2.2.2 *NuSTAR*

The *Nuclear Spectroscopic Telescope Array* (*NuSTAR*; Harrison et al., 2013), operating over the X-ray energy band of 3–79 keV, is the first orbiting observatory

Table 2.3: Pointed X-ray observations for the D $\leq$ 15 Mpc AGN sample.

Name	*NuSTAR*	*Chandra*	*XMM-Newton*
Circinus	✓	✓	✓
ESO121-G6	✓^{*,c}	✓^{*,c}	✓
NGC 0613	×	✓	✓
NGC 0660	✓^{c}	✓^{c}	✓
NGC 1068	✓	✓	✓
NGC 1448	✓	✓	×
NGC 1792	✓*	✓	✓
NGC 3486	✓	✓	✓
NGC 3621	✓^{*,c}	✓	✓^{*,c}
NGC 3627	✓*	✓	✓
NGC 3628	✓*	✓	✓
NGC 4051	✓	✓	✓
NGC 4565	×	✓	✓
NGC 4945	✓	✓	✓
NGC 5033	✓*	✓	✓
NGC 5128	✓	✓	✓
NGC 5194	✓	✓	✓
NGC 5195	✓	✓	✓
NGC 5643	✓	✓	✓
NGC 6300	✓	✓	✓

Notes. "✓" indicates that the source has been observed by the particular observatory, whilst "×" indicates that it has not been observed. More details on some of these observations are described in Chapters 3–5. Those in red highlight the X-ray observations that have been taken specifically for this research.

$*$ observation scheduled.

c coordinated with the other observatory.

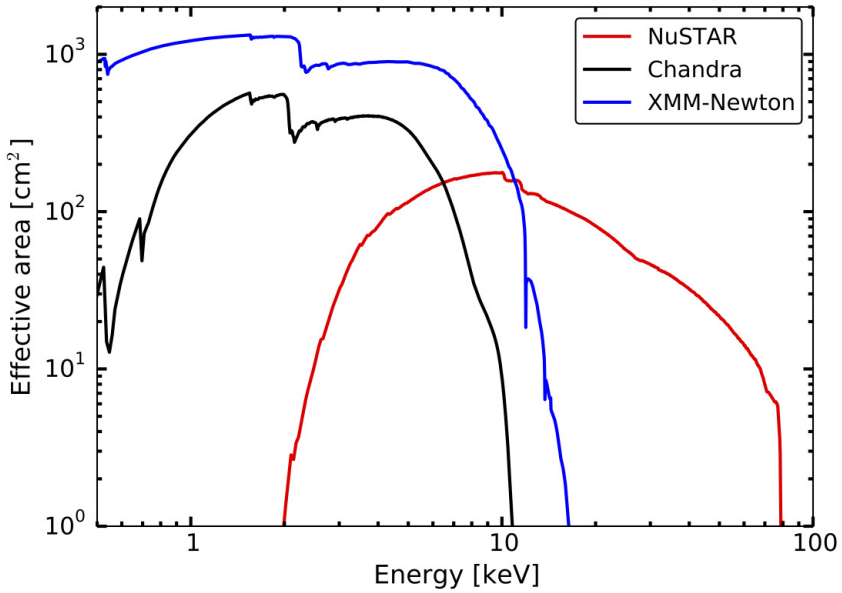

Figure 2.5: A plot of total effective area (mirror collecting area and detector response) as a function of energy for *NuSTAR* (red), *Chandra*/ACIS (black) and *XMM-Newton*/EPIC-PN (blue).

with the ability to focus X-ray photons at hard X-ray energies ($E > 10$ keV).[4] The observatory was launched on June 13th, 2012, as part of the National Aeronautics and Space Administration (NASA) Small Explorer (SMEX) satellite program. The mission is dedicated to observe the universe in hard X-ray energies, beyond what can be probed by the current focusing X-ray observatories such as *Chandra* and *XMM-Newton*. Before *NuSTAR*, X-ray observations at hard energies used collimated or coded mask instruments (instead of focusing optics) in which the image of the X-ray sources are reconstructed based on their shadows (providing indirect images). This results in a low sensitivity observations and high level of background, due to the fact that the photons are not focused and the size of the detectors are often large. *NuSTAR* provides a two orders of magnitude improvement in sensitivity and over

[4]The developments of hard X-ray energy ($E > 10$ keV) focusing in astronomy started with balloon-borne experiments which carry grazing incidence optics up to an altitude of 40 km above sea, $> 99\%$ above the Earth's atmosphere (e.g., the High-Energy Focusing Telescope (HEFT); Harrison et al., 2005).

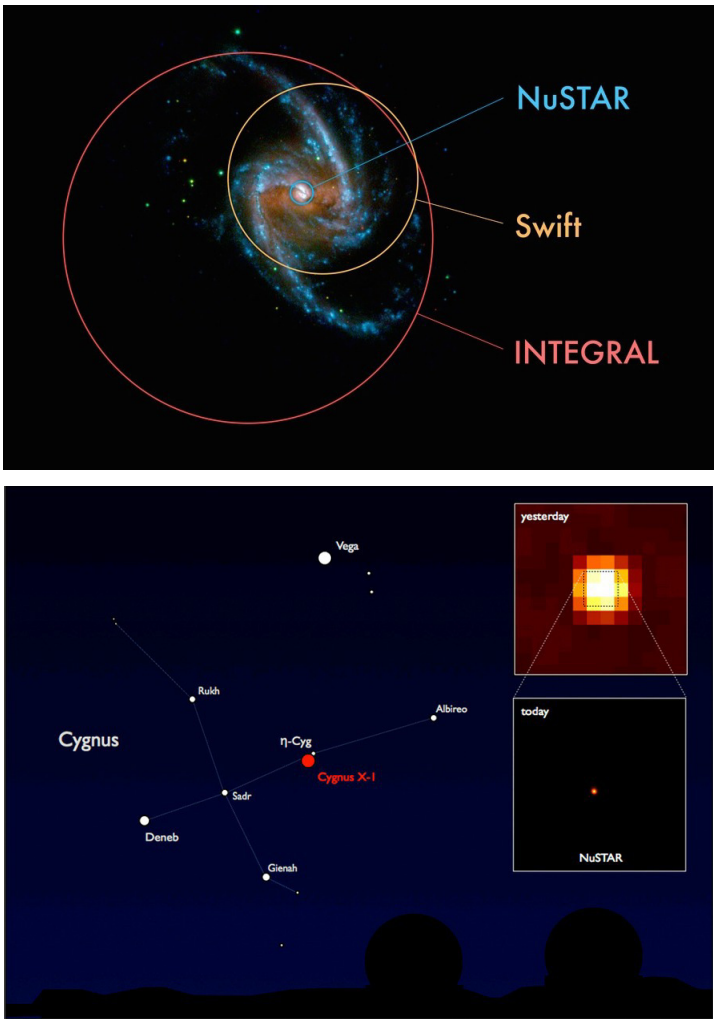

Figure 2.6: *Top*: UV image of the galaxy NGC 1365, with an AGN at its centre, taken by the *XMM-Newton*/OM telescope. Extensive hard X-ray energy emission is produced not only by the AGN, but also by sources in the host galaxy, and unrelated background sources. The larger angular resolution of previous hard X-ray observatories such as *INTEGRAL* and *Swift*-BAT would not be able to resolve any contaminating host galaxy emission from the AGN at the centre of this galaxy. *NuSTAR* however, with its higher angular resolution, could isolate the AGN emission from significant contamination by the host galaxy. *Bottom*: Example hard X-ray images of the stellar mass black hole ($M_{BH} \sim 5$–10 $M_{\odot}$), Cygnus X–1, in our galaxy, taken using *INTEGRAL* (top right inset; the image is 1 degree across). The *NuSTAR* image of the central part of the *INTEGRAL* image is shown in the bottom right inset. Whilst the *INTEGRAL* image shows a "blob" consisting of X-ray emission from various sources across the sky, *NuSTAR* can zoom into the selected target and provide a much sharper image of the source. Image credit: NASA/JPL-Caltech.

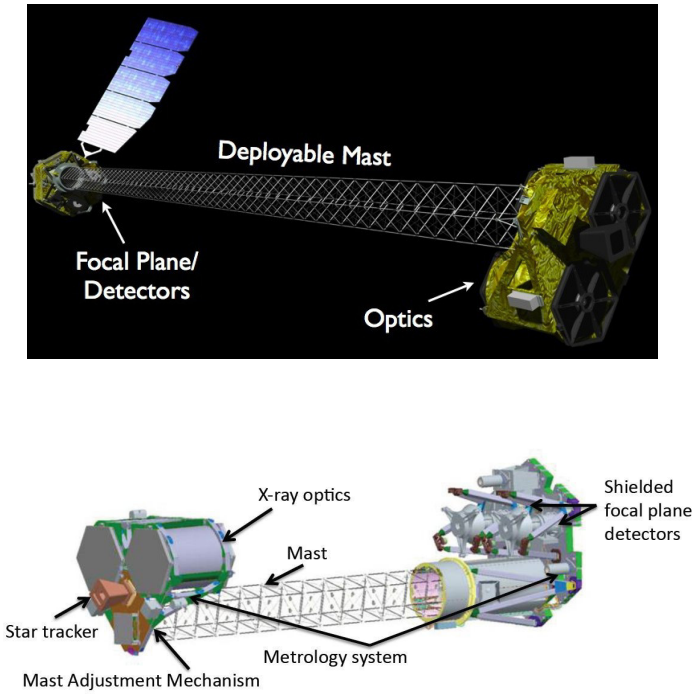

Figure 2.7: Illustrations of the *NuSTAR* observatory with the outer parts removed for the bottom image. The instruments described in this thesis are the focal plane detectors, the deployable mast and the X-ray optics. The reader is referred to Harrison et al. (2013) for further details. Image credit: NASA/JPL-Caltech.

an order of magnitude improvement in angular resolution (18″ at full width half maximum, FWHM; 58″ at half power diameter) with respect to these previous hard X-ray orbiting observatories (e.g., *INTEGRAL* and *Swift*-BAT; see Figure 2.6).

NuSTAR consists of two co-aligned and independent telescopes which are identical in design (see Figure 2.7). Each of the telescopes has its own focal plane module (FPM), referred to as "FPMA" and "FPMB", which are separated from the optics by an extendable mast, which was deployed in orbit to achieve a ∼10 metres focal length (see Figure 2.7). Each FPM covers the same 12.5′ × 12.5′ portion of the sky, and comprises of four solid state detectors, made of Cadmium-Zinc-Telluride, and placed in a 2 × 2 array of 32 × 32 pixel chips. Each of the optical modules adopt the Wolter-I conical approximation design with 133 shells of mirrors multi-coated with layers of Tungsten/Silicon and Platinum/Carbon for the outer and inner shells, respectively, to enhance reflectivity of the high energy incident photons. The *NuS-*

TAR sensitivity is limited up to $E \sim$79 keV as the platinum coating starts to absorb X-ray photons above this energy. The detectors are shielded by Cesium-Iodide crystals, which register photons and cosmic rays coming from directions other than the optical axis; i.e., background events. These can then be subtracted from the data during the data processing step. The detectors provide *NuSTAR* with a relatively high spectral energy resolutions of 0.4 and 0.9 keV (FWHM) at 6 and 60 keV, respectively. The absolute astrometric accuracy of the telescope is $\sim 8''$ at 90% confidence level.

The energy range in which *NuSTAR* is sensitive (3–79 keV) provides excellent coverage for detecting the characteristic signatures of CTAGN, which includes the photoelectric cut-off at $E < 10$ keV, the fluorescence Fe Kα emission line at $\sim$6.4 keV and the Compton hump at $\sim$20–50 keV (see Figure 1.4 in Chapter 1). In addition, the higher angular resolution and better sensitivity as compared to the previous generation of hard X-ray telescopes make it an ideal instrument to characterise the spectral shape of CTAGN in the local universe (e.g. Baloković et al., 2014; Gandhi et al., 2014; Puccetti et al., 2014; Bauer et al., 2015; Boorman et al., 2016). As part of this project, I was awarded new *NuSTAR* observations (observed or scheduled) for 9/20 AGNs in my sample, boosting up the hard X-ray energy data for this sample to 90% complete, when existing (and scheduled) *NuSTAR* data for a further 9/20 are included (the remaining 10% of the sample; i.e., 2 sources, do not require hard X-ray energy observations since the archival low energy X-ray data have provided reliable measurements on their column density and AGN properties; see Chapter 5).

Throughout this thesis, the *NuSTAR* data are processed using the *NuSTAR* Data Analysis Software (NUSTARDAS) within HEASOFT v6.15.1 using calibration database (CALDB) v20150316. Here I briefly describe the data processing procedures that I have adopted in this work. The reader is referred to the *NuSTAR* data analysis guide for further details.[5] Calibrated and cleaned event files ("level 2 data") are first produced from the telemetry data ("level 1" data) using the NUPIPELINE v0.4.3 script with standard filter flags. The procedures involve metrology processing,

[5]The *NuSTAR* data analysis guide can be found at
https://heasarc.gsfc.nasa.gov/docs/nustar/analysis/nustar_swguide.pdf .

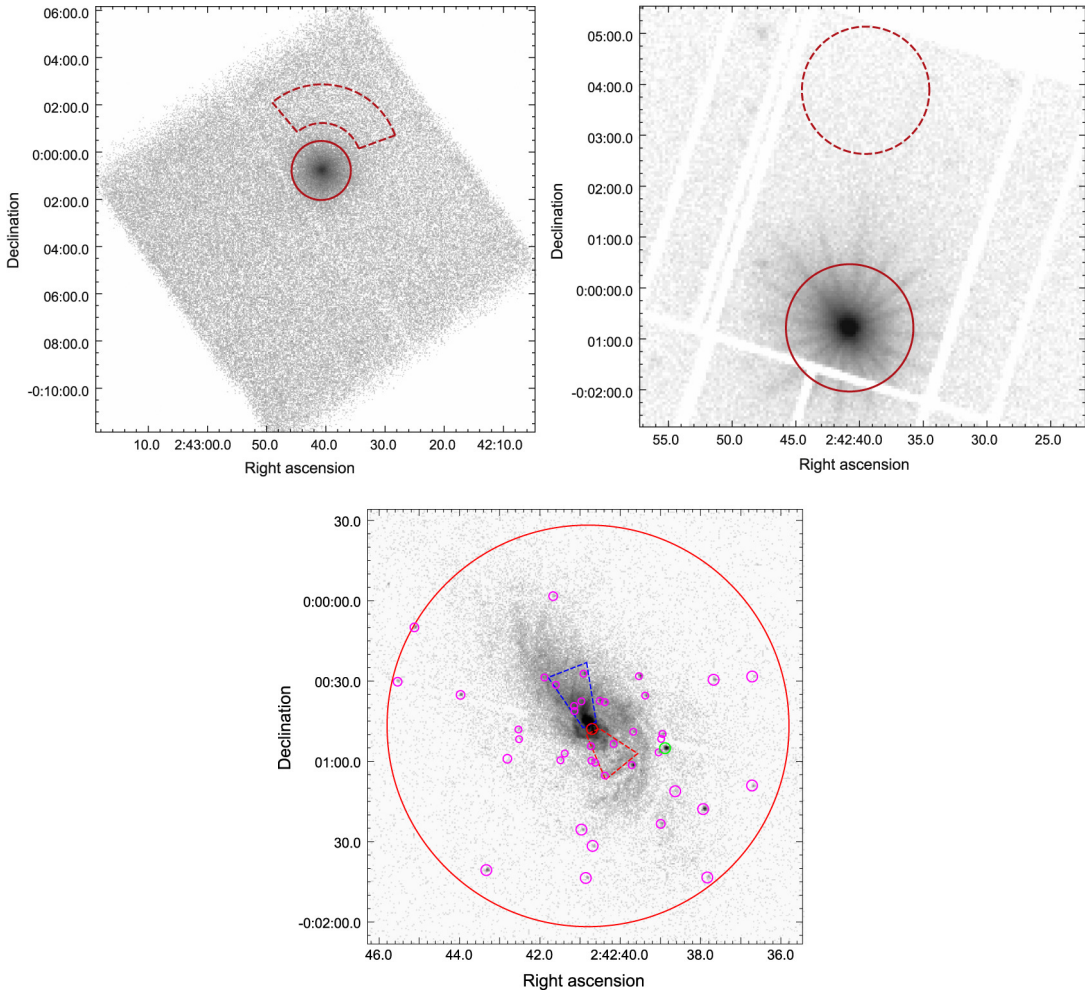

Figure 2.8: *NuSTAR* (top left), *XMM-Newton* (top right) and *Chandra* (bottom) images of NGC 1068. The large circle in red (75″-radius) shows an example of the source extraction region of the AGN in the galaxy, whilst the dashed red regions show examples of background extraction regions (this is not shown in the *Chandra* image). The small red circle (2″-radius) at the centre of the *Chandra* image indicates the AGN position, whilst the circles in magenta mark the off-nuclear point sources within the source extraction region. These images clearly show the higher spatial resolution of *Chandra*, which is crucial in identifying off-nuclear sources that are not resolved by *NuSTAR* and *XMM-Newton*, so that they can then be accounted for in extracted spectrum. Image credit: Bauer et al. (2015).

altitude correction, bad and hot pixel flagging, reconstruction of event and grade assignment (0–32; 27–32 are considered as "bad" grades for *NuSTAR*; see Figure 2.4 and Section 2.2.1), energy calibration, event flagging and coordinate transformation. The calibrated event files are then screened for bad time intervals (e.g., when the Earth is in the field of view of the telescope, when the observatory is passing through the South Atlantic Anomaly, when the instruments have a dead time). The spectra (source and background) and response files were then extracted from these cleaned data using the NUPRODUCTS v0.2.5 task (see Figure 2.8). Details on the apertures used to extract these spectra are given for individual sources in Chapters 3–5. The extracted source spectrum will include the total emission from both the source and the background. The background spectrum is thus used to subtract the background emission from the source spectrum to produce a final net spectrum. This spectrum is then multiplied with the response files to produce the final observed spectrum that is used for analysis. The response files include the ancillary response function (ARF) and redistribution matrix file (RMF). The ARF file contains information on the effective areas of the telescope as a function of energy, whilst the RMF file describes the distribution of photon energies in pulse invariant units (i.e., charge in physical units). In most cases, the spectra and response files from each FPM are combined together using the ADDASCASPEC script to increase the overall signal-to-noise ratio of the data.[6] The final spectrum is then binned into a number of counts per bin (e.g., 3 or 20 counts per bin; see Chapter 3–5), using the GRPPHA task in HEASOFT.[7] In addition to the spectral extraction, we also combined the *NuSTAR* event files from the two FPMs using XSELECT to produce the total event file.[8] The total count images at different energy bands (e.g., 3–8 keV, 8–24 keV) are then produced from the resultant event file using the DMCOPY task in CIAO (see Section 2.2.3).

[6]More details on the ADDASCASPEC script can be found at https://heasarc.gsfc.nasa.gov/docs/asca/adspecinfo.html .

[7]Further details on the GRPPHA task can be found at https://heasarc.gsfc.nasa.gov/docs/journal/grppha4.html .

[8]The XSELECT user guide can be found at https://heasarc.gsfc.nasa.gov/ftools/xselect/xselect.html .

2.2.3 *Chandra*

The *Chandra* X-ray Observatory (CXO; see Figure 2.9) was launched into orbit on July 23rd, 1999 as part of NASA's flagship mission, and is classed as one of the Great Observatories, along with the Hubble Space Telescope, Compton Gamma Ray Observatory (retired), and the Spitzer Space Telescope. The observatory consists of two focal plane science instruments which include the advanced CCD imaging spectrometer (ACIS) and the high resolution camera (HRC), and two objective transmission gratings; i.e., the low and high energy transmission gratings (LETG and HETG, respectively). The observatory adopts the basic Wolter-I mirror design to focus X-ray photons, which is called the High Resolution Mirror Assembly (HRMA). The optics consist of a nested set of 4 grazing incidence mirrors coated with iridium to enhance reflectivity, and has a focal length of 10 metres. These mirrors are very precisely aligned and are currently the smoothest and cleanest mirrors ever made, providing *Chandra* with a very precise optical surface. These lead to the unmatched X-ray resolution of *Chandra*, in which the majority of the incident photons can be focused into a 0.5″-radius circle (at the aimpoint; i.e., on-axis), providing unprecedentedly detailed X-ray imaging.[9] This capability makes *Chandra* a crucial instrument in this thesis, not only to facilitate the broadband spectral analysis at low energies, where the *NuSTAR* (or *Swift*-BAT) sensitivity drops off, but also to resolve and account for the emission from contaminating off-nuclear X-ray sources in the *NuSTAR* data. The telescope has an absolute positional accuracy of ∼0.8″ at 90% confidence level.

The X-ray photons focused by HRMA at the focal point can be recorded with the desired focal plane instruments (either ACIS or HRC). Throughout this research, all of the *Chandra* observations used were made using the ACIS detector without the gratings. Therefore, I will focus more on ACIS here, and only briefly describe the HRC and the gratings. Further details on the observatory and the instruments can be found in the *Chandra* Proposer's Observatory Guide.[10] The HRC has the

[9] We note that the point spread function (PSF) degrades at larger off-axis angles and higher X-ray energies for *Chandra*.

[10] The latest version (19.0) of the *Chandra* Proposer's Observatory Guide can be found at http://cxc.harvard.edu/proposer/POG/html/index.html .

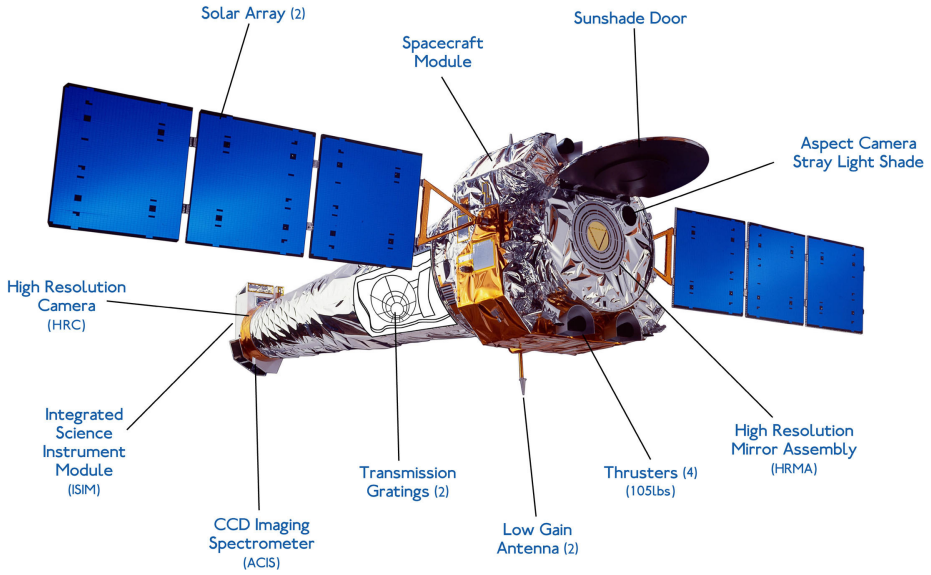

Figure 2.9: An illustration of the *Chandra* observatory and the instruments onboard. The instruments described in this thesis are the ACIS and HRC detectors, the transmission gratings and HRMA. The reader is referred to the *Chandra* webpage for further information (http://chandra.harvard.edu/). Image credit: NASA.

capability to match the point spread function (PSF) of HRMA, and therefore has the highest spatial resolution on *Chandra*. It also has the largest field of view ($30' \times 30'$) and highest temporal resolution (16 μs) for timing studies. However, the spectral resolution of HRC is the poorest; i.e., 1 keV at $E = 1$ keV. On the other hand, the LETG and HETG are specifically built to perform high resolution spectroscopy. These instruments are used (one at a time) simultaneously with either of the two focal plane instruments. Each spectrometer is moved into the optical path behind the mirrors when desired, and consists of hundreds of gratings made of gold that can intercept and disperse the X-ray emission reflected from the mirrors. The LETG is used with the HRC detector, and provides high resolution spectroscopy (1 eV at $E = 1$ keV) at low energy (0.08–0.2 keV). Meanwhilst, the HETG which is used with the ACIS detector is optimised for high resolution spectroscopy (1 eV at $E = 1$ keV) at higher energy (0.4–10 keV).

The ACIS detector is dedicated to optimise both imaging and modest spectral resolution spectroscopy in the 0.1–10 keV band. It comprises two arrays of CCDs of

1024 × 1024 pixel chips; i.e., ACIS-I which is arranged in a 2 × 2 array, and ACIS-S which consists of a 1 × 6 array. Any combination of up to 6 CCDs can be operated simultaneously. ACIS-I is optimised for wide-field imaging (field of view = 16.9′ × 16.9′), whilst ACIS-S (field of view = 8.3′ × 50.6′) can be used in conjunction with the HETG transmission grating to perform high resolution spectroscopy. Two CCDs (ACIS-S1 and S3) are back-illuminated (BI) CCDs, whilst the rest are front-illuminated (FI). BI CCDs are thinner and have their back side facing the telescope mirrors, exposing the photo-sensitive region to the incoming photons. As a result, BI CCDs are more sensitive as they have much higher quantum efficiency than the traditional FI CCDs; i.e., more incident photons are converted into electronic charges. The ACIS-S3 CCD, which is the aimpoint for ACIS-S, provides the best small-field imaging (field of view = 8.3′ × 8.3′) and highest spectral resolution for the ACIS system without the use of the gratings (100 eV at $E = 1$ keV). As part of my research, I have been awarded three *Chandra* observations (observed or scheduled), in which two are coordinated with high energy X-ray observations with *NuSTAR* (see Table 2.3). These new observations will complete (100%) the *Chandra* data for this local AGN sample.

Throughout this thesis, I process the *Chandra* data using the CIAO v4.6 pipeline (Fruscione et al., 2006) to create cleaned event files (level 2) with updated calibration modifications using the CHANDRA_REPRO task. This task automates the recommended data processing procedures detailed in the CIAO analysis threads, such as instrument-dependent corrections (e.g., aspect solution), bad pixels and grade filtering (0–7 ASCA grades; 1, 5 and 7 are the "bad" ASCA grades for *Chandra*; see Section 2.2.1)[11], cosmic ray rejection, and position transformation to celestial coordinates.[12] The source and background spectra (see Figure 2.8), as well as the response files are then extracted using the SPECEXTRACT task, and the net spectrum is binned up using the GRPPHA task (see section 2.2.2). *Chandra* images at different

[11] *Chandra* ACIS has 256 event grades (0–255). These are then binned into 7 ASCA (Advanced Satellite for Cosmology and Astrophysics) grades in order to not saturate the telemetry. Further details can be found at http://www2.astro.psu.edu/xray/acis/technical/cal_report/node254.html .

[12] The CIAO analysis threads can be found at http://cxc.harvard.edu/ciao/threads/all.html .

energy bands (e.g., 0.5–8 keV, 2–8 keV) are also produced using the DMCOPY task in CIAO.

2.2.4 *XMM-Newton*

The X-ray Multi-Mirror Mission (*XMM-Newton*; see Figure 2.10) was launched into orbit on December 10th, 1999. It is one of the cornerstone missions (second) of the European Space Agency (ESA) Horizon 2000 Science programme, along with the Solar and Heliospheric Observatory (SOHO) and the Cluster missions (cornerstone 1), Rosetta (cornerstone 3) and the Herschel Space Observatory (cornerstone 4). The spacecraft carries three co-aligned X-ray telescopes, each adopting the Wolter-I design (see Section 2.2.1), and each consists of 58 nested mirrors coated with gold, with 7.5 metres focal length. These mirrors provide *XMM-Newton* with an unprecedented and unmatched total photon collecting area of $\sim$4500 cm^2 at 1 keV. On the other hand, the telescope has a spatial resolution of 6″ at FWHM, about an order of magnitude poorer than *Chandra* (see Section 2.2.3). The telescope is sensitive between 0.1–12 keV, and has an absolute astrometric accuracy of $\sim$2″ at 90% confidence level. *XMM-Newton* has three science instruments onboard; i.e., the European Photon Imaging Cameras (EPIC), the Reflection Grating Spectrometers (RGS), and the Optical Monitor (OM). These instruments allow for both X-ray and optical/UV observations simultaneously. In this thesis, all of the *XMM-Newton* data were obtained from observations made using the EPIC detector, which is also the primary instrument on the observatory. Therefore, I will focus more on this instrument here, and just briefly describe the other two instruments. Further information on the observatory and the instruments can be found on the *XMM-Newton* webpage.[13]

EPIC consists of three detecting instruments; i.e., a “pn”-camera (PN) and two identical metal-oxide-semiconductor (MOS) cameras (MOS 1 and 2). The PN camera is made of 12 arrays of BI CCDs (see Section 2.2.3) and each consists of 64 $\times$ 200 pixels. By comparison, each of the MOS cameras is comprised of 7 arrays of FI

[13]The *XMM-Newton* webpage can be found at https://www.cosmos.esa.int/web/xmm-newton

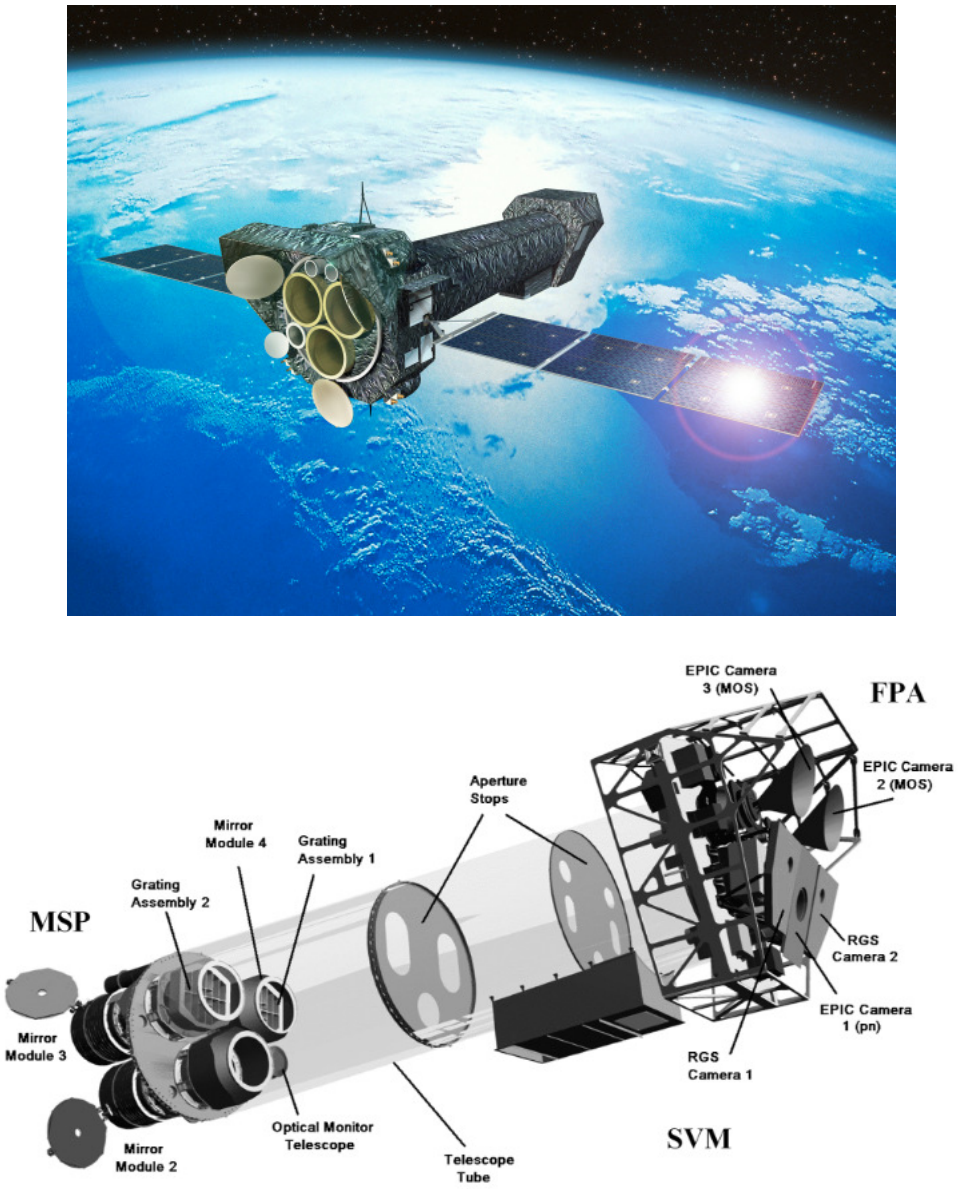

Figure 2.10: Illustrations of the *XMM-Newton* observatory (top) and the assembly of the instruments (bottom). The instruments described in this thesis are the EPIC cameras (PN and MOS), the optical monitor telescope, the gratings and the mirror modules. The reader is referred to the *XMM-Newton* webpage for further details (http://sci.esa.int/xmm-newton/). Image credit: ESA/D. Ducros, Lumb et al. (2012).

CCDs (see Section 2.2.3), each with 600 × 600 pixels. As a result, the PN camera is more sensitive than the MOS cameras, and has higher effective area; i.e., 1227 and 922 cm^2 at 1 keV for PN and MOS, respectively. Each of these three cameras provide a $\sim 30' \times 30'$ field of view, and are used simultaneously during observations. The EPIC cameras are optimised to perform both relatively high resolution imaging and moderate resolution spectroscopy (∼50 eV at 1 keV). To achieve higher resolution spectroscopy, they can be used simultaneously with the RGS to provide high resolution spectroscopy over the 0.35–2.5 keV energy range (spectral resolution $\sim$ 4 eV at 1 keV). The OM instrument is a 30 cm telescope, co-aligned with the other three X-ray telescopes, with a $\sim 17' \times 17'$ field of view and $\sim 1''$ resolution (FWHM). The telescope is sensitive to optical/UV photons between λ = 180–650 nm. This instrument provides simultaneous optical/UV data for each X-ray observation conducted.

For this research, I have been awarded one *XMM-Newton* observation (scheduled) for my sample, which is coordinated with *NuSTAR* (see Table 2.3). These new data will increase the *XMM-Newton* data for this $D \leq 15$ Mpc sample to 95% complete. The remaining AGN which does not have any *XMM-Newton* observations is NGC 1448. The X-ray properties for this AGN can be constrained using the *Chandra* and *NuSTAR* data, and the *Chandra* data also reveal multiple X-ray sources that could significantly contaminate the *XMM-Newton* data (see Chapter 4). Therefore, we did not follow up this source with *XMM-Newton*.

Throughout this thesis, I reduce the *XMM-Newton* data using the *XMM-Newton*'s Science Analysis System (SAS) v1.2.[14] Here I briefly describe the data reduction approach that I have adopted in this thesis. Further details on the data processing and analysis can be found in the *XMM-Newton*'s users handbook.[15] For each observation, the Observation Data Files (ODF), which consist of uncalibrated science files, are automatically process by the Processing Pipeline Subsystem (PPS) to produce top level scientific products such as the event and source lists, net source spectra and

[14]The SAS webpage can be found at https://www.cosmos.esa.int/web/xmm-newton/sas .

[15]The *XMM-Newton*'s users handbook can be fount at https://xmm-tools.cosmos.esa.int/external/xmm_user_support/documentation/uhb/XMM_UHB.html

source light curves. These PPS products are made available to the observer after the observations have been carried out. The event files produced from the PPS are reprocessed to include updated calibration. Using the EVSELECT task, the event files for each of the EPIC cameras are then screened using the standard filter flags. This includes filtering the data for, e.g., hot pixels, low pulse height and bad "patterns" (this is similar to grades; the pattern range is 0–12, and pattern >4 and >12 are often excluded for PN and MOS, respectively). In addition, the event files are also filtered for bad time intervals when there is particle flaring.[16] This is done manually by examining the light curve of the event files (i.e., by binning the count rates over a time interval) to see the times when particle flarings occur. The event files are then filtered by excluding the count rates that significantly exceed the count rates during the times when there are no flares, using the TABGTIGEN task. The source and background spectra for each detector are then extracted from the cleaned event files using the EVSELECT task (see Figure 2.8), and are filtered for bad pixels using the BACKSCALE task. The ARF and RMF files are produced using the ARFGEN and RMFGEN tasks, respectively. In most cases, the spectra and the response files for the MOS 1 and MOS 2 cameras are combined together using the EPICSPECCOMBINE task. All of the net spectra are then binned up using the GRPPHA task (see section 2.2.2). The *XMM-Newton*'s count images at different energy bands (e.g., 0.5–8 keV, 2–8 keV) are produced using the EVSELECT task (we only show images for the PN camera in this thesis).

[16]Particle flaring is a common issue for *XMM-Newton* since its orbit coincides with the Earth's radiation belt, and these flares can significantly affect BI CCDs (which is the CCDs for the PN camera).

Chapter 3

NuSTAR Observations of the Compton-thick Active Galactic Nucleus and Ultraluminous X-ray Source Candidate in NGC 5643

In this chapter, I present two *NuSTAR* observations of the local Seyfert 2 active galactic nucleus (AGN) and an ultraluminous X-ray source (ULX) candidate in NGC 5643. Together with archival data from *Chandra*, *XMM-Newton* and *Swift*-BAT, we perform a high-quality broadband spectral analysis of the AGN over two decades in energy (∼0.5–100 keV). Previous X-ray observations suggested that the AGN is obscured by a Compton-thick (CT) column of obscuring gas along our line-of-sight. However, the lack of high-quality $\gtrsim$ 10 keV observations, together with the presence of a nearby X-ray luminous source, NGC 5643 X–1, had left significant uncertainties in the characterisation of the nuclear spectrum. *NuSTAR* now enables the AGN and NGC 5643 X–1 to be separately resolved above 10 keV for the first time and allows a direct measurement of the absorbing column density toward the nucleus. The new data show that the nucleus is indeed obscured by a CT column of $N_{\rm H} \gtrsim 5 \times 10^{24}$ cm^{-2}. The range of 2–10 keV absorption-corrected luminosity inferred from the best fitting models is $L_{2-10,\rm int} = (0.8–1.7) \times 10^{42}$ erg s^{-1}, consistent with that predicted from multiwavelength intrinsic luminosity indicators. We also study the *NuSTAR*

data for NGC 5643 X–1, and show that it exhibits evidence for a spectral cut-off at energy, $E \sim 10$ keV, similar to that seen in other ULXs observed by *NuSTAR*. Along with the evidence for significant X-ray luminosity variations in the 3–8 keV band from 2003–2014, our results further strengthen the ULX classification of NGC 5643 X–1.

3.1 Introduction

Compton-thick (CT) active galactic nuclei (AGNs) are predicted to constitute a significant fraction of the overall AGN population in our local universe (up to ∼30%; e.g., Risaliti et al., 1999; Goulding et al., 2011; Ricci et al., 2015). However, our current census of the CTAGN population appears to be highly incomplete. The high line-of-sight column density in CTAGN ($N_{\rm H} \geq 1.5 \times 10^{24}$ cm^{-2}) results in severe attenuation of the direct X-ray emission from the nuclear source, even at high energies ($E > 10$ keV), making the identification and characterisation of CTAGN a challenging task (see Chapter 1 for further details). Having a complete census of their population is important in order to form an accurate census of accretion in the local universe, since much of the growth of supermassive black holes is thought to occur in such heavily obscured phases (e.g. Fabian, 1999; Alexander & Hickox, 2012).

We have started a program to study a complete, volume-limited ($D < 15$ Mpc), mid-infrared (MIR) selected AGN sample from Goulding & Alexander (2009), with the main goal of constraining the population of CTAGN and the $N_{\rm H}$ distribution of AGN in the local universe. CTAGN candidates from the sample were identified using multiwavelength selections, such as X-ray spectroscopy, and intrinsic 2–10 keV luminosity indicators from high spatial resolution MIR 12μm continuum and [OIII]λ5007Å line luminosity corrected for the Balmer decrement (see Chapter 5). One of the candidates that stands out in the sample as being CT based on these analyses is NGC 5643. NGC 5643 is a nearby face-on ($i \approx 30°$)[1] SAB(rs)C galaxy

[1]The host galaxy inclination was obtained from the HyperLeda website (http://leda.univ-lyon1.fr/).

hosting a low-luminosity Seyfert 2 nucleus (Phillips et al., 1983). It has a redshift of $z = 0.0040$, corresponding to a metric/proper distance of $D = 13.9$ Mpc under the assumption of the Mould et al. (2000) cosmic attractor model (Sanders et al., 2003).[2]

NGC 5643 features a compact radio core with two-sided, kiloparsec-scale lobes in an east-west orientation (Morris et al., 1985), and a cospatial one-sided Hα and [OIII] emission line region extending east-ward of the nucleus for at least 1.8 kpc (Simpson et al., 1997). Despite the intense star formation episodes occuring in the spiral arm, MIR diagnostics suggest that the AGN still dominates the overall IR (8–1000μm) energy budget (Genzel et al., 1998). Comparisons of optical spectra with synthesis models, however, are consistent with a "starburst/Seyfert 2 composite" spectrum (Cid Fernandes et al., 2001). Using Brγ emission, Davies et al. (2014) found no on-going star formation activity in the nucleus, although the possibility of a recent (terminated) starburst cannot be excluded. This source also shows spatially resolved molecular gas flowing out from the AGN at a rate of 10 $M_\odot$ yr^{-1} (Davies et al., 2014). Although water maser emission associated with the AGN has been detected in NGC 5643, a corresponding spatially resolved map, which would allow for a direct measurement of the supermassive black hole mass ($M_{\rm BH}$), is not yet available (Greenhill et al., 2003). However, an indirect $M_{\rm BH}$ measurement from the galaxy stellar velocity dispersion (σ_*) provides an estimated black hole mass of $M_{\rm BH} = 10^{6.4}$ $M_\odot$ (Goulding et al., 2010).[3]

In X-rays, NGC 5643 has been observed by *ASCA* (Guainazzi et al., 2004), *BeppoSAX* (Maiolino et al., 1998), *ROSAT* (Guainazzi et al., 2004), *Chandra* (Bianchi et al., 2006) and *XMM-Newton* (Guainazzi et al., 2004; Matt et al., 2013). Dramatic spectral changes were observed between the *XMM-Newton* observation carried out

[2]Mould et al. (2000) adjusts heliocentric redshifts to the centroid of the Local Group, taking into account the gravitational attraction towards the Virgo Cluster, the Great Attractor and the Shapley supercluster.

[3]The same $M_{\rm BH}$ estimate is obtained using an updated value of σ_* derived from the [O III]λ5007Å emission line width from Gu et al. (2006) and the latest $M_{\rm BH}$–σ_* correlation by McConnell & Ma (2013).

in 2003, and the *ASCA* and *BeppoSAX* observations performed earlier. However, the point spread function (PSF) of *ASCA* and *BeppoSAX* were not sufficient to separate the emission of the nucleus from that of a nearby X-ray source (at an angular separation of $\sim 50''$), NGC 5643 X–1, which was found to be very bright at the time of the *XMM-Newton* observation (Guainazzi et al., 2004; hereafter G04). Therefore, it remained unclear which source was responsible for the spectral variability observed. Comparisons of the *XMM-Newton* observations in 2003 and 2009 showed that there is no significant variation in the spectrum of the AGN (Matt et al., 2013; hereafter M13). However, the off-nuclear source was found to be more than a factor of two fainter in flux in 2009 (M13) than in 2003 (G04).

The *Chandra* image of the AGN shows that the soft X-ray emission ($E \lesssim 2$ keV) of the nucleus is spatially correlated with the [OIII] emission (Bianchi et al., 2006), consistent with what is commonly observed for many Seyfert 2 galaxies. The dominant power source of this soft X-ray emission appears to be photoionization from the AGN, although it is still unclear how much collisional ionization contributes to the overall X-ray emission (M13). Above 2 keV, the X-ray spectra from these various observations show indications of the nucleus being absorbed by CT material. The evidence for this are the detection of a prominent Fe Kα line (EW > 1 keV) and a flat photon index below 10 keV ($\Gamma_{2-10} < 1$), which are characteristics of a reflection-dominated spectrum (see Chapter 1). Analysis of the low signal-to-noise ratio (S/N) *BeppoSAX* spectrum where NGC 5643 was detected only up to 10 keV, combined with an upper limit for the 15–100 keV band, suggested a tentative lower limit to the column density of $N_{\rm H} > 10^{25}$ cm^{-2} (Maiolino et al., 1998).

The true nature of the off-nuclear X-ray source, NGC 5643 X–1, is still uncertain. It is located in the outskirts of the host galaxy optical emission and identification of counterparts at other wavelengths has been ambiguous (G04). It is highly likely that the source is located inside the galaxy and therefore would be a powerful ultraluminous X-ray source (ULX) with $L_{2-10} \approx 1.7 \times 10^{40}$ erg s^{-1} based on the flux observed in 2003 (G04). This is comparable to the observed luminosity of the AGN itself; i.e., $L_{2-10} \approx 1.9 \times 10^{40}$ erg s^{-1} (G04).

In this chapter, we present new *NuSTAR* observations of NGC 5643 in which the

AGN and the off-nuclear source, NGC 5643 X–1, are clearly resolved and detected at hard X-ray energies (> 10 keV) for the first time. This allows us to provide the most accurate spectral analysis of the AGN to date. The aim of this chapter is to characterise the broadband spectrum of the AGN by combining our *NuSTAR* data with existing data from *Chandra*, *XMM-Newton* and *Swift*-BAT. We also present the *NuSTAR* data for NGC 5643 X-1, which is detected above 10 keV for the first time.

The chapter is organised as follows: we describe details of the X-ray observations and data reduction of the AGN in Section 3.2, followed by the spectral fitting procedures and results in Section 3.3. In Section 3.4, we present the data analysis and results on NGC 5643 X–1. This is followed by a discussion in Section 3.5. The chapter concludes with a summary in Section 3.6.

3.2 Observations

In this section, we describe the *NuSTAR* (see Section 2.2.2 in Chapter 2) observations and data analysis procedures for the AGN. We also detail the archival *Chandra* (see Section 2.2.3 in Chapter 2), *XMM-Newton* (see Section 2.2.4 in Chapter 2) and *Swift* data that were used to facilitate our broadband spectral analysis. Details of these observations are provided in Table 3.1, and the data reduction is described below.

3.2.1 *NuSTAR*

NGC 5643 was observed twice by *NuSTAR* in 2014 – an initial observation with a nominal exposure time of 22.5 ks taken in May, followed by an additional 19.7 ks observation in June. The second observation was conducted to improve the S/N of NGC 5643 as it fell near the detector gap in the first observation. The data were processed with the *NuSTAR* Data Analysis Software (NUSTARDAS) v1.4.1 within HEASOFT v6.15.1 with CALDB v20150316. Calibrated and cleaned event files were produced using the NUPIPELINE v0.4.3 script with standard filter flags. Spectra and response files were extracted using the NUPRODUCTS v0.2.5 task (see Chapter 2).

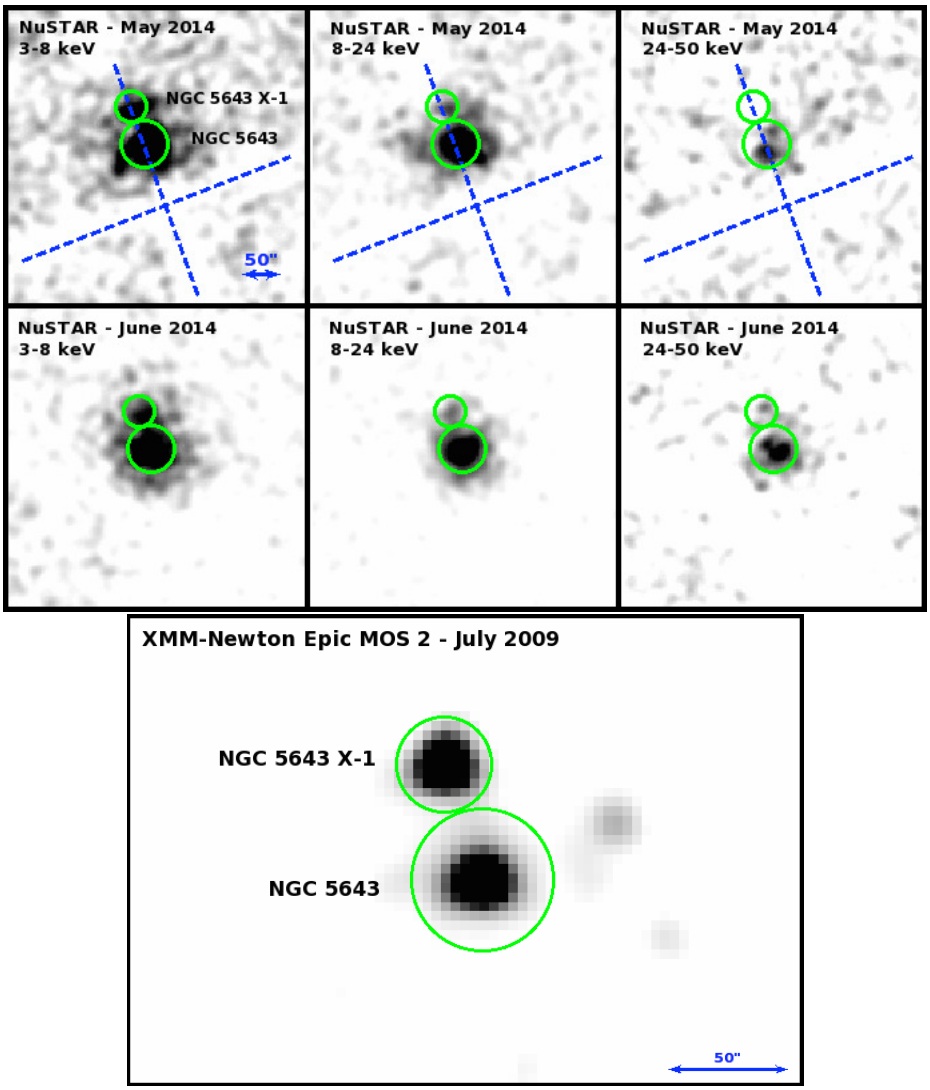

Figure 3.1: *NuSTAR* and *XMM-Newton* images of the AGN (NGC 5643) and the ULX candidate (NGC 5643 X–1). The sources are circled in green with 30″ and 20″-radius apertures, respectively. Images are smoothed with a Gaussian function of radius 5 and 3 pixels, corresponding to 12.3″ and 3.3″ for *NuSTAR* and *XMM-Newton*, respectively. North is up and East is to the left in all images. Top: *NuSTAR* combined FPMA+B images in the 3–8, 8–24 and 24–50 keV band for the May 2014 observation (first row) and June 2014 observation (second row). Blue dashed lines correspond to the gap between the *NuSTAR* detectors for the May observation. Bottom: *XMM-Newton* EPIC MOS 2 image (July 2009) in the 0.5–10 keV band shown to provide a clearer view of the two sources at lower energies.

Table 3.1: X-ray Observations log of NGC 5643

Instrument	ObsID	Date	Energy Band (keV)	Net Exposure time (ks)	Net count Rate (10^{-2} cts s^{-1})
(1)	(2)	(3)	(4)	(5)	(6)
Chandra ACIS-S	5636	2004-12-26	0.5–8	7.63	4.96
XMM-Newton PN/MOS1+2	0601420101	2009-07-25	0.5–10	45.4/53.4	14.6/3.76
Swift-BAT	-	2004-2010	14–100	7340	0.00223
Swift-XRT	00080731001	2014-05-24	0.5–10	3.96	0.472
NuSTAR FPMA/FPMB	60061362002	2014-05-24	3–50	22.5/22.4	2.44/1.94
NuSTAR FPMA/FPMB	60061362004	2014-06-30	3–50	19.7/19.7	2.32/2.36

Notes. (1): List of observatories and instruments; (2): Observation identification number (obsID); (3): Observation UT start date; (4) Energy band in keV; (5) The net exposure time in ks; (6): Net count rate for the AGN in the given energy band in units of 10^{-2} cts s^{-1}.

For each observation, the AGN spectra were extracted using a circular aperture region of 30″-radius centered on its peak emission. The background photons were collected from polygon-shaped regions lying on the same detector as the source for the June observation, and from two adjacent detectors for the May observation (since the source fell close to the detector gap in this observation). We excluded background photons that lay within a circular region of $\sim$ 70″-radius around the source to exclude emission from NGC 5643 X–1. Significant counts are detected up to 50 keV for the AGN. We show the combined FPMA+B images of the AGN and NGC 5643 X–1 in the 3–8, 8–24 and 24–50 keV bands in Figure 3.1.

3.2.2 *XMM-Newton*

NGC 5643 was also observed on two occasions by *XMM-Newton*, for 10 ks in 2003 and 55 ks in 2009. In both cases, the observations were performed with the EPIC CCD cameras (PN, MOS1, MOS2), operated in full frame mode with the medium filter. The observations were discussed in detail in G04 and M13, respectively. For the AGN, we only extracted and used the spectra from the longer 2009 observation as it has the highest S/N. Data were reduced within SAS v1.2 (see Chapter 2), screened for flaring particle background as described in M13.

Source spectra were extracted within a 25″-radius aperture centered on the AGN for all cameras. Background photons were selected from source-free circular regions of 100″-radius on the same chip as the source. Patterns 0 to 4 and 0 to 12 were used for the PN and MOS spectra, respectively. The spectra from MOS1 and MOS2 were co-added as the data were consistent with each other (see Section 3.3 for further details).

3.2.3 *Chandra*

NGC 5643 has only been observed once by *Chandra*. This observation was conducted in 2004 with the ACIS-S detector with an exposure time of $\sim$ 8 ks. The results of the observation were first published in Bianchi et al. (2006). We reprocessed the data to create event files with updated calibration modifications using the CIAO

v4.6 pipeline following standard procedures (see Chapter 2).

Source counts were extracted using the SPECEXTRACT task in CIAO from a circular region of 25″-radius centered on the AGN to match the *XMM-Newton* extraction region. The background was extracted from a source-free 30″-radius circular region close to the source.

3.2.4 *Swift*

The first *NuSTAR* observation in May 2014 was accompanied by a $\sim$ 5 ks *Swift* X-ray Telescope (XRT; Burrows et al., 2005) observation, which started approximately an hour after the *NuSTAR* observation began. The purpose of this observation was to provide simultaneous coverage for the soft X-ray end of the spectrum ($\lesssim$ 3 keV) where the *NuSTAR* sensitivity drops off. The data were reduced using the XRTPIPELINE v0.13.0, which is part of the XRT Data Analysis Software (XRT-DAS) within HEASOFT. However, with only $\sim$ 20 counts between 0.5–10 keV, the exposure is not long enough to provide additional constraints beyond those already obtained with *NuSTAR*, *XMM-Newton* and *Chandra*. Therefore, we only used these data to check for consistency with the *XMM-Newton* and *Chandra* data at 0.5–10 keV (see Section 3.3).

The Burst Alert Telescope (BAT; Barthelmy et al., 2005) onboard *Swift* has been continuously monitoring the sky at 14–195 keV, producing images of a large number of hard X-ray sources thanks to its wide field of view and large sky coverage. We used the stacked 70-month spectrum and its associated response file downloaded from the *Swift*-BAT 70-month Hard X-ray Survey Source Catalog (Baumgartner et al., 2013) to provide X-ray constraints above the *NuSTAR* band.[4] NGC 5643 is detected at the 5.4σ significance level with significant counts up to $\sim$ 100 keV.

[4]The *Swift*-BAT 70-month Hard X-ray Survey Source Catalog is available online at http://swift.gsfc.nasa.gov/results/bs70mon/

3.3 Broadband Spectral Modelling of the AGN

We describe the broadband X-ray spectral analysis of the AGN in this section. The analysis was carried out using XSPEC v12.8.2.[5] All spectra were binned to a minimum of 25 counts per bin to allow the use of χ^2 statistics. Absorption through a fixed Galactic column along the line-of-sight, $N_{\rm H}^{\rm Gal} = 8.01 \times 10^{20}$ cm^{-2} (Kalberla et al., 2005), was included in all spectral fits using the XSPEC model "PHABS", and solar abundances were assumed for all models. All errors are quoted at 90% confidence, unless stated otherwise. Details of the main results are summarised in Table 3.2, and the best fit spectra are shown in Figure 3.2.

We began our spectral modelling with an examination of the *NuSTAR* data alone. We started by modelling the spectra of each of the *NuSTAR* observations in the 3–50 keV band using a simple absorbed power-law model with the column density fixed to the Galactic value. A prominent excess of counts just above 6 keV was observed in both spectra, suggesting the presence of Fe Kα emission. The parameters returned by the two spectra were consistent with each other, indicating that there are no significant differences between the two observations. Therefore, we co-added the spectra for each FPM using the ADDASCASPEC script (the same test and procedures were also done for the two *XMM-Newton* MOS spectra).

We then modelled the combined *NuSTAR* spectra in the 3–50 keV band with an absorbed power-law model (column density fixed to $N_{\rm H}^{\rm Gal}$) and a Gaussian line at $E \approx 6.4$ keV. The model measured a photon index and Fe Kα EW of $\Gamma = 0.55 \pm 0.07$ and $\rm EW_{Fe} = 2.22^{+0.35}_{-0.34}$ keV, respectively, with a fit statistic of $\chi^2 = 115$ for 76 degrees of freedom (d.o.f). The line energy is centered at $E = 6.36 \pm 0.04$ (statistical) $\pm$ 0.04 (systematic; Madsen et al., 2015) keV, consistent with neutral Fe Kα emission. The very flat Γ and large $\rm EW_{Fe}$, which were also found in previous observations, are characteristic signatures of Compton-thick absorption and reflection from optically thick cold gas.

We checked for variability in the flux of the AGN in the 0.5–10 keV band by

[5]The XSPEC manual can be downloaded from
http://heasarc.gsfc.nasa.gov/xanadu/xspec/XspecManual.pdf

comparing the *XMM-Newton* and *Chandra* data with the *Swift*-XRT data. The fluxes of all spectra are consistent with each other, $f_{0.5-10.0} \sim 10^{-12}$ erg s^{-1} cm^{-2}, suggesting that there are no significant differences between the three observations. We also checked for variability at hard X-ray energies by constructing power spectra from the 3–50 keV *NuSTAR* lightcurves from the two observations. These were then compared to the power spectra expected for pure Poisson noise and for the expected transmitted component variability observed in an unobscured AGN with a similar black hole mass and accretion rate (see Arévalo et al., 2014 for further details). No evidence for variability was found, however, given the low count rates, this test is not very sensitive. Given that the *NuSTAR* spectra from the two observations are consistent with each other, we assumed that the AGN has not varied.

We therefore proceeded to fit the *XMM-Newton* and *Chandra* spectra combined with the *NuSTAR* and *Swif*-BAT spectra using more detailed physical models to better characterise the broadband spectrum of the AGN. We describe the details and results of each model used: Model P (PEXRAV model by Magdziarz & Zdziarski, 1995), T (TORUS model by Brightman & Nandra, 2011) and M (MYTORUS model by Murphy & Yaqoob, 2009), in Section 3.3.1, 3.3.2 and 3.3.3, respectively. In addition to these models, we added extra components required to provide a good fit to the data, briefly described below.

The soft energy ($\lesssim$ 2 keV) part of the spectra covered by *XMM-Newton* and *Chandra* is dominated by emission from photoionized material (M13). We modelled this emission based on M13 using a soft power-law[6] and 10 Gaussian components (9 for Model M; see Section 3.3.3) to model the emission lines (refer to Table 1 in M13). We also added four and one more Gaussian component(s) to Model P and M, respectively, to model the fluorescence lines emitted at $E \gtrsim 2$ keV which are not included in these models (see Section 3.3.1 and 3.3.3 respectively).

Cross-calibration uncertainties between each observatory with respect to *NuSTAR* were included as free parameters (CONSTANT, C). Initially, we left both the

[6]The soft power-law used to model the unresolved $\lesssim$ 2 keV emission also includes the scattered power-law component which is commonly used to simulate the AGN emission scattered into our-line-of sight by diffuse hot gas.

XMM-Newton EPIC-MOS and PN cameras constants free to vary. However, we found that their values are consistent with each other and decided to tie them together in the final fittings of all models.

Our three models are described in XSPEC as follows:

$$\text{Model P} = \text{CONSTANT} \times \text{PHABS} \times (\text{POW} + \text{PEXRAV} + 14 \times \text{ZGAUSS}) \tag{3.3.1}$$

$$\text{Model T} = \text{CONSTANT} \times \text{PHABS} \times (\text{POW} + \text{TORUS} + 10 \times \text{ZGAUSS}) \tag{3.3.2}$$

$$\text{Model M} = \text{CONSTANT} \times \text{PHABS} \times (\text{POW} + \text{zpow} \times \text{MYTZ} + \text{MYTS} + \text{MYTL} + 10 \times \text{ZGAUSS}) \tag{3.3.3}$$

3.3.1 Model P

In our fitting of the AGN broadband spectrum, we first consider the PEXRAV reflection model ('Model P'; Magdziarz & Zdziarski, 1995). This model has commonly been used to model reflection-dominated spectra. However, it assumes reflection off a slab geometry with an infinite column density, which is unlikely to represent the true geometry of the AGN torus. It also does not incorporate fluorescence emission lines expected from a CTAGN such as the Fe Kα and Kβ lines. Because of these limitations, we also fitted the spectra of the AGN using more physically motivated reflection/obscuration models as described in Section 3.3.2 and 3.3.3. However, Model P can provide useful comparison with the other reflection models and previous studies of this source, as well as other CT sources.

We started by fixing all the line energies and normalizations of the soft Gaussian components to the values presented in M13. We also fixed the redshift at $z = 0.0040$. Initially, we set the intrinsic line widths to $\sigma = 50$ eV, as we expect them to be unresolved. We then allowed the widths for each line to vary in turn, to improve

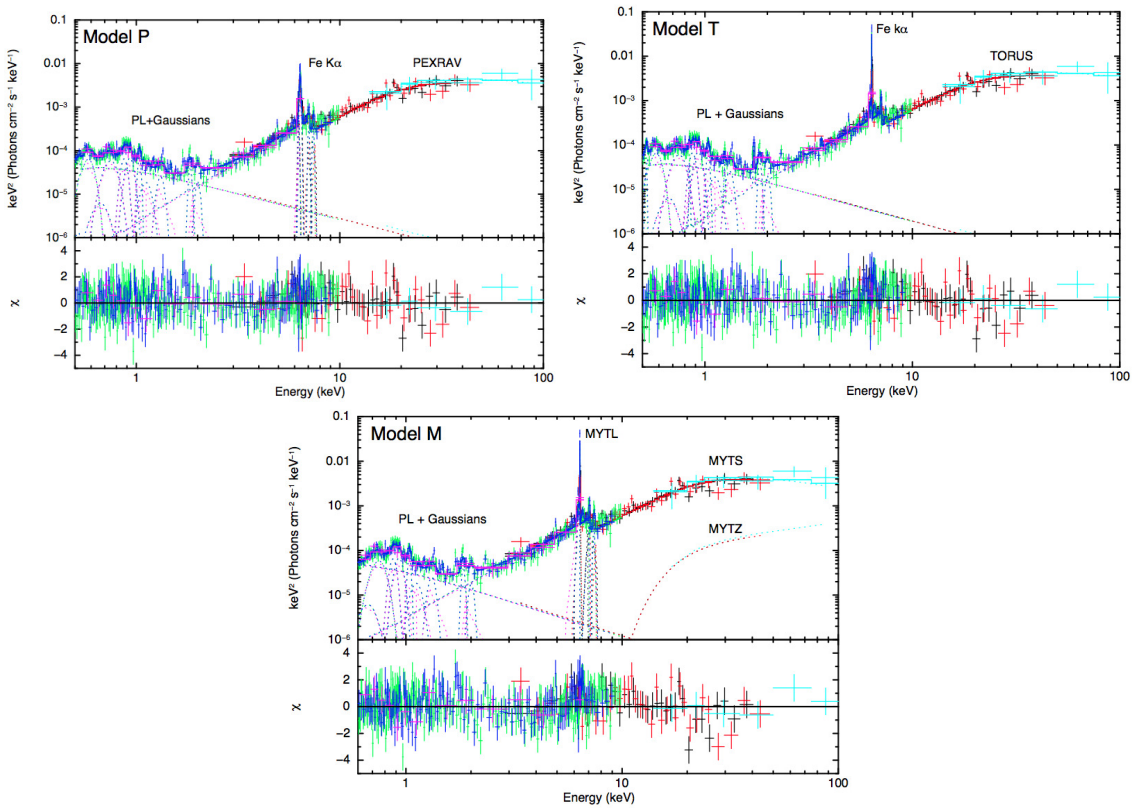

Figure 3.2: Best-fit models to the combined *NuSTAR*, *Chandra*, *XMM-Newton* and *Swift*-BAT data of the AGN - Model P (top left), Model T (top right), and Model M (bottom). Model P and T were fitted between 0.5–100 keV, and Model M was fitted between 0.6–100 keV since we found strong residuals near ∼0.5 keV for this model. The lower energy data ($\lesssim$ 2 keV) were modelled using a soft power-law (PL) and Gaussian lines to simulate photoionization by the AGN. The top panels of each plot show the unfolded model in E^2F_E units, whilst the bottom panels show the fit residuals in terms of sigma with error bars of size one. Colour scheme: black (*NuSTAR* FPMA), red (*NuSTAR* FPMB), blue (*XMM-Newton* PN), green (*XMM-Newton* MOS), purple (*Chandra*), cyan (*Swift*-BAT).

Table 3.2: X-ray spectral fitting results for the AGN in NGC 5643.

Component	Parameter	Units	Model P	Model T	Model M
Absorber/Reflector	$N_{\rm H}$(eq)	10^{24} cm^{-2}	-	100^{+u}_{-85}	$10.0^{+u}_{-0.5}$
	$N_{\rm H}$(los)	10^{24} cm^{-2}	-	100^{+u}_{-85}	$5.8^{+u}_{-1.2}$
	$\theta_{\rm inc}$	deg	65^{f}	65^{f}	$65.9^{+2.3}_{-1.9}$
	$\theta_{\rm tor}$	deg	-	$60.0^{+0.01}_{-1.33}$	-
AGN Continuum	$\Gamma_{\rm soft}$		3.19±0.13	$3.28^{+0.14}_{-0.12}$	$3.54^{+0.16}_{-0.15}$
	$\Gamma_{\rm hard}$		1.79±0.05	$1.97^{+0.03}_{-0.05}$	$2.10^{+0.04}_{-0.03}$
	$L_{0.5-2,\rm obs}$	10^{40} erg s^{-1}	0.4	0.4	0.4
	$L_{2-10,\rm obs}$	10^{40} erg s^{-1}	1.7	1.7	1.6
	$L_{30-100,\rm obs}$	10^{40} erg s^{-1}	15.9	16.2	16.3
	$L_{0.5-2,\rm int}$	10^{42} erg s^{-1}	0.4	0.6	0.3
	$L_{2-10,\rm int}$	10^{42} erg s^{-1}	1.7	0.8	0.9
	$L_{30-100,\rm int}$	10^{42} erg s^{-1}	1.6	0.8	0.6
$C^{\rm XMM}_{\rm NuSTAR}$			0.94±0.05	$0.97^{+0.06}_{-0.04}$	0.94±0.05
$C^{\rm Chandra}_{\rm NuSTAR}$			0.91±0.10	$0.94^{+0.11}_{-0.09}$	$0.90^{+0.10}_{-0.05}$
$C^{\rm BAT}_{\rm NuSTAR}$			$1.23^{+0.32}_{-0.31}$	1.20±0.30	$1.15^{+0.28}_{-0.29}$
$\chi^2_{\rm r}$/d.o.f.			1.10/500	1.16/499	1.21/471

Notes. ^{f}fixed, ^{u}unconstrained. Best-fitting model parameters for Model P (PEXRAV model by Magdziarz & Zdziarski, 1995), T (TORUS model by Brightman & Nandra, 2011) and M (MYTORUS model by Murphy & Yaqoob, 2009). Details of each model are described in Section 3.3.

the fit. For those that returned values deviating significantly from 50 eV, we fixed them to this new value.

We added several more Gaussian components to account for the Fe Kα and Fe Kβ lines, the Ni Kα line and also the Compton shoulder associated with the Fe Kα line which are not included in the model.[7] The parameters were also fixed to values obtained in M13, except for the line energy and normalization of the Fe Kα line which were allowed to vary throughout. We fixed the inclination of the reflector to $\theta_{\rm inc} = 65°$, which is equal to that modelled by Fischer et al. (2013) for NGC 5643 (with an uncertainty of $\pm5°$) based on mapping the kinematics of the Hα and [OIII] narrow line region (NLR) emission observed by the *Hubble Space Telescope* (*HST*). The reflection scaling factor was fixed to $R = -1$ to simulate a reflection-dominated spectrum. Model P provides a good fit to the data (χ^2/d.o.f = 551/500), indicating that the spectra can be well-fitted by a pure reflection model without the need for any direct component.

The cross-calibration constants of *XMM-Newton*, *Chandra* and *Swift*-BAT relative to *NuSTAR* are consistent with each other with $C \sim 1$ within the statistical errors (see Table 3.2), indicating that the spectra are in good agreement with each other (see also Madsen et al., 2015 for the current cross-calibration status between different X-ray observatories and instruments with respect to *NuSTAR*). We estimated the intrinsic X-ray luminosities from this model by assuming that the observed luminosities at 0.5–10 keV and 30–100 keV are about 1% and 10% of the intrinsic luminosities at these energy bands, respectively (see Table 3.2). These inferred fractions were taken from detailed studies of NGC 1068 and have been widely used to estimate the intrinsic luminosities of other reflection-dominated AGN (e.g. Matt et al., 1997; Baloković et al., 2014).

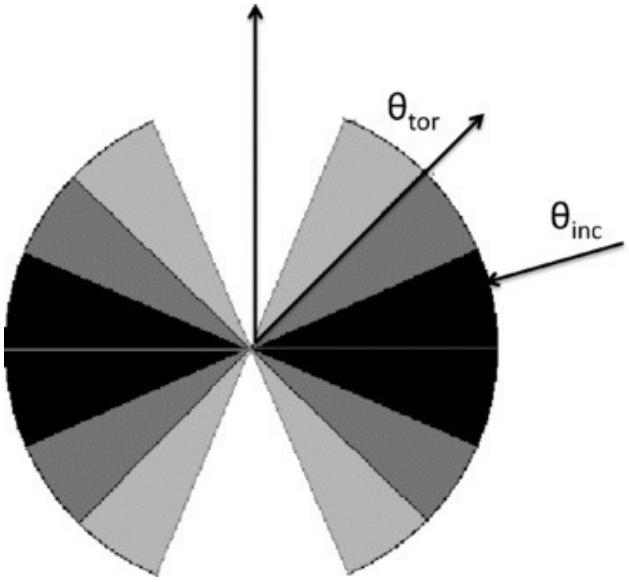

Figure 3.3: The geometry of the torus simulated by Brightman & Nandra (2011) (Model T). Different shadings are used to show the different torus opening angles ($\theta_{\rm tor}$) that can be simulated by the model. Image credit: Brightman & Nandra (2011).

3.3.2 Model T

We then proceeded to fit the AGN broadband spectrum using more physically motivated models, starting with the TORUS model by Brightman & Nandra (2011) (Model T; Figure 3.3). This model simulates obscuration by a medium with a conical section cut from a sphere, with a variable biconical polar opening angle ($\theta_{\rm tor}$) ranging between 26–84°. Small values of $\theta_{\rm tor}$ correspond to a geometrically thick torus, whilst large values indicate a geometrically thin torus. The line-of-sight $N_{\rm H}$(los) through the torus, which is equal to the equatorial column density $N_{\rm H}$(eq), extends up to 10^{26} cm^{-2}, allowing investigations of the most extreme obscuration, and is defined such that it is independent of the inclination angle ($\theta_{\rm inc}$). The model is defined between 0.1–320 keV and self-consistently predicts lines commonly found

[7]We note that modelling the Compton shoulder using a Gaussian component is incorrect since it is not exactly Gaussian, but we adopted this approach as an approximate parameterization for this particular model.

in obscured AGN, such as Fe Kα, Fe Kβ and also Kα emission from several other elements (C, O, Ne, Mg, Si, Ar, Ca, Cr, Fe and Ni).

The soft components of the spectrum ($\lesssim$ 2 keV) were modelled as described earlier in Section 3.3 and 3.3.1. Since $\theta_{\rm inc}$ and $\theta_{\rm tor}$ could not be constrained simultaneously, we fixed $\theta_{\rm inc}$ to 65° (Fischer et al., 2013). This model also yields a good fit to the data (χ^2/d.o.f = 579/499) with most fit residuals lying at the soft energies ($\lesssim$ 2 keV) and around the iron line emission ($\sim$6–7.5 keV; e.g. χ^2/d.o.f = 447/417 when fitting the model by ignoring the data around the iron line emission). The fitted intrinsic continuum power-law emission from this model has a photon index of $\Gamma = 1.97^{+0.03}_{-0.05}$ and is absorbed by a column density of $N_{\rm H}({\rm los}) > 1.5 \times 10^{25}$ cm^{-2}; i.e., heavily Compton-thick. The upper limit is unconstrained, with values of up to 10^{26} cm^{-2} allowed by the model. We found that the best-fit $\theta_{\rm tor}$ measured by this model is $\approx 60°$. As with Model P, the cross-calibration constants of each observation with respect to *NuSTAR* are consistent with 1. We inferred the intrinsic luminosities from this model based upon the best-fit parameters obtained, as presented in Table 3.2.

We also tried to fit the spectrum using different $\theta_{\rm inc}$ to see how the key parameters would change. Setting $\theta_{\rm inc}$ to a lower value of 45° produced an unacceptable fit (χ^2/d.o.f = 3989/499). Fixing $\theta_{\rm inc}$ to a higher value of 85° to simulate a near edge-on torus inclination, however, provides a slight improvement to the fit (χ^2/d.o.f = 549/499). The column density obtained is consistent with what was inferred before, but is more constrained, $N_{\rm H}({\rm los}) = 1.8^{+4.3}_{-0.6} \times 10^{25}$ cm^{-2}. The photon index is slightly lower, $\Gamma = 1.75^{+0.01}_{-0.03}$, and the opening angle of the torus suggests a surprisingly thin torus, $\theta_{\rm tor} = 78.5^{+0.01}_{-0.74}$ degrees. However, we note that Liu & Li (2015) claim that for an edge-on torus inclination, this model overestimates the reflection component, and therefore the parameters obtained may not be reliable. We thus favor the best-fitting model solution using $\theta_{\rm inc} = 65°$.

A closer look at the fitted spectrum between 6–7.5 keV (Figure 3.5) indicates that the model overpredicts the data at $\approx$6.3 keV, which encompasses the Compton shoulder associated with the Fe Kα line emission, and underpredicts the data at $\approx$6.4–6.8 keV, which includes the Fe Kα line emission. We investigated whether the

observed residuals could be caused by the presence of emission lines at 6.70 and 6.96 keV corresponding to ionized iron by adding Gaussian components at these energies. However, we found that the normalizations of the components are consistent with zero. We also tried to add a line smoothing component to the model (GSMOOTH; energy index, $\alpha = 1$) to see if the statistics could be further improved, but the fit indicated that this is not required ($\sigma_{\rm gsmooth} \lesssim 40$ eV). We noticed that the residuals are dominated by the *XMM-Newton* data, and therefore checked whether these could be caused by a shift in the energy scale of the data. Indeed we found that, applying an $\sim +11$ eV offset in the PN data can improve the overall quality of the fit (χ^2/d.o.f = 551/497) and diminish the residuals around the iron line complex (see also Bauer et al., 2015 for similar finding). However, this energy shift is consistent with the current calibration uncertainty of *XMM-Newton*[8], and the final results of the fitting are consistent with those presented in Table 3.2. Therefore, we decided not to apply this energy shift to the *XMM-Newton* PN data in the final fitting of all models.

3.3.3 Model M

We next fitted the AGN spectrum using the MYTORUS model by Murphy & Yaqoob (2009) (Model M; Figure 3.4). This model simulates obscuration toward an AGN using a toroidal absorber geometry (circular cross-section) with a fixed opening angle $\theta_{\rm tor} = 60^\circ$. The advantage of this model over Model T is that it allows the separation of the direct (MYTZ), scattered (MYTS) and line emission (MYTL) components, allowing more freedom to explore complex geometries in the modelling. On the other hand, the line-of-sight $N_{\rm H}$(los) is tied to the inclination angle and the equatorial $N_{\rm H}$(eq), which is available only up to an absorbing column density of $N_{\rm H}$(eq) = 10^{25} cm^{-2}. The MYTL component self-consistently includes neutral Fe Kα and Fe Kβ fluorescence lines, and the associated Compton shoulders. The model is defined between 0.5–500 keV, but we noticed strong residuals in our fit near the

[8]The current calibration documentation of *XMM-Newton* EPIC cameras can be downloaded from http://xmm2.esac.esa.int/docs/documents/CAL-TN-0018.pdf

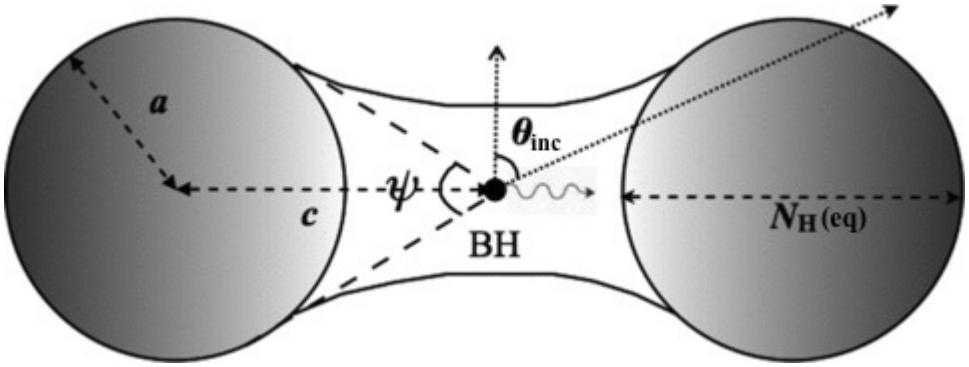

Figure 3.4: The geometry of the torus simulated by Murphy & Yaqoob (2009) (Model M). The half-opening angle of the torus ($\theta_{\rm tor} = [\pi - \phi]/2$) is assumed to be 60° (or $c/a = 2$). $\theta_{\rm inc}$ indicates the inclination angle between the line-of-sight of the observer and the symmetry axis of the torus. The equatorial column density of the torus, $N_{\rm H}$(eq), is defined as the hydrogen column density as measured through the diameter of the torus. Image credit: Murphy & Yaqoob (2009).

lower energy threshold, and therefore restricted our fits to above 0.6 keV for this model.[9]

We fitted the AGN spectrum using the simplest version of the MYTorus model, which couples all the parameters of the scattered and fluorescence line components to the direct continuum component. We added an extra Gaussian component to account for the Ni Kα line which is not included in the model (parameters were fixed to values obtained in M13). The relative normalizations of MYTS (A_S) and MYTL (A_L) with respect to MYTZ (A_Z) were set to 1. Model M also fits the data well with χ^2/d.o.f = 569/471. The best-fitting global column density inferred is $N_{\rm H}({\rm eq}) = 10.0^{+u}_{-0.5} \times 10^{24}$ cm^{-2}, which is at the upper limit of the MYTorus model. Reassuringly, the best-fitting inclination angle is $\theta_{\rm inc} = 65.9^{+2.33}_{-1.87}$ degrees, consistent with that determined by Fischer et al. (2013). However, we note that the MYTorus model does not allow for complete freedom in the fitting of the inclination angles.

[9]Since the fit for Model M was restricted to $E \geq 0.6$ keV, a Gaussian component that was added to model the emission line at $E \approx 0.58$ keV (M13) in Model P and T was excluded for this model.

Due to the assumption made for $\theta_{\rm tor}$, the model treats a torus with $\theta_{\rm inc} < 60^\circ$ as unobscured, and as a result, the best-fit $\theta_{\rm inc}$ measured by the model for obscured AGN are usually in the range of ≈60–70°. The $N_{\rm H}$(los) measured from this model is well within the CT regime, with an unconstrained upper limit; i.e., $N_{\rm H}({\rm los}) = 5.8^{+u}_{-1.2} \times 10^{24}$ cm^{-2}. Similar to Model T, the residuals of the fit are dominated by the soft energy emission, and the emission around the iron line, which can be improved if an energy offset is allowed in the *XMM-Newton* PN data (see Section 3.3.2). All parameters obtained by Model M, including the cross-calibration normalization constants and intrinsic luminosities of the AGN, agree very well with Model T (see Table 3.2).

3.3.4 The SPHERE Model

In addition to the TORUS model described in Section 3.3.2, Brightman & Nandra (2011) also present a model in which the source is fully covered by a spherical geometry ($\theta_{\rm tor} = 0^\circ$) with variable elemental and iron abundances with respect to hydrogen. This model is referred to as the SPHERE model. We tried to fit the spectra using this model. However, the fit was very poor (χ^2/d.o.f = 1169/501) and difficult to constrain. Leaving the metal abundances free to vary, which is allowed in this model, did improve the fit slightly, but the fit was still poor (χ^2/d.o.f = 848/499), and returned very low values of $N_{\rm H}$ and Γ, and a high Fe abundance ($\sim$ 7). Therefore, we will not discuss this model any further.

3.4 NGC 5643 X-1

In addition to the AGN, we also analysed the *NuSTAR* data for the ULX candidate, NGC 5643 X–1. ULXs are off-nuclear point sources with X-ray luminosities exceeding the Eddington limit for the typical $\sim 10 M_\odot$ stellar-remnant black holes observed in Galactic black hole binaries (e.g. Orosz, 2003); i.e., $L_{\rm X} \gtrsim 10^{39}$ erg s^{-1}, potentially implying exotic super-Eddington accretion (e.g. Poutanen et al., 2007). Whilst the majority of ULXs have luminosities of the order of 10^{39} erg s^{-1} (Walton et al., 2011b; Swartz et al., 2011), a small subset of the population has been observed

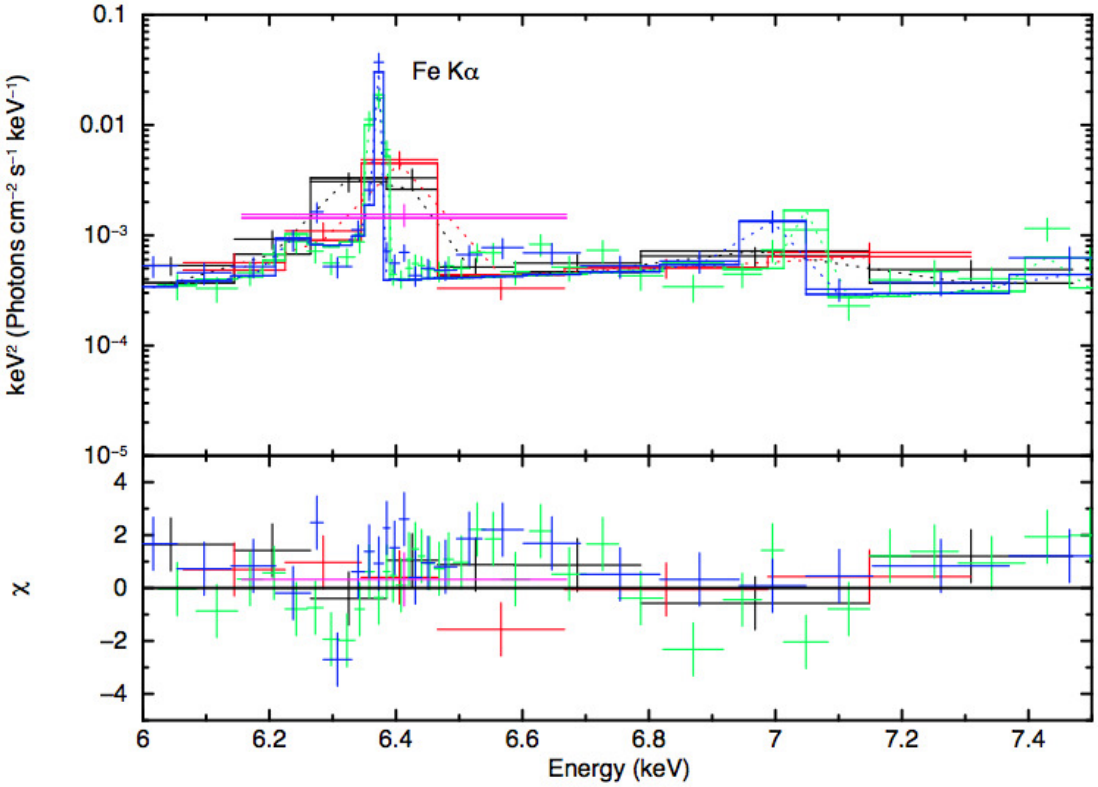

Figure 3.5: A zoom in of the spectral fit for Model T between 6–7.5 keV showing the asymmetric residuals around the iron line emission; the x-axis has been de-redshifted to show the rest-frame energy. The colour scheme of the data and the model are the same as Figure 3.2. The residuals are dominated by the *XMM-Newton* data at ≈6.3–6.8 keV, with the model overestimating the emission at ≈6.3 keV, and underpredicting the data at ≈6.4–6.8 keV. These residuals are diminished when applying an $\sim +11$ eV offset in the *XMM-Newton* PN data.

to have $L_{\rm X} > 10^{40}$ erg s^{-1} (Walton et al., 2011a; Jonker et al., 2012; Sutton et al., 2012). Given their luminosities, it has been suggested that these more luminous sources might be good candidates for hosting intermediate mass black holes ($10^2 \lesssim M_{\odot} \lesssim 10^5$; e.g. Miller et al., 2004; Strohmayer, 2009) accreting at sub-Eddington rates. With a luminosity of $L_{0.5-10} = 2.6 \times 10^{40}$ erg s^{-1} as measured by G04, NGC 5643 X–1 would therefore be a member of this latter population.

We extracted the *NuSTAR* spectra of NGC 5643 X–1 by defining a smaller circular region of 20″-radius around the source using the AGN as a reference point for its relative position. For the background region, we used an annular segment centered on the AGN (excluding a region of ∼50″-radius around NGC 5643 X–1 which accounts for the ∼70% encircled energy fraction), and with the same radial distance (relative to the AGN position) and width as the source region. This background region was designed to account for contamination by the AGN. We then determined the significance of the *NuSTAR* detection by calculating a no-source probability assuming binomial statistics ($P > 1\%$ for non-detection; i.e. $\lesssim 2.6\sigma$, following other *NuSTAR* studies of faint sources – e.g. Luo et al., 2013; Lansbury et al., 2014; Stern et al., 2014). Whilst the source is significantly detected in both of the *NuSTAR* observations in the 3–8 keV band, it is only significantly detected in the second observation in the 8–24 keV band ($P = 2.21 \times 10^{-6}$ in the combined FPMA+B image).

We next combined the data from the two FPMs for each epoch and binned the spectra to a minimum of 5 counts per bin due to low counts. We then fitted the spectra from each epoch using a simple power-law model, absorbed by the Galactic column. The spectral fitting parameters were calculated using C-statistics, appropriate for low count statistics (Cash, 1979). Although the source is not formally detected in the 8–24 keV band in the first epoch, we modelled the spectrum including the data point in this band to provide a better constraint to the fit. We found that the spectra of the source during the first and second epoch are consistent with each other, $\Gamma = 2.7^{+0.6}_{-0.5}$ and $\Gamma = 1.7^{+0.6}_{-0.5}$, $f_{3-24} = 3.6^{+0.9}_{-0.8} \times 10^{-13}$ erg s^{-1} cm^{-2} and $3.8^{+1.4}_{-1.0} \times 10^{-13}$ erg s^{-1} cm^{-2}, respectively, suggesting that the source has not varied significantly between the two observations. The lack of a detection at 8–24 keV in

the first epoch may be due to the location of NGC 5643 X–1 relative to the *NuSTAR* detector gap (Figure 3.1), which reduced the overall sensitivity of the data.

Motivated by the lack of significant flux variability, we therefore combined the *NuSTAR* spectra of NGC 5643 X–1 from the two epochs and fitted the total spectrum with the *Swift*-XRT data that were taken simultaneously with the first epoch. We reduced the *Swift*-XRT data as detailed in Section 3.2.4, and extracted the spectrum using a 20″-radius circular source region to match the *NuSTAR* extraction region. The background photons were selected from a source-free 100″-radius circular region close to the source. We grouped the data to a minimum of 40 and 20 counts per bin for *NuSTAR* and *Swift*-XRT, respectively, allowing the use of χ^2 statistics.

We first fitted the broadband spectrum of NGC 5643 X–1 over 0.5–24 keV using a simple power-law model absorbed by a column density intrinsic to the host galaxy (TBABS) in addition to the Galactic absorption. We fixed the cross-normalization constants between *NuSTAR* and *Swift*-XRT to 1. The fit is acceptable with χ^2/d.o.f = 9.21/7. The spectrum seems to drop off at E $\approx$ 11 keV, which could be an indication of a spectral cut-off at around 10 keV, as found for other *NuSTAR*-observed ULXs (e.g. Walton et al., 2013; Bachetti et al., 2013; Walton et al., 2014; Rana et al., 2015). If shown to be statistically significant, this would be the first time that such a cut-off is observed for NGC 5643 X–1. We therefore proceeded to fit the spectrum using an absorbed cut-off power-law model. The fit is also acceptable (χ^2/d.o.f = 8.46/6), and returned a cut-off energy of $E_{\rm cut} = 10.7^{+u}_{-7.6}$ keV. We also fitted the spectrum using a multi-colour blackbody accretion disk model with a variable temperature disk profile, DISKPBB (Mineshige et al., 1994), which is commonly used to model ULX spectra. This model provides a marginal improvement to the fit over the simple and cut-off power-law model (χ^2/d.o.f = 7.67/6). The measured temperature profile, p, is less than that expected for a thin disk ($p < 0.75$; Shakura & Sunyaev, 1973), consistent with an accretion disk in which advection of radiation is important, as expected at very high accretion rates where radiation pressure dominates and modifies the structure of the disk (e.g. Abramowicz et al., 1988). This would be consistent with NGC 5643 X–1 exhibiting

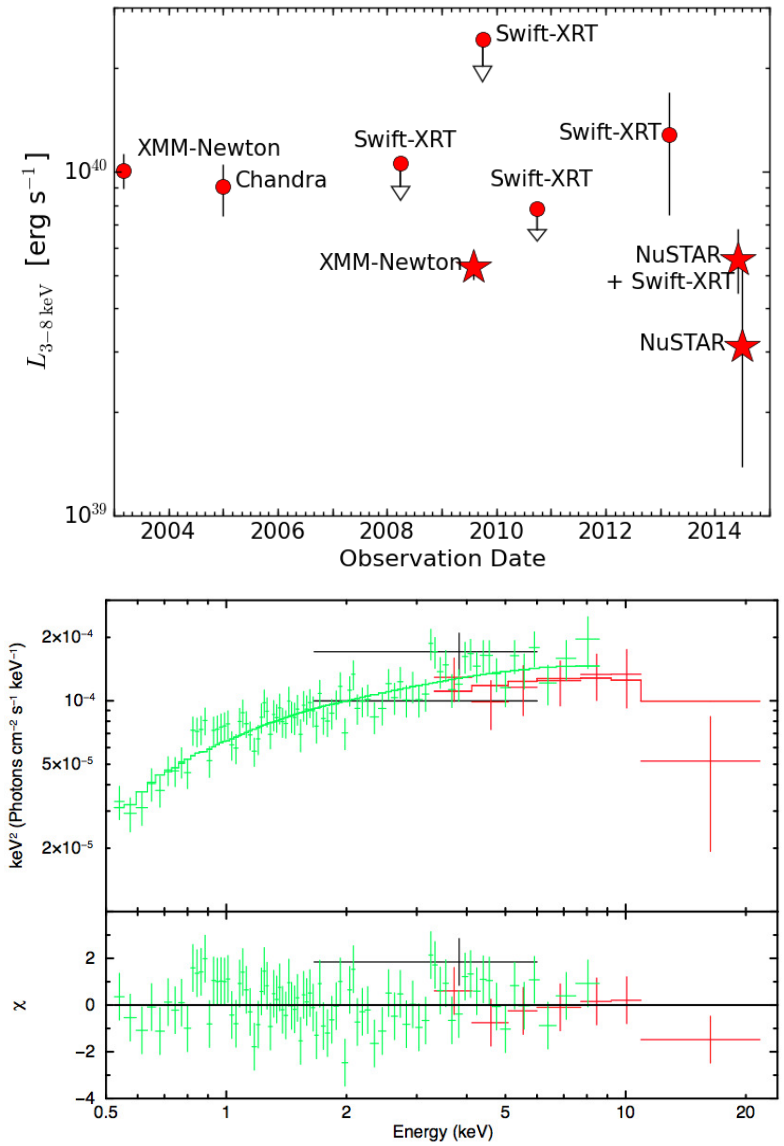

Figure 3.6: *Top*: X-ray luminosity variations of NGC 5643 X–1 in the 3–8 keV band observed between 2003–2014 by *XMM-Newton*, *Chandra*, *Swift*-XRT and *NuSTAR*. Observations marked with stars are those that we used to fit the broadband spectrum of the source. *Bottom*: Best-fit DISKPBB model to the combined *Swift*-XRT+*XMM*+*NuSTAR* spectra of NGC 5643 X–1. The top panel shows the unfolded model in E^2F_E units, whilst the bottom panel shows the fit residuals in terms of sigma with error bars of size one. The data have been rebinned to a minimum of 3-sigma significance with a maximum of 50 bins for visual clarity. Colour scheme: red (*NuSTAR*), black (*Swift*-XRT), green (*XMM-Newton* MOS).

high-Eddington rate accretion onto a stellar remnant black hole. The luminosity inferred by this model is $L_{0.5-24} = 1.01^{+0.36}_{-0.20} \times 10^{40}$ erg s^{-1}, assuming that NGC 5643 X–1 is at the distance of NGC 5643.

To obtain a better constraint to the broadband spectral fit of NGC 5643 X–1, we fitted the *Swift*-XRT and *NuSTAR* spectra simultaneously with the 2009 *XMM-Newton* spectrum of the source, in which M13 measured a luminosity of $L_{2-10} = (8.11 \pm 0.23) \times 10^{39}$ erg s^{-1}, consistent with that inferred by our *Swift*-XRT+*NuSTAR* best-fit DISKPBB model $L_{2-10} = 7.53^{+1.21}_{-1.39} \times 10^{39}$ erg s^{-1}. Data were reduced as described in Section 3.2.2. Because NGC 5643 X–1 fell on the detector gap in the PN camera, we only extracted the spectra of the source from the two MOS cameras, and co-added the spectra together. We extracted the spectra using a 20″-radius circular source region, and a 45″-radius circular background region. We left the cross-normalization between the *XMM-Newton* spectrum relative to *NuSTAR*, $C^{\rm XMM}_{\rm NuSTAR}$, free to vary.

We found that both the cut-off power-law and DISKPBB models provide better fits to the *Swift*-XRT+*XMM*+*NuSTAR* data than a simple power-law model (χ^2/d.o.f = 93.6/91, 90.2/91 and 99.0/92, respectively). The F-test null hypothesis probability between the simple power-law and cut-off power-law model is 0.023. This low value is strongly suggestive of the need for the high energy cut-off, though deeper observation will be required to validate this. $C^{\rm XMM}_{\rm NuSTAR}$ measured by the two models are, within the uncertainties, consistent with 1, providing further evidence that the spectra are in good agreement with each other. The cut-off power-law model measured a cut-off energy of $E_{\rm cut} = 16.3^{+35.9}_{-9.6}$ keV, and the DISKPBB model inferred a temperature disk profile, $p = 0.55 \pm 0.01$ and an inner disk temperature, $T_{\rm in} = 4.98^{+2.46}_{-1.80}$ keV. This temperature is consistent with that measured for some ULXs when fitting their whole broadband spectrum with just a single disk component (e.g. Walton et al., 2014; Rana et al., 2015). The best-fitting parameters for all models are presented in Table 3.3, and the broadband *Swift*-XRT+*XMM*+*NuSTAR* spectrum of NGC 5643 X–1 fitted by the best-fit model, namely DISKPBB, is shown in Figure 3.6.

Strong X-ray luminosity variations are often observed in ULXs. Motivated by

Table 3.3: X-ray spectral fitting results for NGC 5643 X–1.

Parameter	Unit	*Swift*-XRT+*NuSTAR*	*Swift*-XRT+*XMM*+*NuSTAR*
Model = TBABS × ZPOWERLAW			
$N_{\rm H}$	10^{21} cm^{-2}	< 23.2	< 0.46
Γ		$2.35^{+0.44}_{-0.33}$	$1.70^{+0.09}_{-0.08}$
$L_{0.5-24}$	10^{40} erg s^{-1}	$1.18^{+0.16}_{-0.31}$	$1.22^{+0.07}_{-0.03}$
$C^{\rm XMM}_{\rm NuSTAR}$		-	$1.31^{+0.31}_{-0.23}$
$\chi^2_{\rm r}$/d.o.f.		1.32/7	1.08/92
Model = TBABS × CUTOFFPOWERLAW			
$N_{\rm H}$	10^{21} cm^{-2}	< 18.5	< 0.22
Γ		$1.70^{+0.98}_{-1.64}$	$1.52^{+0.13}_{-0.11}$
$E_{\rm cut}$	keV	$10.7^{+u}_{-7.6}$	$16.3^{+35.9}_{-9.6}$
$L_{0.5-24}$	10^{40} erg s^{-1}	$1.08^{+0.22}_{-0.11}$	1.18±0.07
$C^{\rm XMM}_{\rm NuSTAR}$		-	$1.12^{+0.36}_{-0.20}$
$\chi^2_{\rm r}$/d.o.f.		1.41/6	1.03/91
Model = TBABS × DISKPBB			
$N_{\rm H}$	10^{21} cm^{-2}	< 16.8	...
$T_{\rm in}$	keV	$4.02^{+4.81}_{-1.47}$	$4.98^{+0.17}_{-0.20}$
p		< 0.74	0.55±0.01
$L_{0.5-24}$	10^{40} erg s^{-1}	$1.01^{+0.36}_{-0.20}$	$1.07^{+0.06}_{-0.08}$
$C^{\rm XMM}_{\rm NuSTAR}$		-	$1.19^{+0.24}_{-0.23}$
$\chi^2_{\rm r}$/d.o.f.		1.28/6	0.99/91

Notes. ^{u}unconstrained.

this, we also reduced the 2003 *XMM-Newton* data (ObsID 0140950101; UT 2003-02-08), as well as the *Chandra* data, and fitted the 3–8 keV spectra of NGC 5643 X–1 using a simple power-law model absorbed by the Galactic column, to infer its 3–8 keV luminosities at these epochs. In addition to these observations, the galaxy has also been observed by *Swift*-XRT between 2008–2013 on ∼30 occasions (mostly ∼1 ks exposure time), with most observations close to each other in 2013 targetted on an ongoing supernova in the galaxy. For simplicity, for each year in which there are multiple *Swift*-XRT observations of the source, we only analysed the data with the highest nominal exposure time to provide the best estimate of NGC 5643 X–1 luminosity in that particular year (ObsID 00037275001, 00037275002, 00037275004 and 00032724009; UT 2008-03-16, 2009-09-20, 2010-10-01 and 2013-02-26, respectively). Among these observations, NGC 5643 X–1 is only significantly detected by *Swift*-XRT in the 2013 observation. Therefore for this observation, we extracted the data as described earlier, and fitted the 3–8 keV spectrum using a simple power-law model absorbed by the Galactic column. For the other observations where NGC 5643 X–1 is not detected, we provided the upper limit luminosities at 90% confidence, estimated using aperture photometry assuming $\Gamma = 2$.

We compare the 3–8 keV luminosities between all the observations described above, as well as the *NuSTAR* observations at each epoch in Figure 3.6 to show the long term luminosity variability of NGC 5643 X–1. Note that the photon indices were left free to vary in all spectral fittings. In general, the plot shows that NGC 5643 X–1 can vary by a factor of ∼2–3 (up to ∼5) between epochs. This is broadly similar to the level of variability observed in other ULXs (e.g. Kong et al., 2010; Sutton et al., 2013; Walton et al., 2013). These results, combined with the parameters inferred by the DISKPBB model and evidence of an energy cut-off at E ∼ 10 keV, as well as the lack of a counterpart at other wavelengths (G04), further support the ULX classification of NGC 5643 X–1.

3.5 Discussion

In Section 3.3, we first investigated *NuSTAR* observations of the CTAGN candidate in NGC 5643. We combined our new data with archival *Chandra*, *XMM-Newton* and *Swift*-BAT data, and performed a broadband (∼0.5–100 keV) spectral analysis of the AGN. On the basis of three different reflection/obscuration models, we found that the AGN is consistent with being CT with a column density of $N_{\rm H}({\rm los}) \gtrsim 5 \times 10^{24}$ cm^{-2}. The absorption-corrected 2–10 keV luminosity obtained from the models range between $L_{2-10} = (0.8–1.7) \times 10^{42}$ erg s^{-1}, although we note that this could be a factor of a few lower/higher due to the fact that the spectra are dominated by reflection with negligible contribution from the direct emission, causing large uncertainties in the measurements of the intrinsic emission from the AGN. The intrinsic luminosity inferred is at the lower end of the luminosity range of the local bona-fide CTAGN population (see Figure 4 in Gandhi et al., 2014). Despite the presence of a nearby ULX with a 2–10 keV luminosity comparable to the observed luminosity of the AGN itself (G04), the spectrum of the ULX drops off at $E \sim 10$ keV, and the overall emission above this energy is dominated by the AGN.

This chapter provides the first intrinsic X-ray luminosity measurements for the AGN in NGC 5643 using Compton-thick solutions. To provide a basic test of the intrinsic luminosity estimate from our X-ray spectral fitting, we can compare the luminosity obtained to predictions from multiwavelength indicators. The obscuring torus absorbs disk radiation from the nucleus, but then re-emits it in the MIR. We can therefore use the intrinsic MIR:X-ray luminosity relationship found by Gandhi et al. (2009) based upon high angular resolution MIR 12μm observations to estimate the intrinsic X-ray luminosity of the AGN. The advantage of such observations is that because of their high angular resolution (∼0.4″), they provide MIR fluxes that are intrinsic to the nucleus, minimizing contamination from the host galaxy. The 12μm nuclear luminosity for NGC 5643, measured from VLT VISIR and Gemini T-ReCS observations, is $L_{12\mu m} = (1.5\pm0.4) \times 10^{42}$ erg s^{-1} (Asmus et al., 2014). Using the Gandhi et al. (2009) relationship, this corresponds to an X-ray luminosity of $L_{2-10} = (0.6–2.5) \times 10^{42}$ erg s^{-1}, which agrees well with the 2–10 keV intrinsic

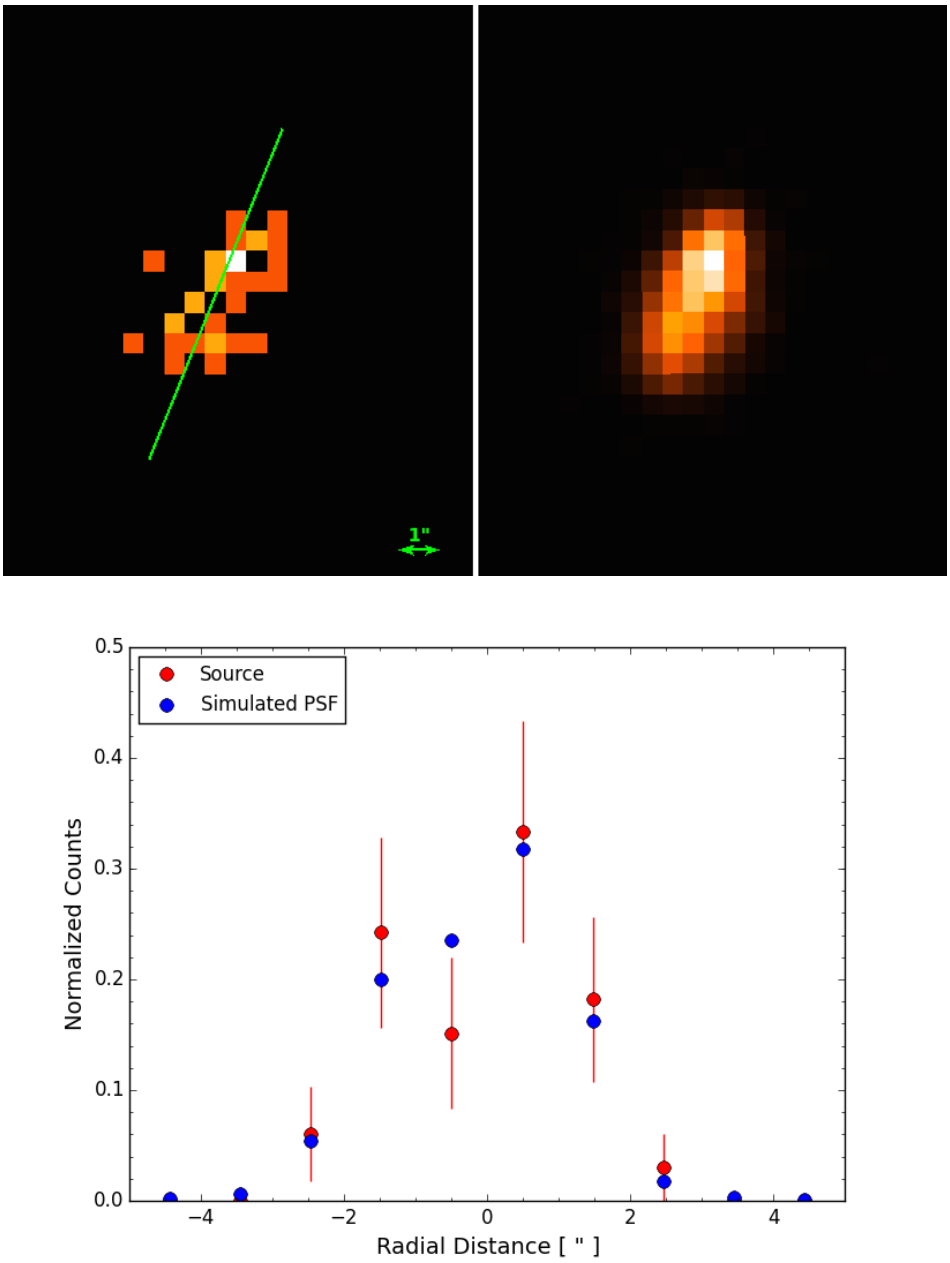

Figure 3.7: *Top*: *Chandra* 6–7.5 keV images of the AGN (left) and the simulated PSF (right). The green line shows the direction of the semi-major axis of the simulated PSF that was used to produce the 1D radial profiles for both the source and the simulated PSF. *Bottom*: The 1D radial profiles of the source (red) and the simulated PSF (blue) normalized to their respective total counts. The error bars indicate the 1-σ poisson errors for the data.

luminosity inferred from our broadband X-ray spectral modelling.[10]

We also compared our intrinsic 2–10 keV luminosity with that predicted from the optical [OIII]λ5007Å emission line luminosity. [OIII]λ5007Å in AGN are mostly produced in the NLR by photoionizing radiation from the central source. Although this line is not affected by the torus obscuration, it can still suffer from obscuration by the host galaxy, which can be corrected for using the Balmer decrement. We obtained our corrected [OIII]λ5007Å luminosity from Bassani et al. (1999), $L_{[\mathrm{OIII}]} = (1.6\pm0.2) \times 10^{41}$ erg s^{-1}. Using the L_{2-10}:$L_{[\mathrm{OIII}]}$ relationship from Panessa et al. (2006), we infer an X-ray luminosity of $L_{2-10} = (2.1\text{–}33.9) \times 10^{42}$ erg s^{-1}.[10] The lower end of this luminosity range is consistent with the luminosity measured from our X-ray spectral fitting. This is supported by the MIR [OIV]λ25.89μm emission line, $L_{[\mathrm{OIV}]} = (2.7\pm0.1) \times 10^{40}$ erg s^{-1} (Goulding & Alexander, 2009). Using L_{2-10}:$L_{[\mathrm{OIV}]}$ relationship defined by Goulding et al. (2010)[11], we determine an X-ray luminosity of $L_{2-10} = (0.9\text{–}5.5) \times 10^{42}$ erg s^{-1}.[10] This luminosity agrees very well with that measured by our best-fit models.

With our updated intrinsic X-ray luminosity, we can estimate the Eddington ratio of the AGN. Using M_{BH} estimated from the M_{BH}–σ_* relation, $M_{\mathrm{BH}} = 10^{6.4}$ M$_\odot$ (Goulding et al., 2010; see also footnote 3), combined with the range of intrinsic X-ray power that we measured from the best-fit models, we infer that the AGN is accreting matter at about 5–10% of the Eddington rate.[11] However, we note that this value is subject to large errors (factor of a few) due to the highly uncertain quantities involved in the calculation (Brandt & Alexander, 2015).

In the past few years, much evidence for the presence of distant cold reflecting regions has been found in nearby CTAGN (e.g. Marinucci et al., 2013; Arévalo et al., 2014; Bauer et al., 2015). To accurately characterise the broadband spectra of these AGN, multiple reflector components are required to model each of these reflecting regions. We investigated whether this could be the case for NGC 5643 by looking at

[10]The given luminosity range accounts for the mean scatter of the correlation.

[11]We assume a typical AGN bolometric correction $L_{\mathrm{bol}}/L_{2-10} \approx 20$ to calculate the bolometric luminosity and hence the mass accretion rate of the AGN (e.g. Elvis et al., 1994; Vasudevan et al., 2010).

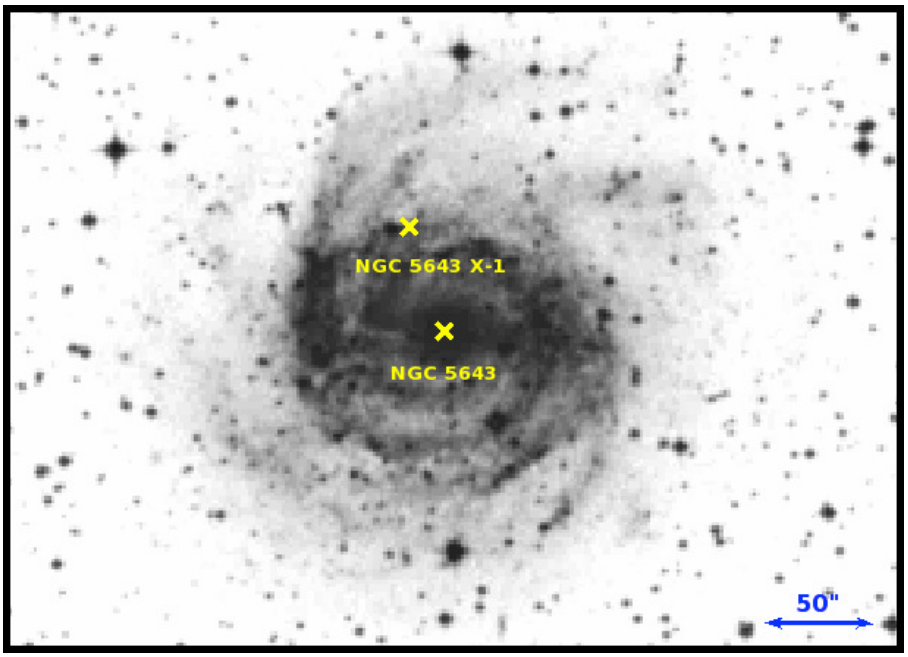

Figure 3.8: Optical image of NGC 5643 retrieved from the ESO Digital Sky Survey image server. *Chandra* position of the AGN (NGC 5643) and the ULX candidate (NGC 5643 X–1) are both labelled and marked with an "×". North is up and East is to the left in the image.

the *Chandra* image of the AGN in the 6–7.5 keV band (∼30 counts). This is shown in the top left panel of Figure 3.7. At first glance, the image appears to show that the iron emission region is extended well beyond the parsec-scale torus, suggesting the presence of distant cold reflecting regions. However, this appearance could also be due to an elongated PSF as a result of the position of the target on the detector, as well as the energy range used to produce the source image. We therefore used the MARX simulator[12] (v4.4) to produce the expected PSF with a much higher count than the source counts (∼ 100 000 counts) at the position of the AGN, and at the mean energy range that we are interested in ($E = 6.75$ keV). This is shown in the top right panel of Figure 3.7. We then plotted 1D radial profiles of the target and the simulated PSF along the semi-major axis of the simulated PSF determined using the WAVDETECT tool within CIAO, and performed a Kolmogorov-Smirnov (KS) test between the two distributions (bottom panel of Figure 3.7). We found that the KS test probability is $P_{\rm KS} = 0.983$, indicating that the iron emission region of the target is consistent with the simulated PSF, and therefore is not extended (see similar finding for NGC 3393 in Koss et al., 2015). A deeper (scheduled) *Chandra* observation could help to confirm this.

The CTAGN in NGC 5643 is located in a face-on grand design spiral galaxy with an undisturbed disk (see Figure 3.8). The emission lines from the AGN are not obscured/extinguished by the host galaxy material (Goulding & Alexander, 2009), indicating that any phenomenon that might contribute to the CT obscuration in this source is therefore likely to occur very close to the nucleus. Indeed, there have been indications that the emission at the west side of the nucleus is obscured by a warped disk or the presence of a dust lane (e.g. Simpson et al., 1997, Fischer et al., 2013, Davies et al., 2014). The torus itself could be the inner structure of this disk. Because of the more direct and "cleaner" view of the central engine in NGC 5643 as compared to some other very nearby bona-fide CTAGNs such as NGC 1068, NGC 4945 and Circinus, this makes NGC 5643 a good candidate for more detailed studies of the CT obscurer in the nuclear region.

[12]The MARX simulation documentation is available at http://space.mit.edu/ASC/MARX/.

3.6 Summary

We observed the AGN and ULX candidate in NGC 5643 using *NuSTAR* on two occasions conducted at about a month separation. A summary of our main results is as follows:

1. Using the combined data from *NuSTAR*, *Chandra*, *XMM-Newton* and *Swift*-BAT, we have extended the broadband spectral analysis of the CTAGN candidate in NGC 5643 to high energies (∼0.5–100 keV). Using physically motivated toroidal obscuration models, we showed that the source is indeed CT with a column density of $N_{\rm H}({\rm los}) \gtrsim 5 \times 10^{24}$ cm^{-2}.

2. The absorption-corrected 2–10 keV luminosity measured by these models is $L_{2-10,{\rm int}} = (0.8–1.7) \times 10^{42}$ erg s^{-1}, consistent with that predicted from multiwavelength intrinsic luminosity indicators. The luminosity inferred is at the lower end of the luminosity range of the local CTAGN population.

3. The *NuSTAR* spectra of the off-nuclear source, NGC 5643 X-1, shows evidence for a spectral cut-off at $E \sim 10$ keV, similar to that observed in other ULXs observed by *NuSTAR*. Combining this information with the evidence for X-ray luminosity variations observed between different observations, along with the absence of unambiguous counterparts at other wavelengths, we concluded that the source is consistent with being a ULX. Future simultaneous low and high energy X-ray observations of this field are needed in order to provide higher quality data to confirm the spectral cut-off that we observed, and to better characterise the broadband spectrum of the source.

Chapter 4

A new Compton-thick AGN in our cosmic backyard - unveiling the buried nucleus in NGC 1448 with *NuSTAR*

NGC 1448 is one of the nearest luminous galaxies ($L_{8-1000\mu m} > 10^9 L_{\odot}$) to ours ($z$ = 0.00390), and yet the active galactic nucleus (AGN) it hosts was only recently discovered, in 2009. In this chapter, I present an analysis of the nuclear source across three wavebands: mid-infrared (MIR) continuum, optical, and X-rays. We observed the source with the *Nuclear Spectroscopic Telescope Array* (*NuSTAR*), and combined this data with archival *Chandra* data to perform broadband X-ray spectral fitting (≈0.5–40 keV) of the AGN for the first time. Our X-ray spectral analysis reveals that the AGN is buried under a Compton-thick (CT) column of obscuring gas along our line-of-sight, with a column density of $N_{\rm H}(\rm los) \gtrsim 2.5 \times 10^{24}$ cm^{-2}. The best-fitting torus models measured an intrinsic 2–10 keV luminosity of $L_{2-10,\rm int}$ = (3.5–7.6) × 10^{40} erg s^{-1}, making NGC 1448 one of the lowest luminosity CTAGNs known. In addition to the *NuSTAR* observation, we also performed optical spectroscopy for the nucleus in this edge-on galaxy using the European Southern Observatory New Technology Telescope. We re-classify the optical nuclear spectrum as a Seyfert on the basis of the Baldwin-Philips-Terlevich diagnostic diagrams, thus identifying the

AGN at optical wavelengths for the first time. We also present high spatial resolution MIR observations of NGC 1448 with Gemini/T-ReCS, in which a compact nucleus is clearly detected. The absorption-corrected 2–10 keV luminosity measured from our X-ray spectral analysis agrees with that predicted from the optical [OIII]λ5007Å emission line and the MIR 12μm continuum, further supporting the CT nature of the AGN.

4.1 Introduction

At a distance of 11.5 Mpc ($z = 0.00390$),[1] NGC 1448 is one of the nearest bolometrically luminous galaxies ($L_{8-1000\mu m} > 10^9 L_\odot$) to our own. Yet, the presence of an active galactic nucleus (AGN) at the center of the galaxy was only discovered less than a decade ago by Goulding & Alexander (2009) through the detection of the high-ionization [NeV]λ14.32μm emission line, as part of a sample of luminous galaxies observed by *Spitzer*. Based on the [NeV]/$f_{8-1000\mu m}$ and [NeV]/[NeII]λ12.82μm luminosity ratios, they found that the AGN contributes a significant fraction (>25%) of the infrared (IR) emission. So far, the focus of the majority of studies of NGC 1448 has been on a number of supernovae occuring in the galaxy (e.g.; Wang et al., 2003; Sollerman et al., 2005; Monard et al., 2014).

Based on its total K-band magnitude from the 2MASS Large Galaxy Atlas, $K_{\rm Tot} = 7.66$ (Jarrett et al., 2003), the total mass of NGC 1448 is log $(M_{\rm gal}/M_\odot) = 10.3$ (using the stellar mass-to-light ratio versus $B-V$ relation of Bell et al., 2003.) The star formation rate (SFR) of the galaxy estimated from its far-IR luminosity measured by the *Infrared Astronomical Satellite* (*IRAS*), log $L_{\rm fir} = 9.70\ L_\odot$ (Sanders et al., 2003), is SFR $\sim 1\ M_\odot$/yr (Kennicutt, 1998). This is consistent with the SFR expected at this redshift, given the mass of the galaxy (Davé, 2008). The nucleus is classified as an HII region in the optical by Veron-Cetty & Veron (1986) using the Hα to [NII]λ6583Å line ratio (Hα/[NII] > 1.7), without any clear evidence for an AGN.

[1] The quoted distance is the metric/proper distance calculated based upon the Mould et al. (2000) cosmic attractor model, using $H_0 = 75$ km s^{-1} Mpc^{-1} and adopting flat cosmology ($\Omega_M = 0.3$, $\Omega_\Lambda = 0.7$, $q_0 = 0.3$) (Sanders et al., 2003).

The [OIII]λ5007Å and Hβ emission lines were not detected in their observation, which could be attributed to obscuration by the highly inclined Scd host galaxy ($i \approx 86°$ relative to the plane of the sky).[2] Based on the [OIV]λ25.89μm to [OIII]λ5007Å lower limit emission line ratio, Goulding & Alexander (2009) found an extinction of $A_V > 5$ mag within the galaxy, suggesting high obscuration towards the AGN.

In recent years, many studies have been done to find the most heavily obscured AGNs, particularly Compton-thick (CT) AGNs (see Chapter 1), in the local universe. However, identifying CTAGNs has been demonstrated to be a very challenging task due the high column density of gas ($N_{\rm H} \gtrsim 1.5 \times 10^{24}$ cm^{-2}) along our line-of-sight that hinders our direct view towards the AGN. Indeed, various studies have shown that we are still missing a large number of CTAGN, even in the local universe (e.g., Ricci et al., 2015). Finding all of CTAGN is important for a complete census of the overall AGN population, as well as helping us understand the cosmic X-ray background radiation and how supermassive black holes grow (see Chapter 1 for further details).

In this chapter, we present *NuSTAR* (see Section 2.2.2 in Chapter 2) and *Chandra* (see Section 2.2.3 in Chapter 2) observations of NGC 1448 in which the AGN is detected in X-rays for the first time. We find that our direct view towards the AGN is hindered by a Compton-thick column of obscuring gas. We also report the results of new high angular resolution mid-infrared (MIR) and optical observations of the source by Gemini/T-ReCS and NTT/EFOSC2, respectively, which also reveal the presence of a buried AGN. We organised the chapter as follows: In Section 4.2, we describe details of the multiwavelength observations and data reduction procedures for NGC 1448. We present the X-ray spectral modeling and results in Section 4.3, followed by the data analysis and results of the optical and MIR observations in Section 4.4. Finally, we discuss and summarise the overall results in Section 4.5 and Section 4.6, respectively.

[2] We obtained the host galaxy inclination from the HyperLeda website (http://leda.univ-lyon1.fr/).

4.2 Observations

In this section, we describe the new *NuSTAR* (Section 4.2.1) and archival *Chandra* (Section 4.2.2) observations of NGC 1448. The *NuSTAR* data are essential for tracing the intrinsic emission from the buried AGN at high X-ray energies ($E \gtrsim 10$ keV). The *Chandra* data were used to aid our X-ray spectral analysis of the AGN at lower energies ($E \lesssim 3$ keV) where *NuSTAR* is not sensitive, and to reliably account for the emission from contaminating off-nuclear X-ray sources in the *NuSTAR* spectrum. Combining both *NuSTAR* and *Chandra* data together allows us to analyse the X-ray spectrum of the AGN in NGC 1448 over a broadband range of energy for the first time. We also describe new optical data (spectroscopy and imaging) obtained with the ESO NTT (Section 4.2.3), and the new high angular resolution MIR observations with the Gemini-South telescope (Section 4.2.4), to provide a multiwavelength view of the AGN.

In addition to these data, we note that NGC 1448 has also been observed by *Suzaku* in X-rays for an exposure time of $\approx$ 53 ks in 2009 (2009-02-17; PI D. M. Alexander; ObsID 703062010). However, it is only significantly detected in the X-ray Imaging Spectrometer (XIS) instrument up to $\sim$10 keV. Analysis of the deepest *Swift*-BAT 104-month maps using custom detection techniques to look for faint sources (Koss et al., 2013), show no significant excess (signal-to-noise ratio, SNR $= -0.1$) in the area near NGC 1448. The source was only detected in 1 out of 5 *Swift* X-ray Telescope (XRT) observations with $\sim$12 counts in $\sim$10 ks exposure time (2009-11-28; ObsID 00031031001). We do not include these data in our X-ray analysis as they do not provide additional constraints beyond those already achieved with our *NuSTAR* and *Chandra* data.

4.2.1 *NuSTAR*

NGC 1448 was observed by *NuSTAR* in 2015 (2015-07-12; ObsID 60101101002) with an effective exposure time of 58.9 ks (60.3 ks on-source time) for each FPM. The source was observed as part of our program to form the most complete census of the CTAGN population and the $N_{\rm H}$ distribution of AGN in the local universe, using a

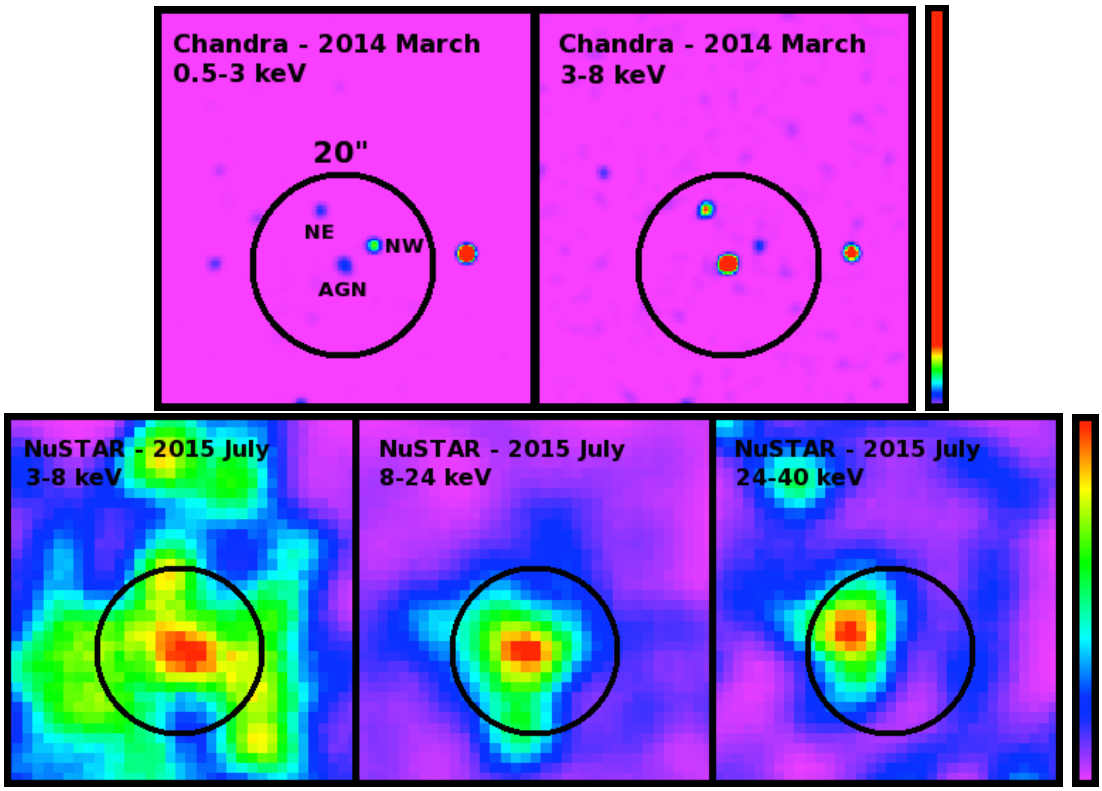

Figure 4.1: *Chandra* images of NGC 1448 in the 0.5–3 keV and 3–8 keV bands (top panel) and *NuSTAR* FPMA+B images in the 3–8 keV, 8–24 keV and 24–40 keV bands (bottom panel). The color scale for *Chandra* and *NuSTAR* images are shown with magenta and red representing the lowest and highest counts in each image, respectively. The black circle marks a 20″-radius region centered on the *Chandra* position of the AGN that was used to extract the X-ray spectra. Images are smoothed with a Gaussian function of radius 5 pixels, corresponding to 2.47″ and 12.3″ for *Chandra* and *NuSTAR*, respectively. North is up and east is to the left in all images. The two off-nuclear X-ray sources detected within the extraction region in the *Chandra* image are at the north-east and north-west of the AGN, labelled as NE and NW, respectively.

volume-limited ($D < 15$ Mpc) AGN sample from Goulding & Alexander (2009).[3]

We processed the *NuSTAR* data of NGC 1448 with the *NuSTAR* Data Analysis Software (NUSTARDAS) v1.4.1 within HEASOFT v6.15.1 with CALDB v20150316. The NUPIPELINE v0.4.3 script were used to produce the calibrated and cleaned event files using standard filter flags. We extracted the spectra and response files using the NUPRODUCTS v0.2.5 task (see Chapter 2).

The AGN is detected in both of the *NuSTAR* FPMs. The combined images of the AGN from the two FPMs in the 3–8, 8–24, and 24–40 keV bands are shown in Figure 4.1. We extracted the *NuSTAR* spectrum of NGC 1448 from each FPM using a circular aperture region of 20″-radius (corresponding to ∼30% *NuSTAR* encircled energy fraction, ECF) centered on the *Chandra* position of the AGN (see Section 4.2.2). The aperture size was chosen to minimize contamination from off-nuclear sources observed in the *Chandra* data. The background photons were collected from an annular region centered on the AGN with inner and outer radii of 40″ and 70″, respectively. The extracted spectra from each FPM were then co-added using the ADDASCASPEC script to increase the overall SNR of the data. We detected significant counts up to ∼40 keV from this combined spectrum, and measured a net count rate of 2.79×10^{-3} counts s^{-1} in the 3–40 keV band.

We note that in the 24–40 keV band image, where we expect the AGN to completely dominate, the peak emission appears to be offset from the center of the extraction region. The offset is not observed in the 3–8 and 8–24 keV band images where *NuSTAR* is more sensitive. Performing our spectral fits up to only 24 keV gave consistent results with those obtained by the 0.5–40 keV spectral fits. We therefore attribute this offset due to *NuSTAR* statistical uncertainty due to lower SNR at this higher energy band. We note that centering the *NuSTAR* extraction region according to this offset, or enlarging the extraction region to account for this apparent offset also do not significantly affect our final results on the analysis of the AGN in NGC 1448.

[3] The results of the first source in the sample observed by *NuSTAR* as part of this program, NGC 5643, was reported in Annuar et al., 2015 (see Chapter 3).

4.2.2 *Chandra*

NGC 1448 was observed by *Chandra* in 2014 with an exposure time of 49.4 ks (50.1 ks on-source time) using the ACIS-S detector as part of the *Chandra* HRC-GTO program (2014-03-09; PI S. Murray; ObsID 15332). We reprocessed the data to create event files with updated calibration modifications, following standard procedures (see Chapter 2).

We determined the centroid position of the AGN in the *Chandra* hard energy band of 2–8 keV using the WAVDETECT tool within CIAO with the threshold parameter set to 1×10^{-7}. We detected three sources within the central 20″-radius of the galaxy in this energy band (see Figure 4.1). The brightest source was detected at position of RA = 3:44:31.83, and Dec. = −44:38:41.22, with errors of 0.″17 and 0.″11, respectively. This is consistent with the 2MASS and Gemini/T-ReCS (see Section 4.2.4) positions of the nucleus within ∼1″. Therefore, we adopted this *Chandra* position as the AGN position.

We extracted the source spectrum using the SPECEXTRACT task in CIAO from a circular region of 20″-radius centered on the detected position of the AGN to match the *NuSTAR* extraction region. A 50″-radius circular aperture was used to extract the background counts from an offset, source-free region. The total net count rate within the 20″-radius extraction region in the 0.5–8 keV band is 5.69×10^{-3} counts s^{-1}. The net count rate measured by WAVDETECT for the AGN is 1.39×10^{-3} counts s^{-1} in the 0.5–8 keV band. The two other sources detected within the extraction region are located to the north-east (NE) and north-west (NW) of the AGN. They do not have counterparts at other wavelengths, and are likely to be X-ray binaries within NGC 1448 (see Section 4.3.2.1). These sources have 0.5–8 keV count rates of 6.67×10^{-4} counts s^{-1} and 8.61×10^{-4} counts s^{-1}, for the NE and NW sources, respectively, as measured by WAVDETECT.

4.2.3 NTT/EFOSC2

At optical wavelengths, we performed spectroscopy for NGC 1448 using the European Southern Observatory (ESO) New Technology Telescope (NTT) on 2015-12-07,

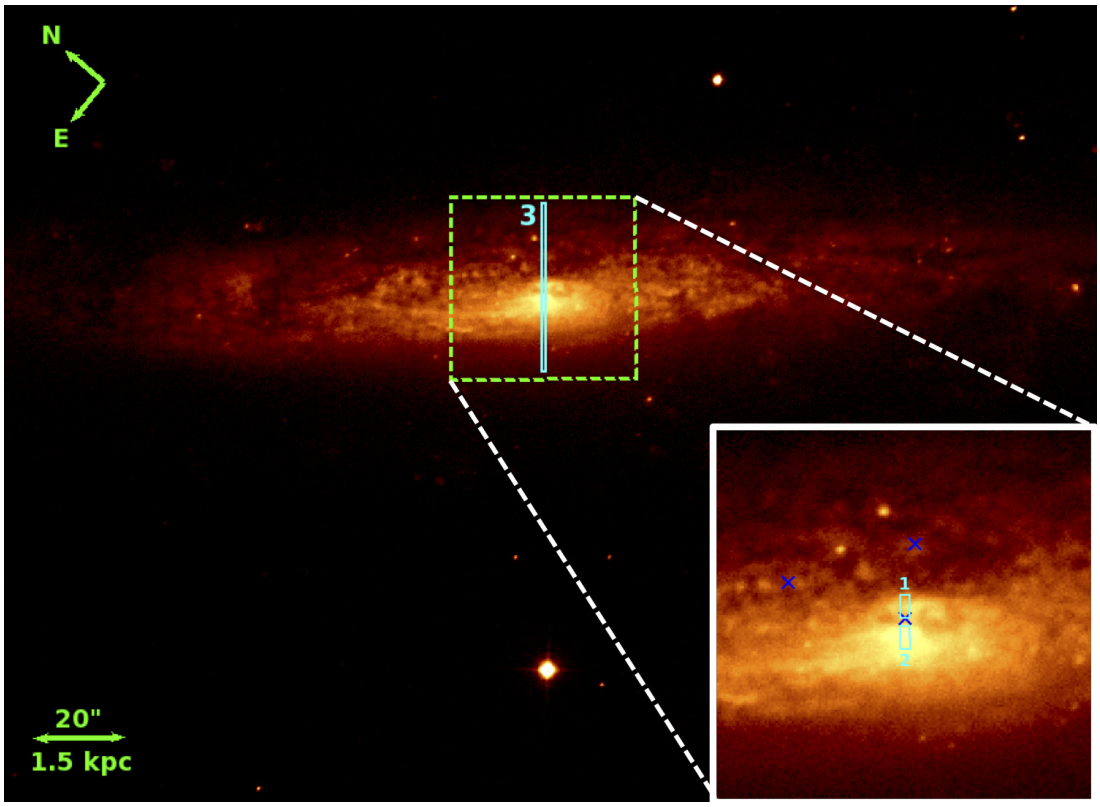

Figure 4.2: Optical R-band image of NGC 1448 taken with the ESO NTT. The aperture used to extract the optical spectra of the AGN, optical peak and the total galaxy are plotted using cyan rectangle regions, and labelled as 1, 2 and 3, respectively. The zoom-in image of the central 20″ × 20″ of the galaxy is shown in the bottom-right panel. "×" marks the sources detected within a 20″ circular radius of the AGN in the *Chandra* 2–8 keV band image.

using the Faint Object Spectrograph and Camera v.2 (EFOSC2) instrument (Program ID 096.B-0947(A); PI G. B. Lansbury). The source was observed for four 5 min exposures centered on the *Chandra* position (see Section 4.2.2). The slit adopted was $1''$ (75 pc) in width, and the adopted grism yielded a spectral coverage of 4085–7520Å, and spectral resolution of FWHM = 12.6Å. The seeing at the time of the observation was $\sim 0\farcs7$. Standard IRAF routines were followed to reduce the spectra, and spectrophotometric standard star observations from the same night were used for calibration. As shown in Figure 4.2, we extracted spectra from three different apertures along the slit, corresponding to: (1) the AGN (using the *Chandra* position as a reference); (2) the "optical peak"; and (3) the total galaxy. The optical peak corresponds to the position where the optical emission is the brightest in the imaging data and in the 2-dimensional spectra, and is offset from the AGN position by $\sim 3''$ (RA = 3:44:31.99 and Dec. = −44:38:42.33). The spatial apertures adopted were $2\farcs4$ for the AGN and the optical peak, and $36\farcs9$ for the total galaxy (see Figure 4.2). The apertures for the AGN and the optical peak correspond to two spatially distinct, prominent line-emitting regions which are separated by a dust lane, from which we do not see any prominent line emission. The aperture extents for the AGN and the optical peak were chosen based on the light profile of the Hα and [OIII]λ5007Å emission lines in spatial direction, to ensure that we included the total emission of these lines.

Before we can measure the fluxes of the emission lines, we first need to subtract stellar emission from the extracted spectra. This was done by fitting the emission line-free regions of each spectrum with a combination of a small subset of galaxy template spectra from the Bruzual & Charlot (2003) stellar library. This library consists of model templates for 39 stellar populations with ages between 5.0×10^6 and 1.2×10^{10} yr, and metallicities between 0.008 and 0.05, with a spectral sampling of 3Å. This library has been used to fit the continua and measure the emission line fluxes of the Sloan Digital Sky Survey (SDSS) galaxy spectra (Tremonti et al., 2004). We performed our spectral synthesis for the three spectra in XSPEC v12.8.2,[4] assuming $z = 0.00390$, solar metallicity ($Z_\odot = 0.02$), and the Cardelli et al.

[4] The XSPEC manual is available at

(1989) extinction law. The best-fitted stellar spectra were then subtracted from the observed spectra, which resulted in residual spectra with emission lines only. We then analysed the detected emission lines using the SPLOT tasks in IRAF.

4.2.4 *Gemini*/T-ReCS

NGC 1448 was observed at MIR wavelengths in 2010 with high spatial resolution using the Thermal-Region Camera Spectrograph (T-ReCS; field of view $28\farcs8 \times 21\farcs6$; 0.09 arcsec pixel^{-1}; Telesco et al., 1998), mounted on the Gemini-South telescope. The observation was carried out on 2010-08-19 (Program ID GS-2010B-Q-3) for ≈319 s on-source time using the N-band filter (λ = 7.4–13.4 μm) in parallel chop and nod mode. The data were reduced using the MIDIR pipeline in IRAF provided by the Gemini Observatory, and the image analysis was performed using the IDL package MIRPHOT, following Asmus et al. (2014). The data were flux-calibrated with a standard star, HD22663, which was observed immediately before NGC 1448. The resolution of the observation is $\sim 0\farcs4$ as measured from the FWHM of the standard star.

A compact nucleus is clearly detected in the MIR continuum at position RA = 3:44:31.75 and Dec. = −44:38:41.8 (telescope astrometric uncertainty is on the order of 1″) with a SNR ∼5. The source appears to be embedded in $\sim 0\farcs7$ extended emission along the host major axis (position angle PA ∼ 44°). However, owing to the small extent and often unstable point spread function (PSF) in ground-based MIR observations, a second epoch of high spatial resolution MIR images is required in order to confirm this extension. The source is best-fitted with a 2-dimensional Gaussian model (see Figure 4.3), which measured a flux density of $f_{12\mu\mathrm{m}} = 12.5 \pm 2.3$ mJy.

http://heasarc.gsfc.nasa.gov/xanadu/xspec/XspecManual.pdf

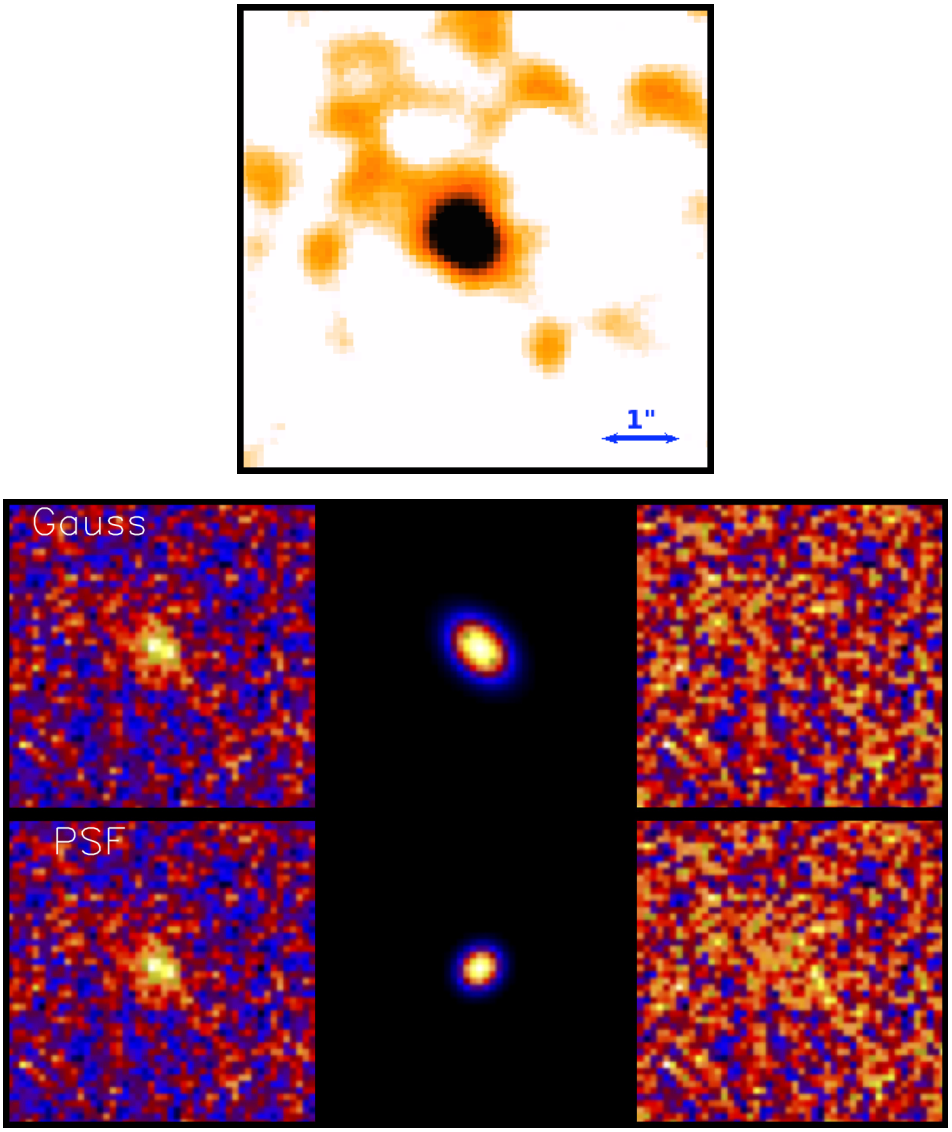

Figure 4.3: *Top*: High spatial resolution MIR image of NGC 1448 taken by Gemini/T-ReCS. *Bottom*: Image fits performed using the MIRPHOT task in IDL following Asmus et al. (2014). Shown are the central 4.″5 × 4.″5 of the image. The left column is the original image, the middle column is the fit performed on the data, and the right column is the residual after subtracting the fit from the data. The top row shows the results from a Gaussian fit to the total emission, and the bottom row shows the results from fitting the standard star (as a PSF reference) to the total emission. In all images, North is up and east is to the left.

4.3 X-ray Spectral Fitting

4.3.1 Basic Characterisation

In this section, we describe the broadband X-ray spectral analysis of the AGN in NGC 1448, performed using XSPEC. Given the non-negligible contribution of the background flux to the weak source flux, particularly in the *NuSTAR* data at high energies, we binned both the *Chandra* and *NuSTAR* spectra to a minimum of 1 count per bin and optimized the fitting parameters using the Poisson statistic, C-statistic (Cash, 1979).[5,6] We included a fixed Galactic absorption component, $N_{\rm H}^{\rm Gal}$ $= 9.81 \times 10^{19}$ cm^{-2} (Kalberla et al., 2005), using the XSPEC model "PHABS" in all spectral fits, and assumed solar abundances for all models. The redshift was fixed at $z = 0.00390$ in all analyses. We quoted all errors at 90% confidence, unless stated otherwise. We summarise the main results of the analysis in Table 4.1, and present the X-ray data and best-fitting models in Figure 4.4.

We began our spectral modeling by examining the *NuSTAR* and *Chandra* data separately. At this point we are not yet considering non-AGN contributions to the X-ray spectrum, such as from the two off-nuclear point sources within the extraction region. We modelled the two spectra in the 3–40 keV and 2–8 keV bands, respectively, using a simple power-law model with Galactic absorption. The best fitting photon indices are very flat: $\Gamma = -0.29 \pm 0.38$ for *NuSTAR* (C-stat/d.o.f = 229/237), and $\Gamma = 0.82^{+0.88}_{-0.77}$ for *Chandra* (C-stat/d.o.f = 125/126). A slight excess of counts just above 6 keV was observed in both the *NuSTAR* and *Chandra* spectra. This is likely an indication of a fluorescent Fe Kα line emission, associated with a spectral component produced by AGN emission that is being reflected off a high column of gas. The fluxes of the two spectra within the common energy range of 3–8

[5] We note that grouping the *Chandra* and *NuSTAR* data to a minimum of 20 and 40 counts per bin, respectively, and performing the spectral fits using χ^2 minimization yields consistent results with the C-statistic approach.

[6] For C-statistic, the goodness of fit can be measured using the ratio between the C-statistic (C-stat) value and the number of degrees of freedom (d.o.f). A good fit is defined when C-stat/d.o.f ≈ 1 (see http://cxc.harvard.edu/sherpa/statistics/#cstat).

keV measured by the model are $f_{3-8} = 2.00^{+0.23}_{-0.57} \times 10^{-14}$ erg s^{-1} cm^{-2} for *NuSTAR*, and $f_{3-8} = 3.50^{+0.56}_{-1.34} \times 10^{-14}$ erg s^{-1} cm^{-2} for *Chandra*. These fluxes are consistent with each other within the measurement uncertainties, indicating that there was no significant variability between the two observations.

We then fitted the *NuSTAR* spectrum simultaneously with the *Chandra* spectrum between 3 and 40 keV using a simple power-law model and a Gaussian component to model the possible Fe Kα emission line, with the line energy and width fixed to $E = 6.4$ keV and $\sigma = 10$ eV, respectively. This model measured a photon index of $\Gamma = 0.02^{+0.27}_{-0.28}$ and Fe Kα line equivalent width of EW $= 2.1^{+1.0}_{-0.8}$ keV (C-stat/d.o.f = 315/331). The flat photon index and large EW measured for the Fe Kα line (EW $\gtrsim 1$ keV), are characteristic signatures for CT absorption.

To test for this, we model both spectra simultaneously from 3–40 keV with the PEXRAV model (Magdziarz & Zdziarski, 1995), which has historically been used to model reflection-dominated AGN spectra. This model produces an AGN continuum which is reflected from a slab-geometry torus with an infinite column density, which is highly unlikely to represent the actual AGN torus. However, it can provide a useful initial test to investigate the AGN spectrum for CT obscuration. Because it does not self-consistently model the fluorescence emission lines expected from a CTAGN, we included a Gaussian component in the model to simulate Fe Kα narrow line emission, which is the most prominent line produced by CTAGNs. The centroid energy and width of the line were fixed to $E = 6.4$ keV and $\sigma = 10$ eV, respectively. Due to the limited number of counts, the inclination of the reflector was fixed to the default value set by the model; i.e., $\theta_{\rm inc} \approx 63°$. However, we note that fixing $\theta_{\rm inc}$ to other values (e.g., near the lower and upper limits of the model; $\theta_{\rm inc} \approx 26°$ and $84°$, respectively) have insignificant effects on the parameters obtained. We also fixed the reflection scaling factor to $R = -1$, to simulate a pure reflection spectrum. In addition, we included the absorbed transmitted component of the AGN, simulating the Compton scattering and photoelectric absorption by the torus using CABS and ZPHABS models, respectively. This model provides a decent fit to the data (C-stat/d.o.f = 318/330), and measured a column density of $N_{\rm H}({\rm los}) = 2.7^{+u}_{-1.2} \times 10^{24}$

cm^{-2}, consistent with CT column.[7] The intrinsic photon index inferred from the best-fit model is $\Gamma = 1.57 \pm 0.35$, in agreement with the typical intrinsic value for an AGN (e.g., Burlon et al., 2011; Corral et al., 2011). The reflection component of the model dominates the transmitted component at all spectral energies probed, indicating that the spectrum is reflection-dominated, consistent with being heavily obscured.

4.3.2 Physical Modeling

We proceeded to model the X-ray broadband spectrum of the potentially heavily obscured AGN in NGC 1448 using more physically motivated obscuration models to better characterise the broadband spectrum. The two models used are the TORUS model by Brightman & Nandra, 2011 (Model T), and MYTORUS model by Murphy & Yaqoob, 2009 (Model M). Details and results of the two models are described in Sections 4.3.2.2 and 4.3.2.3, respectively. In addition to these models, we added extra components required to account for non-AGN contributions to the X-ray spectrum, and to provide a good fit to the data as described below, and in Section 4.3.2.1.

At low energies, typically at $E \lesssim 2$ keV, where the direct emission from a heavily obscured AGN is completely absorbed, other processes can dominate. These processes include X-ray emission radiated by unresolved off-nuclear X-ray sources, thermal emission from a hot interstellar medium, gas photoionized by the AGN, and scattered emission from the AGN. Our data are not of sufficient quality to accurately distinguish between these different physical processes. Therefore, we simply parametrized the low energy part of the spectrum covered by *Chandra* using the thermal model "APEC" (Smith et al., 2001),[8] and a power-law component to simulate the scattered emission from the AGN.

A constant parameter, C is often included when analysing data from multiple X-ray observatories simultaneously to account for the cross-calibration uncertainties between the various instruments, and to account for any significant variability of the

[7] "u" is unconstrained.

[8] We note that the APEC component is mainly contributed by the unresolved emission within the 20″-radius extraction region.

targets between the observations. As detailed earlier, we do not find any significant differences between the *Chandra* and *NuSTAR* spectra, indicating that there has not been significant variability between the two observations. Based on the *NuSTAR* calibration paper (Madsen et al., 2015), the cross-calibration uncertainty of *Chandra* with respect to *NuSTAR* is ≈1.1. We therefore decided to fix this parameter to the value found by Madsen et al. (2015) as a conservative approach. However, we note that allowing this parameter to vary in all models, returns results that are consistent with this value within the statistical uncertainties.

Our two models are described in XSPEC as follows:

$$\text{Model T} = \text{CONSTANT} * \text{PHABS} * (\text{APEC} + \text{CONS} * \text{ZPOW} + 2 \times \text{TBABS} * \text{ZPOW} + \text{TORUS}) \tag{4.3.1}$$

$$\text{Model M} = \text{CONSTANT} * \text{PHABS} * (\text{APEC} + \text{CONS} * \text{ZPOW} + 2 \times \text{TBABS} * \text{ZPOW} + \text{ZPOW} * \text{MYTZ} + \text{MYTS} + \text{MYTL}) \tag{4.3.2}$$

The two additional absorbed power-law components (TBABS∗ZPOW) are included in the models to take into account the two off-nuclear sources detected within the extraction region in the *Chandra* data. We discuss these sources in the following section.

4.3.2.1 Off-nuclear X-ray Sources

In this section, we present the analysis of the two off-nuclear point sources detected in the 0.5–8 keV *Chandra* band within the 20″-radius extraction region (see Figure 4.1). We extracted their spectra using extraction regions of 3″ and 2″ for the NE and NW sources, respectively. Due to limited counts (∼30 counts at 0.5–8 keV for each source), we binned their spectra to a minimum of 5 counts per bin and optimized the fitting parameters using the C-statistic. We model both sources using a simple power-law model absorbed by host galaxy absorption (TBABS), in addition to the

Galactic absorption.

The photon indices and intrinsic absorption columns measured by the fits are $\Gamma = 1.02^{+1.84}_{-1.28}$ and $N_{\rm H}(\rm int) \leq 2.19 \times 10^{22}$ cm^{-2} (C-stat/d.o.f = 8.1/7) for the NE source, and $\Gamma = 2.15^{+2.03}_{-1.30}$ and $N_{\rm H}(\rm int) \leq 2.11 \times 10^{22}$ cm^{-2} (C-stat/d.o.f = 7.4/10) for the NW source. The 0.5–8 keV intrinsic luminosities for both sources, assuming that they are located within NGC 1448, are $2.23^{+1.83}_{-0.85} \times 10^{38}$ erg s^{-1} and $1.56^{+1.77}_{-0.09} \times 10^{38}$ erg s^{-1} for the NE and NW sources, respectively. These luminosities are almost an order of magnitude lower than the threshold luminosity for ultraluminous X-ray sources (ULXs; $L_{\rm X} \gtrsim 10^{39}$ erg s^{-1}).

The best-fitted photon index for the NE source is potentially flat (although with large uncertainties), and may suggest that it is a background obscured AGN. We estimate the probability of finding an AGN within a random 20″-radius region with at least the observed flux of the NW source ($f_{0.5-8} \gtrsim 4 \times 10^{-15}$ erg s^{-1} cm^{-2}) using the AGN number counts of the 4 Ms *Chandra* Deep Field South (CDFS) Survey (Lehmer et al., 2012). Based on this, the probability of finding two or more background AGNs within a 20″-radius circular region is $< 1\%$. In addition, we do not find counterparts to these *Chandra* sources at other wavelengths (e.g., MIR and optical). Given their high Galactic latitudes ($|b| \sim 51°$), it is unlikely that these are Galactic sources. Based on these arguments, we conclude that the two off-nuclear X-ray sources are more likely to be X-ray binaries within NGC 1448. Given the stellar mass and SFR of the galaxy, we would expect to find ∼3 X-ray binaries with $L_{0.5-8} > 10^{38}$ erg s^{-1} in NGC 1448 (Gilfanov, 2004; Mineo et al., 2012). This is consistent with our detections of two potential candidates within the central 20″ circular radius of the galaxy. We therefore included the two absorbed power-law components detailed above into Model T and M to account for their maximum contributions to our X-ray spectra of NGC 1448. We fixed all the parameters at the best-fit values measured from the *Chandra* data.

Due to the *NuSTAR* PSF, sources that lie outside the 20″-radius extraction region could also contaminate our spectrum. We tested whether these sources contribute a significant fraction of our X-ray broadband spectrum by including the best-fit power-law model of the source ∼30″ west of the AGN to our X-ray spectral

modeling of NGC 1448. This source is the brightest in a 50″-radius circular region around the AGN which corresponds to a ∼70% *NuSTAR* ECF. We left the normalization of the source component free to vary, and found that the value is consistent with zero, suggesting that the source does not significantly contaminate our broadband AGN spectrum. We therefore did not include this source, and consequently any of the fainter sources outside the extraction region, in our modeling of the AGN X-ray spectra.

4.3.2.2 Model T

As described in Chapter 3, the TORUS model by Brightman & Nandra (2011) (Model T) simulates obscuration by a spherical torus with variable biconical polar opening angle ($\theta_{\rm tor}$) ranging between 26–84°. The line-of-sight column density, $N_{\rm H}$(los), through the torus, which is equal to the equatorial column density $N_{\rm H}$(eq), is independent of the inclination angle ($\theta_{\rm inc}$), and extends up to 10^{26} cm^{-2}, an order of magnitude higher than that allowed by the MYTORUS model (see Section 4.3.2.3). The model also self-consistently predicts the Compton scattering and fluorescent Fe Kα and Fe Kβ lines, as well as Kα emission from C, O, Ne, Mg, Si, Ar, Ca, Cr, and Ni, which are commonly seen in CTAGNs. The model is available between 0.1 and 320 keV.

In addition to the TORUS model, we included several other model components as described earlier in Section 4.3 and 4.3.2.1 to provide a good fit to the data. Initially, we left both $\theta_{\rm inc}$ and $\theta_{\rm tor}$ free to vary; however, they were both unconstrained. We then fixed the torus inclination angle to the upper limit of the model ($\theta_{\rm inc} = 87°$), to simulate an edge-on inclination torus, and to allow for the full exploration of $\theta_{\rm tor}$ (Brightman et al., 2015). The column density measurement is insensitive to $\theta_{\rm inc}$ when $\theta_{\rm inc} > \theta_{\rm tor}$ (Brightman et al., 2015), and therefore should not significantly affect the $N_{\rm H}$(los) measured. In addition, we fixed the photon index to $\Gamma = 1.9$ as it could not be constrained simultaneously with $\theta_{\rm tor}$.

The model implied a column density of $N_{\rm H}(\rm los) = 4.2^{+u}_{-1.7} \times 10^{24}$ cm^{-2} (C-stat/d.o.f = 431/445). The lower limit of this column density is well above the CT threshold, and therefore this model confirms that the AGN is CT. The best-fit torus

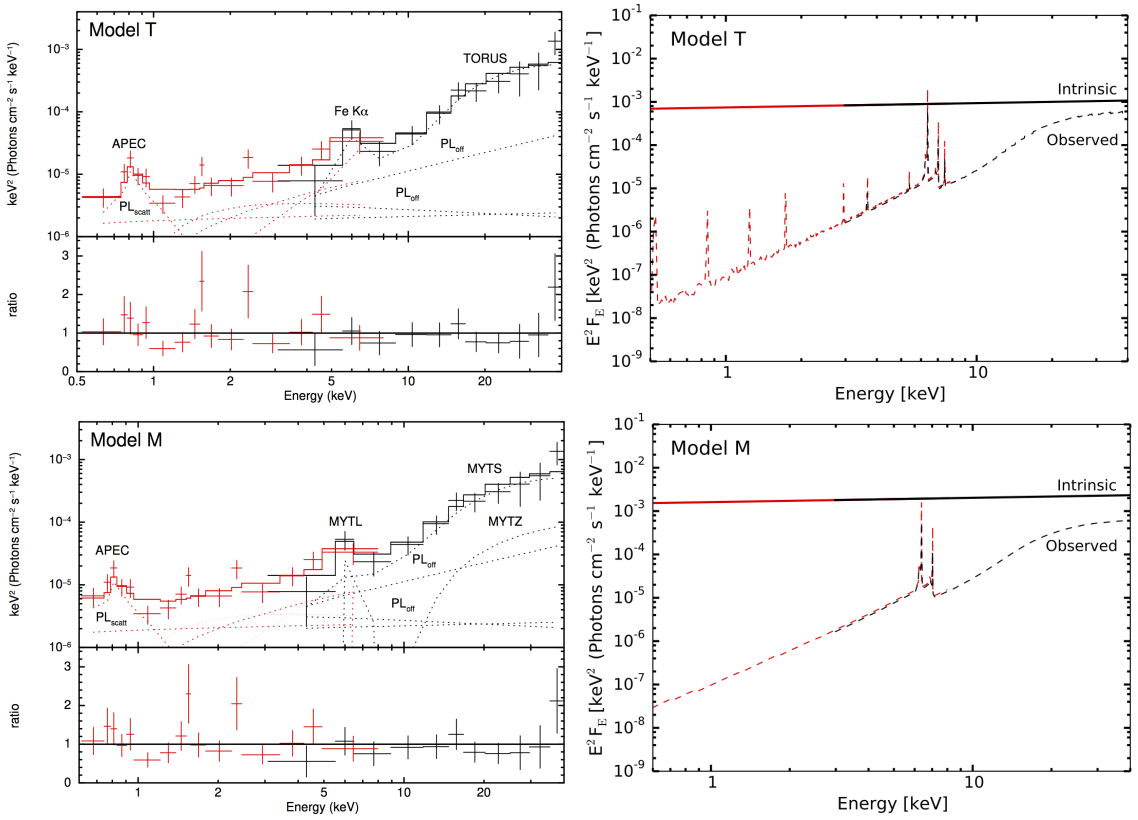

Figure 4.4: Best-fitting models to the combined *NuSTAR* and *Chandra* data of NGC 1448 - Model T (top) and Model M (bottom). Model T was fitted between 0.5 and 40 keV, and Model M was fitted between 0.6 and 40 keV due to the strong residuals found at ∼0.5 keV for this model. The data have been rebinned to a minimum of 3σ significance with a maximum of 25 and 100 bins for *NuSTAR* and *Chandra*, respectively, for visual clarity. Color scheme: black (*NuSTAR* FPMA+B), red (*Chandra*). Plots on the left show the model components fitted to the data (dotted lines), with the total model shown in solid lines. We included an APEC component and a scattered power-law component to model the emission at the softest energies, and two power-law components to model the two off-nuclear sources located within the extraction region in all models. The iron line modelled in Model T is labelled as "Fe Kα", and the direct, scattered and line components of Model M are labelled as MYTZ, MYTS and MYTL, respectively. The top panels of the left plots show the data and unfolded model in E^2F_E units, whilst the bottom panels show the ratio between the data and the folded model. Plots on the right show the observed (dashed lines) and intrinsic spectra (solid line) of the AGN component for each model. The slight offset between the red and black lines are due to the cross-calibration uncertainties between *Chandra* and *NuSTAR* (Madsen et al., 2015). These plots show that even at $E \geq 10$ keV, the spectra that we observed for CTAGNs are still significantly suppressed (up to ∼2 orders of magnitude for the case of NGC 1448), demonstrating the extreme of CT absorption.

Table 4.1: X-ray spectral fitting results for NGC 1448.

Component	Parameter	Units	Model T	Model M
(1)	(2)	(3)	(4)	(5)
APEC	kT	keV	$0.63^{+0.14}_{-0.33}$	$0.63^{+0.14}_{-0.42}$
Absorber/Reflector	$N_{\rm H}$(eq)	10^{24} cm^{-2}	$4.2^{+u}_{-1.7}$	$4.9^{+u}_{-2.0}$
	$N_{\rm H}$(los)	10^{24} cm^{-2}	$4.2^{+u}_{-1.7}$	$4.5^{+u}_{-1.8}$
	$\theta_{\rm inc}$	deg	87^{f}	$78.6^{+6.5}_{-11.8}$
	$\theta_{\rm tor}$	deg	$45.9^{+33.1}_{-18.9}$	60^{f}
AGN Continuum	$f_{\rm scatt}$	%	$0.2^{+0.3}_{-0.2}$	$0.1^{+0.2}_{-0.1}$
	Γ		1.9^{f}	1.9^{f}
	$L_{0.5-2,\rm obs}$	10^{39} erg s^{-1}	0.2	0.2
	$L_{2-10,\rm obs}$	10^{39} erg s^{-1}	0.9	0.9
	$L_{10-40,\rm obs}$	10^{39} erg s^{-1}	11.7	11.8
	$L_{0.5-2,\rm int}$	10^{40} erg s^{-1}	2.6	5.6
	$L_{2-10,\rm int}$	10^{40} erg s^{-1}	3.5	7.6
	$L_{10-40,\rm int}$	10^{40} erg s^{-1}	3.5	7.6
C-stat/d.o.f.			431/445	429/440

Notes. (1) Model component; (2) parameter associated with each component; (3) units of each parameter; (4) best-fitting parameters for Model T (TORUS model by Brightman & Nandra, 2011); (5) best-fitting parameters for Model M (MYTORUS model by Murphy & Yaqoob, 2009). "f" is a fixed parameter and "u" is an unconstrained parameter. Details of each model are described in Section 4.3.

opening angle is $\theta_{\rm tor} = 45.9^{+33.1}_{-18.9}$ degrees, suggesting a geometrically thick torus. The model measured a small scattering fraction of $0.2^{+0.3}_{-0.2}$ % with respect to the intrinsic power-law. This is consistent with that found in other obscured AGN (e.g., Noguchi et al., 2010; Gandhi et al., 2014; Gandhi et al., 2015). However we note that given the modest quality of our data, the scattered power-law component will also include contributions from other processes such as unresolved X-ray binaries. Therefore, the true AGN scattering fraction could be lower than this value. We inferred the intrinsic luminosities of the AGN in three different bands based upon the best-fit parameters obtained, as presented in Table 4.1.

4.3.2.3 Model M

As described in Chapter 3, the MYTorus model by Murphy & Yaqoob (2009) (Model M) simulates a toroidal absorber geometry with a fixed opening angle of $\theta_{\rm tor}$ = 60° and variable inclination angle. The line-of-sight column density, $N_{\rm H}$(los), is derived from the measured inclination angle and equatorial column density, $N_{\rm H}$(eq), which is simulated only up to a column density of $N_{\rm H}$(eq) = 10^{25} cm^{-2}. There is more freedom in exploring complex absorbing geometry in the MYTorus model as it allows the user to disentangle the direct (MYTZ), scattered (MYTS) and line-emission (MYTL) components from each other. The MYTL component simulates the neutral Fe Kα and Fe Kβ fluorescence lines, and the associated Compton shoulders for the AGN. The model is defined between 0.5 and 500 keV. However, we noticed strong residuals at ∼0.5 keV which could be attributed to the fact that we are probing the lower limit of the model. Therefore for this model, we restricted our fit to above 0.6 keV.

For simplicity, we fitted the AGN spectrum by coupling all the parameters of the scattered and fluorescent line components to the direct continuum component. The relative normalizations of MYTS (A_S) and MYTL (A_L) with respect to MYTZ (A_Z) were set to 1. At first, we left the photon index free to vary; however, it reached the lower limit of the model, suggesting that it is not well constrained. Therefore, we fixed the value of this parameter to $\Gamma = 1.9$.

Model M also gives as good a fit to the data as Model T, with C-Stat/d.o.f =

429/440. Using this model, we measured an equatorial column density of $N_{\rm H}({\rm eq}) = 4.9^{+u}_{-2.0} \times 10^{24}$ cm^{-2}. The model measured a high inclination angle of $\theta_{\rm inc} = 78.6^{+6.5}_{-11.8}$ degrees, close to the maximum value fixed in Model T. The corresponding $N_{\rm H}({\rm los})$ value is well within the CT regime, within the uncertainties, $N_{\rm H}({\rm los}) = 4.5^{+u}_{-1.8}$ $\times 10^{24}$ cm^{-2}, and agrees very well with that measured by Model T.[9] This model also measured a small scattering fraction; i.e., $0.1^{+0.2}_{-0.1}$ %, consistent with Model T. As with Model T, we determined the intrinsic luminosity of the AGN in different bands from the best-fitting parameters (see Table 4.1).

4.4 Multiwavelength Results

In this section, we present the results from the optical and MIR observations of NGC 1448 as detailed in Section 4.2.3 and 4.2.4, respectively. We use these data to calculate the properties of the AGN at different wavelengths to compare with the results of our X-ray spectral analysis.

4.4.1 Optical

As described in Section 4.2.3, we extracted optical spectra from three different regions along the slit; i.e, the AGN, optical peak and across the whole galaxy. The extracted spectra, along with the fits obtained from the spectral synthesis modeling (see Section 4.2.3), and the fit residuals, are shown in Figure 4.5. As shown in this figure, no significant residuals were left after fitting the observed spectra with stellar population templates, without the need of additional AGN continuum components. This suggests that the AGN optical continuum is highly obscured. The spectral analysis revealed that the stellar emission from all three regions is due to both young (5 Myr) and old (5 Gyr) stellar populations, dominated by the latter with ∼75–84% contributions measured between the three spectra. Although the optical peak is where the total optical emission is the brightest, the emission lines

[9] The line-of-sight column density for Model M was derived using equation 3.1 of Murphy & Yaqoob (2009), and assuming an inclination angle at the best-fit value.

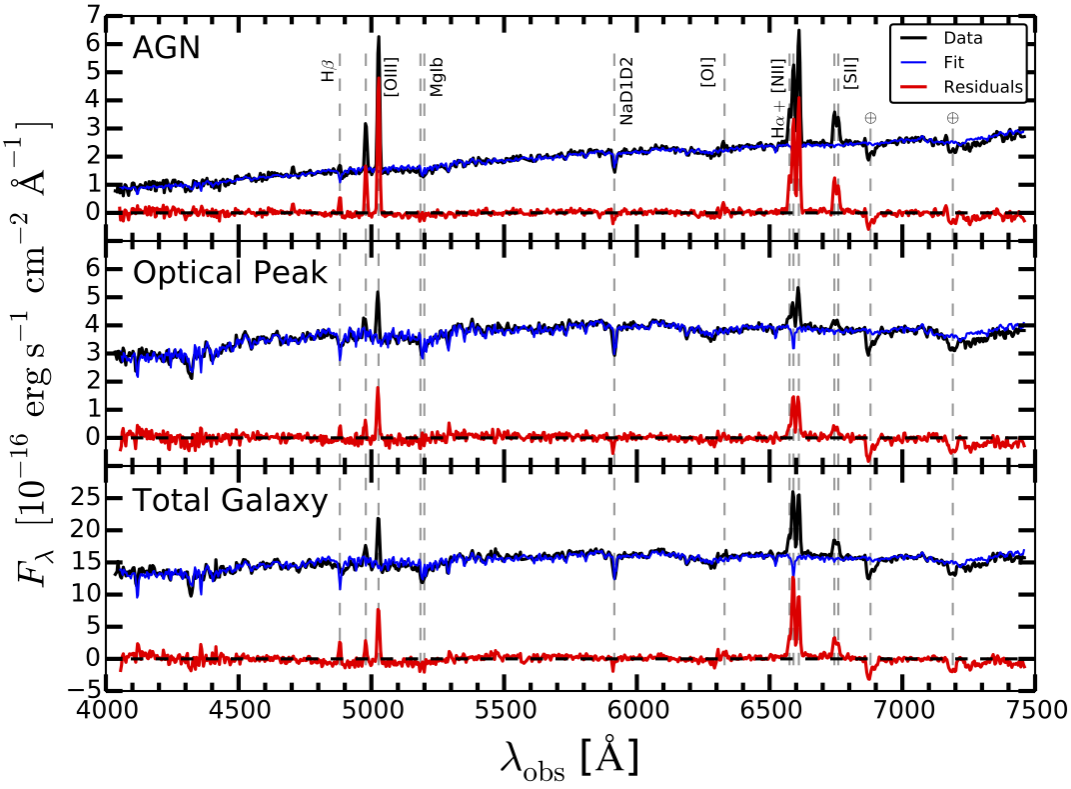

Figure 4.5: The optical spectra for the AGN (top), optical peak (middle) and the whole galaxy (bottom) extracted from the aperture regions shown in Figure 4.2. Black are the observed spectra, blue are the best-fitted stellar template spectra, and red are the residual spectra obtained after subtracting the best-fitted stellar template spectra from the observed spectra. Detected emission and absorption lines are labelled with dotted lines. The absorption lines labelled with ⊕ are Telluric.

Table 4.2: Optical emission line fluxes and ratios for spectra shown in Figure 4.5.

Emission Line	AGN	Optical Peak	Total Galaxy
Hα	3.79 ± 0.08	1.51 ± 0.17	15.2 ± 0.50
Hβ	0.65 ± 0.05	0.40 ± 0.07	3.60 ± 0.32
[OIII]λ4959	1.85 ± 0.05	0.74 ± 0.10	3.51 ± 0.38
[OIII]λ5007 (obs.)	5.38 ± 0.06	2.07 ± 0.09	9.78 ± 0.37
[OIII]λ5007 (int.)	43.7 ± 0.49	16.8 ± 0.73	79.4 ± 3.00
[OI]λ6300	0.38 ± 0.08	< 0.34	2.22 ± 0.60
[NII]λ6549	1.51 ± 0.08	0.58 ± 0.19	3.44 ± 0.55
[NII]λ6583	4.71 ± 0.06	1.73 ± 0.10	11.7 ± 0.39
[SII]λ6717	1.36 ± 0.09	0.40 ± 0.27	3.41 ± 0.87
[SII]λ6731	1.12 ± 0.09	0.57 ± 0.29	3.14 ± 0.93
Line Ratio			
Hα/Hβ	5.83 ± 0.47	3.78 ± 0.79	4.22 ± 0.40
[OIII]λ5007/Hβ	8.28 ± 0.64	5.18 ± 0.93	2.72 ± 0.26
[OI]λ6300/Hα	0.10 ± 0.02	< 0.23	0.15 ± 0.04
[NII]λ6583/Hα	1.24 ± 0.03	1.15 ± 0.15	0.77 ± 0.04
[SII](λ6717+λ6731)/Hα	0.65 ± 0.04	0.64 ± 0.27	0.43 ± 0.08

Notes. The fluxes are given in units of 10^{-15} erg s^{-1} cm^{-2}. The intrinsic [OIII] λ5007 flux was corrected for the Balmer decrement.

are the strongest at the *Chandra* position, providing independent evidence of the AGN location within the galaxy.

The interstellar extinction measured towards the stellar population at the AGN position from the spectral synthesis modeling is much higher than at the optical peak position, $A_V^{\rm AGN} = 2.15^{+0.16}_{-0.06}$ mag and $A_V^{\rm peak} = 0.59^{+0.04}_{-0.05}$ mag, respectively, further suggesting that the optical emission from the AGN is obscured along our line-of-sight. The total extinction measured from the whole galaxy spectra, $A_V^{\rm gal} = 0.73 \pm 0.06$ mag, is $\sim$3$\times$ lower than that measured at the AGN position, demonstrating that the extinction across the galaxy is non-uniform and inhomogeneous.

We measured the emission line fluxes and ratios for the AGN, optical peak and the whole galaxy from the extinction-corrected residual spectra (see Table 4.2). Firstly, we calculated the extinctions toward the AGN narrow line region (NLR) from the Balmer decrements at the three positions. We assumed an intrinsic Balmer decrement of $({\rm H}\alpha/{\rm H}\beta)_{\rm int} = 2.86$, which corresponds to a temperature of $T = 10^4$ K and an electron density $n_e = 10^2$ cm^{-3} for Case B recombination (Osterbrock, 1989). Based on these, we found $A_V^{\rm AGN}$ =1.89 $\pm$ 0.03 mag, $A_V^{\rm peak} = 0.74 \pm 0.09$ mag, and $A_V^{\rm gal} = 1.03 \pm 0.04$ mag. The high extinction measured at the AGN position provides strong evidence that the AGN is heavily obscured at optical wavelength by the host galaxy.

Using the emission line ratios tabulated in Table 4.2, we constructed the Baldwin-Philips-Terlevich (BPT) diagnostic diagrams (Baldwin et al., 1981) for NGC 1448. This is shown in Figure 4.6. Based on these diagrams, all three spectra fall within the region of Seyfert galaxies, with the AGN having slightly higher emission line ratios. These results provide the first identification of the AGN in NGC 1448 at optical wavelengths, and also confirm the position of the AGN in the galaxy. The total galaxy spectrum is located close to the HII/low ionization emission line regions (LINERs) of the BPT diagrams. This might explain why the AGN was misidentified as an HII region in Veron-Cetty & Veron (1986); i.e., due to host galaxy contaminations as a result of the larger slit size used to extract the spectrum.

The separation between the AGN and the optical peak, $\sim$225 pc, is consistent with the NLR scale observed in AGNs with comparable luminosities as NGC 1448

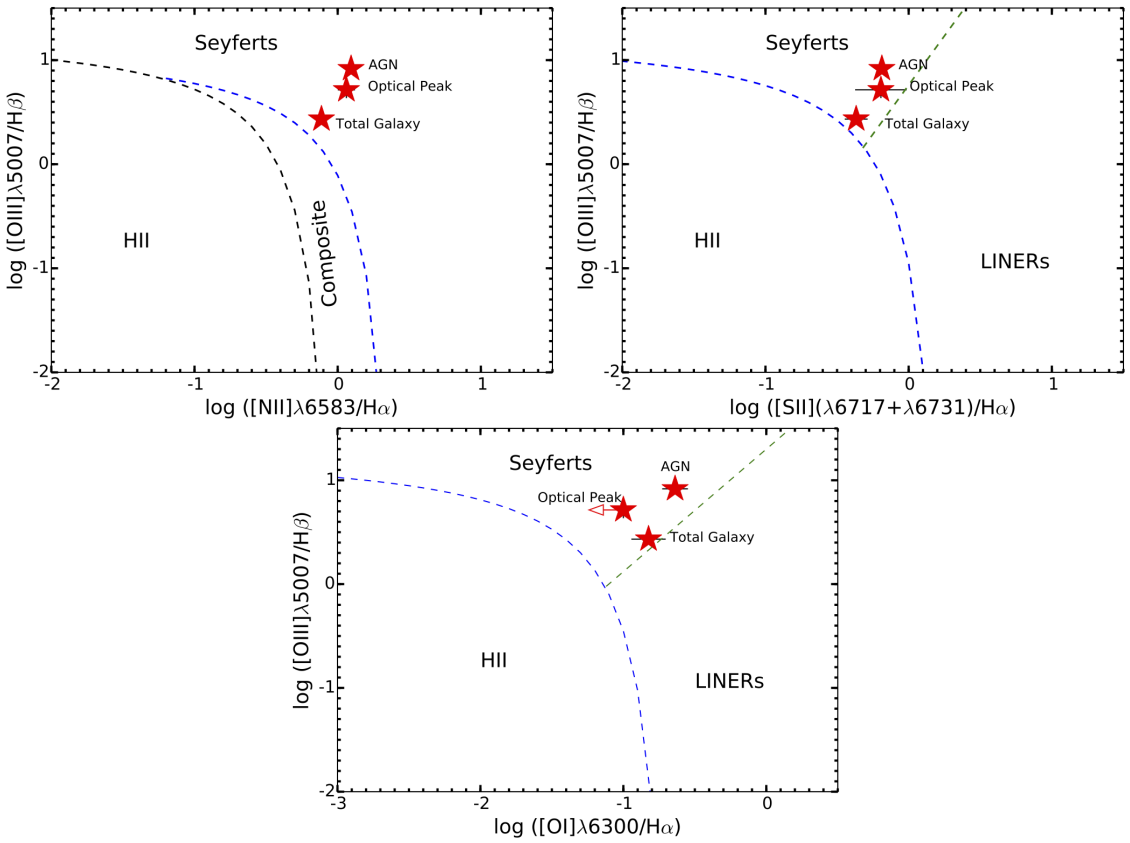

Figure 4.6: The location of the AGN, optical peak and the total galaxy in the BPT diagnostic diagrams. The blue dashed lines indicate the maximum limit for the ionization of gas by a starburst found by Kewley et al. (2001), black dashed lines are the empirical division between HII regions and AGNs proposed by Kauffmann et al. (2003), and the green dashed lines are the division between LINERs and Seyfert galaxies, proposed by Kewley et al. (2006). All three regions from our narrow slit spectroscopy show evidence for an AGN in NGC 1448.

(Bennert et al., 2006). The apparent separation observed between the two can be attributed to the presence of a dust lane which obscures part of the system along our line-of-sight.

The intrinsic [OIII]λ5007Å flux of the AGN corrected for the Balmer decrement is about an order of magnitude higher than the observed luminosity (see Table 4.2). The [OIII] line emission in AGN is mostly produced in the NLR due to photoionization from the central source. Since this region extends beyond the torus, it does not suffer from nuclear obscuration like the X-ray emission. However as we demonstrated earlier, it can suffer from significant optical extinction from the host galaxy. Indeed, in extreme cases, the host galaxy obscuration can be so high that the optical Balmer decrement only provides a lower limit on the extinction (Goulding & Alexander, 2009).

Using our intrinsic [OIII] luminosity measured for the AGN, $L_{[OIII]} = (6.89 \pm 0.08) \times 10^{38}$ erg s^{-1}, we proceeded to compare the intrinsic X-ray luminosity determined from our X-ray spectral fitting with that predicted from the X-ray:[OIII] intrinsic luminosity relationship of Panessa et al. (2006). Based on this correlation, we infer an intrinsic X-ray luminosity of $L_{2-10,\mathrm{int}} = (0.2\text{–}4.5) \times 10^{40}$ erg s^{-1} (see footnote 10). This is consistent with that determined from our X-ray spectral fittings, providing confidence that our analysis is reliable.

4.4.2 Mid-Infrared

The high spatial resolution MIR observation by Gemini/T-ReCS measured a 12μm luminosity of $\lambda L_{12\mu\mathrm{m}} = (4.90 \pm 0.93) \times 10^{40}$ erg s^{-1} for NGC 1448 (see Section 4.2.4). MIR luminosity is predicted to provide an accurate estimate for the intrinsic luminosity of the AGN. This is because the absorbed X-ray radiation from the central engine is mostly re-emitted in the MIR by the torus. To further test the absorption-corrected X-ray luminosity measured from our spectral analysis, we also compared the luminosity measured from our analysis with that predicted from the X-ray:MIR correlation constructed based upon high angular resolution MIR observations of

[10] The given luminosity range accounts for the mean scatter of the correlation.

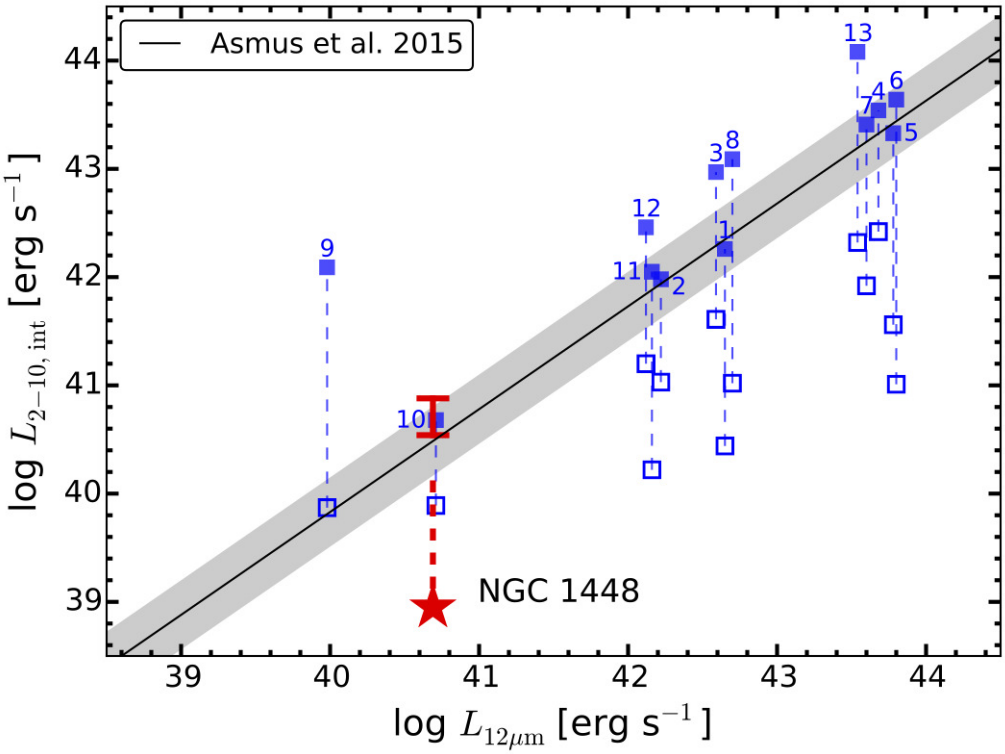

Figure 4.7: The 2–10 keV vs. 12μm luminosity plot of NGC 1448. The observed 2–10 keV luminosity is plotted using the red star, and the red solid line marks the range of the intrinsic luminosity measured from our X-ray spectral analysis. The black solid line is the 2–10 keV vs. 12μm luminosity relationship of AGN from Asmus et al. (2015). The shaded region indicates the intrinsic scatter of the relation. The plot shows that our measured intrinsic 2–10 keV luminosity agrees very well with the Asmus et al. (2015) correlation, providing evidence that our spectral analysis reliably characterises the intrinsic power of the AGN. The observed and intrinsic luminosity of the Gandhi et al. (2014) local bona-fide CTAGNs with high spatial resolution 12μm available from Asmus et al. (2014), are shown in open and filled blue squares, respectively.[9] As can be seen from this plot, NGC 1448 is consistent with the other bona-fide CTAGNs with a typical observed 2–10 keV luminosities that are ∼2 orders of magnitude lower than the Asmus et al. (2015) relation. However, when corrected for absorption, their luminosities are more in agreement with the correlation, with the exception for NGC 4945, which is known to be overluminous in X-rays. The local CTAGNs plotted in the figure are as follows, with the reference for X-ray data given in parentheses if they were not obtained from Asmus et al. (2015): 1) Circinus; 2) ESO5-G4 (Ueda et al., 2007); 3) ESO138-G1; 4) Mrk 3; 5) NGC424; 6) NGC 1068; 7) NGC 3281; 8) NGC 3393; 9) NGC 4945; 10) NGC 5194 (Terashima et al., 1998; Goulding et al., 2012); 11) NGC 5643 (Annuar et al., 2015); 12) NGC 5728; 13) NGC 6240.

local Seyferts, which has been shown to trace the intrinsic X-ray luminosity of AGN very well (e.g., Horst et al., 2008; Gandhi et al., 2009; Asmus et al., 2015). The correlation with respect to the recent Asmus et al. (2015) relation is shown in Figure 4.7. The figure shows that the observed 2–10 keV luminosity of the AGN in NGC 1448 is about two orders of magnitude lower than this relation, similar to other local bona-fide CTAGNs (Gandhi et al., 2014), indicating extreme obscuration.[11] However, after correcting for absorption measured from our X-ray spectral modeling, the luminosity agrees very well with the intrinsic relationship of Asmus et al. (2015), further supporting our analysis.

4.5 Discussion

In this chapter, we presented a multiwavelength view of the AGN in NGC 1448 across three wavebands; i.e., the MIR continuum, optical and X-rays. Our new data provide the first identifications of the AGN at these wavelengths. Combining our *NuSTAR* data with an archival *Chandra* observation, we performed broadband X-ray spectral analysis (≈0.5–40 keV) of the AGN.

We fitted the spectra with two different obscuration models, the TORUS and MYTORUS models (Section 4.3.2.2 and 4.3.2.3, respectively), which fitted the spectra equally well and gave results that are consistent with each other. Considering both models, we found that the AGN is buried under a CT column of obscuring gas, with a column density of $N_{\rm H}(\rm los) \gtrsim 2.5 \times 10^{24}$ cm^{-2}. Despite the uncertainties in the parameters and the different geometries simulated by the two models, as well as the phenomenological model simulated by the PEXRAV model discussed in Section 4.3.1, a Compton-thick solution is required to get a best-fit to the data in all cases. The 2–10 keV intrinsic luminosity measured from the two physical models range between $L_{2-10,\rm int} = (3.5\text{–}7.6) \times 10^{40}$ erg s^{-1}, making NGC 1448 one of the lowest luminosity bona-fide CTAGNs in the local universe, comparable to NGC 5194 (Terashima et al.,

[11] We note that the bona-fide CTAGN sample (Gandhi et al., 2014) plotted in Figure 4.7, 4.8 and 4.9 was updated to include a new local bona-fide CTAGN, NGC 5643 (Annuar et al., 2015), and exclude NGC 7582 which has been shown to have variable $N_{\rm H}$ (Rivers et al., 2015).

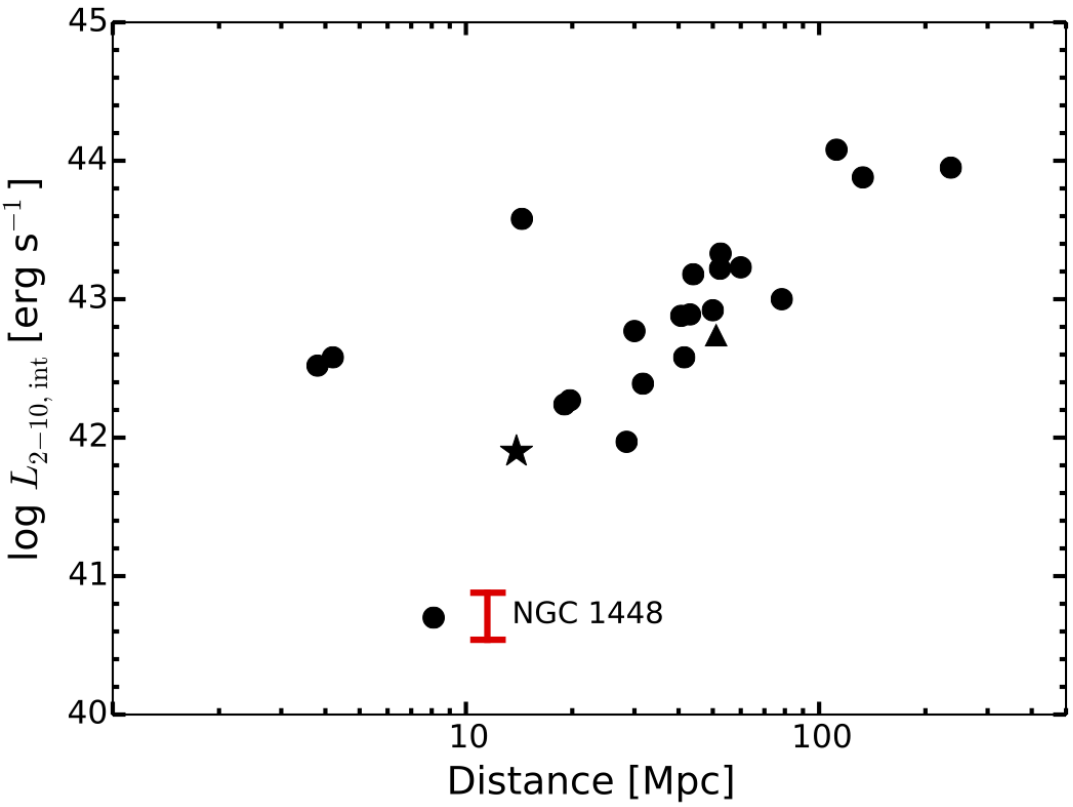

Figure 4.8: The plot of intrinsic 2–10 keV luminosity vs. distance of local bona-fide CTAGN (black circles) updated from Gandhi et al. (2014) to include NGC 5643 (black star; Annuar et al., 2015) and NGC 1448.[9] Black triangle indicates NGC 4939 which has the lower limit to its 2–10 keV luminosity plotted. The range of intrinsic luminosity of NGC 1448 is plotted in red.

1998; see Figure 4.8). The measured column density is so extreme that even at $E >$ 10 keV, the observed spectrum is still significantly suppressed (up to ∼two orders of magnitude lower than the intrinsic spectrum; see Figure 4.4). This demonstrates why it is very challenging to identify CTAGNs, even at hard X-ray energies, and at this distance. The predicted 14–195 keV flux of the AGN, $f_{14-195} \sim 10^{-12}$ erg s^{-1} cm^{-2}, is an order of magnitude lower than the deepest flux level reached by the *Swift*-BAT all sky survey ($f_{14-195} \sim 10^{-11}$ erg s^{-1} cm^{-2}; Baumgartner et al., 2013), demonstrating that pointed observations with *NuSTAR* have better sensitivity in finding faint CTAGN.

We used our measured 2–10 keV intrinsic X-ray luminosities to estimate the Eddington ratio of NGC 1448. Goulding et al. (2010) made an estimation of the supermassive black hole mass ($M_{\rm BH}$) using the $M_{\rm BH}$ to bulge K-band luminosity relation by Marconi & Hunt (2003), and inferred log $(M_{\rm BH}/M_{\odot}) = 6.0^{+0.1}_{-0.5}$. Based on this black hole mass, we found that the AGN is accreting matter at ∼0.6–1.2% of the Eddington rate.[12,13]

Some studies have suggested that the AGN torus is not developed at low luminosity, $L_{\rm bol} \lesssim 10^{42}$ erg s^{-1}, and/or at low mass accretion rate, $\lambda_{\rm Edd} \lesssim 2 \times 10^{-4}$ (e.g., Elitzur & Shlosman, 2006; Hönig & Beckert, 2007; Kawamuro et al., 2016). The identification of NGC 1448 as a low luminosity CTAGN (as demonstrated from the X-ray spectral fitting and mid-IR analysis) with a bolometric luminosity potentially below the quoted limit, $L_{\rm bol} \sim (0.7–1.5) \times 10^{42}$ erg s^{-1} however, does not provide clear evidence for the disappearance of the torus at the low AGN luminosities proposed by some studies.

The CTAGN in NGC 1448 is hosted by a nearly edge-on spiral galaxy, which could contribute to at least some of the X-ray obscuration we observed. Our X-ray data are not of sufficient quality to allow us to investigate the origin of the CT obscuration in NGC 1448 in detail. However, our optical spectral synthesis modeling

[12] We assumed an AGN bolometric correction of $L_{\rm bol}/L_{2-10} = 20$ (e.g., Vasudevan et al., 2010)

[13] The calculation for the Eddington ratio involves highly uncertain quantities, therefore the inferred value is subjected to errors of a factor of a few (Brandt & Alexander, 2015).

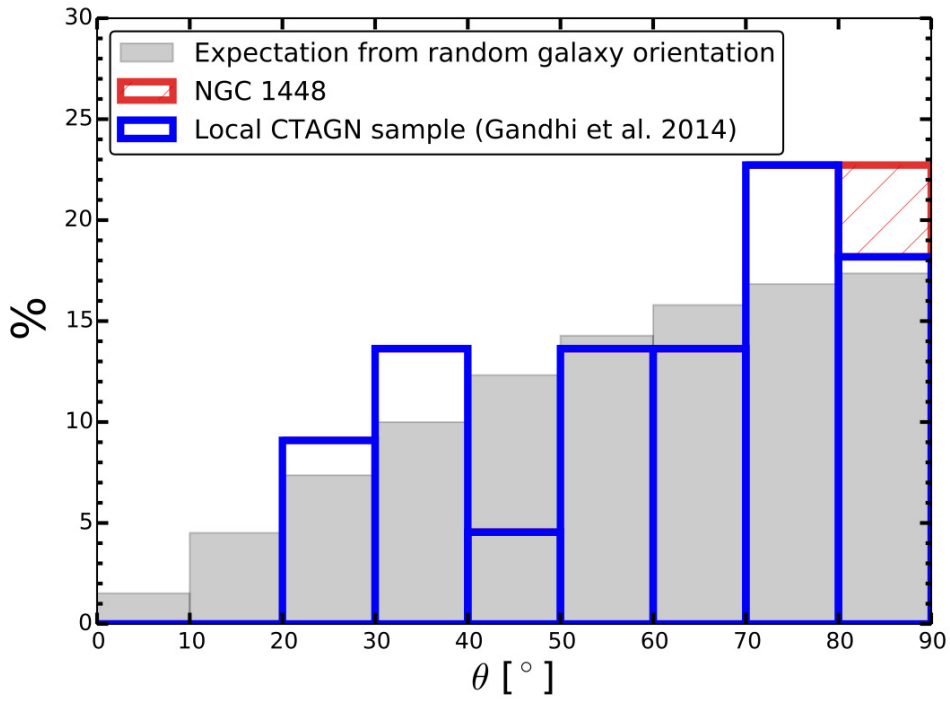

Figure 4.9: Distribution of host galaxy inclination angles (θ) for the Gandhi et al. (2014) local CTAGN sample (where available) plotted in blue.[9] NGC 1448 is plotted in hatched red. The shaded region shows the expected distribution from random galaxy orientation. The total distribution of the local CTAGNs is consistent with the expected random distribution, suggesting that the current sample of local CTAGNs are independent of host galaxy inclinations.

suggests an extinction of $A_V = 2.15$ towards the AGN along our line-of-sight, which translates into a column density of $N_{\rm H}(\rm los) = 4.8 \times 10^{21}$ cm^{-2}, assuming the gas to dust ratio of the Milky Way (Güver & Özel, 2009). This suggests that the CT column density we measured from the X-ray spectral fittings is not due to the host galaxy material, but is due to the AGN circumnuclear material itself.

High host galaxy inclinations along our line-of-sight can also affect AGN selection in the local universe as demonstrated by, e.g., Goulding & Alexander (2009). Material in the host galaxies of highly inclined systems can severely suppress optical emission from AGNs, causing them to be misidentified at optical wavelengths. Figure 4.9 shows the distribution of host galaxy inclinations for local CTAGNs (adapted from Gandhi et al., 2014),[9] as compared to the expected distribution from random

galaxy orientations. If we are missing CTAGNs in the local universe due to AGN host inclination selection effects, we might expect the local CTAGN sample to be lacking at high host inclinations. However, Figure 4.9 suggests that this is not the case. Performing a Kolmogorov–Smirnov (KS) test between the two distributions inferred a KS test probability of $P_{\rm KS} \sim 0.4$. This indicates that the two distributions are not significantly different from each other, and suggests that the current sample of local CTAGNs is not affected by host galaxy inclinations (see also Koss et al., 2016). Therefore, although the census of CTAGN is incomplete, even in the local universe (at $D \approx 200$ Mpc), we do not find strong evidence that the incompleteness is due to host galaxy inclination.

4.6 Summary

In this chapter, we have presented a multiwavelength view of the AGN in NGC 1448 across MIR continuum, optical, and X-rays. Our data provide the first identifications of the AGN at these wavelengths. The main results can be summarised as follows:

1. A broadband (≈0.5–40 keV) X-ray spectral analysis of the AGN using data from *NuSTAR* and *Chandra* observations reveals that our direct view towards the AGN is hindered by a CT column of obscuring material, with a column density of $N_{\rm H}({\rm los}) \gtrsim 2.5 \times 10^{24}$ cm^{-2}. The range of 2–10 keV intrinsic luminosity measured between the best-fitting torus models is $L_{2-10,{\rm int}} = (3.5–7.6) \times 10^{40}$ erg s^{-1}, consistent with that predicted from our optical and MIR data. These results indicate that NGC 1448 is one of the lowest luminosity CTAGNs known. The identification of NGC 1448 as a faint CTAGN also demonstrates the depth to which we can find CTAGN with *NuSTAR* as compared to *Swift*-BAT.

2. Optical spectroscopy performed using ESO NTT re-classifed the nuclear spectrum as a Seyfert galaxy based on BPT emission line diagnostics, thus identifying the AGN at optical wavelenghts for the first time.

3. MIR imaging conducted by Gemini/T-ReCS detected a compact nucleus, pro-

viding the first identification of the AGN at MIR continuum, further confirming the presence of an AGN in the galaxy.

4. Comparing the host galaxy inclination distribution of local CTAGNs with that expected from random galaxy orientations, we do not find any evidence that the incompleteness of the current CTAGN census is due to host galaxy inclination effects.

Chapter 5

Towards A Complete Census of the Compton-thick AGN Population and the $N_{\rm H}$ Distribution of AGN in the Local Universe

In this chapter, I present an updated census of the Compton-thick (CT) active galactic nucleus (AGN) population and the column density ($N_{\rm H}$) distribution of AGN in the local universe using a volume-limited AGN sample complete to D = 15 Mpc. We used X-ray spectroscopy with data from multiple observatories, including high energy X-ray data from *NuSTAR*, as well as multiwavelength data to further assist the identifications of CTAGN in our sample. Based on direct $N_{\rm H}$ measurements made from X-ray spectroscopy, we found that 30^{+23}_{-14}% of the AGN in our sample are CT. Indirect multiwavelength techniques used to identify potential CTAGN in the sample, such as $f_{2-10,\rm obs}$:$f_{\rm [OIII]\lambda5007A}$, $L_{2-10,\rm obs}$:$L_{12\mu\rm m}$, and $L_{2-10,\rm obs}$:$L_{\rm [Nev]\lambda14.32\mu m}$ ratios, found two strong candidates, increasing the CTAGN fraction to 40^{+25}_{-17}%. However, this fraction can be as high as ≈60%, accounting for sources that lack data. The CTAGN fraction that we found for the sample is significantly higher than that directly observed in the *Swift*-BAT AGN survey, but agrees very well with

the intrinsic CTAGN fraction predicted, after accounting for instrument sensitivity. Using our sample, we are able to identify intrinsically lower luminosity CTAGNs that are missed by the *Swift*-BAT survey, down to $L_{2-10,\mathrm{int}} \sim 10^{40}$ erg s^{-1}, about an order of magnitude lower than that probed by the *Swift*-BAT survey at these distances. Given the unique luminosity space probed by our sample as compared to the *Swift*-BAT AGN sample (i.e., lower luminosity), we investigate whether there are any significant differences between the two samples in terms of the general AGN and host galaxy properties. We found that the two samples have consistent star formation rates; however, our sample shows a much diverse optical nuclear spectral type; dominates at lower black hole mass and galaxy stellar mass; and has a broader range of AGN Eddington ratio, extending down to a lower Eddington ratio than the *Swift*-BAT sample.

5.1 Introduction

Many studies have shown that obscured active galactic nucleus (AGN) dominates the accretion energy budget of the cosmos. Yet, our understanding of the AGN distribution as a function of N_{H} remains highly uncertain, even in the nearby universe, particularly at Compton-thick (CT) column densities; i.e., $N_{\mathrm{H}} \gtrsim 1.5 \times 10^{24}$ cm^{-2} (see Chapter 1). These CTAGNs are very difficult to identify due to their weak X-ray fluxes as a result of the extreme level of obscuration. In most cases, high X-ray energy telescopes ($E > 10$ keV) are required to detect the direct emission from the nuclear source that is able to penetrate through the obscuring gas and dust. To date, only ∼20 AGNs within ≈ 200 Mpc have been confirmed as CT based upon detailed X-ray spectral characterisation (Della Ceca et al., 2008; Goulding et al., 2012; Gandhi et al., 2014; Boorman et al., 2016). This corresponds to a fraction of $\ll 1\%$ of the *total* AGN population expected within that volume, suggesting that the vast majority of CTAGN are yet to be found even in the local universe. Forming an accurate local benchmark of their population is important for extrapolating the results to higher redshifts, where it is even more challenging to identify them.

NuSTAR is an ideal instrument to identify CTAGN due to its high X-ray en-

ergy coverage as well as the better sensitivity and angular resolution it provides as compared to previous high energy X-ray observatories (see Chapter 2). Nine (out of twenty) AGNs in our sample have been observed (or scheduled to be observed) by *NuSTAR* (see Chapter 2). As part of our program to form the most complete census of the CTAGN population and the column density distribution of AGN in the local universe, we observed a further 5 AGNs in the sample with *NuSTAR*, namely, NGC 660, 1448, 3486, 5195 and 5643. These targets were chosen as they were either suggested to be CT from previous studies or multiwavelength data, and were predicted to be detected by *NuSTAR* if they are indeed CT (except for NGC 5195 which was observed as part of the M51 system; see Section 5.2.3). The results for the first two targets that we observed; i.e., NGC 1448 and 5643, were presented in Chapter 3 (Annuar et al., 2015) and 4 (Annuar et al., 2017), respectively, in which we confirmed that these AGNs are indeed CT.

In this chapter, we present the *NuSTAR* observations for the three remaining objects, NGC 660, 3486 and 5195, as well as unpublished archival and new low X-ray energy data for ESO 121-G6 and NGC 1792, respectively (Section 5.2-5.3). In addition, we also re-analyse the archival X-ray data for 5 AGNs in our sample which have been published in previous literature for consistency with our analysis techniques (Appendix A.1). The X-ray observations for the remaining 8 AGNs are not presented in this work due to the complexities of their data, which have been presented in great detail in previous works. In Section 5.4, we detail the multiwavelength diagnostics to select CTAGN candidates in the sample, followed by the overall results of our analyses in Section 5.5. We discuss the AGN and host galaxy properties of our sample in Section 5.6, and provide a summary of our results in Section 5.7.

5.2 X-ray Observations

In this section, we detail our *NuSTAR* observations of NGC 660, NGC 3486 and NGC 5195 (Section 5.2.1, 5.2.2 and 5.2.3, respectively). In addition, we also present the unpublished archival *XMM-Newton* data for ESO 121-G6 in Section 5.2.4, and

our new *Chandra* observation of NGC 1792 in Section 5.2.5 (see Chapter 2 for further details on these observatories).

We processed the *NuSTAR* data for our sources with the *NuSTAR* Data Analysis Software (NUSTARDAS) v1.4.1 within HEASOFT v6.15.1 with CALDB v20150316. The NUPIPELINE v0.4.3 script were used to produce the calibrated and cleaned event files using standard filter flags. We extracted the spectra and response files from each FPM using the NUPRODUCTS v0.2.5 task (see Chapter 2 for more details).

In addition to *NuSTAR*, we also used new and archival low energy X-ray observations from *Chandra* and *XMM-Newton* to facilitate our X-ray spectral analysis of the AGNs at low energies ($E \lesssim 3$ keV), which is beyond the *NuSTAR* sensitivity. The higher spatial resolution imaging capability provided by *Chandra*, is crucial in helping us to reliably account for contaminating emission from off-nuclear X-ray sources to the *NuSTAR* spectrum.

The *Chandra* data were reprocessed to create event files with updated calibration modifications using the CIAO v4.6 pipeline, following standard procedures. We then used the DMCOPY task to produce X-ray images of each sources at different energy bands, and extracted the source spectra using the SPECEXTRACT in CIAO (see Chapter 2). For *XMM-Newton* data, we analysed the Pipeline Processing System (PPS) data products using the Science Analysis Software (SAS v13.5.0; see Chapter 2).

5.2.1 NGC 660

NGC 660, located at a distance of 12.3 Mpc, is classified as a rare polar ring galaxy with a LINER-type (low ionization nuclear emission-line region) nuclear spectrum in the optical. In 2015, a high resolution radio observation by e-MERLIN detected a radio outburst at the centre of the galaxy which revealed a compact and extremely bright continuum source (Argo et al., 2015). This source, which was not detected in previous radio observations, is probably associated with a newly awoken AGN in the galaxy (Argo et al., 2015).

The galaxy has been observed multiple times in X-ray at low energies by *Chandra* and *XMM-Newton* between 2001 and 2012. We first looked at two of the archival

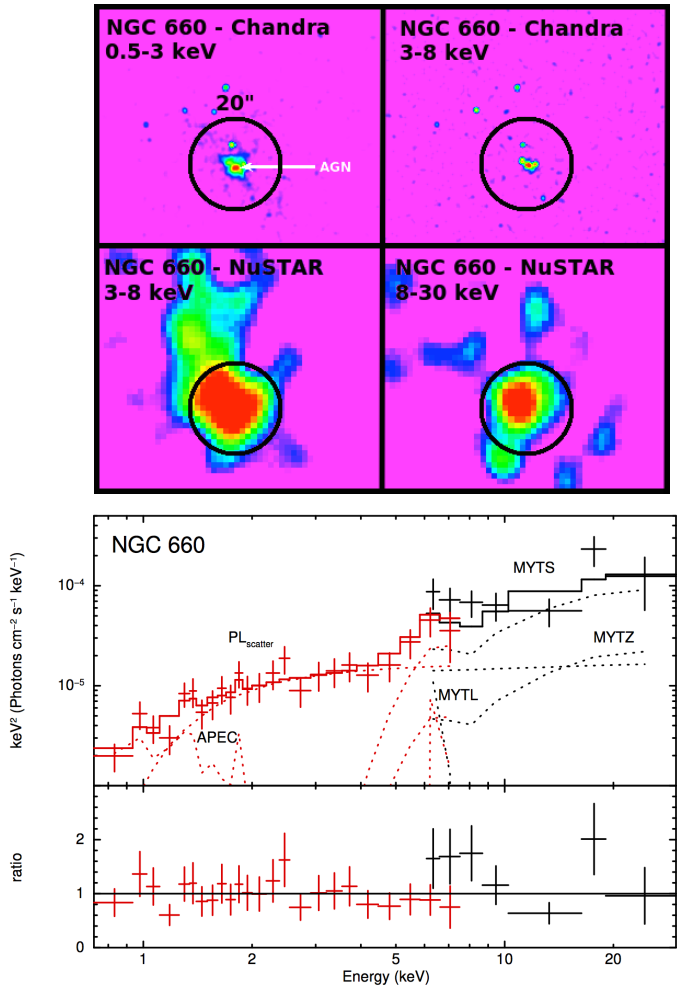

Figure 5.1: *Top*: *Chandra* images of NGC 660 in the 0.5–3 keV and 3–8 keV bands (top panel) and *NuSTAR* FPMA+B images in the 3–8 keV and 8–30 keV bands (bottom panel). The black circle marks a 20″-radius region centred on the radio position of the AGN (Argo et al., 2015) that was used to extract the *NuSTAR* spectra. The *Chandra* spectrum was extracted using a smaller circular region of 1.5″ in radius to minimise significant contamination from off-nuclear emission. Images are smoothed with a Gaussian function of radius 3 and 5 pixels for the *Chandra* and *NuSTAR* data, respectively, corresponding to 1.5″ and 12.3″, respectively. North is up and east is to the left in all images. *Bottom*: Best-fitting model to the combined *NuSTAR* (black) and *Chandra* (red) data of NGC 660. The data have been rebinned to a minimum of 3σ significance with a maximum of 500 bins for visual clarity. Colour scheme: black (*NuSTAR* FPMA+B), red (*Chandra*). The top panel shows the data and unfolded model in E^2F_E units, whilst the bottom panel shows the ratio between the data and the folded model. The spectra were fitted using the MYTORUS model to simulate the obscuring torus (Murphy & Yaqoob, 2009), an APEC component as well as a scattered power-law component to model the emission at the softest energies. The direct, scattered and line components of Model M are labelled as MYTZ, MYTS and MYTL, respectively. The model components fitted to the data are shown as dotted curves, and the total model are shown as solid curves.

Chandra data of the source with sufficiently long exposure times ($t_{\rm exp} \geq 10$ ks), conducted in 2012 November (ObsID 15333; exposure time, $t_{\rm exp} = 23.1$ ks) and 2012 December (ObsID 15587; exposure time, $t_{\rm exp} = 28.1$ ks). The *Chandra* data revealed diffuse emission at the centre of the galaxy, which peaks at the position of the radio source; i.e., the AGN (RA = 01:43:02.32 and Dec = 13:38:44.90; Argo et al., 2015). The diffuse X-ray emission heavily contaminated the AGN emission up to ~ 6 keV. Although radio observations indicate that there is a significant variability over the recent years at this wavelength, we found that there are no significant spectral or flux variabilities between the two X-ray observations conducted by *Chandra*.

Comparing the X-ray flux of the source with the radio and other multiwavelength data (see Section 5.4), we found that the AGN in NGC 660 is likely to be CT. Therefore, we observed the source at hard X-ray energies with *NuSTAR* in 2015 for 56.0 ks (2015-08-23; ObsID 60101102002). We also coordinated our *NuSTAR* observation with a short *Chandra* observation to further check potential variability of the nuclear source at X-ray wavelengths (ObsID 18352; $t_{\rm exp} = 10.1$ ks).

We reduced our new *Chandra* data of NGC 660, and compared it to the two archival *Chandra* observations. We found that there is no significant variability between the three *Chandra* observations at $E = 0.5$–8 keV, and therefore combined the event files for the observations together using XSELECT ($t_{\rm exp,tot} = 60.5$ ks). We produced the resultant *Chandra* images of the source at 0.5–3 keV and 3–8 keV using DMCOPY, and show them in Figure 5.1. We extracted the total spectrum of the AGN from a small circular region of $1.5''$-radius centred on the radio position, to exclude as much contamination as possible from the complex non-AGN emission. A $20''$-radius circular aperture was used to extract the background counts from an offset, source-free region. The total count rate measured from the combined *Chandra* data in the 0.5–8 keV band is 4.05×10^{-3} counts s^{-1}.

The AGN is detected in both of the *NuSTAR* FPMs. The combined images of the AGN from the two FPMs in the 3–8 and 8–24 keV bands are shown in Figure 5.1. We extracted the *NuSTAR* spectrum of NGC 660 from each FPM using a circular aperture of $20''$-radius (corresponding to $\sim$30% of the *NuSTAR* encircled energy fraction) centred on the radio position of the AGN. The aperture size was

chosen to minimise contamination from off-nuclear sources observed in the *Chandra* data. The background photons were collected from an annular segment centred on the AGN with inner and outer radii of 50″ and 100″, respectively. We detected significant counts up to ∼30 keV from the combined FPM spectrum, and measured a net count rate of 1.45×10^{-3} counts s^{-1} in the 3–30 keV band. However because the *Chandra* data revealed that the nuclear source is heavily contaminated at up to ∼6 keV, we only used the *NuSTAR* data above this energy for our analysis. The *NuSTAR* count rate of the AGN in the 6–30 keV band is 9.49×10^{-4} counts s^{-1}. The X-ray spectral analysis of NGC 660 is presented in Section 5.3.1.

5.2.2 NGC 3486

NGC 3486 is a face-on galaxy located at a distance of 9.2 Mpc and has an optical nuclear spectrum which identifies it as a Seyfert 2 (Ho et al., 1997). The object has previously been observed in X-rays by *Chandra* (ObsID 393; 1999-11-03; $t_{\rm exp}$ = 1.8 ks) and *XMM-Newton* (ObsID 0112550101; 2001-05-09; $t_{\rm exp}$ = 15.2 ks). While a source associated with the optical nuclear position of the galaxy is detected in the *XMM-Newton* data, along with an ultraluminous X-ray source (ULX) at ∼23″ from the nucleus (Foschini et al., 2002), nothing was detected in the short *Chandra* observations (Ho et al., 2001). NGC 3486 is one of the galaxies in GA09 which lacks high-resolution *Spitzer*-IRS spectroscopic data, and therefore no [NeV] flux measurement was made. However, an [OIV] emission line is clearly detected in the low-resolution *Spitzer*-IRS spectroscopy and the optical spectrum indicates that NGC 3486 hosts an AGN. The central part of the galaxy has been observed at high spatial resolution at $12\mu m$, however the AGN was not detected (Asmus et al., 2014).

Previous works have performed X-ray spectral analysis on the *XMM-Newton* data of NGC 3486 and found some evidence for it to be CT; e.g., relatively flat power-law photon index at 2–10 keV (Brightman & Nandra, 2008; Cappi et al., 2006). As a follow up observation of these studies, we observed the source at hard X-ray energies with *NuSTAR* on 2015-01-26 for $t_{\rm exp}$ = 28.9 ks (ObsID 60001150002), coordinated with a short *Swift X-ray Telescope* (XRT; Burrows et al., 2005) observation to facilitate our X-ray analysis at low energies (ObsID 00080813001; $t_{\rm exp} \sim$ 5 ks).

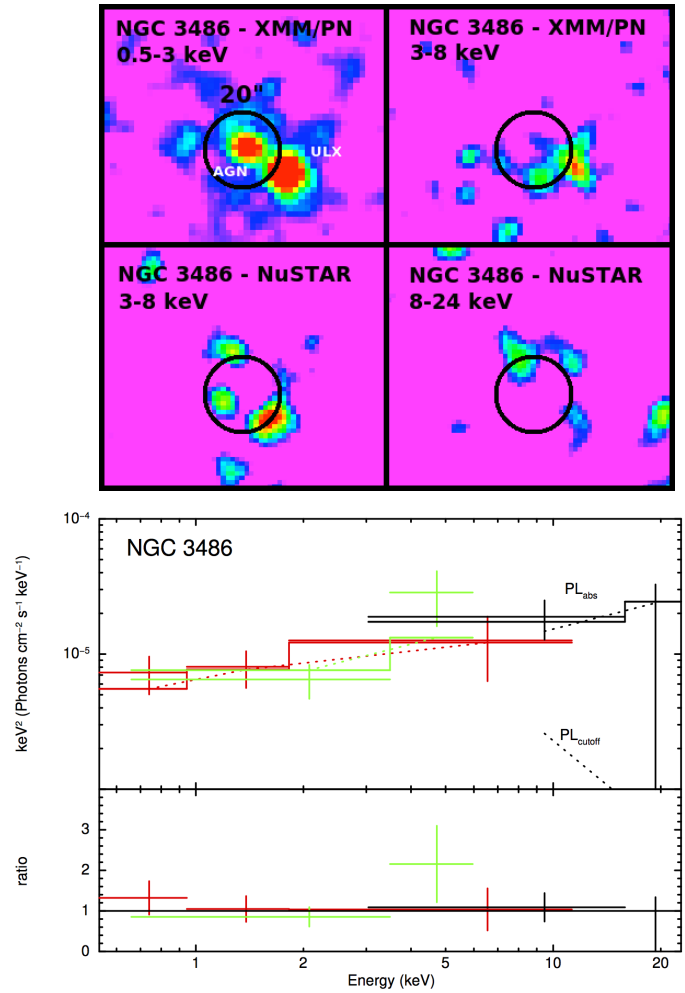

Figure 5.2: *Top*: *Chandra* images of NGC 3486 in the 0.5–3 keV and 3–8 keV bands (top panel) and *NuSTAR* FPMA+B images in the 3–8 keV and 8–24 keV bands (bottom panel). The black circle marks a 20″-radius region centred on the optical position of the AGN that was used to extract the *NuSTAR* spectra. The *XMM-Newton* spectra were extracted using a smaller circular region of 10″ in radius to avoid emission from the ULX. Images are smoothed with a Gaussian function of radius 3 and 5 pixels for the *XMM-Newton* and *NuSTAR* data, respectively, corresponding to 9.6″ and 12.3″, respectively. North is up and east is to the left in all images. *Bottom*: Best-fitting model to the combined *NuSTAR* (black), *XMM-Newton* PN (red) and MOS1+2 (green) data of NGC 3486. The data have been rebinned to a minimum of 3σ significance with a maximum of 500 bins for visual clarity. The spectra were fitted using an absorbed power-law model to simulate the AGN emission, and a cut-off power-law to account for possible contamination by the ULX in the *NuSTAR* spectrum. The model components fitted to the data are shown as dotted curves, and the total model are shown as solid curves.

Both the AGN and the ULX in NGC 3486 were not significantly detected in either of our *NuSTAR* and *Swift*-XRT observations.[1] The upper limits to the count rates measured for the AGN in the XRT and *NuSTAR* observations (total for both FPMs) are $\mathrm{CR}_{0.5-10,\mathrm{AGN}} < 3.75 \times 10^{-3}$ counts s^{-1} and $\mathrm{CR}_{3-24,\mathrm{AGN}} < 0.74 \times 10^{-3}$counts s^{-1} at 0.5–10 keV and 3–24 keV, respectively. Based on WEBPIMMS[2], the XRT flux corresponds to an upper limit flux of $f_{0.5-10,\mathrm{AGN}} < 1.41 \times 10^{-13}$ erg s^{-1} cm^{-2}, assuming $z = 0.00272$, $N_{\mathrm{H}}^{\mathrm{Gal}} = 1.90 \times 10^{20}$ cm^{-2} (Kalberla et al., 2005), and $\Gamma = 1.9$. This is consistent with that measured in the *XMM-Newton* data (Brightman & Nandra, 2008; Cappi et al., 2006), suggesting that the AGN has not significantly varied between the *XMM-Newton* observation and the *Swift*-XRT and *NuSTAR* observations. This is also the case for the ULX. The upper limit count rate measured for the ULX is $\mathrm{CR}_{0.5-10,\mathrm{ULX}} = 4.41 \times 10^{-3}$ counts s^{-1}, which corresponds to an upper limit flux of $f_{0.5-10,\mathrm{ULX}} = 1.66 \times 10^{-13}$ erg s^{-1} cm^{-2}, consistent with that measured in the archival *XMM-Newton* data (Foschini et al., 2002).

Although the AGN in NGC 3486 is not detected in our *NuSTAR* data, we extracted the spectra to assist our broadband X-ray spectral analysis of the source with the archival *XMM-Newton* data. We extracted the *XMM-Newton* spectra of the AGN from the three EPIC cameras (PN, MOS1 and MOS2) using a circular source region of 10″ in radius, centred on the optical position of the AGN obtained from the Sloan Digital Sky Survey Catalog (RA = 11:00:23.87, Dec = +28:58:30.49). The background photons were collected from an annular segment around the source, with inner and outer radii of 15″ and 30″, respectively, avoiding the ULX emission. For the *NuSTAR* data, we extracted the spectrum from both FPMs using a 20″-radius circular region for the source, and an annular segment with inner and outer radii of 50″ and 100″ for the background spectrum. For our spectral analysis, we did not use the *Swift*-XRT data as it does not provide additional constraints beyond those already achieved by the *XMM-Newton* and *NuSTAR* data. We present the

[1]The XRT data were reduced using the XRTPIPELINE v0.13.0, which is part of the XRT Data Analysis Software (XRT-DAS) within HEASOFT.

[2]WEBPIMMS is a mission count rate simulator tool, available online at https://heasarc.gsfc.nasa.gov/cgi-bin/Tools/w3pimms/w3pimms.pl .

X-ray spectral analysis of NGC 3486 in Section 5.3.2, and show the X-ray images at different energy bands in Figure 5.2.

5.2.3 NGC 5195

NGC 5195 (also known as M51b), located at a distance of 8.3 Mpc, is an irregular galaxy interacting with NGC 5194 (M51a). The nucleus is classified as a LINER in the optical band, and the galaxy has been observed numerous times in X-rays by *Chandra*, *XMM-Newton* and *NuSTAR*, most of the time as part of the overall M51 system. Whilst much of the attention of previous studies have focused on its brighter and more picturesque companion, NGC 5195 managed to grab attention recently when it was observed to be undergoing a violent X-ray outburst, potentially associated with AGN feedback (Schlegel et al., 2016).

Its companion, NGC 5194, has been confirmed to be a low luminosity CTAGN using multiple X-ray data including *NuSTAR* (Xu et al., 2016). A variable ULX (ULX-7), identified in the northern spiral arm of NGC 5194, has been suggested to be a candidate intermediate mass black hole (Earnshaw et al., 2016). To follow up to these interesting discoveries, we observed the M51 system in 2017 March with *NuSTAR* (PI M. Brightman; ObsID 60201062002 & 60201062003; $t_{\rm exp}$ = 47.2 & 163 ks, respectively), coordinated with *Chandra* (ObsID 19522; 38.2 ks).

Our *Chandra* data revealed two point sources within $\sim$4″ of the 2MASS position of NGC 5195, which were not resolved in previous observations (e.g., Terashima & Wilson, 2001; Schlegel et al., 2016; see Figure 5.3). This is likely due to the fact that NGC 5195 has generally been located off-axis in previous *Chandra* observations, where the size of the point spread function is larger. We used the WAVDETECT tool within CIAO to determine the centroid position of the two central sources in the *Chandra* energy band of 2–8 keV, setting the threshold parameter to 1×10^{-7}. One of the *Chandra* sources is located at position of RA = 13:29:59.41, and Dec. = +47:15:57.29, with errors of 0.″10 and 0.″10, respectively, and is consistent with the 2MASS position of NGC 5195 within $\sim$1″. Therefore, we used the position of this *Chandra* source when extracting the X-ray spectra of the AGN. The other point source (off-nuclear) was detected at RA = 13:29:59.21, and Dec. = +47:16:00.01,

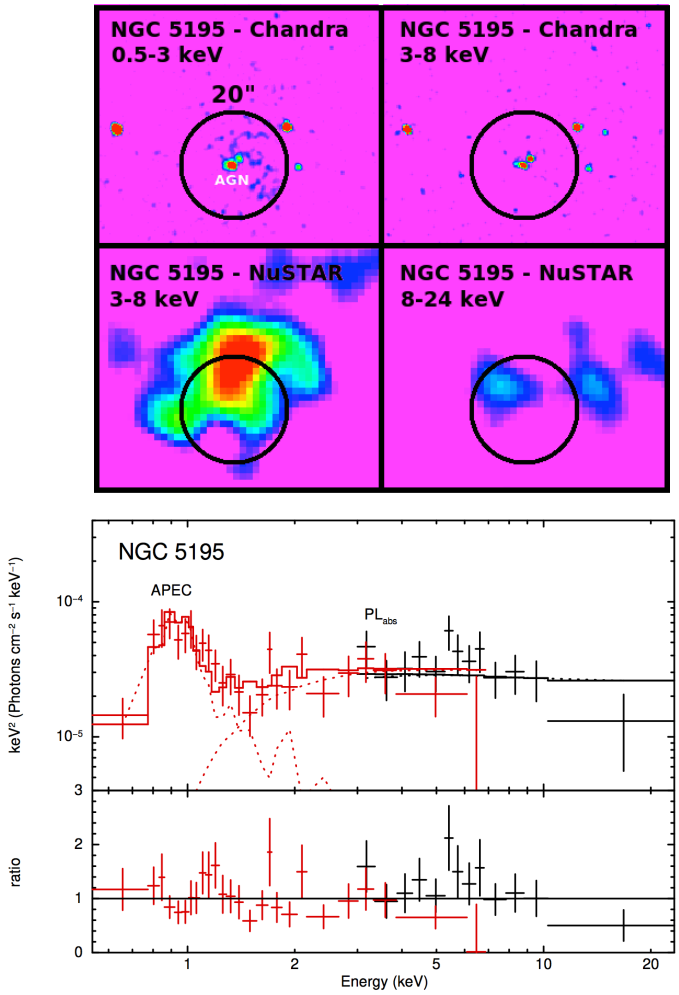

Figure 5.3: *Top*: *Chandra* images of NGC 5195 in the 0.5–3 keV and 3–8 keV bands (top panel) and *NuSTAR* FPMA+B images in the 3–8 keV and 8–24 keV bands (bottom panel). The black circle marks a 20″-radius region centred on the *Chandra* position of the AGN that was used to extract the *Chandra* and *NuSTAR* spectra. Images are smoothed with a Gaussian function of radius 3 and 5 pixels for the *Chandra* and *NuSTAR* data, respectively, corresponding to 1.5″ and 12.3″, respectively. North is up and east is to the left in all images. *Bottom*: Best-fitting model to the combined *NuSTAR* (black) and *Chandra* (red) data of NGC 5195. The data have been rebinned to a minimum of 3σ significance with a maximum of 500 bins for visual clarity. The spectra were fitted using an absorbed power-law model, an APEC component to model the emission at the softest energies, and an additional power-law component to model the off-nuclear source at the north-west of the AGN (this component is not visible in the plot as the flux normalisation is very low). The model components fitted to the data are shown as dotted curves, and the total model are shown as solid lines.

with errors of 0.″19 and 0.″11, respectively.

A source near the *Chandra* position of the AGN was detected in both of the *NuSTAR* observations, with significant counts up to ∼10 keV. The combined *NuSTAR* images of the source at 3–8 and 8–24 keV are shown in Figure 5.3. The count rate detected in the combined *NuSTAR* data in the 3–10 keV band is 4.59×10^{-4} counts s^{-1}. This source could be associated with either the AGN or the off-nuclear source. We extracted the *NuSTAR* spectra using a 20″-radius circular region adopting the *Chandra* position of the AGN as the centroid position. The background was extracted using a 100″-radius circular aperture from an offset source-free region. The *Chandra* spectrum was also extracted using a 20″-radius circular region to match the *NuSTAR* extraction region. The background for the *Chandra* spectrum was extracted using a circular region of 50″-radius from a source-free area. We detail the X-ray spectral analysis of NGC 5195 in Section 5.3.3.

In addition, we also extracted the spectrum of the off-nuclear point source detected within the extraction region of the *Chandra* data to reliably account for its contribution to the extracted spectra. The source flux was extracted using a small 1.5″-radius circular region, and the background flux was extracted using a 50″-radius circular aperture from a source-free region. We describe the spectral analysis of this source and discuss its nature in Section 5.3.3.

We note that, we did not include the archival *NuSTAR* data (2012-10-29; ObsID 60002038002; $t_{\rm exp} = 16.7$ ks) in our spectral analysis of NGC 5195 as we found that the source fluxes in the 3–8 keV bands are significantly different from each other within the statistical uncertainties; i.e., $L_{3-8,\rm obs} = 0.55^{+0.09}_{-0.07} \times 10^{-13}$ erg s^{-1} cm^{-2} and $L_{3-8,\rm obs} = 1.08^{+0.49}_{-0.41} \times 10^{-13}$ erg s^{-1} cm^{-2}, for our new data and the archival data, respectively. The difference in flux may be attributed to either the AGN or the nearby off-nuclear source that is not resolved by *NuSTAR*. Due to this potential variability between different observations, we also did not include other archival X-ray data of NGC 5195 in our analysis.

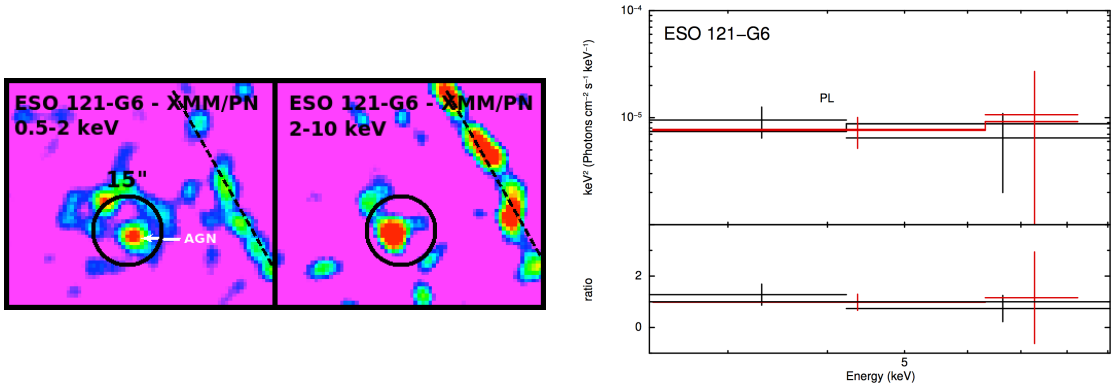

Figure 5.4: *Left*: *XMM-Newton* (PN) images of ESO 121-G6 in the 0.5–2 keV and 2–10 keV bands. The black circle marks a 15″-radius region centred on the 2MASS position of the AGN that was used to extract the spectra. The dotted black line indicates the chip gap of the PN detector. Images are smoothed with a Gaussian function of radius 5 pixels corresponding to 8″. *Right*: Best-fitting model to the *XMM-Newton* PN (black) and MOS1+2 (red) data of ESO 121-G6. The spectra were fitted using a simple power-law model over 2–10 keV to minimise potential non-AGN emission that generally dominates at $E \lesssim 2$ keV.

5.2.4 ESO 121-G6

ESO121-G6 is a highly inclined ($i = 90°$) galaxy located at a distance of 14.5 Mpc away from us.[3] The source lacks sensitive nuclear optical spectroscopy, and therefore is unclassified at optical wavelengths. However, due to the edge-on inclination of the galaxy along our l.o.s, the optical emission from the AGN is expected to be severely absorbed by the host galaxy. This galaxy has only been observed in X-rays by *XMM-Newton* (2007-01-20; ObsID 0403072201; $t_{\rm exp} = 15.0$). It has been observed at high spatial resolution in the mid-IR ($12\mu m$) with Gemini/T-ReCS ($t_{\rm exp} = 319$ s), which shows a weak detection of a nuclear source at 1.5σ (but is formally considered undetected due to low significance).[4]

The *XMM-Newton* data of ESO 121-G6 shows a weak point source consistent with the nuclear position of the galaxy (see Figure 5.4). We extracted the spec-

[3]The host galaxy inclination was obtained from the HyperLeda website (http://leda.univ-lyon1.fr/).

[4]Private communication with D. Asmus.

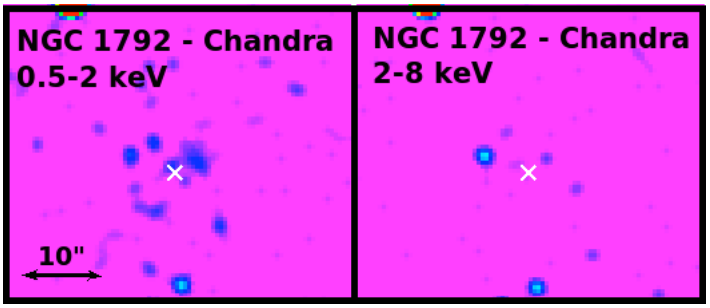

Figure 5.5: *Chandra* images of NGC 1792 in the 0.5–2 keV (left) and 2–10 keV (right) bands. The AGN was not detected in our *Chandra* data. The 2MASS position of the nucleus is marked using "×" in the images. Images are smoothed with a Gaussian function of radius 3 pixel, corresponding to 1.5″.

tra of this source from the three EPIC cameras using a 15″-radius circular region, centred on the 2MASS position of the source (RA = 06:07:29.86, and Dec. = −61:48:27.3s). The background region was extracted using a 60″-radius circular region from a source-free area. The average net count rates for the AGN measured by the three EPIC cameras are $\sim 1.3 \times 10^{-3}$ counts s^{-1} and $\sim 2.6 \times 10^{-3}$ counts s^{-1} in the 0.5–10 keV and 2–10 keV bands, respectively. We present the spectral analysis of ESO 121-G6 in Section 5.3.4.

5.2.5 NGC 1792

NGC 1792, located at a distance of 12.5 Mpc, is classified as an HII galaxy in the optical (Veron-Cetty & Veron, 1986). The source has been observed at high spatial resolution at $12\mu m$ by Gemini/T-ReCS ($t_{\rm exp}$ = 319 s), but was not detected.[4] In X-rays, it has only been previously observed by *XMM-Newton* (2007-03-29; ObsID 0403070301; $t_{\rm exp}$ = 23.3 ks). The *XMM-Newton* observation revealed diffuse soft emission at the nuclear position of the galaxy, with no clear indication of a point source. However, a [NeV] emission line is clearly detected at the central part of the galaxy, indicating that it hosts an AGN.

We observed NGC 1792 with *Chandra* in 2016 for 19.8 ks (2016-11-23; ObsID 19524), to provide a complete *Chandra* coverage for this volume-limited sample. However, an X-ray source associated with the nuclear position of NGC 1792 was

not detected. The nearest source to the 2MASS nuclear position of the galaxy is detected $\sim 5''$ away. The upper limit fluxes measured at this central position are 7.61×10^{-15} erg s^{-1} cm^{-2} and 8.54×10^{-15} erg s^{-1} cm^{-2}, in the 0.5–2 keV and 2–8 keV bands, respectively. We show our *Chandra* images of NGC 1792 at 0.5–2 and 2–8 keV in Figure 5.5.

5.3 X-ray Spectral Fitting Results

In this section, we present the X-ray spectral fitting results for NGC 660, NGC 3486, NGC 5195 and ESO 121-G6, performed using XSPEC v12.8.2.[5] We included a fixed Galactic absorption component for each source (Kalberla et al., 2005) using the XSPEC model "PHABS" in all spectral fits, and assumed solar abundances for all models. Due to the modest quality of our data, we also fixed the cross-calibration uncertainties of each observatory with respect to *NuSTAR* to the values found by Madsen et al. (2015) using a constant parameter, *C*.

In all cases, the spectra extracted from the two *NuSTAR* FPMs were co-added using the ADDASCASPEC script to increase the overall signal-to-noise ratio (SNR) of the data. For *XMM-Newton*, spectra extracted for the EPIC MOS1 and MOS2 cameras were combined using the EPICSPECCOMBINE task in SAS (see Chapter 2).

Given the non-negligible contribution of the background flux to the weak source flux in most cases, particularly in the *NuSTAR* and *XMM-Newton* data, we binned our spectra to a minimum of 5 counts per bin for the *NuSTAR* and *XMM-Newton* data, and 1 count per bin for the *Chandra* data, unless stated otherwise. We then optimised the fitting parameters using the Poisson statistic, C-statistic (Cash, 1979). All errors are quoted at 90% confidence, unless stated otherwise. We summarise the main results of our spectral analysis in Table 5.1.

[5]The XSPEC manual is available at http://heasarc.gsfc.nasa.gov/xanadu/xspec/XspecManual.pdf.

5.3.1 NGC 660

We first fitted the *Chandra* and *NuSTAR* spectra of NGC 660 simultaneously between 3–30 keV using a simple power-law model, absorbed by the Galactic column ($N_{\rm H}^{\rm Gal} = 4.64 \times 10^{20}$ cm^{-2}; Kalberla et al., 2005). The redshift was fixed at $z = 0.003896$ in the spectral analysis. As mentioned earlier in Section 5.2.1, we expect that the *NuSTAR* data are heavily contaminated by non-AGN emission up to ∼6 keV. We therefore ignored the *NuSTAR* spectrum below this energy for our X-ray spectral analysis. The best fitting photon index measured from the spectra is relatively flat; i.e., $\Gamma = 0.69 \pm 0.19$ (C-stat/d.o.f = 206/236), indicating significant X-ray absorption along our l.o.s.

We then proceeded to fit the broadband X-ray spectrum of NGC 660 (0.5–30 keV) with a physically motivated obscuration model by Murphy & Yaqoob (2009), called the MYTORUS model. This model was produced using a Monte Carlo approach to simulate obscuring gas and dust with different toroidal geometries (see Section 3.3.3 for a more detailed description of the model). Due to the modest quality of our data, we used the simplest version of the MYTORUS model by coupling all of the parameters for the scattered (MYTS) and fluorescent line components (MYTL) to the direct continuum component (MYTZ). The relative normalisations of MYTS (A_S) and MYTL (A_L) with respect to MYTZ (A_Z) were fixed to 1.

At $E \lesssim 2$ keV, the direct X-ray emission from a heavily obscured AGN is typically dominated by other sources such as unresolved off-nuclear X-ray sources and thermal emission from a hot interstellar medium. However, our data are not of sufficient quality to accurately distinguish between these different processes, therefore, we simply parametrised the low energy part of the spectrum covered by *Chandra* using the thermal model "APEC" (Smith et al., 2001), and a power-law component to simulate the scattered emission from the AGN. The XSPEC description of this model is the same as equation 4.3.2 (see Chapter 4).

We fixed the photon index and inclination angle of the model to $\Gamma = 1.9$ (approximately the typical mean value for an AGN; e.g., Burlon et al., 2011) and $\theta_{\rm inc} = 90°$ (to simulate an edge-on torus), respectively, as they could not be constrained. Our model measured a column density of $N_{\rm H} = 6.84^{+3.05}_{-2.35} \times 10^{23}$ cm^{-2} (C-stat/d.o.f =

171/187), indicating a heavily obscured AGN, but not CT within the statistical uncertainties. The scattering fraction measured with respect to the intrinsic power-law is small; i.e., $f_{\rm scatt} = 0.1^{+0.07}_{-0.04}$ %, consistent with that found in many other obscured AGNs (e.g., Noguchi et al., 2010; Gandhi et al., 2014; Gandhi et al., 2015). We note that however, given the relatively low quality data, this scattered component will also include contributions from other processes such as unresolved X-ray binaries, meaning that the intrinsic scattering fraction of the AGN could be smaller than this value. The APEC thermal component constrained a plasma temperature of kT = $0.32^{+0.78}_{-0.18}$ keV. We show the broadband X-ray spectrum of the AGN in NGC 660 in Figure 5.1.

5.3.2 NGC 3486

Due to the low quality of the archival *XMM-Newton* data (∼75 counts) and our *NuSTAR* data of NGC 3486 (in which it was undetected), we modelled its spectrum between 0.5–24 keV using a simple power-law model, absorbed by a fixed Galactic column, $N_{\rm H}^{\rm Gal} = 1.90 \times 10^{20}$ cm^{-2} (Kalberla et al., 2005), and an additional absorption component, ZWABS, to simulate the intrinsic absorption of the source. We fixed the redshift to $z = 0.002272$ in our model. Although the ULX is not significantly detected in the *NuSTAR* data, a faint emission that is consistent with the ULX position can be seen in the *NuSTAR* 3–8 keV image (see Figure 5.2). Therefore, we include a cut-off power-law component in our model to account for the ULX contribution in the *NuSTAR* data. We set the photon index of the ULX to that measured by Foschini et al. (2002) using the *XMM-Newton* data (i.e., $\Gamma_{\rm ULX} = 2.2$), assuming that it has not significantly varied between the *XMM-Newton* and *NuSTAR* observations, and fixed the X-ray energy cut-off at 10 keV (as that found in other ULXs; e.g., Walton et al., 2013; Bachetti et al., 2013; Walton et al., 2014; Rana et al., 2015). The flux normalisation of the component was left free to vary. We did not include any additional component (e.g., APEC) to model potential additional non-AGN emission at the soft energies as they could not be constrained.

The best fitting photon index and column density measured by our model for the AGN are $\Gamma = 1.59^{+0.40}_{-0.33}$ and $N_{\rm H} < 1.52 \times 10^{21}$ cm^{-2} (C-stat/d.o.f = 36/35),

respectively. The column density measured indicates that NGC 3486 is unobscured. The photon index measured is consistent with the typical value found for an AGN within the statistical uncertainties (1.7–2.3; e.g., Burlon et al., 2011). Our results rule out suggestions that the source is likely CT by previous low X-ray energy studies (Cappi et al., 2006; Brightman & Nandra, 2008). The spectrum for NGC 3486 and the best-fit model are shown in Figure 5.2.

5.3.3 NGC 5195

To reliably measure the properties of the AGN in NGC 5195, we first need to constrain the contribution from the off-nuclear source detected near the AGN in the *Chandra* data. We modelled the X-ray spectrum of the off-nuclear source between 0.5–8 keV using a simple power-law model, absorbed by the host galaxy absorption (TBABS), in addition to the Galactic column, $N_{\rm H}^{\rm Gal} = 1.79 \times 10^{20}$ cm^{-2} (Kalberla et al., 2005), assuming that it is located within NGC 5195 ($z = 0.001551$). The best-fitting photon index and host galaxy absorption measured by the model are $\Gamma = 0.48^{+0.81}_{-0.65}$ and $N_{\rm H} < 5.61 \times 10^{21}$ cm^{-2}, respectively (C-stat/d.o.f = 26/25). The 0.5–8 keV intrinsic luminosity inferred from the model is $L_{0.5-8,\rm int} = 1.61^{+0.93}_{-0.33} \times 10^{38}$ erg s^{-1}, below the luminosity threshold for a ULX ($L_{\rm X} \geq 10^{39}$ erg s^{-1}), suggesting that the off-nuclear source may be an X-ray binary. The photon index measured is relatively flat, and suggests that the absorption level suffered by the off-nuclear source might be higher than what we measured. However given the low quality of the data (∼30 counts), this could not be accurately determined.

We then modelled the broadband X-ray spectrum of the AGN between 0.5–24 keV using a power-law model absorbed by the Galactic and intrinsic absorption (ZWABS), an APEC component to model the soft energy emission, and the off-nuclear source component to reliably account for its contribution in the extracted spectra of the AGN. The photon index and host galaxy absorption of the off-nuclear source were fixed to the values measured earlier, but the flux normalisation parameter was left free to vary in the spectral analysis.

Based on this model, we measured an obscuring column density of $N_{\rm H} < 2.50 \times 10^{22}$ cm^{-2} (C-stat/d.o.f = 234/245), indicating that the AGN is potentially not

obscured. The best-fitting photon index measured is $\Gamma = 2.12^{+0.42}_{-0.38}$, in agreement with the typical value measured for an AGN (e.g., Burlon et al., 2011). The APEC thermal component measured a plasma temperature of $kT = 0.95^{+0.09}_{-0.18}$ keV. We show the broadband X-ray spectrum of NGC 5195 in Figure 5.3.

5.3.4 ESO 121-G6

Given the low quality of the *XMM-Newton* data of ESO 121-G6 ($\sim$ 30 counts), we modelled its spectrum simply using a power-law model, absorbed by a fixed Galactic column, $N_{\rm H}^{\rm Gal} = 4.00 \times 10^{20}$ cm^{-2} (Kalberla et al., 2005), with its redshift fixed to $z = 0.004039$. For this source, we restricted our modelling between 2–10 keV to allow us to measure the AGN properties at energies where the emission from an AGN is believed to start dominating over other processes. We did not include an additional absorption component to measure the intrinsic absorption of the source due to the low quality of the data, and the absence of a high energy constraint by *NuSTAR* or *Swift*-BAT. Previous studies have shown that column density measurements made in such cases can be misleading; i.e., underestimate the actual absorption columns (e.g., Lansbury et al., 2015).

The best fitting photon index inferred by our model is $\Gamma = 1.74^{+1.14}_{-1.26}$ (C-stat/d.o.f = 10/14), consistent with the typical intrinsic value found for AGNs (e.g., Burlon et al., 2011). This suggests that ESO 121-G6 may also be unobscured, or just mildly obscured. However, our work has shown that off-nuclear emission can provide significant contribution to the AGN spectra extracted from relatively lower spatial resolution X-ray observations such as *XMM-Newton* and *NuSTAR*, even at $E > 2$ keV. Therefore, the measured photon index could include significant contribution from contaminating off-nuclear sources such as X-ray binaries or ULXs. This will be further investigated with our scheduled *Chandra* observations of the source (co-ordinated with *NuSTAR*). The *XMM-Newton* spectra of ESO 121-G6 are shown in Figure 5.4.

Table 5.1: X-ray spectral fitting results.

Name	Facility	Model	Energy Band [keV]	Γ	$\log N_{\rm H}$ [cm^{-2}]	$\log L_{2-10,\rm obs}$ [erg s^{-1}]	$\log L_{2-10,\rm int}$ [erg s^{-1}]	χ^2 or C-stat / d.o.f	Ref.
(1)	(2)	(3)	(4)	(5)	(6)	(7)	(8)	(9)	(10)
Circinus	*C + XMM + N*	MYTORUS	2–79	2.40 ± 0.03	$24.87^{+1.68}_{-0.20}$	40.45	42.57	2785 / 2637 (χ^2)	Arévalo et al. (2014)
ESO121-G6	*XMM*	ZPOW	2–10	$1.74^{+1.14}_{-1.26}$	-	38.73	-	10 / 14 (C-stat)	This work[a]
NGC 0613	*XMM*	MEKAL+WABS(PO+ZGAU)	2–10	1.76 ± 0.06	23.56 ± 0.05	40.46	41.1	470/454 (χ^2)	Castangia et al. (2013)
NGC 0660	*C + N*	MYTORUS	0.5–30	1.9[f]	$23.83^{+0.16}_{-0.18}$	39.09	39.83	171 / 187 (C-stat)	This work[a]
NGC 1068	*C + XMM + N + BAT*	MYTORUS	2–195	$2.10^{+0.06}_{-0.07}$	$25.00^{+u}_{-0.01}$	41.21	43.30	1899.2 / 1666 (χ^2)	Bauer et al. (2015)
NGC 1448	*C + N*	MYTORUS	0.6–40	1.9[f]	$24.65^{+u}_{-0.22}$	38.95	40.88	429 / 440 (C-stat)	Annuar et al. (2017)[b]
NGC 1792	*C*	ZPOW	2–8	1.9[f]	-	<38.27	-	-	This work[a]
NGC 3486	*XMM + N*	ZWABS(ZPOW)	0.5–24	$1.59^{+0.40}_{-0.33}$	<21.18	38.59	38.59	36 / 35 (C-stat)	This work[a]
NGC 3621	*C*	ZPOW	0.5–8	$2.22^{+0.89}_{-0.67}$	-	37.35	-	18.7 / 21 (C-stat)	This work[c]
NGC 3627	*C*	ZPOW	2–10	1.13 ± 0.56	-	38.80	-	64.1 / 78 (C-stat)	This work[c]
NGC 3628	*C*	ZPOW	2–10	1.24 ± 0.57	-	38.69	-	11.0 / 8 (χ^2)	This work[c]
NGC 4051	*N*	MYTORUS	2–70	2.33 ± 0.05	$20.06^{+0.05}_{-0.04}$	41.09	41.09	569/537 (χ^2)	Turner et al. (2017)
NGC 4565	*C*	ZWABS(ZPOW)	0.5–8	1.94±0.12	$21.40^{+0.07}_{-0.08}$	39.41	39.41	87/82 (χ^2)	This work[c]
NGC 4945	*C + S + N*	MYTORUS	0.5–79	1.96 ± 0.07	$24.54^{+0.02}_{-0.01}$	39.48	42.76	1118 / 1055 (χ^2)	Puccetti et al. (2014)
NGC 5033	*XMM + BAT*	ZGAU+(ZWABS*ZPOW)	0.5–195	1.73±0.02	<19.49	41.00	41.00	286/241 (χ^2)	This work[c]
NGC 5128	*XMM + N*	MYTORUS	3–78	1.82 ± 0.01	$23.04^{+0.06}_{-0.01}$	41.73	42.00	1667 / 1536 (χ^2)	Fürst et al. (2016)
NGC 5194	*C + N*	MYTORUS	0.6–50	1.8 ± 0.3	$24.85^{+0.15}_{-0.24}$	38.99	40.77	169.3 / 155 (χ^2)	Xu et al. (2016)
NGC 5195	*C + N*	ZWABS(ZPOW)	0.5–24	$2.12^{+0.42}_{-0.38}$	<22.40	38.80	38.80	234 / 245 (C-stat)	This work[a]
NGC 5643	*C + XMM + N*	MYTORUS	0.5–100	$2.10^{+0.04}_{-0.02}$	$24.76^{+u}_{-0.10}$	40.20	41.95	570 / 471 (χ^2)	Annuar et al. (2015)[b]
NGC 6300	XRT + *N*	PEXRAV	0.3–195	1.90 ± 0.03	23.23 ± 0.02	41.71	42.07	339 / 304 (χ^2)	Baloković et al. (in prep.)

Notes. Column (1) AGN name; (2) X-ray facilities used in the analysis (BAT: *Swift*-BAT; C: *Chandra*; N: *NuSTAR*; XMM: *XMM-Newton*; XRT: *Swift*-XRT); (3) Best-fit models to the spectra; (4) Energy band used in the analysis in keV; (5) Best-fitting photon index; (6) Best-fitting column density measured in cm^{-2}; (7-8) observed and absorption-corrected 2–10 keV luminosities, respectively, in erg s^{-1}. The intrinsic luminosities are only given for sources which have sufficient X-ray data, and therefore have reliable $N_{\rm H}$ measurements; (9) Fit statistic results and approach; (10) Reference for the results.

[a] see Sections 2–3

[b] see Chapters 3–4

[c] see Appendix A.1

5.4 Multiwavelength Compton-thick diagnostics

In this section, we discuss the multiwavelength techniques used to select CTAGN candidates in our sample which do not have high energy X-ray data and lack good quality low X-ray energy observations. The selected sources are classified as "candidates" as these techniques are indirect indicators for the obscuration level suffered by the AGNs, and do not allow for direct $N_{\rm H}$ measurements to be made, which can only be performed using X-ray spectroscopy. These sources have weak X-ray emission relative to the emission at other wavelengths, suggesting that they may be CT. In addition, we also investigate the reliability of each techniques in identifying CT and non-CT sources using the AGN in our sample with reliable $N_{\rm H}$ measurements as a guide.

5.4.1 X-ray:[OIII] diagnostic

In this section, we present CTAGN candidates selection using the observed 2–10 keV and intrinsic [OIII]λ5007Å emission line flux ratio. The [OIII] emission line in AGN is mostly produced in the narrow line region (NLR) due to photoionisation from the central source, and is therefore considered to be a good indicator for the intrinsic flux of the AGN. Since the physical scale of this region extends beyond the torus, it does not suffer from nuclear obscuration like the X-ray emission. Optical emission from the NLR however, can be affected by extinction from the host galaxy. Although in general this can be corrected for using the Balmer decrement (i.e., Hα/Hβ flux ratio), in extreme cases, the host galaxy obscuration can be so high that the optical Balmer decrement only provides a lower limit on the extinction (GA09).

Using a sample of Seyfert 2 galaxies with good quality X-ray spectra and therefore reliable $N_{\rm H}$ measurements, Bassani et al. (1999) found that all of the CTAGNs in their sample have observed 2–10 keV and intrinsic [OIII] flux ratio of $f_{2-10,\rm obs}/f_{\rm [OIII],corr} \lesssim 1$ (see Figure 1.7 in Chapter 1). We adopted this flux ratio threshold to further identify CT candidates in our AGN sample, using the observed 2–10 keV flux and [OIII] flux corrected for the Balmer decrement as tabulated in Table 5.1 and 2.2

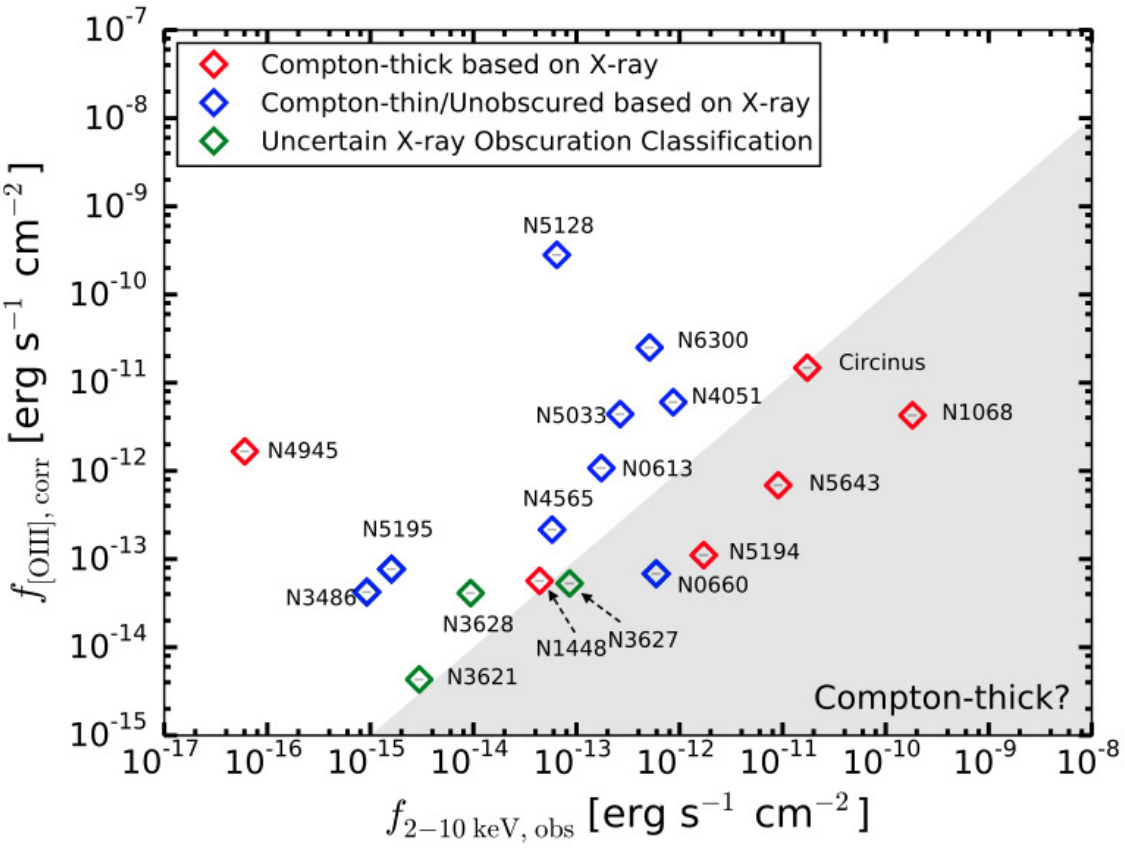

Figure 5.6: Observed 2–10 keV flux vs. [OIII]λ5007Å flux corrected for the Balmer decrement plot for our sample. Red and blue diamonds are AGNs which have been identified to be Compton-thick and Compton-thin on the basis of direct $N_{\rm H}$ measurements from X-ray spectroscopy, and green diamonds are those that do not have reliable $N_{\rm H}$ measurements. The grey area indicates a region where $f_{2-10,\rm obs}/f_{\rm [OIII],corr}$ $\leq$1, which we have used to select CTAGN candidates in the sample, following Bassani et al. (1999). ESO 121-G6 and NGC 1792 are not plotted in the diagram as they lack good quality optical data.

(in Chapter 2), respectively.[6] We identify AGNs with $f_{2-10,\mathrm{obs}}/f_{[\mathrm{OIII}],\mathrm{corr}}$ <1 as CT candidates. In Figure 5.6, we plot the corrected [OIII] and observed 2–10 keV fluxes for our sample.

We found that most of our X-ray identified CTAGNs are selected as CT based on this diagnostic (4/6), with the exception of NGC 1448 and NGC 4945. This is due to the fact that the optical emission from these two AGNs suffer from significant absorption by their highly inclined host galaxies (see Chapter 4 and GA09, respectively). This causes their [OIII] luminosities to be underestimated, even after being corrected for the Balmer decrement. However, we note that NGC 1448 lies very close to the CT region in Figure 5.6. Most of the X-ray identified Compton-thin or unobscured AGNs (8/9) lie outside the shaded region in Figure 5.6, suggesting that they are not CT, consistent with the results of their X-ray spectral analysis. The remaining source, i.e. NGC 660, which is heavily obscured but not CT based upon our X-ray spectral analysis, is selected as CT using this diagnostic. Only one out of three sources without reliable N_{H} measurements, but with good quality optical data, is suggested to be CT on the basis of this diagnostic; i.e., NGC 3627. Overall, this diagnostic selects a further two CTAGN candidates in the sample, NGC 660 and NGC 3627, and found a 30% (i.e., 6/20) CTAGN fraction, with a 40% (8/20) upper limit to account for the two AGNs in our sample which lack optical data (ESO 121-G6, NGC 1792).

5.4.2 X-ray:12μm relationship

To further identify CTAGN candidates in our sample, we also compare the observed X-ray and 12μm luminosities measured for our sources with the intrinsic X-ray:12μm correlation found by Asmus et al. (2015). The mid-IR continuum emission from AGN is produced by the obscuring torus and is due to the reprocessing of the nuclear emission (i.e., accretion disk and corona). Therefore, it should provide a

[6]We assumed an intrinsic Balmer decrement of $(\mathrm{H}\alpha/\mathrm{H}\beta)_{\mathrm{int}} = 2.86$, corresponding to a temperature and an electron density of $T = 10^4$ K and $n_e = 10^2$ cm^{-3}, respectively, for Case B recombination (Osterbrock, 1989).

reliable estimate for the intrinsic luminosity of the AGN. The mid-IR emission can also be produced by dust around massive O-B stars; however, the emission from the AGN will typically dominate in this waveband.

The Asmus et al. (2015) X-ray:12μm intrinsic luminosity relationship has been shown to predict the intrinsic X-ray luminosity of AGN very well (see also Horst et al., 2008; Gandhi et al., 2009; Mason et al., 2012). The relationship was derived using mid-IR data from high angular resolution mid-IR observations ($\sim$0$''$.4) of local Seyfert galaxies. As described in Chapter 1, for CTAGN, the X-ray emission that we observed is generally attributed to X-ray photons that are scattered or reflected from the back side of the torus, which consists of just a few percent of the intrinsic power of the AGN at 2–10 leV band (e.g. Iwasawa et al., 1997; Matt et al., 2000; Baloković et al., 2014). Therefore, we can use the Asmus et al. (2015) X-ray:12μm relationship to identify AGN with observed 2–10 keV luminosity that deviates significantly from this intrinsic relationship, suggesting that they are likely to be CT. We show the X-ray:12μm correlation by Asmus et al., 2015 in Figure 5.7, with a grey region that we have adopted to select CTAGN candidates in our sample, representing a factor of 25$\times$ suppression of the X-ray flux (e.g., Rovilos et al., 2014).

We obtained the majority of the 12μm fluxes for our sources (13/20) from Asmus et al. (2014), which were measured from high spatial resolution mid-IR observations. The high spatial resolution mid-IR observation for one source; i.e., NGC 1448, was described in Chapter 4, and the 12μm measurements for two sources (ESO 121-G6 and NGC 1792) were obtained through private communication with D. Asmus. The fluxes for the remaining four sources which have not been observed at high spatial resolution mid-IR (NGC 660, NGC 3621, NGC 4565 and NGC 5195) were predicted from their [NeV] luminosities (see appendix A.2). These luminosities are listed in Table 2.1 (see Chapter 2).

Based on Figure 5.7, we found that most of our bona-fide CTAGNs are selected as CTAGNs on the basis of this diagnostic (5/6), except for NGC 4945. Two out of nine of our X-ray identified Compton-thin/unobscured AGNs are selected as CT on the basis of this method. NGC 660, which is heavily obscured (but not CT) based upon our X-ray spectral analysis lies deep within the CT region, whilst NGC 5195

which is potentially unobscured from our X-ray analysis is located at the edge of the CT region. We note that however, the $12\mu m$ luminosities for both sources were predicted from the [NeV] luminosities as they have not been observed at high spatial resolution at $12\mu m$. For the remaining 5/20 sources with no $N_{\rm H}$ measurements (ESO 121-G6, NGC 1792, NGC 3621, NGC 3627 and NGC 3628), we found that all of them are located within the CT region (note that the $12\mu m$ luminosity for NGC 3621 was predicted from the [NeV] luminosity). However 3/5 of these sources; i.e., ESO121-G6, NGC 1792, NGC 3628, have upper limit 12μm luminosity measurements. Therefore for these sources, we cannot conclude their classifications on the basis of this diagnostic. Based on this approach, we found that the X-ray:$12\mu m$ relationship selects a higher fraction of 45% (9/20) CTAGN population in the sample, up to 60% (12/20) if we include the three sources with upper limit $12\mu m$ luminosity measurements.

5.4.3 X-ray:[NeV] relationship

Our parent sample from GA09 was derived using the detections of high-ionisation [NeV] line as an unambiguous indicator for AGN activity in the galaxies. Thus, it should also be a reliable proxy for the intrinsic AGN power. Like the [OIII] emission line, the [NeV] line is also produced in the NLR which extends far beyond the torus. However, since it is produced in the mid-IR ($\lambda = 14.32$ μm), it is less likely to be affected by extinction through the host galaxy, unlike the optical [OIII] line (the optical depth at $14.32\mu m$ is $\sim$50$\times$ lower than that at the optical V-band; Li & Draine, 2001). Therefore, in addition to the two widely used CTAGN selection criteria described in previous sections, we also explore the use of the [NeV] line as an intrinsic AGN luminosity indicator to search for CT candidates in the sample.

We compared the observed 2–10 keV and [NeV] luminosities for our sample with the intrinsic correlation found by Weaver et al. (2010), which was derived using the *Swift*-BAT AGN sample. Again, we classified those AGNs with observed 2-10 keV luminosities lying more than 25$\times$ below this intrinsic relationship provided by Weaver et al. (2010) as highly likely to be CT. This is shown in Figure 5.7. This technique managed to identify all of our confirmed CTAGNs (6/6), including NGC

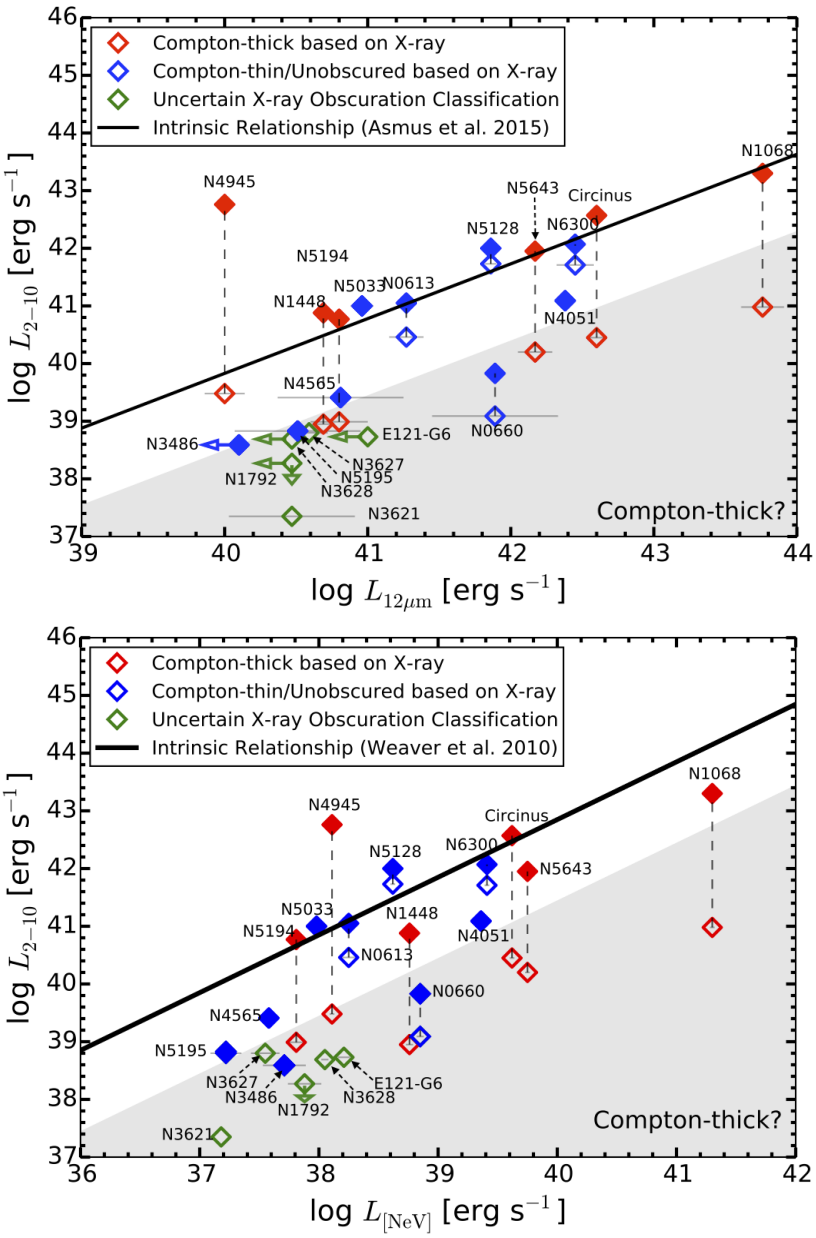

Figure 5.7: Observed 2–10 keV luminosities vs. 12μm (top) and [NeV] luminosities (bottom) for our sample. The solid lines for each plot corresponds to the intrinsic relationships derived by Asmus et al. (2015) (scatter, $\sigma \approx 0.3$ dex) and Weaver et al. (2010) (scatter, $\sigma \approx 0.5$ dex), respectively. The symbols are the same as in Figure 5.6, with filled diamonds indicating the intrinsic 2–10 keV luminosities of the AGNs as measured from X-ray spectroscopy. We identified sources which lie $> 25\times$ below the relation (grey region) as CTAGN candidates, following detailed X-ray studies on CTAGNs (e.g. Iwasawa et al., 1997; Matt et al., 2000; Baloković et al., 2014).

4945, which was not identifed using the optical and mid-IR continuum selections. Two out of nine of our X-ray identified Compton-thin/unobscured AGNs are identified as CTAGN candidates based on this method; i.e., NGC 3486 and NGC 660. We note however, the [NeV] luminosity for NGC 3486 was predicted from the [OIV] luminosity (as it does not have [NeV] luminosity measurement; see Chapter 2). The remaining 5/20 sources which do not have $N_{\rm H}$ measurements are all selected as CTAGN candidates. Overall, this technique found a large fraction of 65% (13/20) CTAGN population in the sample, significantly higher than that identified using the optical diagnostic and $12\mu m$ selection.

5.4.4 Final Classification

The results for the multiwavelength selection of CTAGN candidates in our sample are summarised in Table 5.2. Overall, the X-ray:[NeV] selection found the highest fraction of CTAGN candidates in the sample, while the X-ray:[OIII] diagnostics found the least, comparable to X-ray spectroscopy. The X-ray:[NeV] technique also managed to identify all of the bona-fide CTAGNs in the sample, whilst the X-ray:[OIII] and X-ray:$12\mu m$ methods missed a number of X-ray selected CTAGNs. However with our current lack of data, we could not strongly conclude which of these multiwavelength CT indicators is the most reliable method of identifying CTAGN candidates. We concluded the CT classification of each AGN in our sample by considering all of these indirect diagnostics, in addition to the X-ray spectroscopy analysis. Although these indirect methods are useful in helping us identify potential CTAGNs in the sample, ultimately, only X-ray spectroscopy can provide us with the direct $N_{\rm H}$ measurements, and confirm whether or not they are CT. Therefore, sources which have reliable $N_{\rm H}$ values measured from X-ray spectroscopy are classified as those indicated by this analysis, unless strongly suggested as CTAGN by all three indirect techniques.

This is true for one source, NGC 660. This source is suggested to be CT using all three indirect diagnostics (however, we note that the $12\mu m$ luminosity was inferred from the [NeV] luminosity). Although our X-ray spectral analysis did not measure a CT column, the $N_{\rm H}$ value inferred is near the CT regime within the statistical

Table 5.2: Multiwavelength Compton-thick indicators.

	Compton-thick?				
Name	X-ray:[OIII]	X-ray:12μm	X-ray:[NeV]	X-ray Spectroscopy ($N_{\rm H}$)	Final Classification
(1)	(2)	(3)	(4)	(5)	(6)
Circinus	CT	CT	CT	CT	CT
ESO121-G6	?	?	CT	?	?
NGC 0613	No	No	No	No	No
NGC 0660	CT	CT*	CT	No	CT?
NGC 1068	CT	CT	CT	CT	CT
NGC 1448	No	CT	CT	CT	CT
NGC 1792	?	?	CT	?	?
NGC 3486	No	No	CT†	No	No
NGC 3621	No	CT*	CT	?	?
NGC 3627	CT	CT	CT	?	CT?
NGC 3628	No	?	CT	?	?
NGC 4051	No	No	No	No	No
NGC 4565	No	No*	No	No	No
NGC 4945	No	No	CT	CT	CT
NGC 5033	No	No	No	No	No
NGC 5128	No	No	No	No	No
NGC 5194	CT	CT	CT	CT	CT
NGC 5195	No	CT*	No	No	No
NGC 5643	CT	CT	CT	CT	CT
NGC 6300	No	No	No	No	No
CT %	30-40%	45-60%	65%	30-55%	40-60%

Notes. Column (1) AGN; (2-4) X-ray:[OIII], X-ray:12μm and X-ray:[NeV] CT selections, respectively; (5) CT on the basis of reliable N_H measurements from X-ray spectroscopy; (6) Final classifications made by considering all 4 techniques. AGNs with reliable $N_{\rm H}$ values are classified as those indicated by these analysis, unless strongly suggested otherwise by the three indirect techniques. The last row of the table summarises the CT fraction found by each technique. The upper limit fraction are determined when including sources with inconclusive CT classifications (i.e., "?").

* the 12μm luminosity was predicted from the [NeV] luminosity (see Appendix A.2).

† the [NeV] luminosity was predicted from the [OIV] luminosity (see Chapter 2).

uncertainties ($N_{\rm H} = 6.84^{+3.05}_{-2.35} \times 10^{23}$ cm^{-2}). The multiwavelength data strongly suggest that the X-ray emission in NGC 660 is significantly more luminous than the intrinsic luminosity we determined from the X-ray analysis. This indicates that the obscuring column must be higher than what we actually measured, and is likely in the CT regime. The $N_{\rm H}$ value we determined from the X-ray spectra could be underestimated due to the relatively low quality data.

For the remaining 5 AGNs in our sample which do not have $N_{\rm H}$ measurements, we determined their final classifications on the basis of the three multiwavelength diagnostics. We found that only one source is identified as a CTAGN candidate based on all three selection methods; i.e., NGC 3627. We could not conclude the final classifications for the remaining 4 sources due to insufficient evidence.

To summarise, based on X-ray spectral analysis, we found a CTAGN population of 30%. Performing multiwavelength diagnostics to find potential CTAGNs in the sample found a further two candidates, NGC 660 and NGC 3627. This increases our CTAGN population to 40% (8/20). The CT classifications for 4 AGNs in the sample are inconclusive, therefore, this fraction could be higher, up to 60% (12/20).

5.5 Overall Results

In this chapter, we presented a multiwavelength analysis on our $D \leq 15$ Mpc AGN sample in an attempt to form a complete census of the CTAGN population and the $N_{\rm H}$ distribution of AGN in our local universe. This includes X-ray spectral analysis (Section 5.3 and appendix A.1), as well as multiwavelength CT diagnostics (Section 5.4). In this section, we present the overall results of our analyses. In Figure 5.8, we show the $N_{\rm H}$ distribution of our AGN sample as compared to the observed and intrinsic $N_{\rm H}$ distributions of the *Swift*-BAT AGNs with comparable X-ray luminosities to our sample ($\log L_{14-195} = 40.0$–43.7 erg s^{-1}; Ricci et al., 2015). Based on this figure, the $N_{\rm H}$ distribution of the AGN in our sample seems to be different from the observed $N_{\rm H}$ distribution of the *Swift*-BAT AGN, particularly at the CT regime, but similar to the intrinsic $N_{\rm H}$ distribution inferred taking into account the *Swift*-BAT sensitivity limit. This demonstrates the bias against finding

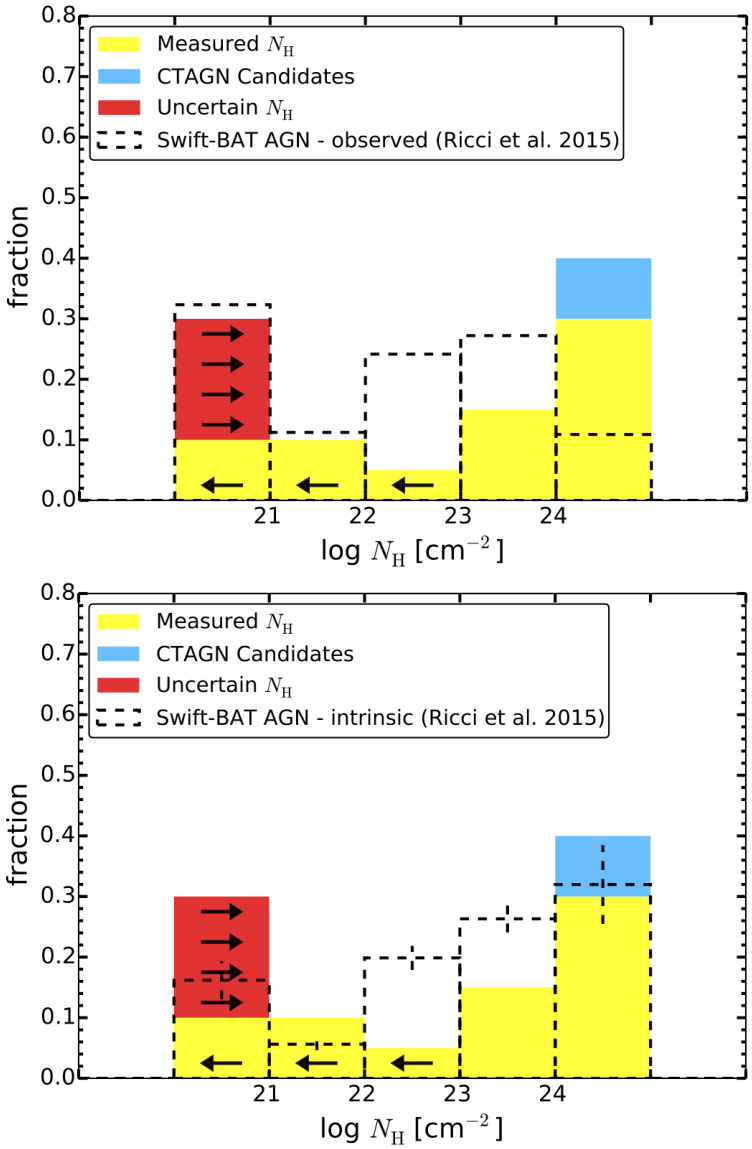

Figure 5.8: The $N_{\rm H}$ distribution for our sample as compared to the observed (top) and intrinsic (bottom) $N_{\rm H}$ distributions of the *Swift*-BAT AGN sample with log L_{14-195} = 40.0–43.7 erg s^{-1} (Ricci et al., 2015). Yellow indicates the distribution of the $N_{\rm H}$ measured from X-ray spectroscopy and blue are CTAGN candidates in our sample identified using the multiwavelength techniques. Red are the remaining sources in our sample which have no reliable $N_{\rm H}$ measurements and lack multiwavelength CT evidence. For these sources, we have used their Galactic absorptions as lower limit $N_{\rm H}$. The dashed lines are the $N_{\rm H}$ distributions of the *Swift*-BAT AGN sample, with error bars plotted for the intrinsic distribution.

CTAGN in the *Swift*-BAT sample. On the other hand, the obscured Compton-thin AGN fraction in our sample (log $N_{\rm H}$ = 22-24) is significantly lower than that observed and inferred in the *Swift*-BAT sample, suggesting that the majority of the remaining four AGNs in our sample which have uncertain CT classifications may have $N_{\rm H}$ values in this regime.

Using our sample, we managed to directly identify a 30^{+23}_{-14}% CTAGN fraction using X-ray spectroscopy, significantly higher than that directly observed in the entire *Swift*-BAT sample (i.e., $7.6^{+1.1}_{-2.1}$% over the entire X-ray luminosity range of the *Swift*-BAT AGN sample; log L_{14-195} = 40–46 erg s^{-1}; Ricci et al., 2015), even after accounting for the uncertainties due to small number statistics for our sample.[7] However, our fraction is consistent with the intrinsic CTAGN fraction inferred using the *Swift*-BAT sample after correcting for selection biases (27 ± 4 %). In fact, our CTAGN fraction considering the two CTAGN candidates, 40^{+25}_{-17}% (see footnote 7), still agrees very well with that predicted by Ricci et al. (2015). Although the overall observed CTAGN fraction found in the *Swift*-BAT sample is significantly lower than the intrinsic fraction inferred, and also determined using our sample, Ricci et al. (2015) shows that this is due to bias against finding relatively faint CTAGN at larger distances. This is demonstrated in Figure 5.9. From this figure, we can see that at a smaller distance of 20 Mpc, Ricci et al. (2015) found that the CTAGN population in the *Swift*-BAT sample is consistent with their inferred intrinsic fraction. Their CT fraction at $D \leq 20$ Mpc is also consistent with our fraction at $D \leq 15$ Mpc, either excluding or including the CTAGN candidates. However with our sample, we managed to detect CTAGN at lower luminosity than that found using the *Swift*-BAT sample; i.e., down to $L_{2-10,\rm int} \sim 10^{40}$ erg s^{-1} (assuming that the actual 2–10 keV luminosities for NGC 660 and NGC 3627 are about two orders of magnitude higher than their observed luminosities, typical of that found in other CTAGNs).[8] This is about an order of magnitude lower than that probed by the *Swift*-BAT survey.

[7]The uncertainties were calculated using the small number Poisson statistic based upon 90% confidence levels given in Gehrels (1986).

[8]The 2–10 keV intrinsic luminosities for the *Swift*-BAT AGNs were converted from their 14–195 keV luminosities using the scaling relation from Rigby et al. (2009).

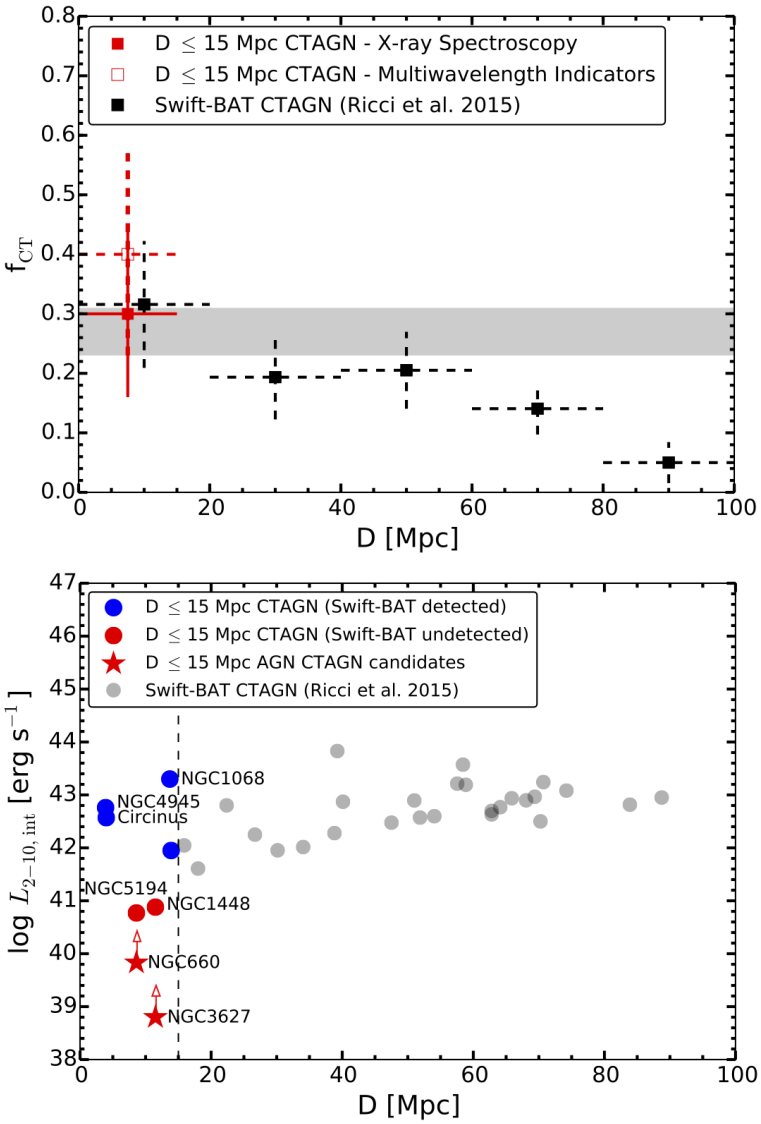

Figure 5.9: *Top*: CTAGN fraction as a function of distance for our sample (red) and the *Swift*-BAT AGN located within 100 Mpc (black). The filled red square indicates the bona-fide CTAGN fraction for our sample, while the open square indicates the CT fraction when including the two CTAGN candidates identified using multiwavelength techniques. The error bars for our sample correspond to the small number statistic uncertainties at 90% confidence level (see footnote 7). The grey region shows the range of the intrinsic CTAGN fraction inferred using the whole *Swift*-BAT AGN sample (i.e., over the entire range of X-ray luminosity; log L_{14-195} = 40–46 erg s^{-1}; Ricci et al., 2015). *Bottom*: Absorption-corrected 2–10 keV luminosities for the CTAGNs in our sample (the lower limit intrinsic luminosities for NGC 660 and NGC 3627 are plotted using their currently measured intrinsic and observed luminosities, respectively) and the entire *Swift*-BAT sample (grey) vs. distance up to D = 100 Mpc.[8] Blue and red markers indicate CTAGNs in our sample that are detected and not detected in the *Swift*-BAT survey, respectively, while circles indicate true CTAGN and stars mark the CTAGN candidates. Dashed line indicate D = 15 Mpc, the distance limit for our volume-limited sample.

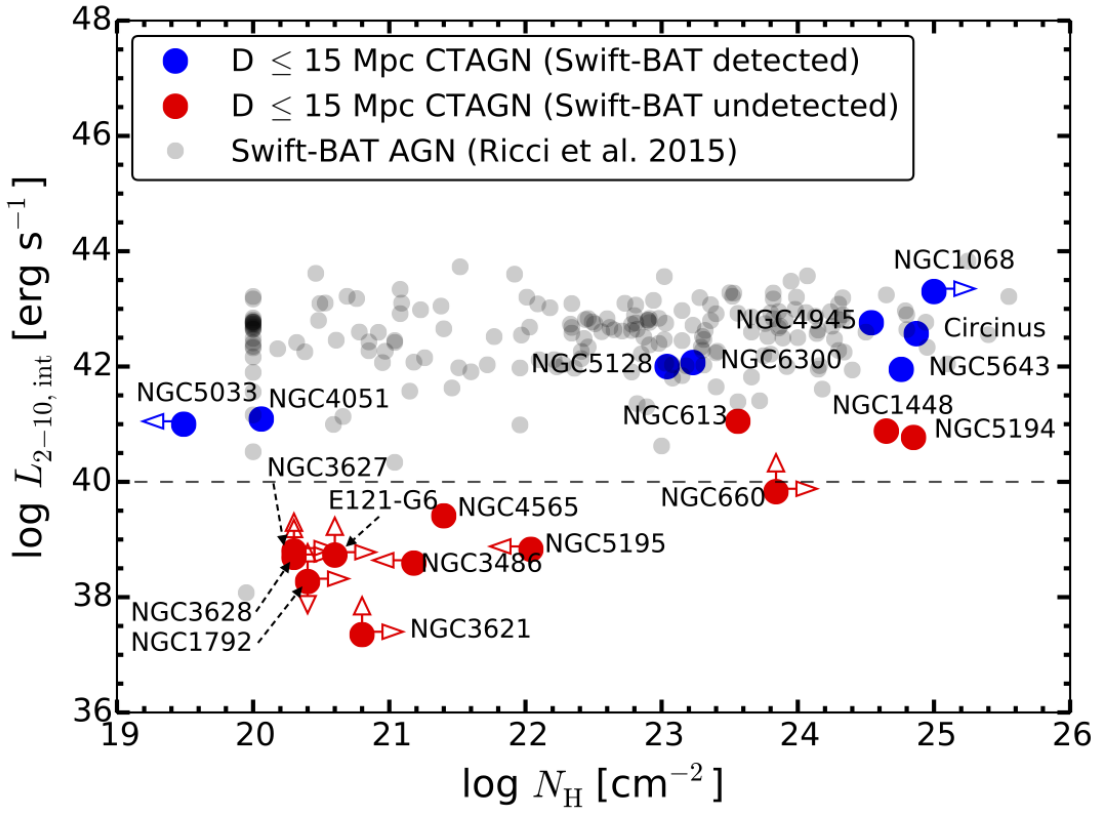

Figure 5.10: Intrinsic 2–10 keV luminosity vs. N_{H} for our sample (the lower limit intrinsic luminosities for NGC 660 and other sources with uncertain N_{H} values are plotted using their currently measured intrinsic and observed luminosities, respectively) and the *Swift*-BAT AGN (grey) at $D \leq 100$ Mpc.[8] Blue and red markers show the AGNs in our sample that are detected and undetected by *Swift*-BAT, respectively. The dashed line indicates $L_{2-10,\mathrm{int}} = 10^{40}$ erg s^{-1}, the lower luminosity end of the *Swift*-BAT AGN sample.

We show a plot of intrinsic 2–10 keV luminosity as a function of $N_{\rm H}$ for our sample and the *Swift*-BAT AGN sample in Figure 5.10.[8] Similar to Figure 5.9, this plot shows that we managed to identify intrinsically lower luminosity CTAGN, but it also shows the wider range of AGN luminosity in our sample, even if we assume that all the AGNs with uncertain $N_{\rm H}$ values are CT (and therefore will have $L_{2-10,\rm int} \sim 10^{40}$ erg s^{-1}); i.e., $L_{2-10,\rm int} \sim 10^{39}$–$10^{44}$ erg s^{-1}. Based on this plot, if we apply a luminosity cut-off of $L_{2-10,\rm int} = 10^{40}$ erg s^{-1}, consistent with the lower luminosity end of the entire *Swift*-BAT AGN sample, the CTAGN fraction calculated for our sample above this luminosity can be as high as $\sim 71\%$ (12/17), assuming that all of the AGNs with no $N_{\rm H}$ measurements and NGC 660 are CT. Even if we exclude these sources, the CTAGN fraction for our sample above this luminosity is still higher than that observed and predicted using the *Swift*-BAT sample; i.e., $\sim 54\%$ (6/11). This demonstrates the large uncertainty in determining an accurate $N_{\rm H}$ distribution of the AGN population at this high obscuration regime. We note however, the lower limit fraction calculated (i.e., 54%) is consistent with the intrinsic fraction inferred by the *Swift*-BAT survey if we take into account the uncertainties due to small number statistics (i.e., $54^{+41}_{-26}\%$; see footnote 7).

5.6 Discussion

In this section we compare the AGN and host galaxy properties of our sample with that of the *Swift*-BAT AGN sample to investigate any potential differences between the two samples, given the unique parameter space (i.e., lower AGN luminosity) that we probed using our $D \leq 15$ Mpc AGN sample.

In Figure 5.11 we show a plot of the AGN bolometric luminosity, $L_{\rm bol}$, as a function of black hole mass, $M_{\rm BH}$, for our sample and the *Swift*-BAT AGN sample (Winter et al., 2012). The bolometric luminosities for the AGNs in our sample were calculated using their absorption-corrected 2–10 keV luminosities, assuming a typical AGN bolometric correction of $L_{\rm bol}/L_{2-10} \approx 20$ (e.g., Elvis et al., 1994; Vasudevan et al., 2010). The bolometric luminosities for the *Swift*-BAT AGNs given in Winter et al. (2012) were determined from their 14–195 keV luminosities. Winter

et al. (2012) measured the $M_{\rm BH}$ for the *Swift*-BAT AGN sample using the bulge luminosity, whilst for our AGN sample, the $M_{\rm BH}$ values were determined using a more diverse technique (e.g., maser mapping, velocity dispersion and bulge luminosity; see Chapter 2 and GA09 for more details). As can be interpreted from Figure 5.7 and 5.10, Figure 5.11 shows that our sample has a broader range of AGN bolometric luminosity (i.e., $L_{\rm bol} \sim 10^{41}$–10^{45} erg s^{-1}, assuming that the AGNs with uncertain $N_{\rm H}$ values are CT). In addition, this plot shows that our sample also has a wider range of Eddington ratio (i.e., accretion rate) as compared to the *Swift*-BAT sample. The *Swift*-BAT detected AGNs generally have higher bolometric luminosities ($L_{\rm bol} \gtrsim 10^{42}$ erg s^{-1}) and higher accretion rates. The $M_{\rm BH}$ distribution of the two samples are significantly different from each other, with our sample dominating lower $M_{\rm BH}$. Performing a Kolmogorov–Smirnov (KS) test on the $M_{\rm BH}$ distributions between the two sample inferred a KS test probability of $P_{\rm KS} \sim 9 \times 10^{-6}$, indicating that the two distributions are significantly different from each other. The mean $M_{\rm BH}$ calculated for our sample, log $<M_{\rm BH,15Mpc}>= 6.85 \pm 0.63$ $M_{\odot}$, is lower than that determined for the *Swift*-BAT sample, log $<M_{\rm BH,BAT}>= 7.91 \pm 0.66$ $M_{\odot}$. However, they are consistent with each other within the statistical uncertainties. We note that the Winter et al. (2012) *Swift*-BAT AGN sample plotted in the figure consists of only Seyfert 1s, which are unobscured AGNs by definition. Therefore, the fact that the CTAGNs in our sample have similar accretion rates as these unobscured AGNs may argue against the AGN evolutionary scenario which suggests that AGN obscuration is associated with a rapid accretion phase (e.g., Draper & Ballantyne, 2010; Treister et al., 2010).

Next, we compare the distribution of the optical classification of the AGN in our sample (see Table 2.1 in Chapter 2) with that of the *Swift*-BAT AGN sample (Baumgartner et al., 2013). This is shown in Figure 5.12. From this diagram, it can be seen that the AGN population in our sample is more diverse in terms of optical type, with most AGNs classified as Seyfert 2s. We have significantly more LINERs and HII galaxies, but lower fraction of Seyfert 1. The higher fraction of LINER and HII galaxy found in our sample show that we managed to identify weaker AGN that are not identified in the optical. The *Swift*-BAT survey is limited by its sensitivity

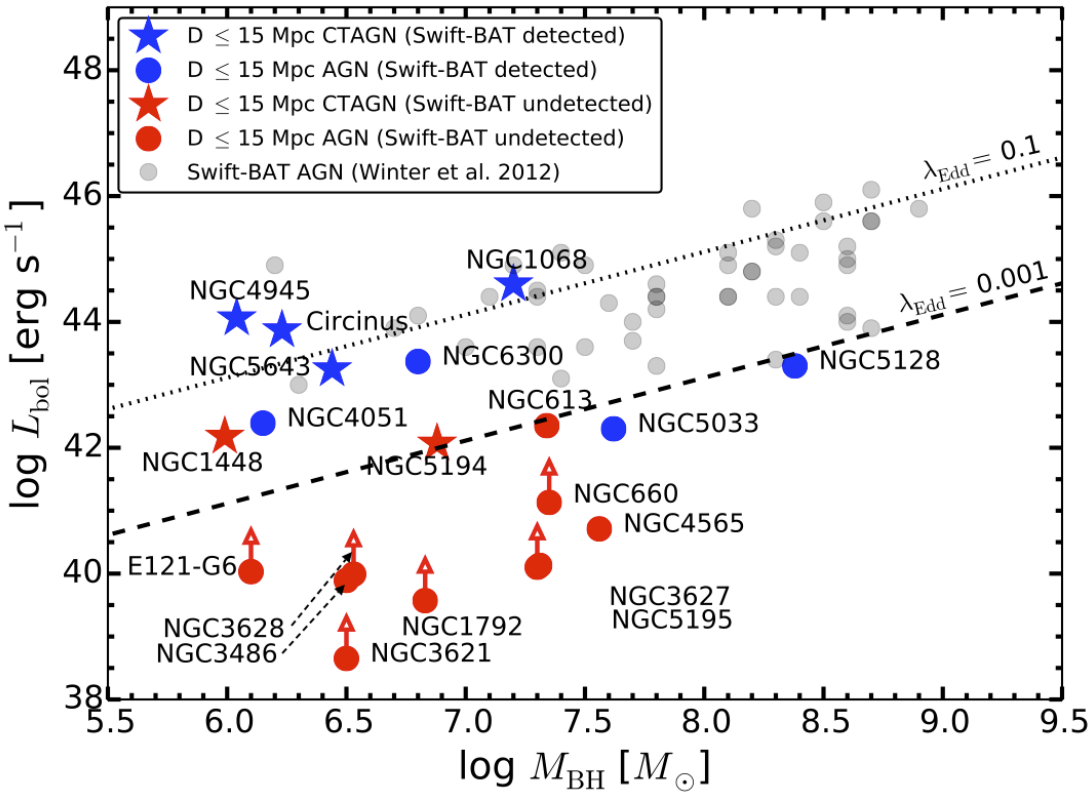

Figure 5.11: The bolometric luminosity vs. $M_{\rm BH}$ for our sample and the *Swift*-BAT AGN sample (grey). Blue and red markers show the AGNs in our sample that are detected and undetected by *Swift*-BAT, respectively, with CTAGNs plotted using the star symbol. The dashed and dotted lines indicate constant Eddington ratios of $\lambda_{\rm Edd} = 0.001$ and 0.1, respectively. The lower limit bolometric luminosities for NGC 660 and other sources with uncertain $N_{\rm H}$ values were calculated using their currently measured intrinsic and observed 2–10 keV luminosities, respectively. Figure adapted from Goulding et al. (2010).

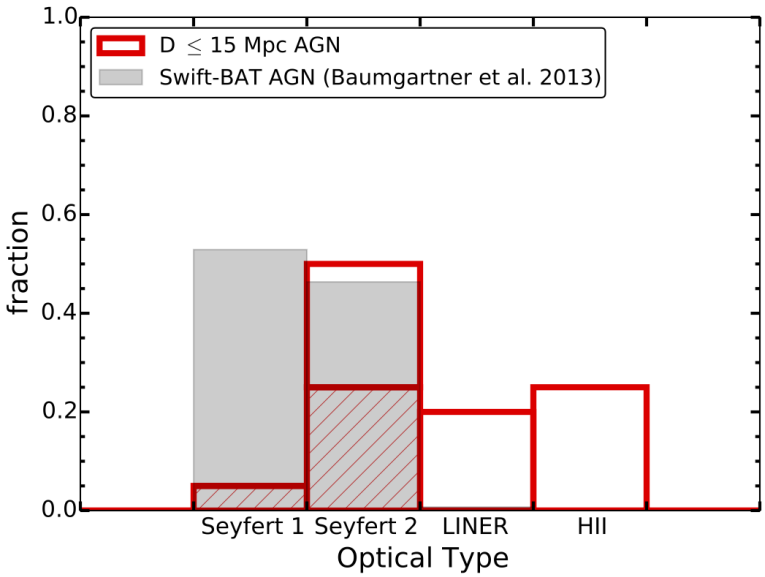

Figure 5.12: The distributions of the optical nuclear classifications for our sample (red) and the *Swift*-BAT sample (grey). Red hatch indicates sources in our sample which are *Swift*-BAT detected.

($f_{14-195} \sim 10^{-11}$ erg s^{-1} cm^{-2}), and is therefore also biased against finding weak AGNs. This is why the survey only find $\lesssim$1% LINER AGN, and do not find any AGN with HII-type nuclear spectrum. This may also be the reason why our sample has a lower fraction of Seyfert 1; i.e., due to the challenge in identifying the broad line components in the optical spectra of weak AGNs since they generally have lower black hole masses, and the optical spectra can also be significantly contaminated by the host galaxies.

In addition, we also compare the star formation rate (SFR) distributions between our sample and the *Swift*-BAT sample. The two distributions are shown in Figure 5.13. We calculated the star formation rate (SFR) for our sample using far-IR luminosity from IRAS (Sanders et al., 2003) following Murphy et al. (2012). For the *Swift*-BAT sample, Shimizu et al. (2017) determined the SFR of the AGNs using SF luminosity obtained through spectral energy distributions decomposition. Despite the different methods that were used to calculate SFR for the two samples, we found that the median SFR for our sample, log $<$SFR$>_{15\mathrm{Mpc}}$= 0.17 $\pm$ 0.38 $M_\odot$/yr is consistent with that found for the *Swift*-BAT AGN sample within the statistical uncertainties; i.e., log $<$SFR$>_{15\mathrm{Mpc}}$= $0.23^{+0.58}_{-0.80}$ $M_\odot$/yr (Shimizu et al.,

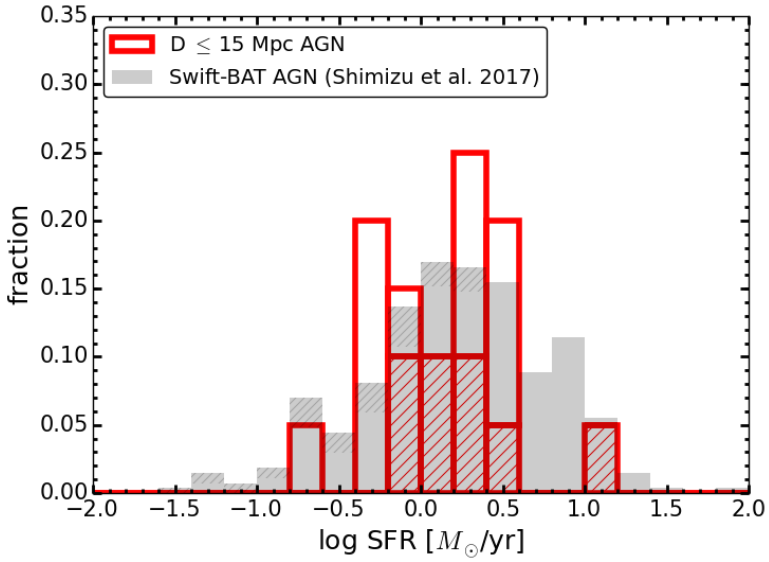

Figure 5.13: SFR distributions for our sample (red) and the *Swift*-BAT sample (grey). Red hatch indicates sources in our sample which are *Swift*-BAT detected, whilst grey hatch indicates the *Swift*-BAT AGNs which have upper limit SFRs.

2017). Performing a KS test on the SFR distributions between the two sample inferred a KS test probability of $P_{\rm KS} \sim 0.1$ and 0.3 when excluding and including sources with upper limit SFR in the *Swift*-BAT sample, respectively. This indicates that the two distributions are not significantly different from each other.

Finally, we investigate the stellar mass (M_*) distributions for our sample and the *Swift*-BAT sample. We show the comparison between the two distributions in Figure 5.14. The stellar mass for our sample was determined using the K-band magnitude and the $J-K$ colour from the 2MASS Large Galaxy Atlas (Jarrett et al., 2003). We calculated M_* for our sample using the relation derived by Westmeier et al. (2011) between the K-band stellar mass-to-light ratio and the $J-K$ colour index. Meanwhilst, M_* for the *Swift*-BAT sample was derived using spectral energy distribution fitting by Koss et al. (2011). Comparing to the *Swift*-BAT AGN sample, we found that the galaxies in our sample generally have lower stellar masses. We performed a KS test between the stellar mass distributions of our sample and the *Swift*-BAT sample and found that the two distributions are significantly different from each other with $P_{\rm KS} \sim 5 \times 10^{-4}$. However, although the mean stellar mass measured for our sample, log $<M_{*,15\rm Mpc}>= 9.90 \pm 0.35$ $M_\odot$, is lower than that

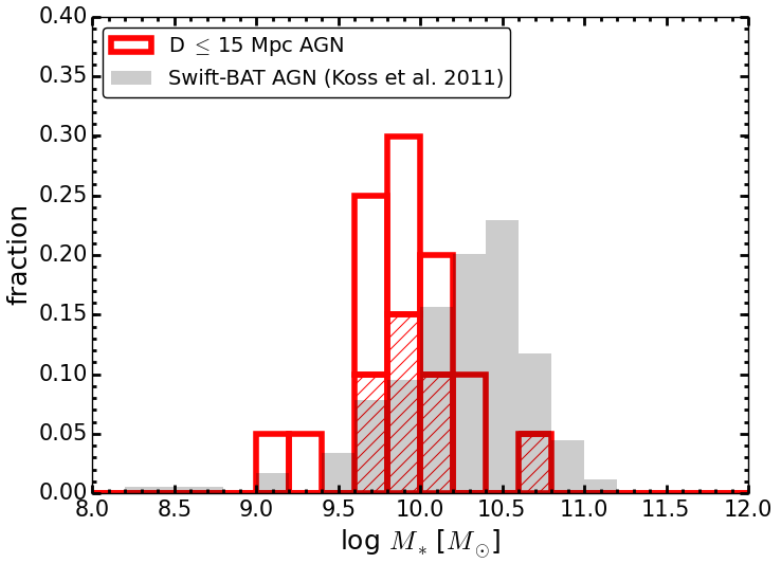

Figure 5.14: M_* distributions for our sample and the *Swift*-BAT sample. Symbols are the same as Figure 5.12.

determined in the Swift-BAT sample, log $<M_{*,\mathrm{BAT}}>$= 10.27 ± 0.40 $M_\odot$, we found that there are in agreement with each other within the statistical uncertainties.

5.7 Summary

In this chapter, we presented an updated census of the CTAGN population and the N_H distribution of AGN in the local universe using a volume-limited AGN sample complete to $D = 15$ Mpc. We performed X-ray spectroscopy using data from multiple observatories, as well as multiwavelength data to identify CTAGN in our sample. Below is a summary of our main results:

- Based on direct N_H measurements using X-ray spectroscopy, we found a 30% fraction of CTAGN in the sample. Multiwavelength techniques select a further two strong CTAGN candidates in the sample (NGC 660 and NGC 3627), increasing the CT fraction to 40%. However, this is still a lower limit given that 20% of the sample have uncertain CT classifications due to insufficient evidence.

- The CTAGN fraction that we found in the sample is significantly higher than

that observed in the *Swift*-BAT AGN sample, but agrees very well with the intrinsic CT fraction predicted, after accounting for the *Swift*-BAT sensitivity limit. In addition, we also found that using our sample, we are able to find intrinsically lower luminosity CTAGNs that are missed by the *Swift*-BAT survey; i.e., down to $L_{2-10,\mathrm{int}} \sim 10^{40}$ erg s^{-1}.

- Motivated by the unique luminosity space that we were able to probe using our AGN sample (i.e., lower luminosity), we compared the general AGN and host galaxy properties between our sample and the *Swift*-BAT AGN sample to investigate any potential differences. We found that our AGN sample has a wider range of Eddington ratio, extending down to a lower Eddington ratio than the *Swift*-BAT sample; our sample also shows a much diverse optical nuclear spectral classification; and a significant fraction of AGN in our sample has lower black hole mass and galaxy stellar mass, as compared to the *Swift*-BAT AGN sample. However, the star formation rates of both samples are consistent with each other.

Chapter 6

Summary & Future Work

In this thesis, I presented an updated census on the Compton-thick (CT) active galactic nucleus (AGN) population and the column density ($N_{\rm H}$) distribution of AGN in our local universe. In this chapter, I provide a summary of the work presented in this thesis (Section 6.1), and discuss ongoing and future work planned to address outstanding issue, and potentially extend this work further (Section 6.2).

6.1 Summary of the presented work

Obscured AGNs ($N_{\rm H} \geq 10^{22}$ cm^{-2}) are known to dominate the AGN population in our universe. Yet, our knowledge of the distribution of AGN as a function of $N_{\rm H}$ remains highly uncertain, especially at the CT regime ($N_{\rm H} \gtrsim 1.5 \times 10^{24}$ cm^{-2}). Based on the synthesis of the cosmic X-ray background (CXB) radiation, the fraction of CTAGN is predicted to be significant ($\sim$10–25% at $\sim$30 keV; e.g., Gilli et al., 2007; Treister et al., 2009; Ueda et al., 2014). However observationally, we are still unable to directly identify a large number of their population, even in our nearby universe (e.g., Ricci et al., 2015). Having a complete census of the CTAGN population is important in our understanding of the CXB radiation and the growth of supermassive black holes.

In this thesis, I have used a very nearby AGN sample located within a volume of $D \leq 15$ Mpc, which was identified using a mid-infrared (mid-IR) selection technique, in an attempt to construct a complete census of the CTAGN population in our local

universe. This sample has provided me with the most local and complete AGN sample that is least limited by flux, and unbiased against both host galaxy and AGN torus obscuration. This has allowed me to directly identify the CTAGN population predicted from other approaches. I used multiwavelength methods to achieve this, mainly direct $N_{\rm H}$ measurements through broadband X-ray spectroscopy, using data from various low and high energy X-ray observatories such as *Chandra* and *NuSTAR*, respectively. In the following section, I summarise the main results from this work.

6.1.1 *NuSTAR* Observations of the Compton-thick Active Galactic Nucleus and Ultraluminous X-ray Source Candidate in NGC 5643

In Chapter 3, I presented the first *NuSTAR* observations of NGC 5643, which provide the first detections of the AGN and the ultraluminous X-ray source (ULX) candidate in the galaxy at high X-ray energies ($E \gtrsim 10$ keV), separately resolved from each other. The AGN has been suggested to be CT from previous X-ray observations. However, there have been significant uncertainties in the characterisation of the nuclear spectrum due to the lack of high-quality high energy X-ray observations, and the presence of a nearby ULX candidate, NGC 5643 X–1. Using our new *NuSTAR* observations, combined with archival *Chandra*, *XMM-Newton* and *Swift*-BAT data, we performed a high quality broadband X-ray spectral analysis of the CTAGN candidate in NGC 5643 over two decades in energy (∼0.5–100 keV). This has allowed us to directly measure the obscuring column density toward the nucleus, and unambiguously confirmed that the AGN is CT, with $N_{\rm H} \gtrsim 5 \times 10^{24}$ cm^{-2}. The absorption-corrected 2–10 keV luminosity range measured from the best fitting physically motivated torus models is $L_{2-10,\rm int} = (0.8–1.7) \times 10^{42}$ erg s^{-1}. This is consistent with that predicted from multiwavelength intrinsic luminosity indicators, and is at the lower end of the luminosity range of the local bona-fide CTAGN population (e.g., Gandhi et al., 2014).

In addition to the AGN, we also analysed the *NuSTAR* data, as well as archival X-ray data for NGC 5643 X–1. The *NuSTAR* data shows evidence for a spectral cut-

off at $E \sim 10$ keV, similar to that seen in other ULXs observed by *NuSTAR*. Based on the 3–8 keV luminosities measured for the source from the archival X-ray data and our new *NuSTAR* data, we found that it has significantly varied between different observations carried out between 2003 and 2014. Based on these results, along with the absence of unambiguous counterparts of the source at other wavelengths, we concluded that NGC 5643 X–1 is highly likely to be a ULX.

6.1.2 A new CTAGN in our cosmic backyard: Unveiling the buried nucleus in NGC 1448 with *NuSTAR*

In Chapter 4, I presented a multiwavelength view of the AGN in NGC 1448 across the mid-IR continuum, optical, and X-rays. These data provide the first identifications of the AGN at these wavelengths. At a distance of 11.5 Mpc, NGC 1448 is one of the nearest bright galaxies ($L_{8-1000\mu m} > 10^9 L_{\odot}$) to our own. Yet, the presence of an AGN in the galaxy was only recently discovered, less than a decade ago, by Goulding & Alexander (2009). As a follow-up to this study, we observed the source at low and high energy X-rays using *Chandra* and *NuSTAR*, respectively. Our data not only provide the first detection of the AGN in X-rays, but also revealed that the AGN is buried under a CT column of obscuring gas. We performed a broadband X-ray spectral analysis on the AGN and directly measured an obscuring column density of $N_{\rm H}({\rm los}) \gtrsim 2.5 \times 10^{24}$ cm^{-2}. The intrinsic 2–10 keV luminosity we inferred from the best-fitting torus models is $L_{2-10,{\rm int}} = (3.5–7.6) \times 10^{40}$ erg s^{-1}, consistent with that predicted from our optical and mid-IR data. This makes the AGN in NGC 1448 one of the lowest luminosity CTAGNs known to date. This discovery demonstrates the capability of *NuSTAR* for finding faint CTAGN, which are missed by previous generations of high energy X-ray telescopes such as *Swift*-BAT.

In addition to the X-ray observations, we also performed optical spectroscopy on the nucleus using the European Southern Observatory New Technology Telescope. Based on emission line diagnostic diagrams (Kewley et al., 2001; Kauffmann et al., 2003), we re-classified the optical nuclear spectrum of NGC 1448 as a Seyfert, therefore identifying the AGN at optical wavelengths for the first time. Our analysis of the optical spectra of NGC 1448 at different regions and using different slit

sizes demonstrate the challenges in identifying AGNs at optical wavelengths, especially when they are located in highly inclined galaxies that can significantly dilute and/or extinguish the optical emission from the AGNs. This may explain why the optical nuclear spectrum of NGC 1448 was misidentified as an HII region previously. We also observed the source at high spatial resolution mid-IR continuum using Gemini/T-ReCS. Our observation revealed a compact source coincident with the nuclear position of NGC 1448. This result further confirms the presence of an AGN in the galaxy.

6.1.3 Towards a complete census of the CTAGN population and the $N_{\rm H}$ distribution of AGN in the local universe

In Chapter 5, I presented a multiwavelength analysis on all of the AGNs in my sample. We used X-ray spectroscopy with new and archival data from multiple observatories, including high X-ray energy data from *NuSTAR*, as well as multiwavelength data to identify CTAGNs and CTAGN candidates in the sample. On the basis of $N_{\rm H}$ measurements made from X-ray spectral analysis, we directly identified a ≈30% population of CTAGN in the sample. Using multiwavelength techniques; i.e., $f_{2-10,\rm obs}$:$f_{\rm [OIII]\lambda5007A}$, $L_{2-10,\rm obs}$:$L_{12\mu\rm m}$, and $L_{2-10,\rm obs}$:$L_{\rm [Nev]\lambda14.32\mu m}$ ratios, we found a further two strong CTAGN candidates in the sample (NGC 660 and NGC 3627). Including these two sources as CTAGNs increases the fraction to ≈40%. The CTAGN fraction in the sample could be up to ≈60% if we assume all of the remaining AGNs with "uncertain classifications" (i.e., no reliable $N_{\rm H}$ measurements and insufficient CT evidence from multiwavelength data) are CT. The lower limit fraction that we found; i.e., ≈30%, is significantly higher than that directly observed in the *Swift*-BAT AGN sample, but agrees very well with the intrinsic CTAGN fraction predicted (taking into account the sensitivity limit of the *Swift*-BAT survey). Using our very local AGN sample, we are able to identify intrinsically lower luminosity CTAGNs which have been missed by the *Swift*-BAT survey; i.e., down to $L_{2-10,\rm int} \sim 10^{40}$ erg $\rm s^{-1}$, about an order of magnitude lower than that identified by *Swift*-BAT. Given the unique region probed by our AGN sample in the 2–10 keV luminosity vs. $N_{\rm H}$ parameter space as compared to the *Swift*-BAT AGN sample (i.e., lower luminosity),

we investigated whether there are any differences between the two AGN samples. Comparing the AGN and host galaxy properties between the two samples, we found that the majority of the AGNs in our sample have lower black hole masses and lower galaxy stellar masses. Our sample also has a much diverse optical nuclear spectral type, and the range of the AGN Eddington ratio for our sample is much broader than the *Swift*-BAT AGN sample, extending down to a lower value. However, we found that the star formation rates of both samples are consistent with each other.

6.2 Ongoing/Future work

The work presented in this thesis has provided the first, and so far, the most complete census of the CTAGN population and the AGN $N_{\rm H}$ distribution in our cosmic backyard ($D \leq 15$ Mpc). In the following section, I outline ongoing work and follow-up projects to further complete this census, and suggest plans to potentially extend this research into the future.

6.2.1 Completing the census of the CTAGN population and the $N_{\rm H}$ distribution of AGN in our local universe

The $N_{\rm H}$ distribution of AGN that I have presented in this work (see Chapter 5) is so far 60–70% complete (excluding and including CTAGN candidates, respectively). In order to achieve 100% completeness, we require sufficient quality X-ray data, particularly high energy X-ray data, for the remaining sources with uncertain $N_{\rm H}$ measurements to allow us to directly measure their $N_{\rm H}$ values through broadband X-ray spectral fittings. We have successfully proposed for *NuSTAR* observations for the 4 AGNs in our sample with uncertain CT classifications; i.e., ESO 121-G6, NGC 1792, NGC 3621 and NGC 3628, as well as for one of our CTAGN candidates which has not been observed by *NuSTAR*, NGC 3627 (see Table 2.3 in Chapter 2). The total *NuSTAR* observing time we will receive for these 5 sources is 210 ks, and this will boost the high X-ray energy data for this $D \leq 15$ Mpc AGN sample to 90% complete. We did not propose for *NuSTAR* observations for the remaining 10% of the sample (two sources - NGC 613 and NGC 4565) as the archival

low energy X-ray data have provided reliable constraint on their $N_{\rm H}$ measurements (obscured but Compton-thin for the case of NGC 613; Castangia et al., 2013, and unobscured for the case NGC 4565; see Chapter 5 and also Chiaberge et al., 2006). In addition to *NuSTAR*, we will also receive coordinated low energy X-ray observations for ESO 121-G6 (*Chandra*) and NGC 3621 (*XMM-Newton*) to facilitate our X-ray analysis of these sources. Obtaining the *Chandra* observation for ESO 121-G6 will provide *Chandra* coverage for *all* of the AGN in this local sample. These X-ray observations will help us to improve the current constraints that we have on the CTAGN population and the $N_{\rm H}$ distribution of AGN at $D \leq 15$ Mpc, either through broadband X-ray spectroscopy for the case of sufficient quality data, or hard to soft X-ray band ratios otherwise.

6.2.2 Does the AGN torus disappear at low luminosity?

In Chapter 5, I showed a plot of $L_{2-10,\rm int}$ vs. $N_{\rm H}$ for my AGN sample (Figure 5.10). Based on this plot, if we assume that all of the AGNs with no $N_{\rm H}$ measurements are unobscured or mildly obscured ($N_{\rm H} \lesssim 10^{22}$ cm^{-2}), and therefore their $L_{2-10,\rm int} \approx L_{2-10,\rm obs}$, this will mean that the intrinsic 2–10 keV luminosity for the $D \leq 15$ Mpc AGN sample will range between $\sim 10^{37}$–10^{44} erg s^{-1}, spanning over $\sim$7 orders of magnitude. This demonstrates that with our sample, we are able to probe into the lower luminosity end of the AGN population, exploring into a new parameter space that is not possible for more distant samples. Even if we assume that the sources with uncertain $N_{\rm H}$ values are CT, and therefore will have $L_{2-10,\rm int} \sim 100 \times L_{2-10,\rm obs}$, the intrinsic 2–10 keV luminosity range will still probe the lower luminosity end of the AGN population; i.e., down to 10^{39} erg s^{-1}. As a follow-up to our scheduled *NuSTAR* observations of the 5 AGNs in our sample with no $N_{\rm H}$ measurements, we are also hoping to test the AGN torus properties at low luminosity. Based on our current results, all three of our sources with $L_{2-10,\rm int} \lesssim 10^{40}$ erg s^{-1} (NGC 3486, NGC 4565 and NGC 5195) are unobscured, or just mildly obscured; i.e., $N_{\rm H} \lesssim 10^{22}$ cm^{-2}. This may indicate that at low luminosity of $L_{2-10,\rm int} < 10^{40}$ erg s^{-1}, the AGN torus is not well developed or does not exist, supporting the suggestions from some previous studies (e.g., Elitzur & Shlosman, 2006; Hönig & Beckert, 2007). All 5

AGNs in our sample with no $N_{\rm H}$ measurements are expected to be intrinsically low luminosity AGN even if they are CT ($L_{bol} \lesssim 10^{42}$ erg s^{-1}). If these AGNs are also found to be unobscured or just mildy obscured following our *NuSTAR* observations, this will provide further support for these studies. However, if they are indeed found to be obscured as suggested by our $L_{2-10,\rm obs}$:$L_{12\mu\rm m}$ and L_{2-10}:$L_{\rm [NeV]}$ diagnostics (see Chapter 5), this will also be a crucial findings as it will argue againts these studies.

6.2.3 The origin of the [NeV] emission line

Due to the high ionisation energy requires to produce the [NeV] line (97.1 eV), it is only emitted in extreme conditions, and therefore has been used as an unambiguous indicator for AGN activity. Theoretically, it has been predicted to be produced in a dense population of Wolf-Rayet stars (Schaerer & Stasińska, 1999) and extreme high velocity shocks driven by starburst. However, these have not been seen in observations, and do not appear to be the case for the AGNs in our sample (Goulding & Alexander, 2009). Following the complete measurements of obscuration in the AGN sample and therefore the intrinsic X-ray luminosities, we will be able to test whether the $L_{2-10,\rm int}$ vs. $L_{\rm [NeV]}$ relationship found by e.g., Weaver et al. (2010), holds down to lower AGN luminosity. If our *NuSTAR* observations reveal that the remaining AGNs have consistent $L_{2-10,\rm int}$ with the $L_{\rm [NeV]}$ on the basis of the Weaver et al. (2010) relationship, this will indicate that the [NeV] emission line is indeed an accurate indicator for AGN activity (down to $L_{2-10,\rm int} \sim 10^{40}$ erg s^{-1}). However if our data indicate otherwise, this will suggest that other extreme activities within the host galaxies that are producing, or significantly contributing to the [NeV] emission line flux measured from the *Spitzer* high resolution IR Spectrographs (IRS) Short-High (SH) module (aperture size = 4.7 × 11.3 arcsec^2).

If this is true, the launch of the James Webb Space Telescope (JWST) will allow us to address this issue. The JWST mid-IR instrument (MIRI) medium resolution spectroscopy (MRS) will allow us to obtain both spectral and spatial information from the outlying sources (the *Spitzer*-IRS SH module only acquired spectral information). Combined with the higher spatial resolution that will be provided by the instrument (0.1″; i.e., ∼an order of magnitude higher than *Spitzer*), JWST will be

powerful in helping us to trace the [NeV] emission in these galaxies. If the JWST observations reveal that the physical origin of the [NeV] line emission from the outlying sources are solely from the nucleus, then this will indicate that the $L_{2-10,\mathrm{int}}$ vs. $L_{[\mathrm{NeV}]}$ relationship does not hold at low AGN luminosity, and this may also be true for the relationships between the intrinsic X-ray luminosity of AGN and other narrow line region emission lines (e.g., [OIII], [OIV]). If the [NeV] emission is detected at larger physical scales of the galaxies, this will suggest that the [NeV] line emission is not an unambiguous tracer for AGN activity, at least at low luminosity. We can follow-up this finding by investigating what other extreme processes in the galaxies that are able to produce this high ionisation line.

Bibliography

Abazajian, K. N., Adelman-McCarthy, J. K., Agüeros, M. A., et al. 2009, ApJS, 182, 543

Abramowicz, M. A., Czerny, B., Lasota, J. P., & Szuszkiewicz, E. 1988, ApJ, 332, 646

Ackermann, M., Ajello, M., Allafort, A., et al. 2012, ApJ, 747, 104

Akylas, A., Georgakakis, A., Georgantopoulos, I., Brightman, M., & Nandra, K. 2012, A&A, 546, A98

Alexander, D. M., Bauer, F. E., Brandt, W. N., et al. 2003, AJ, 126, 539

Alexander, D. M., Bauer, F. E., Chapman, S. C., et al. 2005, ApJ, 632, 736

Alexander, D. M., & Hickox, R. C. 2012, NewAR, 56, 93

Alonso-Herrero, A., Ramos Almeida, C., Mason, R., et al. 2011, ApJ, 736, 82

Annuar, A., Gandhi, P., Alexander, D. M., et al. 2015, ApJ, 815, 36

Annuar, A., Alexander, D. M., Gandhi, P., et al. 2017, ApJ, 836, 165

Antonucci, R. R. J., & Miller, J. S. 1985, ApJ, 297, 621

Antonucci, R. 1993, ARA&A, 31, 473

Antonucci, R. 2002, in Astrophysical Spectropolarimetry, ed. J. Trujillo-Bueno, F. Moreno-Insertis, & F. Sánchez, 151–175

Arévalo, P., Bauer, F. E., Puccetti, S., et al. 2014, ApJ, 791, 81

Argo, M. K., van Bemmel, I. M., Connolly, S. D., & Beswick, R. J. 2015, MNRAS, 452, 1081

Asmus, D., Hönig, S. F., Gandhi, P., Smette, A., & Duschl, W. J. 2014, MNRAS, 439, 1648

Asmus, D., Gandhi, P., Hönig, S. F., Smette, A., & Duschl, W. J. 2015, MNRAS, 454, 766

Assef, R. J., Stern, D., Kochanek, C. S., et al. 2013, ApJ, 772, 26

Bachetti, M., Rana, V., Walton, D. J., et al. 2013, ApJ, 778, 163

Baldwin, J. A., Phillips, M. M., & Terlevich, R. 1981, PASP, 93, 5

Baloković, M., Comastri, A., Harrison, F. A., et al. 2014, ApJ, 794, 111

Barthelmy, S. D., Barbier, L. M., Cummings, J. R., et al. 2005, Space Sci. Rev., 120, 143

Bassani, L., Dadina, M., Maiolino, R., et al. 1999, ApJS, 121, 473

Bauer, F. E., Arévalo, P., Walton, D. J., et al. 2015, ApJ, 812, 116

Baumgartner, W. H., Tueller, J., Markwardt, C. B., et al. 2013, ApJS, 207, 19

Becker, R. H., White, R. L., & Helfand, D. J. 1995, ApJ, 450, 559

Beckmann, V., & Shrader, C. 2012, in Proceedings of "An INTEGRAL view of the high-energy sky (the first 10 years)" - 9th INTEGRAL Workshop and celebration of the 10th anniversary of the launch (INTEGRAL 2012). 15-19 October 2012. Bibliotheque Nationale de France, Paris, France. Published online at ¡A href="http://pos.sissa.it/cgi-bin/reader/conf.cgi?confid=176"¿http://pos.sissa.it/cgi-bin/reader/conf.cgi?confid=176¡/A¿, id.69, 69

Bell, E. F., McIntosh, D. H., Katz, N., & Weinberg, M. D. 2003, ApJS, 149, 289

Bennert, N., Jungwiert, B., Komossa, S., Haas, M., & Chini, R. 2006, A&A, 456, 953

Bianchi, S., Matt, G., Fiore, F., et al. 2002, A&A, 396, 793

Bianchi, S., Guainazzi, M., & Chiaberge, M. 2006, A&A, 448, 499

Boorman, P. G., Gandhi, P., Alexander, D. M., et al. 2016, ApJ, 833, 245

Boyle, B. J., Fong, R., Shanks, T., & Peterson, B. A. 1990, MNRAS, 243, 1

Brandt, W. N., Alexander, D. M., Hornschemeier, A. E., et al. 2001, AJ, 122, 2810

Brandt, W. N., & Alexander, D. M. 2015, A&A Rev., 23, 1

Brightman, M., & Nandra, K. 2008, MNRAS, 390, 1241

Brightman, M., & Nandra, K. 2011, MNRAS, 413, 1206

Brightman, M., Baloković, M., Stern, D., et al. 2015, ApJ, 805, 41

Bruzual, G., & Charlot, S. 2003, MNRAS, 344, 1000

Buchner, J., Georgakakis, A., Nandra, K., et al. 2015, ApJ, 802, 89

Burlon, D., Ajello, M., Greiner, J., et al. 2011, ApJ, 728, 58

Burrows, D. N., Hill, J. E., Nousek, J. A., et al. 2005, Space Sci. Rev., 120, 165

Capetti, A., Macchetto, F., Axon, D. J., Sparks, W. B., & Boksenberg, A. 1995, ApJ, 452, L87

Cappi, M., Panessa, F., Bassani, L., et al. 2006, A&A, 446, 459

Cardelli, J. A., Clayton, G. C., & Mathis, J. S. 1989, ApJ, 345, 245

Cash, W. 1979, ApJ, 228, 939

Castangia, P., Panessa, F., Henkel, C., Kadler, M., & Tarchi, A. 2013, MNRAS, 436, 3388

Chiaberge, M., Gilli, R., Macchetto, F. D., & Sparks, W. B. 2006, ApJ, 651, 728

Cid Fernandes, R., Heckman, T., Schmitt, H., González Delgado, R. M., & Storchi-Bergmann, T. 2001, ApJ, 558, 81

Comastri, A. 2004, in Astrophysics and Space Science Library, Vol. 308, Supermassive Black Holes in the Distant Universe, ed. A. J. Barger, 245

Condon, J. J., Cotton, W. D., Greisen, E. W., et al. 1998, AJ, 115, 1693

Corral, A., Della Ceca, R., Caccianiga, A., et al. 2011, A&A, 530, A42

Davé, R. 2008, MNRAS, 385, 147

Davies, R. I., Maciejewski, W., Hicks, E. K. S., et al. 2014, ApJ, 792, 101

Della Ceca, R., Severgnini, P., Caccianiga, A., et al. 2008, Mem. Soc. Astron. Italiana, 79, 65

Diamond-Stanic, A. M., Rieke, G. H., & Rigby, J. R. 2009, ApJ, 698, 623

Diamond-Stanic, A. M., & Rieke, G. H. 2012, ApJ, 746, 168

Done, C. 2010, ArXiv e-prints, arXiv:1008.2287

Done, C., Davis, S. W., Jin, C., Blaes, O., & Ward, M. 2012, MNRAS, 420, 1848

Draper, A. R., & Ballantyne, D. R. 2010, ApJ, 715, L99

Earnshaw, H. M., Roberts, T. P., Heil, L. M., et al. 2016, MNRAS, 456, 3840

Edge, D. O., Shakeshaft, J. R., McAdam, W. B., Baldwin, J. E., & Archer, S. 1959, MmRAS, 68, 37

Elitzur, M., & Shlosman, I. 2006, ApJ, 648, L101

Elvis, M., Wilkes, B. J., McDowell, J. C., et al. 1994, ApJS, 95, 1

Elvis, M. 2012, Journal of Physics Conference Series, 372, 012032

Esquej, P., Alonso-Herrero, A., González-Martín, O., et al. 2014, ApJ, 780, 86

Fabian, A. C. 1999, MNRAS, 308, L39

Fabian, A. C. 2012, ARA&A, 50, 455

Fath, E. A. 1909, Lick Observatory Bulletin, 5, 71

Fischer, T. C., Crenshaw, D. M., Kraemer, S. B., & Schmitt, H. R. 2013, ApJS, 209, 1

Foschini, L., Di Cocco, G., Ho, L. C., et al. 2002, A&A, 392, 817

Fruscione, A., McDowell, J. C., Allen, G. E., et al. 2006, in Proc. SPIE, Vol. 6270, Society of Photo-Optical Instrumentation Engineers (SPIE) Conference Series, 62701V

Fürst, F., Müller, C., Madsen, K. K., et al. 2016, ApJ, 819, 150

Gallimore, J. F., Elitzur, M., Maiolino, R., et al. 2016, ApJ, 829, L7

Gandhi, P., Horst, H., Smette, A., et al. 2009, A&A, 502, 457

Gandhi, P., Lansbury, G. B., Alexander, D. M., et al. 2014, ApJ, 792, 117

Gandhi, P., Yamada, S., Ricci, C., et al. 2015, MNRAS, 449, 1845

Gandhi, P., Annuar, A., Lansbury, G. B., et al. 2016, ArXiv e-prints, arXiv:1605.08041

García-Burillo, S., Combes, F., Ramos Almeida, C., et al. 2016, ApJ, 823, L12

Geach, J. E., Smail, I., Moran, S. M., et al. 2011, ApJ, 730, L19

Gebhardt, K., Bender, R., Bower, G., et al. 2000, ApJ, 539, L13

Gehrels, N. 1986, ApJ, 303, 336

Genzel, R., Lutz, D., Sturm, E., et al. 1998, ApJ, 498, 579

Georgantopoulos, I., Comastri, A., Vignali, C., et al. 2013, A&A, 555, A43

George, I. M., & Fabian, A. C. 1991, MNRAS, 249, 352

Giacconi, R., Reidy, W. P., Zehnpfennig, T., Lindsay, J. C., & Muney, W. S. 1965, ApJ, 142, 1274

Gilfanov, M. 2004, MNRAS, 349, 146

Gilli, R., Comastri, A., & Hasinger, G. 2007, A&A, 463, 79

Gliozzi, M., Satyapal, S., Eracleous, M., Titarchuk, L., & Cheung, C. C. 2009, ApJ, 700, 1759

González-Martín, O., Masegosa, J., Márquez, I., Guainazzi, M., & Jiménez-Bailón, E. 2009, A&A, 506, 1107

Goulding, A. D., & Alexander, D. M. 2009, MNRAS, 398, 1165

Goulding, A. D., Alexander, D. M., Lehmer, B. D., & Mullaney, J. R. 2010, MNRAS, 406, 597

Goulding, A. D., Alexander, D. M., Mullaney, J. R., et al. 2011, MNRAS, 411, 1231

Goulding, A. D., Alexander, D. M., Bauer, F. E., et al. 2012, ApJ, 755, 5

Greenhill, L. J., Kondratko, P. T., Lovell, J. E. J., et al. 2003, ApJ, 582, L11

Gu, Q., Melnick, J., Cid Fernandes, R., et al. 2006, MNRAS, 366, 480

Guainazzi, M., Rodriguez-Pascual, P., Fabian, A. C., Iwasawa, K., & Matt, G. 2004, MNRAS, 355, 297

Güver, T., & Özel, F. 2009, MNRAS, 400, 2050

Harrison, F. A., Christensen, F. E., Craig, W., et al. 2005, Experimental Astronomy, 20, 131

Harrison, F. A., Craig, W. W., Christensen, F. E., et al. 2013, ApJ, 770, 103

Harrison, C. 2014, PhD thesis, Durham University ¡EMAIL¿c.m.harrison@durham.ac.uk¡/EMAIL¿

Helou, G., & Walker, D. W., eds. 1988, Infrared astronomical satellite (IRAS) catalogs and atlases. Volume 7: The small scale structure catalog, Vol. 7, 1–265

Hill, M. D., & Shanks, T. 2011, MNRAS, 410, 762

Ho, L. C., Filippenko, A. V., & Sargent, W. L. W. 1997, ApJS, 112, 315

Ho, L. C., Feigelson, E. D., Townsley, L. K., et al. 2001, ApJ, 549, L51

Ho, L. C. 2008, ARA&A, 46, 475

Hönig, S. F., Beckert, T., Ohnaka, K., & Weigelt, G. 2006, A&A, 452, 459

Hönig, S. F., & Beckert, T. 2007, MNRAS, 380, 1172

Hopkins, P. F., Hernquist, L., Cox, T. J., & Kereš, D. 2008, ApJS, 175, 356

Horst, H., Gandhi, P., Smette, A., & Duschl, W. J. 2008, A&A, 479, 389

Houck, J. R., Roellig, T. L., van Cleve, J., et al. 2004, ApJS, 154, 18

Hubble, E. P. 1926, ApJ, 64, doi:10.1086/143018

Ivezić, Ž., Menou, K., Knapp, G. R., et al. 2002, AJ, 124, 2364

Iwasawa, K., Fabian, A. C., & Matt, G. 1997, MNRAS, 289, 443

Jarrett, T. H., Chester, T., Cutri, R., Schneider, S. E., & Huchra, J. P. 2003, AJ, 125, 525

Jonker, P. G., Heida, M., Torres, M. A. P., et al. 2012, ApJ, 758, 28

Kalberla, P. M. W., Burton, W. B., Hartmann, D., et al. 2005, A&A, 440, 775

Kauffmann, G., Heckman, T. M., Tremonti, C., et al. 2003, MNRAS, 346, 1055

Kawamuro, T., Ueda, Y., Tazaki, F., Terashima, Y., & Mushotzky, R. 2016, ArXiv e-prints, arXiv:1604.07915

Kennicutt, Jr., R. C. 1998, ApJ, 498, 541

Kerr, R. P. 1963, Physical review letters, 11, 237

Kewley, L. J., Dopita, M. A., Sutherland, R. S., Heisler, C. A., & Trevena, J. 2001, ApJ, 556, 121

Kewley, L. J., Groves, B., Kauffmann, G., & Heckman, T. 2006, MNRAS, 372, 961

Kirkpatrick, A., Pope, A., Charmandaris, V., et al. 2013, ApJ, 763, 123

Kishimoto, M. 1999, ApJ, 518, 676

Kitaguchi, T., Grefenstette, B. W., Harrison, F. A., et al. 2011, in Proc. SPIE, Vol. 8145, Society of Photo-Optical Instrumentation Engineers (SPIE) Conference Series, 814507

Kocevski, D. D., Brightman, M., Nandra, K., et al. 2015, ApJ, 814, 104

Kong, A. K. H., Yang, Y. J., Yen, T.-C., Feng, H., & Kaaret, P. 2010, ApJ, 722, 1816

Kormendy, J., & Richstone, D. 1995, ARA&A, 33, 581

Kormendy, J., & Ho, L. C. 2013, ARA&A, 51, 511

Koss, M., Mushotzky, R., Veilleux, S., et al. 2011, ApJ, 739, 57

Koss, M., Mushotzky, R., Baumgartner, W., et al. 2013, ApJ, 765, L26

Koss, M. J., Romero-Canizales, C., Baronchelli, L., et al. 2015, ArXiv e-prints, arXiv:1505.03524

Koss, M. J., Assef, R., Balokovic, M., et al. 2016, ArXiv e-prints, arXiv:1604.07825

Lansbury, G. B., Alexander, D. M., Del Moro, A., et al. 2014, ApJ, 785, 17

Lansbury, G. B., Gandhi, P., Alexander, D. M., et al. 2015, ApJ, 809, 115

Lanzuisi, G., Ranalli, P., Georgantopoulos, I., et al. 2015, A&A, 573, A137

Lehmer, B. D., Xue, Y. Q., Brandt, W. N., et al. 2012, ApJ, 752, 46

Li, A., & Draine, B. T. 2001, ApJ, 554, 778

Liu, Y., & Li, X. 2015, MNRAS, 448, L53

Lumb, D. H., Schartel, N., & Jansen, F. A. 2012, Optical Engineering, 51, 011009

Luo, B., Bauer, F. E., Brandt, W. N., et al. 2008, ApJS, 179, 19

Luo, B., Brandt, W. N., Alexander, D. M., et al. 2013, ApJ, 772, 153

Luo, B., Brandt, W. N., Xue, Y. Q., et al. 2017, ApJS, 228, 2

Madsen, K. K., Harrison, F. A., Markwardt, C., et al. 2015, ArXiv e-prints, arXiv:1504.01672

Magdziarz, P., & Zdziarski, A. A. 1995, MNRAS, 273, 837

Magorrian, J., Tremaine, S., Richstone, D., et al. 1998, AJ, 115, 2285

Maiolino, R., Salvati, M., Bassani, L., et al. 1998, A&A, 338, 781

Marconi, A., & Hunt, L. K. 2003, ApJ, 589, L21

Marinucci, A., Miniutti, G., Bianchi, S., Matt, G., & Risaliti, G. 2013, MNRAS, 436, 2500

Mason, R. E., Lopez-Rodriguez, E., Packham, C., et al. 2012, AJ, 144, 11

Mateos, S., Alonso-Herrero, A., Carrera, F. J., et al. 2012, MNRAS, 426, 3271

Matt, G., Perola, G. C., & Piro, L. 1991, A&A, 247, 25

Matt, G., Guainazzi, M., Frontera, F., et al. 1997, A&A, 325, L13

Matt, G., Fabian, A. C., Guainazzi, M., et al. 2000, MNRAS, 318, 173

Matt, G., Bianchi, S., Marinucci, A., et al. 2013, A&A, 556, A91

McConnell, N. J., & Ma, C.-P. 2013, ApJ, 764, 184

McKernan, B., Ford, K. E. S., & Reynolds, C. S. 2010, MNRAS, 407, 2399

Miller, J. M., Raymond, J., Fabian, A. C., et al. 2004, ApJ, 601, 450

Mineo, S., Gilfanov, M., & Sunyaev, R. 2012, MNRAS, 419, 2095

Mineshige, S., Hirano, A., Kitamoto, S., Yamada, T. T., & Fukue, J. 1994, ApJ, 426, 308

Molendi, S., Bianchi, S., & Matt, G. 2003, MNRAS, 343, L1

Monard, L. A. G., Kneip, R., Brimacombe, J., et al. 2014, Central Bureau Electronic Telegrams, 3977

Moorwood, A. F. M., & Glass, I. S. 1984, A&A, 135, 281

Morris, S., Ward, M., Whittle, M., Wilson, A. S., & Taylor, K. 1985, MNRAS, 216, 193

Mould, J. R., Huchra, J. P., Freedman, W. L., et al. 2000, ApJ, 529, 786

Mullaney, J. R., Alexander, D. M., Goulding, A. D., & Hickox, R. C. 2011, MNRAS, 414, 1082

Murphy, K. D., & Yaqoob, T. 2009, MNRAS, 397, 1549

Murphy, E. J., Bremseth, J., Mason, B. S., et al. 2012, ApJ, 761, 97

Narayan, R., & Yi, I. 1994, ApJ, 428, L13

Nenkova, M., Sirocky, M. M., Ivezić, Ž., & Elitzur, M. 2008, ApJ, 685, 147

Netzer, H., Lemze, D., Kaspi, S., et al. 2005, ApJ, 629, 739

Neugebauer, G., Habing, H. J., van Duinen, R., et al. 1984, ApJ, 278, L1

Noguchi, K., Terashima, Y., Ishino, Y., et al. 2010, ApJ, 711, 144

Orosz, J. A. 2003, in IAU Symposium, Vol. 212, A Massive Star Odyssey: From Main Sequence to Supernova, ed. K. van der Hucht, A. Herrero, & C. Esteban, 365

Osterbrock, D. E. 1989, Astrophysics of gaseous nebulae and active galactic nuclei

Panessa, F., Bassani, L., Cappi, M., et al. 2006, A&A, 455, 173

Pereira-Santaella, M., Diamond-Stanic, A. M., Alonso-Herrero, A., & Rieke, G. H. 2010, ApJ, 725, 2270

Phillips, M. M., Charles, P. A., & Baldwin, J. A. 1983, ApJ, 266, 485

Pier, E. A., & Krolik, J. H. 1992, ApJ, 401, 99

Polletta, M., Courvoisier, T. J.-L., Hooper, E. J., & Wilkes, B. J. 2000, A&A, 362, 75

Poutanen, J., Lipunova, G., Fabrika, S., Butkevich, A. G., & Abolmasov, P. 2007, MNRAS, 377, 1187

Prieto, M. A., Mezcua, M., Fernández-Ontiveros, J. A., & Schartmann, M. 2014, MNRAS, 442, 2145

Puccetti, S., Comastri, A., Fiore, F., et al. 2014, ApJ, 793, 26

Rana, V. R., Cook, III, W. R., Harrison, F. A., Mao, P. H., & Miyasaka, H. 2009, in Proc. SPIE, Vol. 7435, UV, X-Ray, and Gamma-Ray Space Instrumentation for Astronomy XVI, 743503

Rana, V., Harrison, F. A., Bachetti, M., et al. 2015, ApJ, 799, 121

Ricci, C., Ueda, Y., Koss, M. J., et al. 2015, ApJ, 815, L13

Richards, G. T., Fan, X., Schneider, D. P., et al. 2001, AJ, 121, 2308

Richards, G. T., Lacy, M., Storrie-Lombardi, L. J., et al. 2006, ApJS, 166, 470

Rigby, J. R., Diamond-Stanic, A. M., & Aniano, G. 2009, ApJ, 700, 1878

Risaliti, G., Maiolino, R., & Salvati, M. 1999, ApJ, 522, 157

Rivers, E., Baloković, M., Arévalo, P., et al. 2015, ApJ, 815, 55

Rovilos, E., Georgantopoulos, I., Akylas, A., et al. 2014, MNRAS, 438, 494

Sanders, D. B., & Mirabel, I. F. 1996, ARA&A, 34, 749

Sanders, D. B., Mazzarella, J. M., Kim, D.-C., Surace, J. A., & Soifer, B. T. 2003, AJ, 126, 1607

Satyapal, S., Vega, D., Heckman, T., O'Halloran, B., & Dudik, R. 2007, ApJ, 663, L9

Schaerer, D., & Stasińska, G. 1999, A&A, 345, L17

Scharwächter, J., Dopita, M. A., Zuther, J., et al. 2011, AJ, 142, 43

Schlegel, E. M., Jones, C., Machacek, M., & Vega, L. D. 2016, ApJ, 823, 75

Schmidt, M. 1963, Nature, 197, 1040

Setti, G., & Woltjer, L. 1989, A&A, 224, L21

Seyfert, C. K. 1943, ApJ, 97, 28

Shakura, N. I., & Sunyaev, R. A. 1973, A&A, 24, 337

Shimizu, T. T., Mushotzky, R. F., Meléndez, M., et al. 2017, MNRAS, 466, 3161

Silva, L., Granato, G. L., Bressan, A., & Danese, L. 1998, ApJ, 509, 103

Simpson, C., Wilson, A. S., Bower, G., et al. 1997, ApJ, 474, 121

Skrutskie, M. F., Cutri, R. M., Stiening, R., et al. 2006, AJ, 131, 1163

Slipher, V. M. 1917, Proceedings of the American Philosophical Society, 56, 403

Smith, R. K., Brickhouse, N. S., Liedahl, D. A., & Raymond, J. C. 2001, ApJ, 556, L91

Sollerman, J., Cox, N., Mattila, S., et al. 2005, A&A, 429, 559

Sparre, M., Hayward, C. C., Springel, V., et al. 2015, MNRAS, 447, 3548

Stanley, F., Harrison, C. M., Alexander, D. M., et al. 2015, MNRAS, 453, 591

Stern, D., Assef, R. J., Benford, D. J., et al. 2012, ApJ, 753, 30

Stern, D., Lansbury, G. B., Assef, R. J., et al. 2014, ApJ, 794, 102

Strohmayer, T. E. 2009, ApJ, 706, L210

Sutton, A. D., Roberts, T. P., Gladstone, J. C., et al. 2013, MNRAS, 434, 1702

Sutton, A. D., Roberts, T. P., Walton, D. J., Gladstone, J. C., & Scott, A. E. 2012, MNRAS, 423, 1154

Swartz, D. A., Soria, R., Tennant, A. F., & Yukita, M. 2011, ApJ, 741, 49

Tadhunter, C., Dicken, D., Holt, J., et al. 2007, ApJ, 661, L13

Takahashi, T., Mitsuda, K., Kelley, R., et al. 2014, in Society of Photo-Optical Instrumentation Engineers (SPIE) Conference Series, Vol. 9144, Society of Photo-Optical Instrumentation Engineers (SPIE) Conference Series, 25

Telesco, C. M., Pina, R. K., Hanna, K. T., et al. 1998, in Proc. SPIE, Vol. 3354, Infrared Astronomical Instrumentation, ed. A. M. Fowler, 534–544

Terashima, Y., Kunieda, H., & Misaki, K. 1999, PSAJ, 51, 277

Terashima, Y., Ptak, A., Fujimoto, R., et al. 1998, ApJ, 496, 210

Terashima, Y., & Wilson, A. S. 2001, ApJ, 560, 139

Thorne, K. S. 1974, ApJ, 191, 507

Trakhtenbrot, B., Ricci, C., Koss, M. J., et al. 2017, MNRAS, 470, 800

Treister, E., Urry, C. M., & Virani, S. 2009, ApJ, 696, 110

Treister, E., Urry, C. M., Schawinski, K., Cardamone, C. N., & Sanders, D. B. 2010, ApJ, 722, L238

Treister, E., & Urry, C. M. 2012, Advances in Astronomy, 2012, 516193

Tremonti, C. A., Heckman, T. M., Kauffmann, G., et al. 2004, ApJ, 613, 898

Turner, T. J., Miller, L., Reeves, J. N., & Braito, V. 2017, MNRAS, 467, 3924

Ueda, Y., Eguchi, S., Terashima, Y., et al. 2007, ApJ, 664, L79

Ueda, Y., Akiyama, M., Hasinger, G., Miyaji, T., & Watson, M. G. 2014, ApJ, 786, 104

Urry, C. M., & Padovani, P. 1995, PASP, 107, 803

Vasudevan, R. V., Fabian, A. C., Gandhi, P., Winter, L. M., & Mushotzky, R. F. 2010, MNRAS, 402, 1081

Veilleux, S., & Osterbrock, D. E. 1987, ApJS, 63, 295

Veron-Cetty, M.-P., & Veron, P. 1986, A&AS, 66, 335

Vignali, C., Mignoli, M., Gilli, R., et al. 2014, A&A, 571, A34

Villforth, C., & Hamann, F. 2015, AJ, 149, 92

Walton, D. J., Gladstone, J. C., Roberts, T. P., et al. 2011a, MNRAS, 414, 1011

Walton, D. J., Roberts, T. P., Mateos, S., & Heard, V. 2011b, MNRAS, 416, 1844

Walton, D. J., Fuerst, F., Harrison, F., et al. 2013, ApJ, 779, 148

Walton, D. J., Harrison, F. A., Grefenstette, B. W., et al. 2014, ApJ, 793, 21

Wang, L., Baade, D., Höflich, P., et al. 2003, ApJ, 591, 1110

Weaver, K. A., Meléndez, M., Mushotzky, R. F., et al. 2010, ApJ, 716, 1151

Weedman, D. W. 1970, ApJ, 159, 405

Werner, M. W., Roellig, T. L., Low, F. J., et al. 2004, ApJS, 154, 1

Westmeier, T., Braun, R., & Koribalski, B. S. 2011, MNRAS, 410, 2217

White, R. L., Becker, R. H., Gregg, M. D., et al. 2000, ApJS, 126, 133

Willott, C. J., Rawlings, S., Archibald, E. N., & Dunlop, J. S. 2002, MNRAS, 331, 435

Winter, L. M., Veilleux, S., McKernan, B., & Kallman, T. R. 2012, ApJ, 745, 107

Wolter, H. 1952, Annalen der Physik, 445, 94

Woltjer, L. 1959, ApJ, 130, 38

Wright, E. L., Eisenhardt, P. R. M., Mainzer, A. K., et al. 2010, AJ, 140, 1868

Xu, W., Liu, Z., Gou, L., & Liu, J. 2016, MNRAS, 455, L26

Xue, Y. Q., Luo, B., Brandt, W. N., et al. 2011, ApJS, 195, 10

Yaqoob, T. 2012, MNRAS, 423, 3360

Yuan, F., & Narayan, R. 2014, ARA&A, 52, 529

Appendix A

Additional material for Chapter 5

A.1 X-ray spectral fitting results

In this thesis, we have presented the X-ray data and spectral analysis of 7/20 AGNs in our sample. The X-ray data for 8/20 AGNs were not presented in this thesis due to the complexities of their data, which have been analysed in great details by previous works. Here, we present the archival X-ray data and spectral analysis for the remaining 5/20 AGNs in our sample; i.e., NGC 3621, NGC 3627, NGC 3628, NGC 4565 and NGC 5033. The X-ray data for these AGNs have been published in previous literature; however, we have re-analysed their X-ray data for consistency with our analysis techniques. The X-ray images and spectra of these 5 AGNs are shown in Figure A.1 and A.2, respectively. Details of the data used and the spectral extraction are tabulated in Table A.1. For cases with multiple archival X-ray observations, we used those with the longest exposure time. Additionally, for sources which have been observed by both *Chandra* and *XMM-Newton*, we used the *Chandra* data if they reveal significant contaminations by off-nuclear emission that are not resolved in the *XMM-Newton* data; otherwise, we used the *XMM-Newton* data due to its larger effective area (see Chapter 2). The data were reduced following standard procedures as described in Chapter 2. For sources with low signal-to-noise ratio data, we only fitted their spectrum above 2 keV, where the AGN emission is believed to dominate over off-nuclear emission. The results of the best fitting models to the data are tabulated in Table 5.1 in Chapter 5.

Table A.1: X-ray observation log and spectral extraction details.

AGN	RA	Dec	Facility	Date	ObsID	$t_{\rm exp}$ [ks]	Source Region [″]	Spectral Gouping counts/bin
(1)	(2)	(3)	(4)	(5)	(6)	(7)	(8)	(9)
NGC 3621	11:18:16.51	−32:48:50.60	*Chandra*	2008-03-06	9278	23.4	3.0	1
NGC 3627	11:20:14.96	+12:59:29.54	*Chandra*	2008-03-31	9548	50.2	2.5	1
NGC 3628	11:20:16.97	+13:35:22.86	*Chandra*	2000-12-02	2039	58.7	4.0	10
NGC 4565	12:36:20.78	+25:59:15.63	*Chandra*	2003-02-08	3950	60.0	3.0	20
NGC 5033	13:13:27.467	+36:35:38.17	*XMM-Newton*	2002-12-18	0094360501	118.7	30.0	100
			Swift-BAT[a]	2004–2010	...	14580.0	...	...

Notes. Column (1) AGN name; (2-3) RA and Dec of the AGN obtained from NED that were used to extract the spectra; (4) X-ray facilities used for the analysis; (5) Observation date; (6) Observation ID; (7) Exposure time in ks; (8) The size (radius) of the circular aperture used to extract the source spectra in arcsecond; (9) Spectral grouping in units of counts/bin.

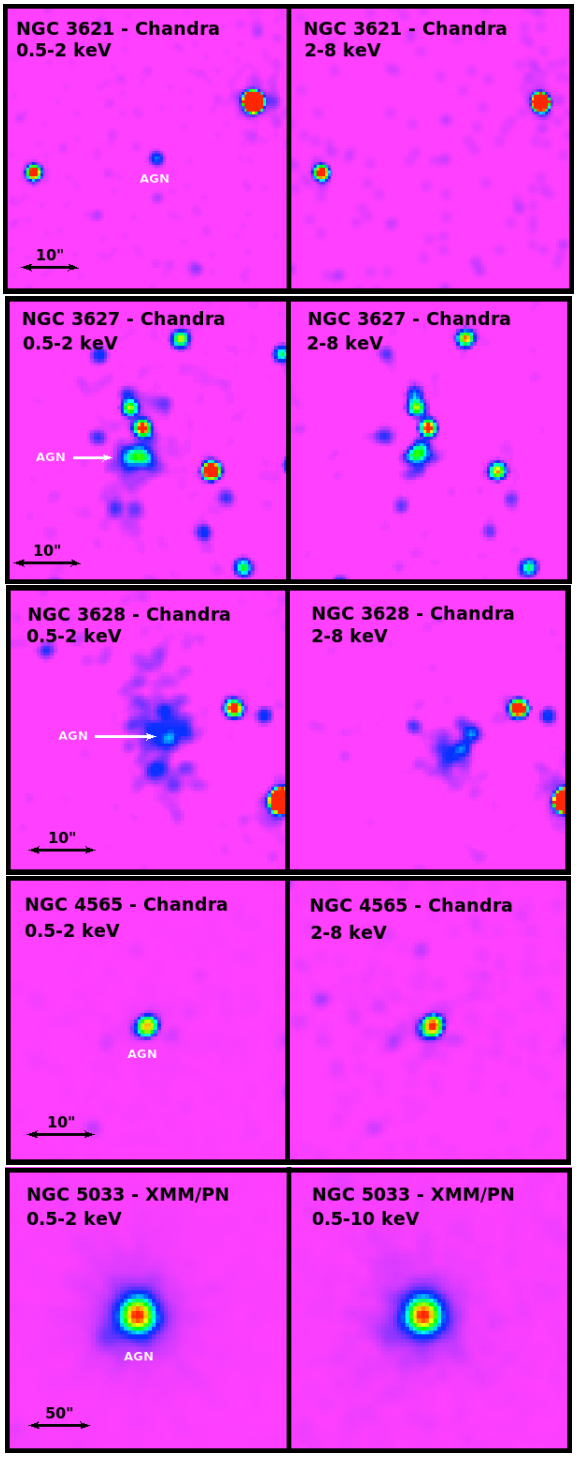

Figure A.1: X-ray images of the five AGNs at different energy bands. Images are smoothed with a Gaussian function of radius 3 pixels corresponding to 1.5″ and 8″ for *Chandra* and *XMM-Newton*, respectively. North is up and east is to the left in all images.

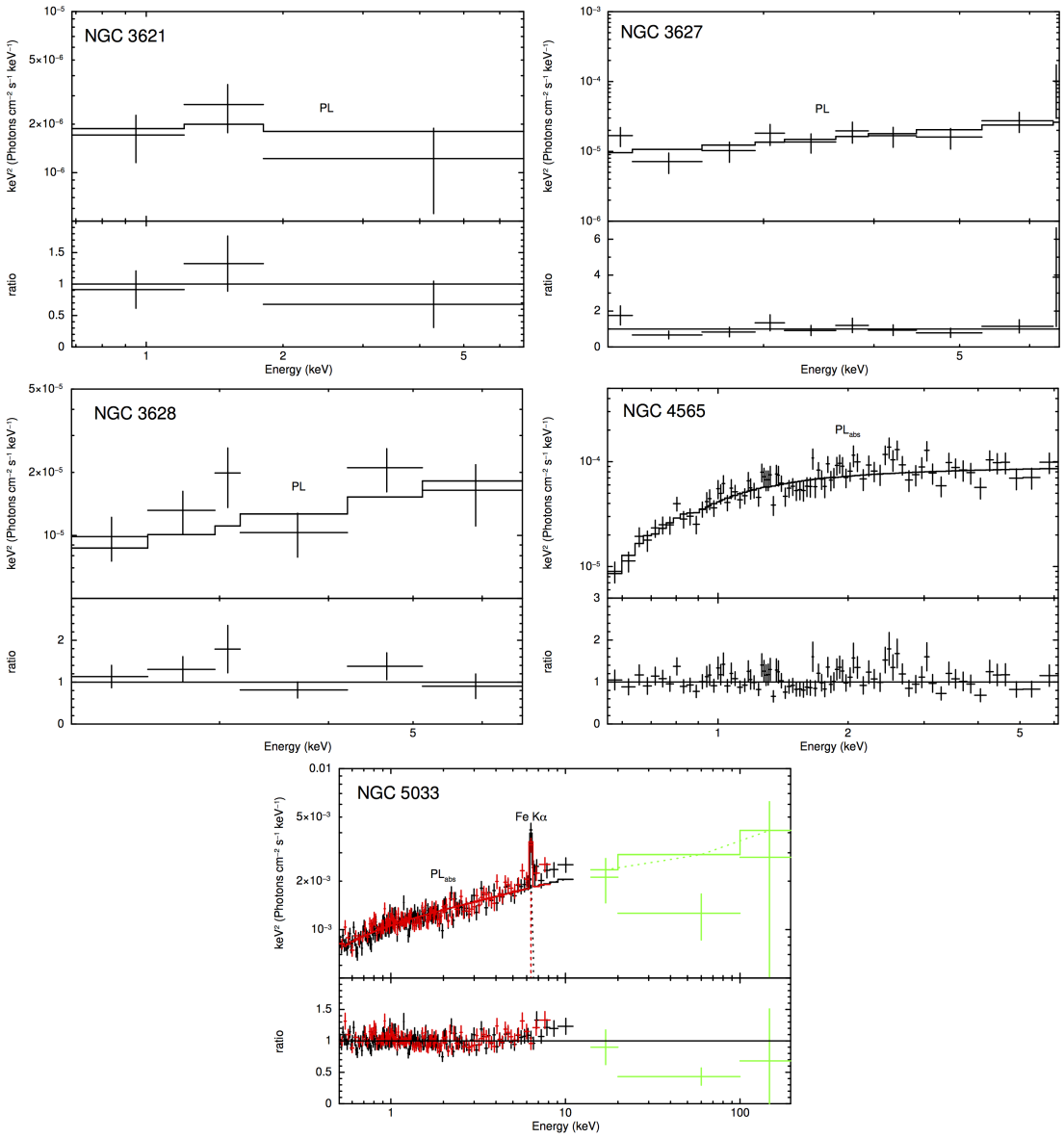

Figure A.2: Best-fitting models to the extracted spectra for each sources. For NGC 5033, black and red indicate the *XMM-Newton* PN and MOS1+2 data, respectively, whilst green indicates the *Swift*-BAT data.

A.2 12μm:[NeV] luminosity relationship

Here, we describe the 12μm:[NeV] luminosity relationship that we derived to help us predict the 12μm luminosities for the AGNs in our sample that have not been observed at high spatial resolution 12μm (i.e., NGC 660, NGC 3621, NGC 4565 and NGC 5195). We derived the relationship using sources in our sample and the *Swift*-BAT AGN sample (Weaver et al., 2010) which have both [NeV] luminosity and 12μm measurements from high spatial resolution observations available. The [NeV] luminosities for the *Swift*-BAT AGNs are given in Weaver et al. (2010), and we obtained their 12μm luminosities from Asmus et al. (2014), if available. We fitted the data using ordinary least square method in *python*, excluding sources with upper limit values. This relation is characterised by equation A.2.1 ($\sigma = 0.50$ dex; Spearman rank, $\rho_s = 0.86$; null hypothesis probability, $\log p =$ - 13.3), and is shown in Figure A.3.

$$\log\left(\frac{L_{12\mu\mathrm{m}}}{10^{43}}\right) = (0.85 \pm 0.07)\log\left(\frac{L_{[\mathrm{Nev}]}}{10^{40}}\right) - (0.13 \pm 0.07) \qquad \text{(A.2.1)}$$

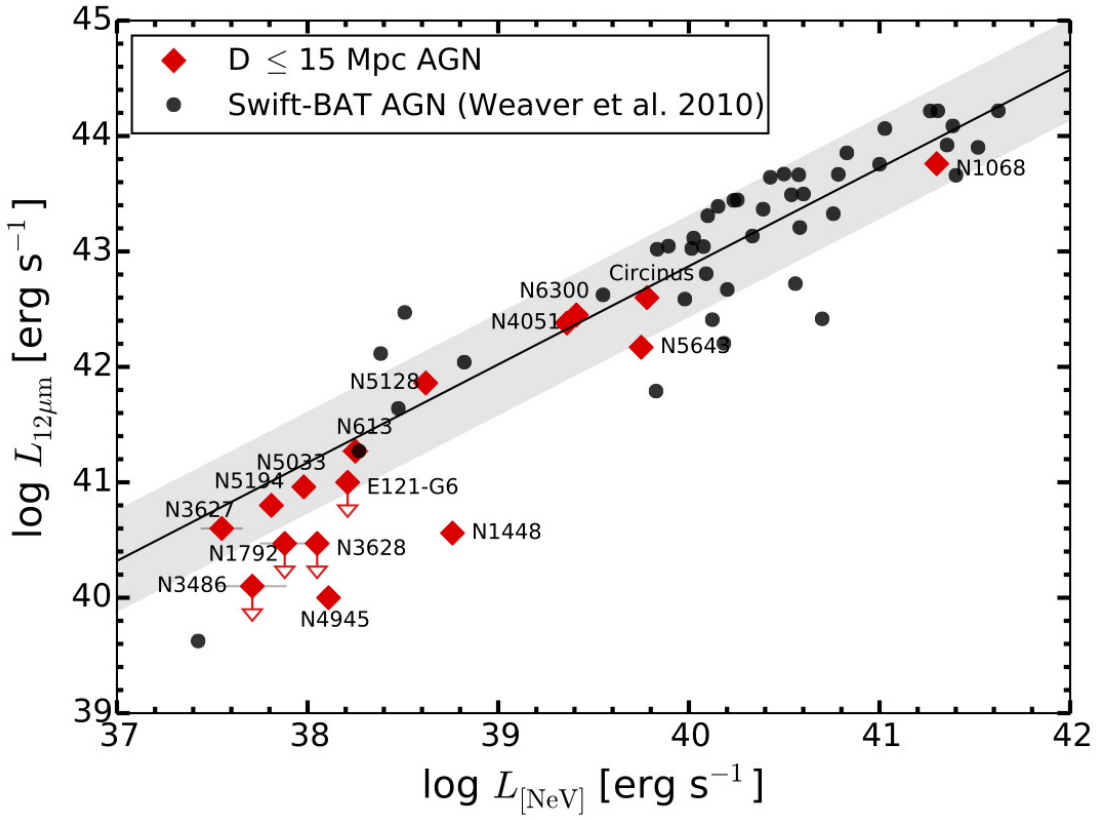

Figure A.3: log $L_{12\mu m}$ vs. log $L_{[NeV]}$ plot for the AGN in our sample (red) and the *Swift-BAT* sample (black) with both [NeV] and high spatial resolution 12μm data available. Solid line indicates the relationship that we derived between the two luminosities (excluding the sources with upper limit measurements), with the scatter of the relation shown in grey.